HYDROGEN PRODUCTION FROM FORMALDEHYDE

A THESIS SUBMITTED TO
THE GRADUATE SCHOOL OF NATURAL AND APPLIED SCIENCES
OF
MIDDLE EAST TECHNICAL UNIVERSITY

BY

CAN AĞCA

IN PARTIAL FULFILLMENT OF THE REQUIREMENTS
FOR
THE DEGREE OF MASTER OF SCIENCE
IN
CHEMICAL ENGINEERING

AUGUST 2016

Approval of the thesis:

HYDROGEN PRODUCTION FROM FORMALDEHYDE

submitted by **CAN AĞCA** in partial fulfillment of the requirements for the degree of **Master of Science in Chemical Engineering Department, Middle East Technical University** by,

Prof. Dr. Gülbin Dural Ünver
Dean, Graduate School of **Natural and Applied Sciences** _____

Prof. Dr. Halil Kalıpçılar
Head of Department, **Chemical Engineering** _____

Prof. Dr. Naime A. Sezgi
Supervisor, **Chemical Engineering Dept., METU** _____

Prof. Dr. Timur Doğu
Co-Supervisor, **Chemical Engineering Dept., METU** _____

Examining Committee Members:

Prof. Dr. Güzide Çalık
Chemical Engineering Dept., Ankara University _____

Prof. Dr. Naime Aslı Sezgi
Chemical Engineering Dept., METU _____

Asst. Prof. Dr. Zeynep Tutumlu
Dept. of Material Science and Nanotechnology, TOBB ETÜ _____

Asst. Prof. Dr. Harun Koku
Chemical Engineering Dept., METU _____

Asst. Prof. Dr. İnci Ayrancı
Chemical Engineering Dept., METU _____

Date: 22.08.2016

I hereby declare that all information in this document has been obtained and presented in accordance with academic rules and ethical conduct. I also declare that, as required by these rules and conduct, I have fully cited and referenced all material and results that are not original to this work.

Name, Last name : Can AĞCA

Signature :

ABSTRACT

HYDROGEN PRODUCTION FROM FORMALDEHYDE

Ağca, Can
M.Sc., Department of Chemical Engineering
Supervisor: Prof. Dr. Naime Aslı Sezgi
Co-Supervisor : Prof. Dr. Timur Doğu

August 2016, 184 pages

Climate change and more efficient energy system research have directed researchers to fuel cells related fields. There is much interest in onboard fuel cell vehicles nowadays. Polymer electrolyte membrane fuel cells (PEMFC) are very widely used and commercial onboard systems are readily on sale. Rather than pressurized hydrogen, much safer liquid hydrogen feedstock such as methanol and ethanol are being used. However, fuel cell's platinum catalyst requires low amounts of carbon monoxide in the cell feed. This study focuses on new reaction types and catalyst syntheses that can produce low amounts of CO. Formaldehyde steam reforming (FSR) is thought to be producing syngas having low amount of CO compatible with the PEMFC at low temperatures.

As support materials SBA-15 synthesized by hydrothermal method and CMK-3 synthesized by nanocasting were used. 18 wt. % of metal loading to SBA-15 and CMK-3 mesoporous supports was performed by wet impregnation method. Their chemical and physical properties were investigated by XRD, N_2 physisorption, XPS, ICP, SEM, TGA and FTIR.

CuZn/SBA-15, Cu/SBA-15 and CuZn/CMK-3 had BET surface areas of 381 m^2/g, 394 m^2/g, and 548 m^2/g, respectively. Pore diameters were 4.80 nm for both CuZn/SBA-15 and Cu/SBA-15, and 3.86 nm for CuZn/CMK-3. The behavior of CuZn/SBA-15 and Cu/SBA-15 catalysts resembled Type IV isotherm behavior with H1 type hysteresis loop. On the other hand, CuZn/CMK-3 showed Type IV isotherm with H2 hysteresis loop. Crystal size of copper increased after activity tests. All the synthesized catalysts had acid sites in their structure except the CuZn/CMK-3 catalyst.

A commercial copper based catalyst's (HIFUEL R120) activity was tested by a fixed-bed flow reactor system between 175-250°C. Other three synthesized catalysts were tested only at 250°C.

HIFUEL R-120 converted formaldehyde 100 % at even low temperatures. Hydrogen yield increased with increasing temperature and reached to its maximum theoretical value at 250°C. Furthermore, CO was not formed, except for startups at 225 and 250°C in the presence of HIFUEL R-120 catalyst. These traits show the suitability of the catalyst and reaction for PEMFC applications.

Cu/SBA-15 was also found the most active one among the synthesized catalysts. However, it lost its activity fast over time due to instability. Zn addition was found to increase stability of catalyst and dispersion of copper efficiently with less crystal size as in the CuZn/SBA-15 catalyst. Zn addition to Cu/SBA-15 was also found to increase the acidity of the catalyst. CuZn/CMK-3 had stability, but had also insufficient activity for methanol and formaldehyde steam reforming due to lack of acidic properties. The synthesized catalysts did not produce any CO. They all are also suitable for PEMFC systems.

In the activity tests of FSR reactions, HIFUEL R-120 resulted in the most successful in terms of overall and methanol conversion, product selectivity and hydrogen yield amongst all the tested catalysts.

Keywords: Steam Reforming, Formaldehyde, Hydrogen, Mesoporous Catalyst, CMK-3, Copper, Zinc

ÖZ

FORMALDEHİTTEN HİDROJEN ÜRETİMİ

Ağca, Can
Yüksek Lisans, Kimya Mühendisliği Bölümü
Tez Yöneticisi : Prof. Dr. Naime Aslı Sezgi
Ortak Tez Yöneticisi : Prof. Dr. Timur Doğu

Ağustos 2016, 184 sayfa

İklim değişikliği ve daha verimli enerji sistem araştırmaları, araştırmacıları yakıt piliyle alakalı alanlara yönlendirmektedir. Günümüzde yakıt piliyle çalışan araçlara da artan bir ilgi vardır. Polimer elektrolit membranı yakıt pilleri (PEMFC) çok yaygın olarak kullanılmaktadır ve bunların ticari olan araçları halihazırda piyasada bulunmaktadır. Yüksek basınçlı hidrojen yerine metanol ve etanol gibi daha emniyetli hidrojen kaynağı sıvılar kullanılmaktadır. Bu yakıt pillerinin platinyum katalizörü besleme gazında düşük miktarda karbon monoksit içermelidir. Bu çalışmada düşük miktarda CO üreten yeni reaksiyon türleri ile katalizör sentezleri üzerinde yoğunlaşılmıştır. Buharlı formaldehit reformlaması (FSR) düşük sıcaklıklarda ürettiği sentez gazında PEM yakıt pillerine uygun, düşük miktarda CO üreteceği düşünülmüştür.

Destek malzemesi olarak hidrotermal metoduyla sentezlenen SBA-15 ve nanodöküm yoluyla sentezlenen CMK-3 kullanılmıştır. Mezogözenekli destek malzemeleri SBA-15 ve CMK-3'e kütlece % 18 oranında metal yüklemesi ıslak impregnasyon yöntemiyle yapılmıştır. Bunların fiziksel ve kimyasal analizleri XRD, N_2 fizisorpsiyon, XPS, ICP, SEM, TGA ve FTIR ile incelenmiştir.

CuZn/SBA-15, Cu/SBA-15 ve CuZn/CMK-3 sırasıyla 381 m^2/g, 394 m^2/g, and 548 m^2/g BET yüzey alanlarına sahiptir. Gözenek çapları CuZn/SBA-15 ve Cu/SBA-15 için 4.80 nm, CuZn/CMK-3 için 3.86 nm'dir. CuZn/SBA-15 ve Cu/SBA-15 katalizörleri 4. Tip izoterm ve H1 tipi histeresis döngüsü göstermişlerdir. Öte yandan CuZn/CMK-3 4. Tip izoterm ile H2 tipi histeresis döngüsü göstermiştir. Bakırın kristal boyutu aktivite testlerinin ardından artmıştır. CuZn/CMK-3 katalizörü hariç bütün sentezlenen katalizörlerin yapısında asit bölgeleri vardır.

Ticari bakır bazlı katalizörün (HIFUEL R120) aktivitesi bir sabit yataklı akışkan reaktör sisteminde 175-250°C sıcaklıkları arasında test edilmiştir. Diğer sentezlenen üç katalizör ise sadece 250°C'de test edilmiştir.

HIFUEL R-120, formaldehiti düşük sıcaklıklarda bile % 100 dönüştürmüştür. Hidrojen verimi artan sıcaklıkla birlikte artarak 250°C'de maksimum teorik değerine ulaşmıştır. Dahası, HIFUEL R-120 katalizörünün 225 ve 250°C'deki başlama evreleri hariç, CO oluşmamıştır. Bu özellikler, katalizörün ve reaksiyonun PEM yakıt pili uygulamalarına uygunluğunu göstermektedir.

Cu/SBA-15 de sentezlenen katalizörler içerisinde en aktifi bulunmuştur. Ancak, katalizör, aktivitesini kararsızlık sebebiyle hızla kaybetmiştir. CuZn/SBA-15 katalizöründeki gibi, katalizöre Zn eklenmesi kararlılığını ve içerisindeki bakır dağılımını verimli bir biçimde artırmış ve kristal boyutunu azaltmıştır. Cu/SBA-15'e Zn eklenmesinin aynı zamanda katalizörün asitliğini artırdığı bulunmuştur. CuZn/CMK-3 kararlılık göstermiş, ama aynı zamanda asitlik özellikleri olmadığı için metanol ve formaldehit buhar düzeltiminde yetersiz aktivite göstermiştir. Sentezlenen katalizörler CO üretmemiştir. Bu katalizörler de PEM yakıt pili sistemlerine uygundur.

FSR reaksiyonlarının aktivite testlerinde, HIFUEL R-120 genel ve metanol dönüşümleri, ürün seçiciliği ve hidrojen verimi bakımından bütün katalizörler içerisinde en başarılı olarak bulunmuştur.

Anahtar Kelimeler: Buharlı Reformlama, Formaldehit, Hidrojen, Mezogözenekli Katalizör, CMK-3, Bakır, Çinko

To my Dear Family

ACKNOWLEDGMENTS

In the completion of thesis, Prof. Dr. Naime Aslı Sezgi's support and guidance cannot be forgotten. She taught me everything she could without hesitation. I gained countless experiences near her. I am sincerely thanking her for what she did for me in these two years. Prof. Dr. Timur Doğu opened my eyes to chemical reaction engineering area and always supported me with futuristic ideas. I acknowledge him for his continuous support over me. Furthermore, I cannot express my gratitude towards my teachers in my whole education life and my professors in our department.

Prof. Suna Balcı and her master's student Gülce Açıl assisted me with the DRIFTS analyses making a contribution to this thesis. I appreciate their kindness and time. My dear fellow Mehmet Çağırıcı of Metallurgical and Materials Engineering Department aided me with additional SEM analyses. I acknowledge him not only for that but for being a good fellow also.

In these two years, I have also learnt that we have golden people here working with us. İsa Çağlar and Süleyman Nazif Kuşhan not only helped me with my thesis work, but also taught me some fundamentals about life that I did not know. One can never know how motivating it is to join the lunch with Machine Shop personnel. Gülten Orakçı was always there for me when I needed something. My conversations with Yüksel Karataş were unique. I will always remember their friendship and it was a pleasure for me to work with them. I am also thankful for Yavuz Güngör, Gazi Saranay, Erkan Kapısuzoğlu, Adil Demir, Naciye Kaya, Gülüstan Görmez, Derviş Ali Mete, Kemal Yıldırım, Mihrican Açıkgöz, Cemil Araçlı, Selahattin Battal, Mustafa Cansuyu, Ertuğrul Özdemir, Mahmut Akdağ, Arap İşleyen, Sedat Taşbaşı.

I have had good friends in Kinetic lab. I cannot express my gratitude towards Saygın Aras. He made me think critically and ask questions about what I do. I have gained

so much experience near him. He is a successful fellow and deserves my acknowledgment. Arzu Arslan was always there when I needed help. I appreciate Burçin İkizer for her friendship and guidance. Saeed Khan was a good roommate and companion. I am also thankful for İlker Şener and Pınar Değirmencioğlu.

All this time, my friends never let me down. I am thankful for Özge Bacık, İlker Tezsevin, Ezgi Akalın, Semih Okyay, Ahmet Emiroğlu, Mustafa Öncül, Utku Yalçın, Elif Kıratlı, Öznur Doğan, Bebeta Hoxha, Cansu Demirtaş, Elif Demet Çalışkan, Mertcan Geyin, Talha Güneş, Satı Ömercan, Yaşar Küçük, Özgül Özdemir, Metin Sırt, Bengüsu Tezel Tanrısever, Burak Eke, Selin Bora, Şükrü Ersoy, Cem Aksoy, Batıkan Şencan, Oğuzhan Sarıalp, Atalay Çalışan, Fatma Şahin, Sevil Demirci, Anıl Kaya, Ufuk Atılmış, Selami Yılmaz, Ahmet Çiçekli and countless others that I could not write here.

The study in this thesis is financially supported solely by METU Scientific Research Coordination, to which I acknowledge, through funds of BAP-07-02-2014-460, BAP-03-04-2014-003 and BAP-03-04-2015-003.

I would like to thank METU Central Lab personnel for their support and small lectures for analyses during my thesis work.

It has been two years since I stepped foot into the academic world. I tried my best to keep up with every work I was assigned to. However, these two years were really hard. Fortunately, my dear family was with me at times desperation, sickness and happiness, guiding me through this road all the times. Therefore, my most sincere appreciations are to Metin, Canan and Mert. I know that my brother will be the best geologist of the planet soon. I thank for my uncle Murat, aunt Çiğdem and cousin İrem that they have never hesitated to support me all this time. I hope İrem will be a great scientist in the future. I appreciate my grandmother Rabiye and grandfathers Naci and Selahattin for their care and wisdom.

TABLE OF CONTENTS

LIST OF TABLES

TABLES

LIST OF FIGURES

FIGURES

NOMENCLATURE

$\hat{a}_i$: Activity of species i

A_i: GC Peak area under the curve of species i

B: Full width at half max, radian

c: Crystal shape factor

$C_{G,total}$: Total gas concentration, mol/ml

$\tilde{C}_{pi}^{o}$: Constant-pressure heat capacity of species i, J/mol.K

E_j: Conservation of elements term

$F_{C,total}$: Total molar flowrate of carbonaceous compounds

$F_{i,G}$: Molar flowrate of gaseous species i, mol/min

$F_{i,L}$: Molar flowrate of liquid species i, mol/min

G_{mix}: Gibbs free energy of mixture

$\bar{G}_i$: Partial molar Gibbs free energy of species i, J/mol

$\tilde{G}_i^o$: Molar Gibbs free energy of species i at the reference state, J/mol

$\tilde{G}_{rxn}^{o}$: Molar Gibbs free energy of reaction at the reference state, J/mol

$\tilde{H}_f^o$: Heat of formation at the reference state, J/mol

$\tilde{H}_{rxn}^{o}$: Heat of reaction at the reference state, J/mol

K_{eq}: Equilibrium constant

M: Gathered liquid mass, g

m_L: Liquid mass flowrate, g/min

MW_i: Molecular weight of species i, g/mol

$N_{C,total}$: Total number of moles of carbonaceous compounds in the system

$N_{G,total}$: Total number of moles of gas in the system

n_i : Number of moles of species i

$N_{i,0}$: Initial moles of species i

$N_{tot,0}$: Total number of moles initially

P: Pressure, Pa

P^o: Pressure at the reference state, Pa

Q_{Ar}: Volumetric flowrate of Argon, ml/min

Q_i: Volumetric flowrate of species i, ml/min

Q_{others}: Gaseous volumetric flowrate of the analysis gas mixture without Argon

Q_{total}: Total volumetric flowrate of the gas, ml/min

R: Gas constant, J/mol.K

S_i: Selectivity of species i

T: Temperature, K

$t_{particle}$: Particle size, nm

$X_{methanol}$: Methanol Conversion

X_{FA}: Formaldehyde Conversion

$x_{i,0}$: Initial mole fraction of liquid species i

x_i: Mole fraction of liquid species i

$X_{overall}$: Overall Conversion

$Y_{H2,max}$: Theoretical maximum hydrogen yield

Y_{H2}: Hydrogen yield

y_i: Mole fraction of gaseous species i

Greek Letters

α: Ratio of initial number of moles of methanol to formaldehyde

β_i: GC calibration factor for species i

λ_j: Molar Gibbs free energy of pure species j

λ: Wavelength of radiation, nm

ρ_L: Density of liquid, g/nl

θ: Bragg angle, °

ξ_j: Elemental species

$\widehat{\varphi}_i$: Fugacity coefficient of species i

τ: Reaction time (min)

Abbreviations

AMS-10: Anionic-surfactant-templated Mesoporous Silica-10

BET: Brunauer Emmett Teller

BJH: Barrett Joyner Halenda

CFC: Chlorofluorocarbon

CHP: Combined Heat and Power

CMK-3: Carbon Mesostructures from KAIST-3

DFT: Density Functional Theory

DRIFTS: Diffuse Reflectance Infrared Fourier Transform Spectroscopy

EDTA: Ethylenediaminetetraacetic acid

EDX: Energy Dispersive X-Ray Spectroscopy

EIA: U.S. Energy Information Administration

FA: Formaldehyde

FDU-5: FuDan University-5

FSR: Formaldehyde Steam Reforming

FTIR: Fourier Transform Infrared

GC: Gas Chromatograph

HAADF-STEM: High Angle Annular Dark Field-Scanning Transmission Electron Microscopy

HEDTA: (2-Hydroxyethyl) ethylenediaminetriacetic acid

HHV: Higher Heating Value, MJ/kg

IBN-1: Institute of Bioengineering and Nanotechnology

ICE: Internal Combustion Engine

ICP: Inductive Couple Plasma

IUPAC: International Union of Pure and Applied Chemistry

KIT-6: Korean Advanced Institute of Technology-6

LHV: Lower Heating Value, MJ/kg

MCF: Mesocellular Foam

MCM-41: Mobile Company of Matter-41

MS: Mass Spectrometer

MSR: Methanol Steam Reforming

NASA: National Aeronautics and Space Administration

NOAA: National Oceanic and Atmospheric Administration

PEMFC: Polymer Exchange Membrane Fuel Cell

R&D: Research & Development

SBA-15: Santa Barbara Amorphous-15

SEM: Scanning Electron Microscopy

STP: Standard Temperature Pressure

TCD: Thermal Conductivity Detector

TEM: Transmission Electron Microscopy

TEOS: Tetraethyl Orthosilicate

TGA: Thermogravimetric Analysis

TPD: Temperature-programmed Desorption

WGS: Water Gas Shift

WHO: World Health Organization

XPS: X-Ray Photoelectron Spectroscopy

XRD: X-Ray Diffraction

CHAPTER 1

INTRODUCTION

Changing climate and fossil fuel depletion led companies and researchers to green and novel technologies for energy production and use.

Firstly, the climate change is vital and should be dealt with. The Earth's climate has changed over the years visibly that the average global temperature rises slowly. However, for the years 2014 and 2015, the average global temperature rise values are reported as 0.74 and 0.90, respectively, much higher than the other 14 warmest years (National Centers for Environmental Information (NOAA), 2016). This temperature rise is caused by human-made industrial activities exposing environment to high levels of greenhouse gases such as carbon dioxide and methane. Before the average global temperature is critical, strict measures must be taken to release less or almost no greenhouse gases to the atmosphere.

The second aspect of looking for novel energy technologies is that crude oil is an unsustainable source and prone to depletion. Most of the transportation system currently uses crude oil products (gasoline, kerosene, diesel) as the energy source. Although there is a changing trend towards electric cars and buses, electrical transportation systems will take a few decades to be a standard. Furthermore, electricity production is also not 100 % sustainable, yet. Novel, more efficient sources in the energy production are required for some years before sustainable energy production becomes acceptable for the World energy demand.

Hydrogen is one of the energy sources that can be used in this temporary changing years through sustainable energy production. Fuel cell technology, which uses hydrogen as the resource, has improved over time that commercial products run by

fuel cells can be found on vehicles such as automobiles, space shuttles. Therefore, hydrogen production became of importance for energy companies, in addition to its other uses in chemical processes. Steam reforming of carbonaceous molecules has been proven to be economic and used as the common hydrogen producing process in chemical plants. Methane is currently very widely used in steam reforming plants and operates at high temperature and pressure. For small processes such as on board fuel cell vehicles methanol can be used for its lower operating temperature (200-350°C) and atmospheric to a few bars of pressure. $Cu/ZnO/Al_2O_3$ commercial catalysts are employed in methanol reformers. However, CO produced by methanol reforming poisons polymer electrolyte membrane fuel cell's platinum catalyst. Catalyst poisoning starts at CO concentration of 10 ppm and tolerable upto 1 vol. % (Peters, 2008). Furthermore, calculations proved that methanol reforming releases less CO_2 than gasoline-run internal combustion engines (Olah *et al.*, 2011)

New research is focused on reforming processes producing tolerable or no CO in the product. Formaldehyde has been recently found to be forming almost no CO in steam reforming reactions (Lorenz *et al.*, 2013). Aside from gas phase reactions, there are experiments carried out using liquid phase reactors proving that formaldehyde produces hydrogen and CO_2 (Bi & Lu, 2008; Heim *et al.*, 2014; Li *et al.*, 2014). Nonetheless, experimental studies with formaldehyde have not proven the features of the reaction extensively. Besides, there are theoretical density functional theory studies proving that steam reforming of formaldehyde produces CO_2 (Bo *et al.*, 2009).

Mesoporous materials have gained importance in several fields such as catalysis, engineering and electronics. Ordered mesoporous silica materials are particularly suitable for catalyst supports, due to their high surface area, pore volume and tunable ordered channels making it feasible for a reactive site. These materials have been studied in the literature since 1990s (Beck *et al.*, 1992; Zhao *et al.*, 1998) and there is still ongoing research to understand the features of these materials. Furthermore, ordered mesoporous carbons such as Carbon Mesostructures from KAIST-3 (CMK-3) are feasible for their higher surface area than ordered mesoporous silica counterparts (Jun *et al.*, 2000).

As stated, formaldehyde steam reforming has not been studied sufficiently, and this thesis work was carried out to enlighten some kinetic data and obtain crucial information. In gas phase, formaldehyde reacts with water to produce hydrogen, carbon dioxide and carbon monoxide. Thermodynamic calculations show that carbon monoxide concentration can be sufficiently low for onboard fuel cell vehicles. Since the reaction mechanism is thought to be very similar to the methanol steam reforming, copper based catalyst can be very active in formaldehyde steam reforming. There are studies synthesizing ordered mesoporous copper based catalysts with high loading to be used in methanol synthesis (Munnik *et al.*, 2011; Prieto *et al.*, 2013). These synthesis procedures can also be applied with ordered mesoporous SBA-15 and CMK-3 supports.

The thesis work can be classified as: literature survey, catalyst syntheses, characterization of the catalysts and the activity tests. First, necessary information about the support materials, catalyst active sites and formaldehyde steam reforming reaction was gathered. Secondly, support materials SBA-15 and CMK-3 were synthesized. Their exact synthesis procedure was prescribed and applied each time. Synthesizing catalyst supports, active sites copper and zinc were loaded to these support by wet impregnation technique. Thirdly, these catalysts were characterized by nitrogen physisorption, XRD, XPS, ICP, SEM, TGA and FTIR. Finally, synthesized catalysts' activities were tested in a packed bed reactor.

CHAPTER 2

CLIMATE CHANGE AND HYDROGEN AS FUEL FOR FUTURE GENERATIONS

Speculations about climate change have continued for decades. Many institutions such as National Aeronautics and Space Administration (NASA), National Oceanic and Atmospheric Administration (NOAA) conduct vast research on how the climate has changed over the years. Nowadays, no research funding is needed: climate change is real and can be observed by bare eyes; although it had been expected for the years to come. Humankind is at the step of changing the environment and see the results how it can affect the nature and countless lives because of the need of energy. Furthermore, another problem still persists that the fossil fuels those produce majority of the current energy is depleted and soon will be at a level that cannot sustain the energy demand. It will become evident that the solution for energy crisis lies in hydrogen, the most abundant molecule of cosmos.

2.1. CLIMATE CHANGE IS REAL

Industrial revolution started with the invention of steam engines and conversion of heat to useful mechanical work. It was one of the most important steps in human history. As technology moved forward, the thermal efficiency of all types engines increased, i.e., heat rejection with the same amount of fuel dropped down dramatically. However, majority of fuels used in energy generation today are from carbon sources that produce greenhouse gas upon use. Carbonaceous gas release such as CO_2 and CH_4 (what natural gas consists of) captures most of the heat coming from the sun and traps it in the atmosphere, a phenomenon called “Greenhouse Effect”. According to U.S. Energy Information Administration (EIA), 4 trillion

kilowatt-hours of electricity was generated in 2015 of which 67 % was produced from the fossil fuels (coal, natural gas and petroleum). Only 7 % of the energy was derived from renewable sources such as biomass, geothermal, solar and wind (https://www.eia.gov/tools/faqs/faq.cfm?id=427&t=3, 2016). As a result, the soil and the oceans heat up gradually.

Findings on climate change due to greenhouse gases are not new; it is a series of research started more than a century ago. In 1896, Svante Arrhenius estimated that if the carbon dioxide amount increases to 2.5-3 times its value at his time, temperature would rise about 8-9°C in the Arctic regions. He concluded that this would cause Arctic ice to melt completely and allow for temperature values sustaining vegetation and animal life (Arrhenius, 1896). Assembling evidences from different measurement stations around the planet Guy S. Callendar (1938) showed that rise in CO_2 amount and global average temperature are connected. Later, Callendar supplied data from 19th and 20th centuries to show how CO_2 level changes. Figure 2.1. shows his observatory results in North Atlantic Region over the years (Callendar, 1958).

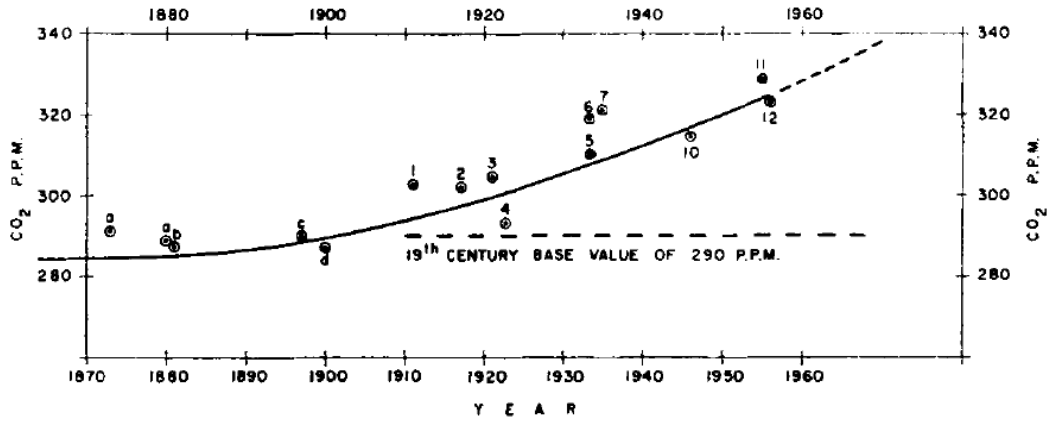

Figure 2.1: Amount of CO_2 in the free air of North Atlantic regions between 1870-1956 (adapted from Callendar, 1958)

Another comparison between normal climate cycle (Camp Century cycle) and CO_2 affected trend was shown in Figure 2.2. It is clear from the figure that at the dawn of 21st century average global temperature is subject to a runaway. Broecker (1975) estimated the current temperature back in 40 years ago with a slight error.

According to measurements atmospheric CO_2 increase was from 280-300 ppm to 335-340 ppm between 1880 and 1980 with the major cause of fossil fuel use in energy generation activities. Average temperature change for this century was estimated to be 2.5°C with slow energy growth and accompanied renewable energy sources which would be the same as Mesozoic period, age of dinosaurs (Hansen, *et al.*, 1981).

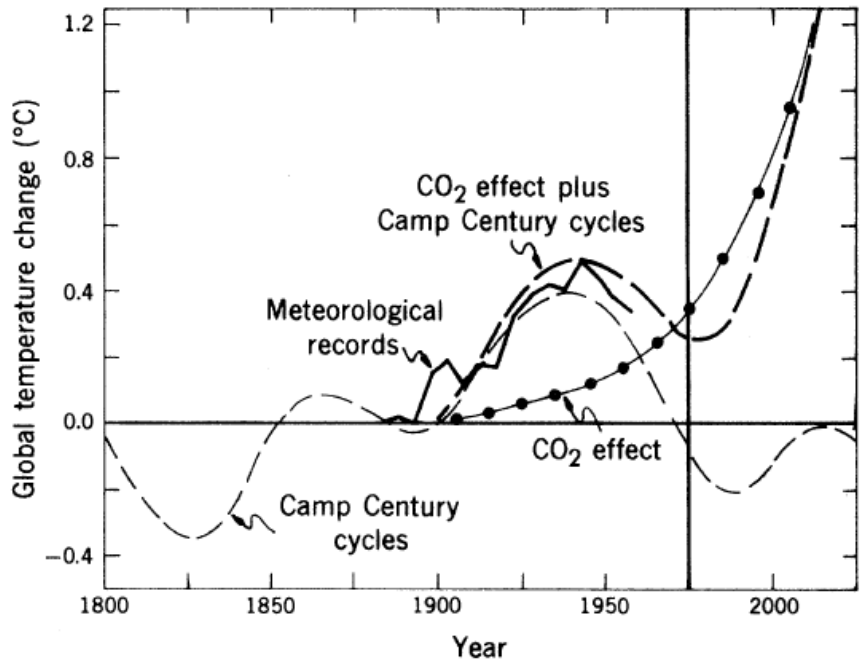

Figure 2.2: Curves for global temperature change due to manmade CO_2 emission (adapted from Broecker, 1975)

Latest data from NASA shows that average global temperature increase is 0.87°C as of January 2015 and CO_2 level is 403.28 ppm as of March 2016.

In addition, new research findings have shown that the acidity of oceans has risen up over the years, parallel to the CO_2 level in the atmosphere (Dean, 2009). This can lead to loss animal and plant life that has also a great impact on the equilibrium of the planet.

Every problem has a solution in all engineering disciplines. An example in which humankind overcame a serious environmental problem can be the ozone layer crisis in 1980s. Chlorofluorocarbon (CFC) emissions causing a great “ozone hole” in

Antarctica were banned the consensus worldwide. A study by NASA Scientists revealed that the hole started to shrink after 30 years of its discovery (Strahan *et al.*, 2014). Climate change can also be overcome in a similar manner. However, world economies and energy sources still depend on carbonaceous compounds. Therefore, the solution may be step by step: increasing the efficiency of carbon energy engine cycles to its maximum in the short term and later shifting to hydrogen and solar energy sources completely. All it takes is to act responsibly.

2.2. HISTORY AND PROPERTIES OF HYDROGEN

Hydrogen derives from words “hydro” and “genes” in Greek having the meaning of water former. Hydrogen is the first formed (after big bang) and the most abundant atom and molecule in the known universe. It contains 1 proton and 1 electron in the most stable form and two isotopes also exist, namely, deuterium (symbolized by D with 1 neutron) and tritium (symbolized by T with two neutrons). On earth’s surface, at standard temperature and pressure hydrogen is in the form of diatomic gaseous (H_2) molecules. It is colorless, odorless, tasteless and highly inflammable gas with molecular weight of 2. All three isotopes of hydrogen molecule exist in a mixture of molecular isomers with different nuclear spins, say, for H_2 ortho-hydrogen (o-H_2) and para-hydrogen p-H_2. Mixture of these two isomers at ambient temperature is called normal hydrogen (n-H_2) containing 25 % (mol) p-H_2 and 75 % o-H_2. Conversion from ortho to para isomers is exothermic. Properties of normal and para-hydrogen molecules at STP can be found in Table 2.1.

Hydrogen molecule was discovered by several scientists at different times. For example, Henry Cavendish (1731-1810) found that when metals dissolved in acids, they had formed inflammable air that is hydrogen. Another instance was when Antoine Lavoisier (1743-1794) passed water from a heated copper tube, he witnessed split of hydrogen and oxygen. In 19^{th} century, electrolysis of water was accomplished by Carlyle and Nicholson, and a century later first commercial electrolysis plant was realized in 1902 by Maschinenfabril Oerlikon in Switzerland.

Table 2.1: Properties of normal and para-hydrogen molecules at STP (adapted from Lauermann *et al.*, 2013)

	p-Hydrogen	*n*-Hydrogen
Properties at IUPAC STP (273.15 K, 100 kPa)		
Density, kg/m^3	0.08871	0.08871
Molar heat capacity		
C_p, J mol^{-1} K^{-1}	30.361	28.621
C_v, J mol^{-1} K^{-1}	22.042	20.301
Viscosity, mPa s	8.397×10^{-3}	8.3969×10^{-3}
Velocity of sound, m/s	1246.5	1261.1
Thermal conductivity, W m^{-1} K^{-1}	182.44×10^{-3}	172.58×10^{-3}
Dielectric constant	1.00027	1.00027
Compressibility factor	1.0006	1.0006
Prandtl number	0.6932	0.6908

E. W. Justi in Germany was the first to describe hydrogen as energy carrier medium in 1955. A common sense by famous engineers (T. N. Veziroğlu, J. O. M. Bockris, D. P. Gregory, C. Marchetti) in 1969 led to development of an overall hydrogen energy concept thanks to favorable chemical and thermodynamic properties of hydrogen. Currently, hydrogen is used as a feedstock in various industries with a worldwide production of 31.330 x 10^6 tons/year of which 20.485 tons/year is produced in USA (Lauermann *et al.*, 2013).

2.3. HYDROGEN PRODUCTION TECHNIQUES

Hydrogen production varies according to use of product afterwards. It can be produced as pure hydrogen or as a part of mixture called syngas. Syngas is mainly a mixture of CO, CO_2, H_2 and it is called syngas due to its wide range possible routes for synthesis of many chemicals in the industry. Uses of different syngas mixture ratios are given in Table 2.2.

Table 2.2: The Uses of Syngas at Different Ratios (Moulijn *et al.*, 2013)

Mixtures	Main Uses
H_2	Hydrotreating & Hydrocracking, Fuel Cells
3 H_2 : 1 N_2	Ammonia
2 H_2 : 1 CO	Substitute Natural Gas (SNG)
2 H_2 : 1 CO	Alkenes (Fischer – Tropsch Synthesis)
2 H_2 : 1 CO	Methanol (or Higher Alcohols)
1 H_2 : 1 CO	Aldehydes (Hydroformulation)
CO	Acids (Acetic and Formic)

There are several major hydrogen production techniques in chemical process industry.

2.3.1. Steam Reforming Reactions

Steam reforming is one of the most commonly used hydrogen production techniques for almost a century. It is a reactive path producing hydrogen from carbonaceous substances such as hydrocarbons and alcohols via fuel processor (generally steam reformers). Fuel is converted to a gas containing high fractions of hydrogen and moderate fractions of carbon dioxide and some amount of carbon monoxide. The reaction scheme for carbon, oxygen and hydrogen containing fuel is given below.

$$C_nH_mO_l + (n-l)H_2O \rightleftharpoons nCO + (m/2 + n - l)H_2 \qquad (\Delta H_R > 0) \qquad \text{(Rxn 2.1)}$$

$$CO + H_2O \rightleftharpoons CO_2 + H_2 \qquad (\Delta H_R < 0) \qquad \text{(Rxn 2.2)}$$

$$CO + 3H_2 \rightleftharpoons CH_4 + H_2O \qquad (\Delta H_R < 0) \qquad \text{(Rxn 2.3)}$$

The second reaction (Rxn 2.2) is called the Water-Gas Shift (WGS) reaction and the last one (Rxn 2.3) is methanation. Except for methane and methanol, the first reaction could be regarded as irreversible at temperatures higher than 773 K. According to Le Chatelier's principle less CH_4 with more CO and H_2 are produced with rising temperature. An increase in water to carbon fuel content in the reactants causes a decrease in carbon monoxide content in WGS reaction and increase in CO and H_2 in methanation (Peters, 2008). Due to their exothermic nature, WGS and methanation rates are lower at high temperatures.

For methanol reforming, following reactions are possible. However, methanol decomposition is another independent reaction in the reaction scheme.

$$CH_3OH \rightleftharpoons CO + 2H_2 \qquad (\Delta H_R > 0)$$
$$CH_3OH + H_2O \rightleftharpoons CO_2 + 3H_2 \qquad (\Delta H_R > 0)$$
$$CO_2 + H_2 \rightleftharpoons CO + H_2O \qquad (\Delta H_R < 0)$$

Methanation is suppressed by the catalysts, despite trace amount methane in the product. Methanol reforming catalysts had been deeply investigated in 1990s by automotive companies such as DaimlerChrysler and US government funded hydrogen on-board production by methanol ever since (Peters, 2008). Nowadays, copper based (Cu/ZnO with Al_2O_3 support) catalysts are commercially available.

2.3.2. Electrolysis of Water

Electrolysis is a process in which water is split into hydrogen and oxygen in two electrochemical reactions occurring two distinct electrodes. These reactions can be represented as

$$2\ OH^-_{(aq)} \longrightarrow \tfrac{1}{2}\ O_{2\ (g)} + H_2O_{(l)} + 2\ e^- \qquad \text{(Anode side)}$$

$$2\ H_2O_{(l)} + 2\ e^- \longrightarrow H_{2}\ (g) + 2\ OH^-_{(aq)} \qquad \text{(Cathode side)}$$

$$H_2O_{(l)} \longrightarrow H_{2\ (g)} + \tfrac{1}{2}\ O_{2\ (g)} \qquad \text{(Overall cell reaction)}$$

Pure water is not used as electrolyte due to its low conductivity; instead, ions are added by solutions such as sodium hydroxide, sodium chloride or hydrochloric acid. Energy supplied to system at 1 atm and 298 K can be calculated as 285.83 kJ/mol.

Electrolysis is also a long established technology. The first large scale production was applied in Norway in 1927. Later, it had continued to emerge and some plants have installed capacity up to 33000 m^3 (STP)/h of hydrogen. These huge plants depend on cheap electric sources of such coming from e.g. hydropower stations or solar power plants. However, small plants having capacity of 50-500 m^3 (STP)/h are eligible for easy operation and commonly the choice of industry. 5 % of world hydrogen production comes from electrolysis (Lohmüller *et al.*, 2000).

Since there is no carbonaceous feedstock in the production of hydrogen, they can be considered as environmentally friendly. A number of studies has focused on the electrolysis assisted by the energy coming from the sun, recently. There are two types of electrolysis by the aforementioned method, namely, active that is photoassisted or passive that is nonphotoassisted. The active method employs photogenerated charge carriers in the electrolysis of water and other products. Passive method electrolysis is performed in the dark at low temperatures (80°C) using alkaline electrolytes, at high temperatures (800°C or higher) using oxide electrolytes such as yttria-stabilized zirconia. Research is still ongoing for intermediate temperatures (200-500°C). Photovoltaic cells can be used as electricity source for those passive method units (Dhere & Bennur, 2009).

2.3.3. Other Production Techniques

There are several other hydrogen production methods widely used in the industry. Major ones are coal, biomass and hydrocarbon gasification; autothermal reforming; thermochemical, photochemical water cleavage; and hydrogen production by biological organisms.

2.4. MAJOR APPLICATIONS

Being one of the most abundant and functional chemical on the planet makes hydrogen eligible for vast area of uses. Major uses of hydrogen in chemical and gas production industry are listed as in Table 2.3.

Furthermore, hydrogen is widely used in metallurgic industry. In iron metallurgy hydrogen, carbon monoxide or a mixture of these two are used as reduction agents for iron ores. Similar to iron metallurgy, nonferrous metallurgy also uses hydrogen as reducing agent as represented in Table 2.4 (Häussinger *et al.*, 2000).

Table 2.3: Major uses of hydrogen in chemical and gas production industry

Ammonia Synthesis
Oil Refining (Hydrotreating, hydrocracking, hydrostripping, hydropyrolysis)
Coal Refining (Hydropyrolysis, hydrogasification)
Methanol Synthesis
Substitute Methane Synthesis
Hydroformylation of Olefins
Hydrogenation of Unsaturated Hydrocarbons and Oils

Table 2.4: Hydrogen use in nonferrous metallurgy (from Häussinger *et al.*, 2000)

Metal	Unit operation	Product
Copper	reduction of copper salt solutions under pressure	Cu powder
Nickel	selective reduction during cobalt production	Ni powder
Cobalt	reduction of aqueous cobalt salt solutions under pressure (4 MPa, 175 °C)	Co powder
Molybdenum, tungsten	reduction of the oxides or molybdates and tungstenates	Mo, W powder
Tantalum	reduction of tantalum chloride, $TaCl_5$, in hydrogen plasma	Ta hydride, Ta powder
Germanium	reduction of germanium tetroxide, GeO_4, at 650 °C	Ge powder for further processing in zone melting
Uranium	reduction of the higher uranium oxides at 650 °C	UO_2

Finally, one of the most important use of hydrogen is using the molecule as the energy carrier. William Cecil of England was the first person to suggest using hydrogen in an engine in 1820. In 1920-30s a great number of scientists and engineers worked on and described every possible route to obtain energy from the gas. These routes helped some fields developed from electricity generation using wind turbines to electrolysis, hydrogen storage in liquid form to utilization in fuel cells and aircrafts, spaceships (Häussinger *et al.*, 2000). Current uses of hydrogen as energy carrier is listed in Figure 2.3. Combustibility property and energy content of hydrogen is also worth noting among all other fuels. It has wide flammability range, high lower heating value (LHV) and higher heating value (HHV), low minimum ignition energy and high flame temperature as compared in Table 2.5.

Table 2.5: Comparison of hydrogen with other fuels (adapted from Gupta & Pant, 2009)

Fuel	LHV (MJ/kg)	HHV (MJ/kg)	Stoichiometric Air/Fuel Ratio (kg)	Combustible Range (%)	Flame Temperature (°C)	Min. Ignition Energy (MJ)	AutoIgnition Temperature (°C)
Methane	50.0	55.5	17.2	5–15	1914	0.30	540–630
Propane	45.6	50.3	15.6	2.1–9.5	1925	0.30	450
Octane	47.9	15.1	0.31	0.95–6.0	1980	0.26	415
Methanol	18.0	22.7	6.5	6.7–36.0	1870	0.14	460
Hydrogen	119.9	141.6	34.3	4.0–75.0	2207	0.017	585
Gasoline	44.5	47.3	14.6	1.3–7.1	2307	0.29	260–460
Diesel	42.5	44.8	14.5	0.6–5.5	2327		180–320

Apart from these, hydrogen can be used in water treatment, semiconductor manufacture, plasma technology and refrigeration (as liquid hydrogen).

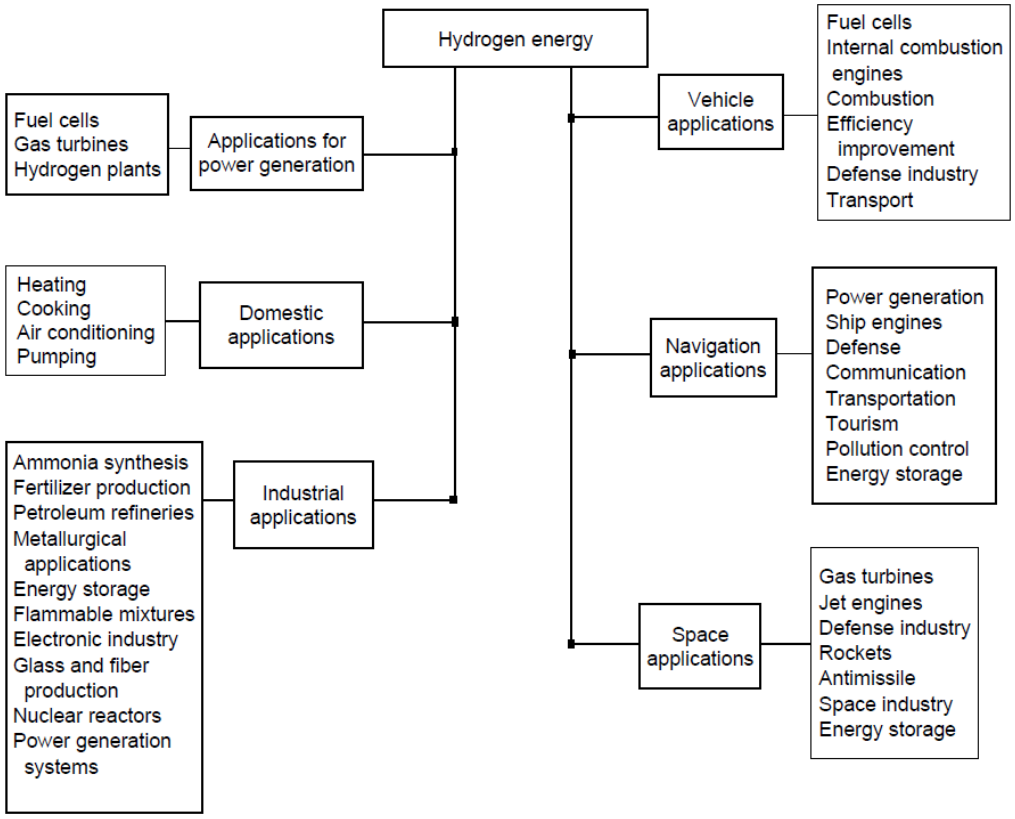

Figure 2.3: Some of the hydrogen energy uses in various applications (adapted from Gupta & Pant, 2009)

2.5. FUEL CELL APPLICATIONS

A fuel cell is an electrochemical device used in the conversion of chemical energy of fuel into electrical and thermal energy directly. Majority of fuel cells work with hydrogen feed to anode and oxygen (air is also possible) feed to the cathode. Working principles and reactions of fuel cells are illustrated in Figure 2.4.

The device removes electrons from oxidized fuel to pass around an external cathode circuit. Using reduction-oxidation reactions fuel cells produce electricity without other turbine type converters. Working principle of them is similar to that of batteries; difference is they do not store energy, their only duty is conversion.

Furthermore, fuel cells produce heat along with electricity which can be used in combined heat and power (CHP) systems or for the energy production from waste heat in high temperature fuel cells (Larminie, 2002).

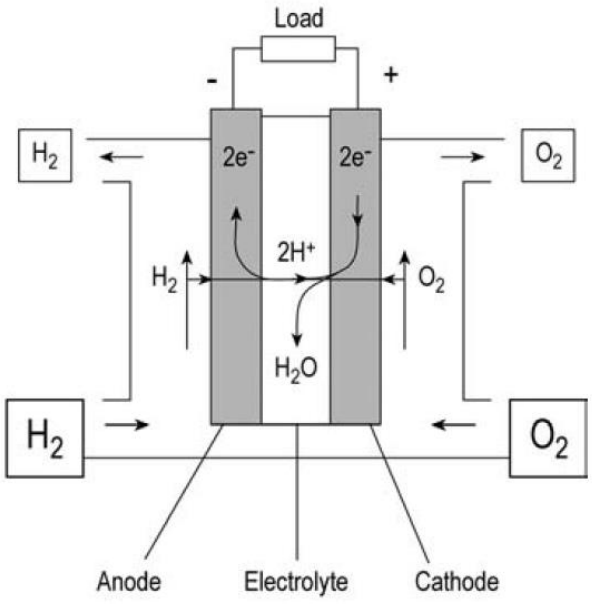

Anode:	H_2	$\rightarrow 2H^+ + 2e^-$
Cathode:	$1/2\ O_2 + 2H^+ + 2e^-$	$\rightarrow H_2O$
Overall reaction:	$H_2 + 1/2\ O_2$	$\rightarrow H_2O$

Figure 2.4: Working principle and reactions during operation in typical fuel cell (adapted from Heinzel *et al.*, 2010)

There are several types of fuel cells depending on unit structure, operating conditions or its fuel. Table 2.6 shows different types of fuel cells with their properties.

Table 2.6: Different types of fuel cells (adapted from Heinzel *et al.*, 2010)

Characteristic	AFC	PEMFC	PAFC	MCFC	SOFC
Temperature	60–90 °C	50–90 °C	160–220 °C	620–660 °C	800–1000 °C
Fuel	pure hydrogen	pure hydrogen, reformate*	pure hydrogen, reformate	natural gas, reformed or directly fed, biogas, coal gas	natural gas, reformed or directly fed, biogas, coal gas
Oxidant	pure oxygen	pure oxygen or air	air	air	air
Application	space and military	space, military, automotive, and stationary	cogeneration power plant	cogeneration or combined cycle power plants, depending on size	
System power at present		up to some 100 kW	several 100 kW	several 100 kW	100 kW demonstration plant
Electrical efficiency					
Stack	69–70%	50–68%	55%	65%	60–65%
System	62%	43–58%	40%	54% (cogeneration) 60–65% (combined cycle)	> 50% (cogeneration) 65–70% (combined cycle)

*Produced by reforming of hydrocarbons or methanol.

Among the types, Polymer Exchange Membrane Fuel Cells (PEMFC) attracted more attention than the others due to its simplicity and commercial use. The reason can be attributed to low operating temperatures, applicability to mobile systems (automotive, space, military) and decent electrical efficiency of the system.

PEMFC can tolerate CO_2 in the feed. However, CO amount fed to the fuel cell is important. Platinum anode catalyst in PEMFC can be poisoned by carbon monoxide existing in the fuel gas (after fuel reformer). CO occupies the catalyst sites and this is tolerated up to 1 % in the feed gas to the unit and target value for operation is about 0.5 % (Larminie, 2002). It is stated that active site blocking can occur with CO concentration as low as 10 ppm (Heinzel *et al.*, 2010). Similarly, sulfur content (mainly in the form of H_2S) in the fuel has significance that it can cause poisoning in the catalyst above 50 ppm.

2.6. ONBOARD FUEL CELL VEHICLES

Transportation currently depends on petroleum products and in the economic aspect gasoline and diesel fuel systems are the most convenient ones, since an immense structure was built and investments made for decades. Alternative onboard approaches should be more economic and plausible than the conventional ones.

Research and development (R&D) departments in automobile manufacture industry currently focused on electric, hybrid and fuel cell driven cars for next generation technology. It was estimated that onboard fuel cell vehicles are 1.66 times more efficient than hybrid internal combustion engine vehicles and 2.4 times more efficient than conventional internal combustion engine vehicles (National Academy of Sciences, 2004).

First approach to onboard fuel cell vehicles came from General Motors Company, a minivan called "Electrovan" in 1966. The prototype took a staff of 250 to construct and 2 years to be built. It had contained liquid hydrogen and oxygen tanks both cooled to hundreds of degrees below zero. The vehicle was powered by a couple of PEMFC having a range of 240 kilometers distance with power of 160 kW and could speed up to 70 miles per hour (Hakim, 2002). However, this vehicle had disadvantages: considerable volume occupation of engine that passengers could not fit in; weighing more than 3.5 ton; cost-prohibitive; and safety concerns due to high flammability of the feedstock.

Onboard fuel cell vehicles today employ PEMFC with gaseous hydrogen in high pressure carbon fiber reinforced polymer tanks (350 to 700 bars) and air as the oxygen source. These cars have improved range of travelled distances (400-600 km) and standard power generation of 100 kW. However, there is still more to do for them to be widely accepted by the consumers. Current market demands alternative approaches that can compete with internal combustion engines (ICE) considering the performance and cost. Table 2.7 shows the current market demands and their relationship to onboard fuel cell vehicles. In addition to initial and fuel operating cost comparable to ICE systems, market demands vary among suitable operating temperature range, fast refueling time, reliability-longevity of the engine, safety, long driving range, high acceleration, swift start-up and transient response times and proper space for passengers.

Table 2.7: Current market demand for alternative approaches to ICE and their relationship to onboard fuel cell vehicles (adapted from Satyapal & Thomas, 2009)

Vehicle Parameter	Expected Performance	Hydrogen Storage Property
Driving range	Greater than 300 mi.	High-energy storage capacity
Acceleration/handling	Similar to or better than current ICE vehicles	Minimal weight (high gravimetric energy density) Rapid hydrogen release kinetic properties
Safety	Meets all the current codes and standards	Codes and standards to be developed for hydrogen fuel usage No environmental, health, or safety issues
Passenger/trunk space	No intrusion into current passenger and trunk volumes	Minimal volume (high volumetric energy density) Conformability
Initial cost	Comparable to current ICE vehicles	Storage system cost similar to gas tank Minimal weight increment to overall vehicle
Reliability/longevity	Consistent performance over life of vehicle	Durability, cycle life, and minimal performance loss due to contaminants and a range of operating conditions over time
Refueling time	About 3 min	Rapid kinetic properties
Fuel operating cost	Comparable to current ICE vehicles	Energy-efficient hydrogen storage
Operating temperature range	Ambient temperature can range from −40°C to 60°C	Operational over ambient temperature range, including high solar loads while parked, cold starts, or high-altitude conditions

These demands require a compact, less-spaced hydrogen stock and a reformer (if necessary) with rapid kinetics converting to hydrogen in a proper gas mixture. Liquid carbon feedstock carrying hydrogen atoms and releasing them at low temperatures and pressures such ethanol and methanol is the main target in this respect.

CHAPTER 3

HYDROGEN PRODUCTION FROM FORMALDEHYDE

Research on onboard fuel cell vehicles continues with new specifications and demands in the industry. As explained in Chapter 2, PEMFC catalyst is sensitive to certain gas mixtures. Carbon monoxide and sulfur should be removed carefully as much as possible to the desired amounts. This can be accomplished either by a separation process or a chemical reaction.

Sulfur is no problem nowadays since it can be separated in refineries by hydrotreating directly before the consumer buys the gas. Furthermore, liquid carbonaceous feedstock that is used in onboard vehicles (ethanol, methanol and now formaldehyde) does not contain problematic amounts of sulfur. However, carbon monoxide elimination in onboard systems is still a continuing research. The dawn of hydrogen production from formaldehyde research dates back to more than a century ago (Loew, 1887) and has promising results concerning this aspect.

3.1. FORMALDEHYDE AS A MOLECULE

Formaldehyde is the simplest and smallest aliphatic aldehyde molecule containing one carbon, one oxygen and two hydrogen atoms having chemical formula of CH_2O and molecular weight of 30.03 g/mol. Its IUPAC systematic name is methanal. It is formed by photochemical reactions from organic materials in atmosphere, and sometimes it is the incomplete combustion product of methane and other hydrocarbons.

Formaldehyde occurs in more than one form in nature. In monomeric state, it is a colorless gas with irritating, pungent odor. It has tendency to polymerize to cyclic

organic molecule meta-formaldehyde and a long chain compound para-formaldehyde. Monomer formaldehyde's molecular structure is shown in Figure 3.1 for illustration. Due to instability of monomeric formaldehyde at ambient conditions, it is commercially sold as solutions of water. Concentrated formaldehyde solutions generally contain a stabilizer, surplus methanol from the production of formaldehyde process. Stabilizer is required to inhibit the reaction paths to higher mass polymers and formic acid (Reuss *et al.*, 2000). Formaldehyde molecule is famous for its reactivity and versatility as a chemical intermediate. This is one of reasons why it is used in many organic syntheses (Gerberich & Seaman, 2013).

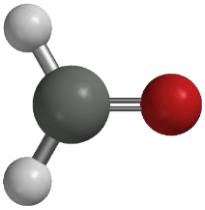

Figure 3.1: Molecular ball and spoke structure of formaldehyde molecule (adapted from Hardinger, 2016)

Gaseous formaldehyde molecule was first discovered by Russian chemist Aleksandr Butlerov in 1859 later confirmed by August Wilhelm von Hofmann with an extensive identification in which he passed methanol-air mixture over heated platinum spiral in 1867. Kekulé developed a method for preparation of pure formaldehyde in 1882. Tollens used platinum spiral catalyst and arranged suitable conditions for industrial production in 1882. Platinum spirals were replaced with a more efficient copper gauze catalyst by Loew in 1886. Formaldehyde market and production at commercial scale was made possible by Mercklin and Lösekann in 1889. Badische Anilin & Soda-Fabrik employed formaldehyde production by a continuous process using silver crystalline catalyst in 1905. A German company, Hugo Blank, patented the first use of silver catalyst in 1910. Later on, efficiency of processes, plant sizes and flow rates continued to grow over the years (Reuss *et al.*, 2000). Zuckerman of University of Maryland and his research group observed

formaldehyde as the first polyatomic organic molecule to be found in the interstellar region and detected it in various zones of Milky Way (Zuckerman *et al.*, 1970).

Some physical properties of formaldehyde are given in Table 3.1. Low boiling point (-19°C) and relatively high solubility in water are the important properties of formaldehyde. Furthermore, as seen from the table, it has a wide range upper and lower flammability limits. It is a colorless gas with irritating odor at room temperature.

Table 3.1: Physical properties of formaldehyde (from Gerberich & Seaman, 2013)

Property	Value
density, g/cm^3	
at −80°C	0.9151
at −20°C	0.8153
boiling point at 101.3 kPa,[a] °C	−19
melting point, °C	−118
vapor pressure, Antoine constants, Pa[b]	
A	9.21876
B	959.43
C	243.392
heat of vaporization,[c] ΔH_v at 19°C, kJ/mol[d]	23.3
heat of formation, ΔH_f° at 25°C, kJ/mol[d]	−115.9
std free energy, ΔG_f° at 25°C, kJ/mol[d]	−109.9
heat capacity, C_p°, J/(mol · K)[d]	35.4
entropy, S°, J/(mol · K)[d]	218.8
heat of combustion, kJ/mol[d]	563.5
heat of solution at 23°C kJ/mol[d]	
in water	62
in methanol	62.8
in 1-propanol	59.5
in 1-butanol	62.4
critical constants	
temperature, °C	137.2–141.2
pressure, MPa[e]	6.784–6.637
flammability in air	
lower/upper limits, mol%	7.0/73
ignition temperature, °C	430

[a] To convert kPa to mm Hg, multiply by 7.5.
[b] $\text{Log}_{10} P_{\text{Pa}} = A - B/(C + t)$; t = °C. To convert $\log_{10} P_{\text{Pa}}$ to $\log_{10 \text{ mm Hg}}$, subtract 2.1225 from A.
[c] At 164 to 251 K, $\Delta H_v = (27,384 + 14.56\text{T} - 0.1207T^2)$ J/mol[d]
[d] To convert J to cal, divide by 4.184.
[e] To convert MPa to atm, divide by 0.101.

Gaseous formaldehyde is hard to handle or store due to its reactivity. Gaseous formaldehyde should be kept at 100-150°C in order to prevent polymerization because polymerization starts below 80°C. Furthermore, it behaves as an ideal gas between 80 and 100 °C. Traces of polar compounds in the gas mixture accelerate the polymerization of formaldehyde. Strong alkali or heated acid presence in formaldehyde solution leads to Cannizzaro reaction producing formic acid and

methanol. Above 400°C, it decomposes to give CO and H_2. At room temperature formaldehyde is soluble in water; however, it is not in monomeric form. The reason why it is highly soluble in water may lie in its complex solution chemistry. Upon dissolving, formaldehyde converts into methylene glycol and its oligomers, i.e., poly(oxymethylene) glycols. Consequently, only 0.1 wt % dissolved monomeric formaldehyde can be observed in aqueous solutions (Reuss *et al.*, 2000).

Some human-made sources produce formaldehyde constantly. Each individual or company produces formaldehyde with very little amounts without noticing. Sources emitting formaldehyde to atmosphere is given in Table 3.2.

Table 3.2: Several human-made formaldehyde emission sources (Reuss *et al.*, 2000)

Emission source	Formaldehyde level
Natural gas combustion	
Home appliances and industrial equipment	2400 – 58 800 µg/m^3
Power plants	15 000 µg/m^3
Industrial plants	30 000 µg/m^3
Fuel-oil combustion	0.0 – 1.2 kg/barrel oil
Coal combustion	
Bituminous	< 0.005 – 1.0 g/kg coal
Anthracite	0.5 g/kg coal
Power plant, industrial, and commercial combustion	2.5 mg/kg coal
Refuse incinerators	
Municipal	0.3 – 0.4 g/kg refuse
Small domestic	0.03 – 6.4 g/kg refuse
Backyard (garden refuse)	up to 11.6 g/kg refuse
Oil refineries	
Catalytic cracking units	4.27 kg/barrel oil
Thermofor units	2.7 kg/barrel oil
Automotive sources	
Automobiles	0.2 – 1.6 g/L fuel
Diesel engines	0.6 – 1.3 g/L fuel
Aircraft	0.3 – 0.5 g/L fuel

Values in Table 3.2 show that mostly small amount of formaldehyde is released to the atmosphere. Released gas does not stay stable and photo-oxidation leads to conversion to CO_2 having half-life range of 35 to 50 minutes (Gerberich & Seaman, 2013).

3.2. FORMALDEHYDE PRODUCTION AND USES

Production of formaldehyde is made possible through three major processes in the industry: complete and incomplete conversion of methanol process using silver catalyst, and formox process using metal oxide catalysts. Other routes using different feed gases such as propane, butane, ethylene, propylene, butylene or dimethyl ether through oxidation were tried but abandoned due to economic incompatibility with methanol processes (Reuss *et al.*, 2000). Nearly 35 % of produced methanol is consumed by the formaldehyde production. Current technology uses the reaction route (dehydrogenation and partial oxidation) in the production (Moulijn *et al.*, 2013).

$$CH_3OH \rightleftarrows CH_2O + H_2 \qquad \Delta_r H_{298} = 85\ \text{kJ/mol}$$

$$CH_3OH + {}^1/_2\, O_2 \rightarrow CH_2O + H_2O \qquad \Delta_r H_{298} = -158\ \text{kJ/mol}$$

In the first process, silver crystal catalyst loaded in the reactor at 600-720°C and pressures of 1.5 to 3 atm. Partial oxidation and dehydrogenation occurs simultaneously. A methanol-water mixture is fed to the reactor with fresh air at 70 to 90°C. Excess methanol is fed to system to ensure near complete conversion of methanol. Methanol conversion of this process is 97-98 %. This process is patented by the chemical company BASF (United States Patent No. 3928461, 1975).

In another process, silver crystalline or gauze catalyst is employed in the reactor. Similar to BASF process, partial oxidation occurs with dehydrogenation simultaneously and excess methanol is fed to the process. Reactor temperature varies between 590°C and 650°C to prevent side reactions occurring at higher temperatures. Methanol conversion from the reactors is about 77-87 %. Later on unreacted methanol is distilled and recovered in the system to increase the conversion to near completion (Reuss *et al.*, 2000).

Third and last main process is called Formox process. Reactors in this process are run by only oxidation reaction with excess air feed opposite to the silver catalyst processes. The catalysts employed are modified iron-molybdenum and vanadium

oxide based and the reactors in the process run between 250-400°C at nearly atmospheric pressure. The process operates at relatively low temperatures, since formaldehyde could be oxidized to carbon monoxide and water at temperatures higher than 470°C. Methanol conversion in this process is about 98-99 % (Reuss *et al.*, 2000).

Formaldehyde has wide range uses in chemical process industry. One of the biggest uses of formaldehyde in the industry is in the field of synthetic resins with urea, melamine and phenol. It has been also used in polyester resin field using its reaction with acetaldehyde to form pentaerythritol (Kent, 1968). Furthermore, more than 40 % of its produced amount is employed as an intermediate in the syntheses of other chemical species such as 1,4-butanediol, trimethylolpropane, and neopentyl glycol (which are used in the manufacture of polyurethane and polyester plastics, synthetic resin coatings, synthetic lubricating oils and plasticizers) due to its property of being an irreplaceable C_1 building block. It is also the source of base chemicals in detergent industry and is used as a building block for products used in the manufacture of dyes, plastic precursors, crop protection agents, animal feeds, perfumes, vitamins, flavorings and drugs. Only a limited portion of formaldehyde is directly used. Examples for direct uses are: corrosion inhibiting agent, aid in mirror finishing and electroplating, preservation and disinfection in medicine. The classic odor in hospital ward comes from formaldehyde. Due to its conversion to carbon dioxide within minutes, it does not accumulate in the environment (Reuss *et al.*, 2000).

3.3. STORAGE, HEALTH AND SAFETY ASPECTS OF FORMALDEHYDE

Storage conditions of formaldehyde solutions (37 % wt.) are significant in order to prevent some reactions to occur at even room temperature. Long storage of formaldehyde may result in rising acidity due to conversion to formic acid. Principal reactions occurring at ordinary temperatures in the storage vessels over time are given below (Walker, 1944).

$$CH_2O + 2\ CH_3OH \longrightarrow CH_2(OCH_3)_2 + H_2O \qquad \text{(Methylal formation)}$$

$$2\ CH_2O + H_2O \longrightarrow CH_3OH + HCOOH \qquad \text{(Cannizzaro reaction)}$$

$CH_2O + ½ O_2 \longrightarrow HCOOH$ (Oxidation to formic acid)

Storage temperature varies depending on the methanol concentration. Increasing amount of methanol concentration in formalin solution provides less minimum temperature for storage inhibiting paraformaldehyde formation.

In terms of health and safety, formaldehyde should be carefully examined before use. There was limited evidence of cancer for humans and sufficient evidence for animals found in the studies conducted by International Agency for Research on Cancer (IARC) working under World Health Organization (WHO) (IARC, 1987). Formaldehyde in gaseous vapor is toxic via inhalation and irritating for the eyes and mucous membranes of the respiratory tract. Aqueous solutions may be corrosive depending on the concentration and skin sensitization could occur upon contact. Dose – response types of formaldehyde for human exposure is given in Table 3.3 (Reuss *et al.*, 2000).

Table 3.3: Dose-response relationship of gaseous formaldehyde for humans (Reuss *et al.*, 2000)

Effect	Exposure Level (ppm)
Odor threshold	0.05 – 1.0
Irritation in eyes, nose or throat	0.2 – 1.6
Stronger irritation of upper respiratory tract, coughing, lacrimation, extreme discomfort	3 – 6
Immediate dyspnea, burning in nose and throat, heavy coughing and lacrimation	10 – 20
Necrosis of mucous membranes, laryngospasm, pulmonary edema	> 50

3.4. FORMALDEHYDE STEAM REFORMING (FSR)

The search for CO_2 selective steam reforming has been continuing for more than two decades. The idea is, as explained in Chapter 2, to produce a gas mixture for an onboard fuel cell that will not damage the fuel cell catalyst or bring about toxic gases. Mainly, studies have been focused on methanol steam reforming (MSR) due to economic and transportation reasons.

In this thesis, focus is on producing a mixture of hydrogen suitable for onboard PEMFC applications via formaldehyde steam reforming reactions. However, since monomeric formaldehyde cannot be stored at room temperature as explained in the previous sections, aqueous solution of 34.5 wt. % formaldehyde containing 9-15 wt. % methanol is used in the experiments.

3.4.1. Thermodynamic Analysis

Before starting experiments, formaldehyde reaction thermodynamic equilibrium composition, hydrogen yield, selectivity of each product and conversion should be determined. Therefore, they are studied with formaldehyde-steam mixtures with (1st case) and without (2nd case) methanol. Possible reactions are the following.

$$CH_2O + H_2O \longleftrightarrow CO_2 + 2\ H_2 \qquad (\Delta H_R = -35.72\ kJ/mol)$$

$$CH_3OH + H_2O \longleftrightarrow CO_2 + 3\ H_2 \qquad (\Delta H_R = 48.97\ kJ/mol)$$

$$CO_2 + H_2 \longleftrightarrow CO + H_2O \qquad (\Delta H_R = 41.16\ kJ/mol)$$

In the analysis, minimization of Gibbs free energy, to estimate equilibrium product distribution was used. At a specified temperature and pressure, total Gibbs free energy of the reacting system including k species can be shown as in Equation 3.1.

$$G_{\text{mix}}(n_1, n_2, \ldots, n_k) = \sum_{i=1}^{k} n_i \overline{G}_i \qquad \text{(Equation 3.1)}$$

where the partial molar Gibbs free energy of species i in a particular mixture can be described by Equation 3.2.

$$\overline{G}_i = \widetilde{G}_i^o + RT \ln \widehat{a}_i \qquad \text{(Equation 3.2)}$$

Conservation of elements can be written as in Equation 3.3.

$$E_j = \sum_{i=1}^{k} \xi_{ji} n_i \qquad j = 1, 2, 3 \ldots, t. \qquad \text{(Equation 3.3)}$$

where ξ denotes each elemental species, t is the number of elements existing in the system. In order to find the set (n_i) minimizing the total Gibbs free energy with the limitation given by Equation 3.3, a function L is defined.

$$L = \sum_{i=1}^{k} n_i \overline{G}_i + \sum_{j=1}^{t} \lambda_j \left(\sum_{i=1}^{k} \xi_{ji} n_i - E_j \right) \qquad \text{(Equation 3.4)}$$

where λ_j is the molar Gibbs free energy of pure species j at unit fugacity. Setting partial derivatives of Equation 3.4 equal to zero,

$$\frac{\partial L}{\partial n_i} = 0 \quad i = 1, 2, \ldots, k \qquad \text{(Equation 3.5)}$$

and consequently Equation 3.5 yields,

$$\overline{G}_i + \sum_{j=1}^{t} \xi_{ji} \lambda_j = 0 \qquad \text{(Equation 3.6)}$$

Incorporating Equation 3.2, Equation 3.6 can be written as

$$\widetilde{G}_i^o + RT \ln \widehat{a}_i + \sum_{j=1}^{t} \xi_{ji} \lambda_j = 0 \qquad \text{(Equation 3.7)}$$

It must be noted that

$$\widetilde{G}_i^o = (\Delta \widetilde{G}_f^o)_i \qquad \text{(Equation 3.8)}$$

$$\widehat{a}_i = \frac{\widehat{\phi}_i y_i P}{P^o} \qquad \text{(Equation 3.9)}$$

where $\widehat{\varphi}_i$ is the fugacity coefficient for species i, and P^o is the pressure at the reference state. Finally, simultaneous solution of the following Equations 3.10-12 minimizes the total Gibbs free energy of the reacting system.

$$\ln\left[\widehat{\phi}_i y_i \left(\frac{P}{P^o}\right)\right] + \sum_{j=1}^{t} \xi_{ji}\lambda_j^* = -\frac{(\Delta\widetilde{G}_f^o)_i}{RT} \quad i = 1, 2, \ldots, k \qquad \text{(Equation 3.10)}$$

$$\sum_{i=1}^{k} \xi_{ji}\, y_i = \frac{E_j}{n_T} \quad j = 1, 2, \ldots, t \qquad \text{(Equation 3.11)}$$

$$\sum_{i=1}^{k} y_i = 1 \qquad \text{(Equation 3.12)}$$

where

$$\lambda_j^* = \frac{\lambda_j}{RT} \qquad \text{(Equation 3.13)}$$

$$\frac{(\Delta\widetilde{G}_f^o)_i}{T} = \frac{(\Delta\widetilde{G}_{f,298}^o)_i}{298} - \int_{298}^{T}\left[(\Delta\widetilde{H}_{f,298}^o)_i + \int_{298}^{T}\Delta\widetilde{C}_{P_i}^o\, dT\right]\frac{dT}{T^2} \qquad \text{(Equation 3.14)}$$

It is important that Gibbs free energy of formation term in Equation 3.10 be evaluated at the reaction temperature by Equation 3.14 (Tosun, 2013).

Calculations were performed using a program called “Gaseq”. Gaseq employs a calculation procedure that is the same as of NASA chemical equilibrium program developed by NASA Glenn Research Center. Detailed information on the calculation procedure is given elsewhere (McBride & Gordon, 1992). Proposed gases entering are formaldehyde, water, and methanol if included. All gases are assumed to behave as an ideal gas at equilibrium conditions. Molar amounts of each species in formalin 34.5 wt. % solution are shown in Appendix A, Table A.1.

Accordingly, mole fractions at the inlet are 0.661, 0.256 and 0.083 for water, formaldehyde and methanol, respectively. Two cases were evaluated separately.

3.4.1.1. Formaldehyde without Methanol in the Feed

At equilibrium, existing gases are assumed to be CO, CO_2, H_2, water and formaldehyde. Different molar proportions of steam-formaldehyde (1/1, 2/1 and 5/1) at different temperatures and pressures were investigated separately. Proposed reactions for this case are

$$CH_2O + H_2O \longleftrightarrow CO_2 + 2\,H_2 \qquad (\Delta H_R = -35.72 \text{ kJ/mol})$$

$$CO_2 + H_2 \longleftrightarrow CO + H_2O \qquad (\Delta H_R = 41.16 \text{ kJ/mol})$$

All results have shown that formaldehyde conversion was very close to **100 %** in all calculations. Investigated pressures were 1, 5 and 10 atm; temperatures were in the range of 298 to 700 K.

How CO amount relatively changes with respect to temperature and steam amount can be observed in Figure 3.2. As temperature increased CO amount increased gradually. Consequently, for onboard fuel cell applications, relatively low temperature and high steam to formaldehyde ratio is favored.

Furthermore, hydrogen yield of these reactions are also drawn in Figure 3.3 with respect to the same changing parameters. As seen in Figure 3.3, hydrogen yield is at its maximum values at low temperatures, while yield prefers higher steam to formaldehyde ratios.

Selectivity values of hydrogen, carbon monoxide and carbon dioxide are also gathered in Figures 3.4-3.6. Figures 3.4 and 3.6 show that increasing temperature has negative effect on the selectivity values of hydrogen and carbon dioxide. On the other hand, increasing steam to formaldehyde molar feed ratio positively affects selectivity values of hydrogen and carbon dioxide. However, carbon monoxide selectivity, as can be seen from Figure 3.5, is positively affected by temperature and negatively affected by steam to formaldehyde molar feed ratio.

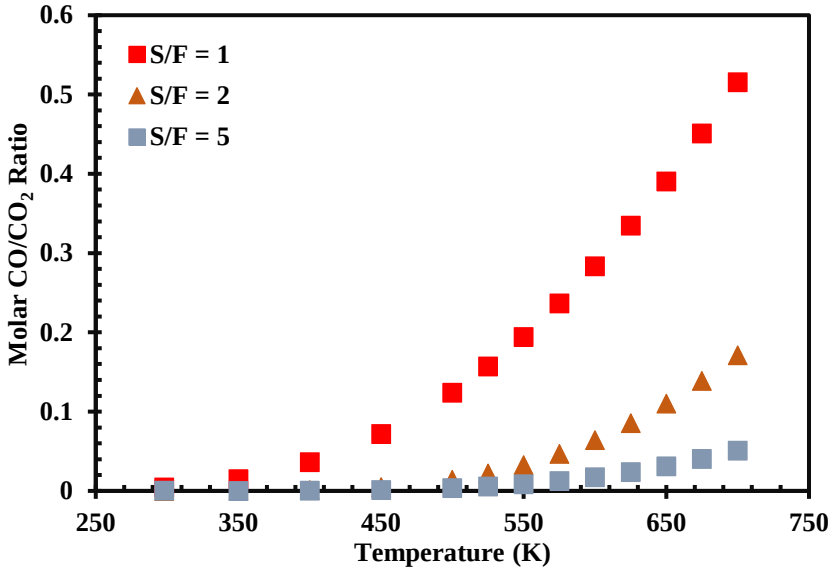

Figure 3.2: Molar CO/CO_2 ratio at different temperatures and S/F feed ratios without methanol

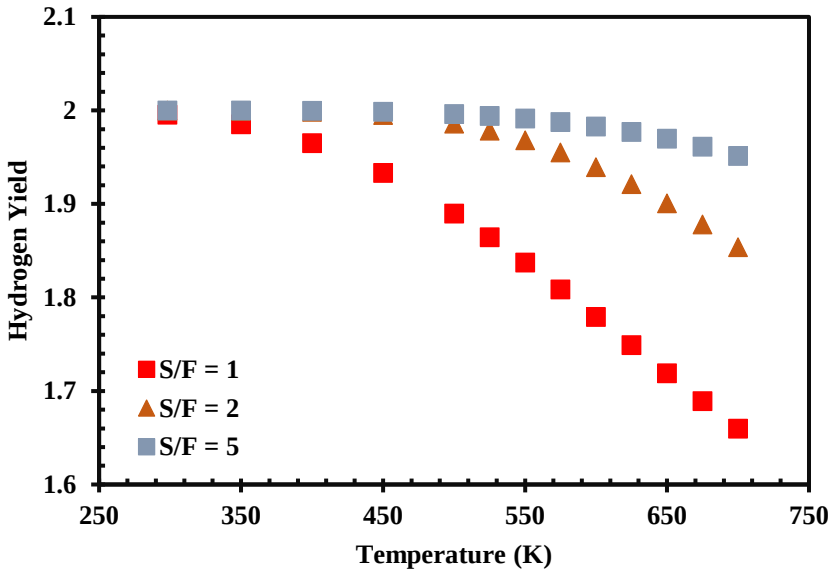

Figure 3.3: Hydrogen yield of the system at different temperatures and S/F feed ratios without methanol

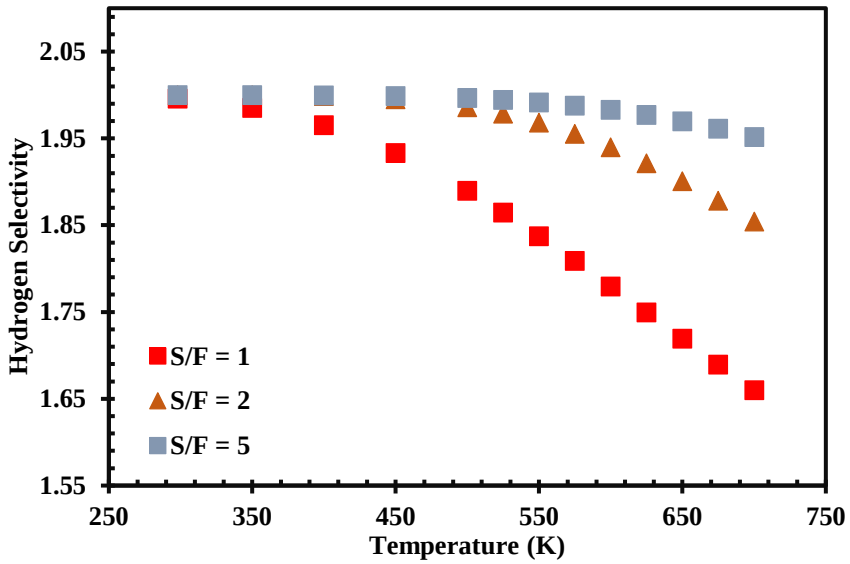

Figure 3.4: Hydrogen selectivity of the system at different temperatures and S/F feed ratios without methanol

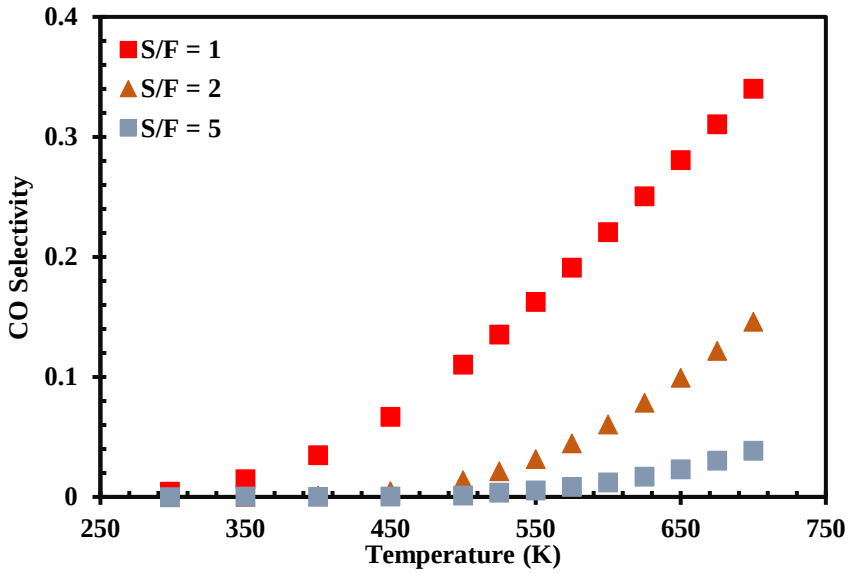

Figure 3.5: CO selectivity of the system at different temperatures and S/F feed ratios without methanol

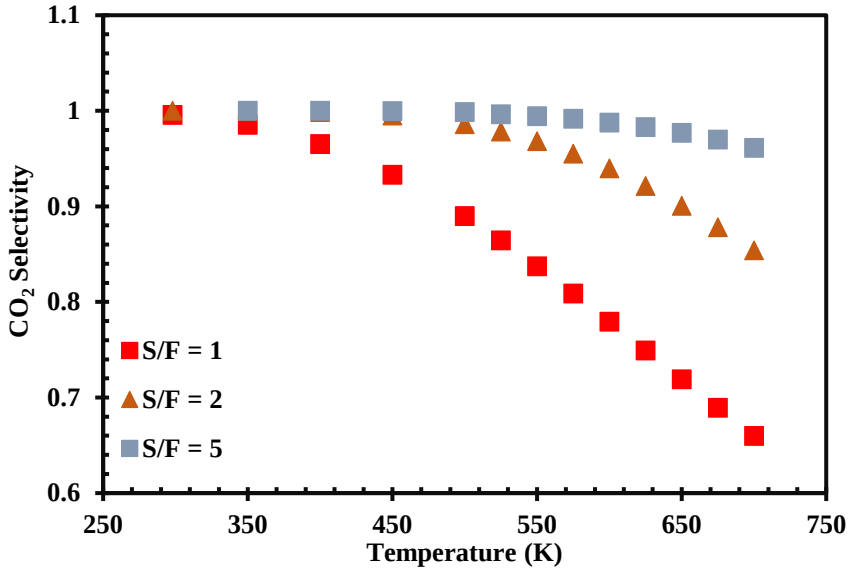

Figure 3.6: CO_2 selectivity of the system at different temperatures and S/F feed ratios without methanol

3.4.1.2. Formaldehyde with Methanol in the Feed

Thermodynamic reaction equilibrium is also evaluated for the commercial formalin mixture 34.5 wt. % procured from Sigma-Aldrich Co. Composition of the solution is given in Appendix A, Table A.1. In Table A.1, molar fractions are 0.661, 0.256 and 0.083 for water, formaldehyde and methanol, respectively. These values are inserted in Gaseq at different temperatures and pressures. Proposed reactions for this system are

$$CH_2O + H_2O \longleftrightarrow CO_2 + 2\ H_2 \qquad (\Delta H_R = -35.72\ kJ/mol)$$

$$CH_3OH + H_2O \longleftrightarrow CO_2 + 3\ H_2 \qquad (\Delta H_R = 48.97\ kJ/mol)$$

$$CO_2 + H_2 \longleftrightarrow CO + H_2O \qquad (\Delta H_R = 41.16\ kJ/mol)$$

Figure 3.7 shows the molar CO/CO_2 ratio at equilibrium conditions. For comparison previous results with steam-formaldehyde mixtures are also presented. CO keeps at negligible values until 500 K for formalin solution. Note that formalin has S/F ratio of 2.58.

Formaldehyde and methanol equilibrium conversion values are also important for the process. In all calculations, formaldehyde converted **nearly completely** no

matter how much pressure is applied**,** and this could be attributed to the irreversibility of FSR.

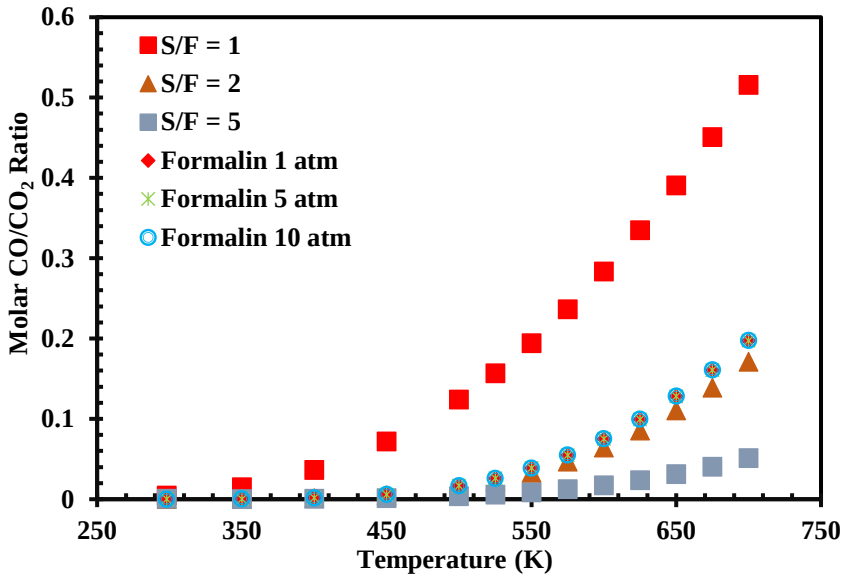

Figure 3.7: Molar CO/CO_2 ratio in chemical equilibrium at different temperatures and pressures (Formalin S/F = 2.58)

On the other hand, methanol equilibrium conversion profiles change with respect to pressure and this is illustrated in Figure 3.8. Methanol conversion is close to 100 % when the system temperature is higher than 450 K at system pressures of 1, 5 and 10 atm. Lower pressure makes system approach 100 % methanol conversion at lower temperatures than in the higher pressure.

Similarly, hydrogen yield at chemical equilibrium at different temperatures and pressures was calculated in the program. Figure 3.9 shows that after 450 K difference between all three pressures vanishes and hydrogen yield gradually decreases with increasing temperature. This is due to increase in the amount of CO released.

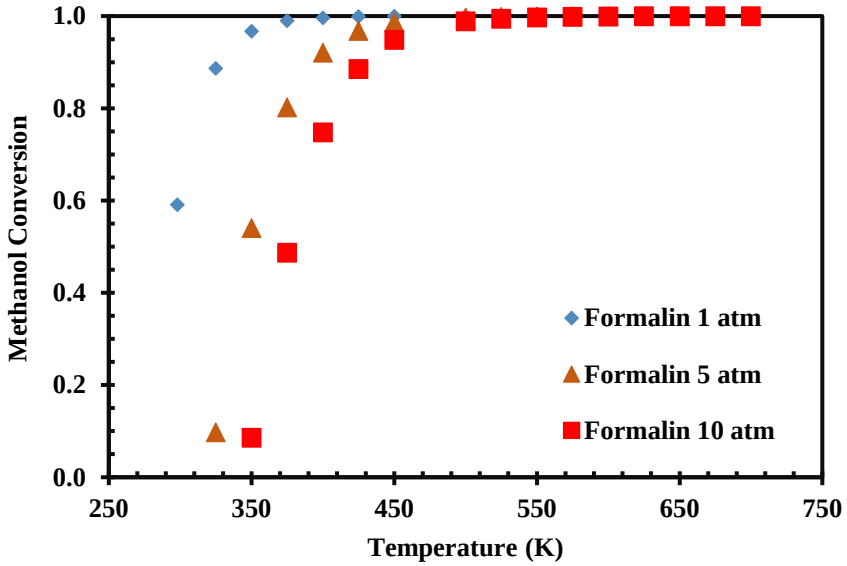

Figure 3.8: Methanol equilibrium conversion values in formalin solution with respect to temperature and pressures (Formalin S/F = 2.58)

Figures 3.10-3.12 represent the product distribution of equilibrium condition at different temperatures for 1, 5 and 10 atm. Figure 3.10 shows that hydrogen and carbon dioxide mole fractions slowly decrease with increasing temperature. This is due to increasing rate of reverse water gas shift reaction.

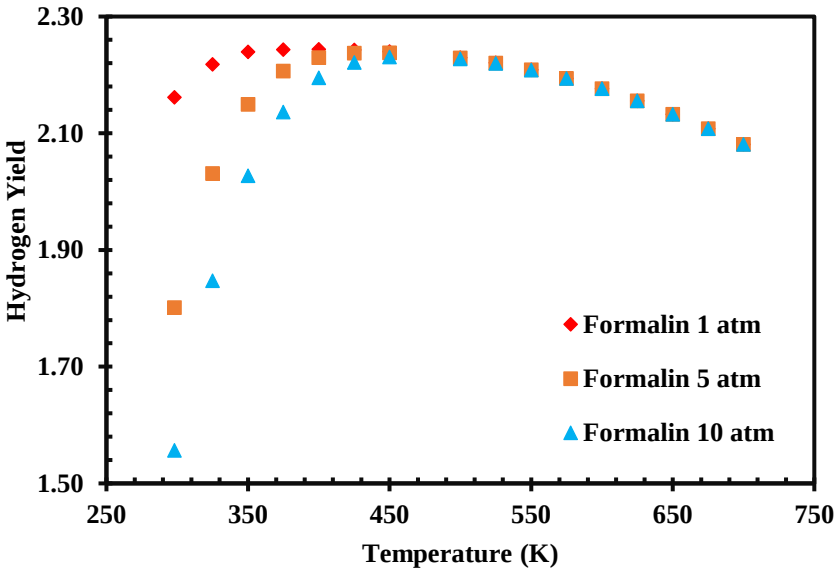

Figure 3.9: Hydrogen yield of reaction formalin solution at different pressure and temperatures

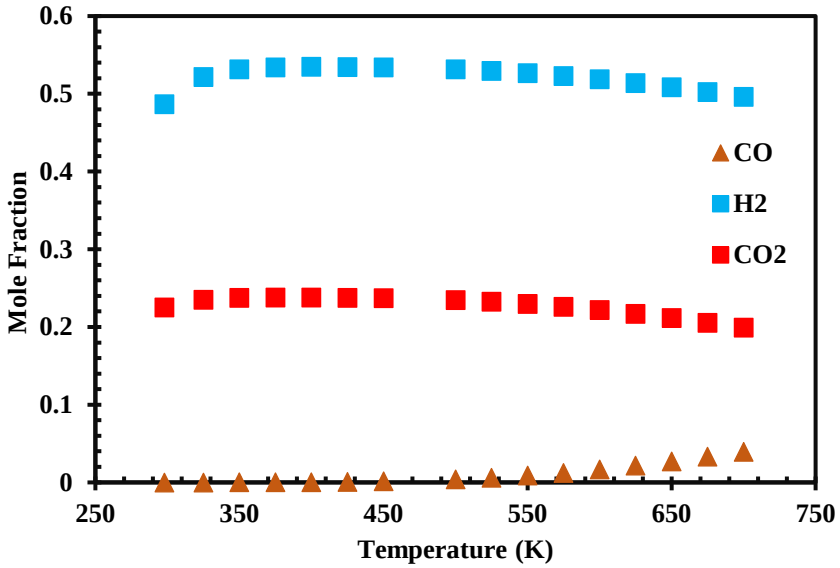

Figure 3.10: Equilibrium product distribution with respect to temperature at 1 atm with the formalin feed

In Figures 3.11 and 3.12, mole fractions of hydrogen and carbon dioxide evidently increase at low temperature zones parallel to the methanol conversion (Figure 3.8). Similar to Figure 3.10 H_2 and CO_2 mole fractions slowly decrease with increasing temperature. In none of these figures, CO mole fraction is higher than 0.05.

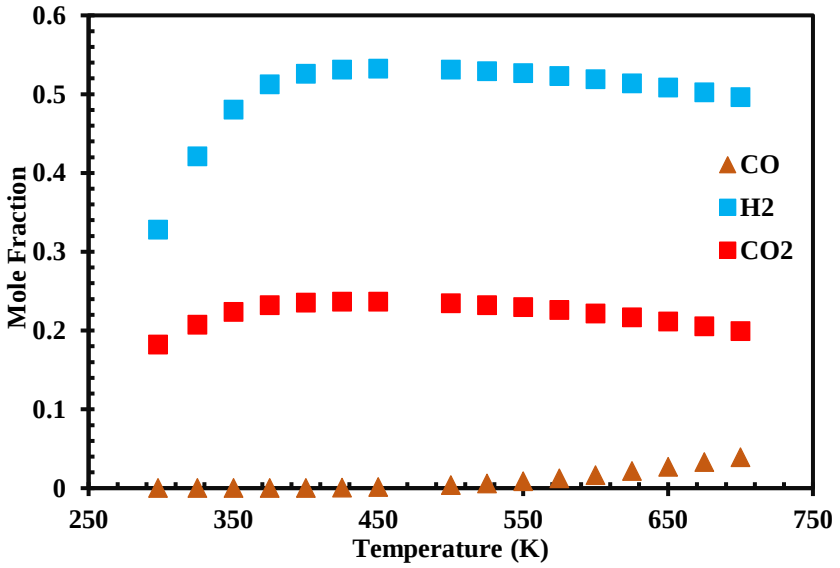

Figure 3.11: Equilibrium product distribution with respect to temperature at 5 atm with the formalin feed

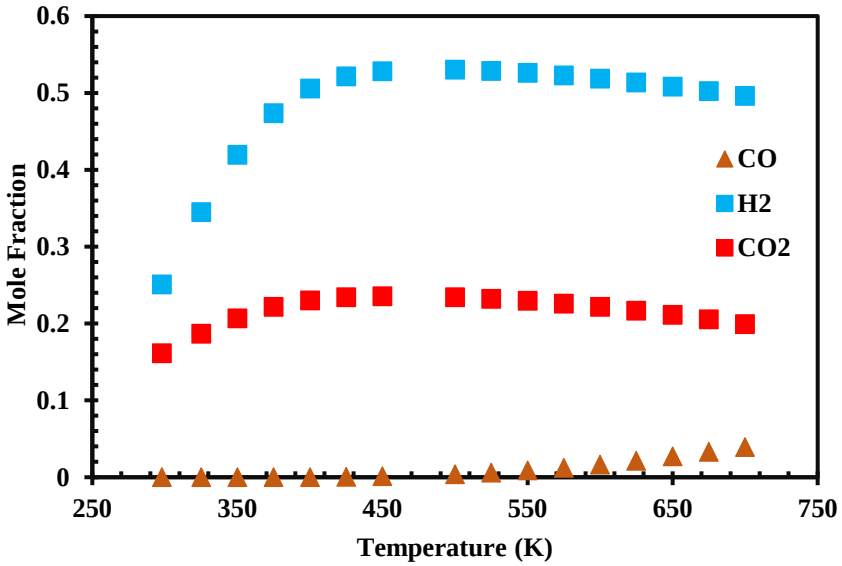

Figure 3.12: Equilibrium product distribution with respect to temperature at 10 atm with the formalin feed

3.4.2. Literature Survey

There are few articles concerning formaldehyde steam reforming in theoretical and experimental studies. There is experimental data for hydrogen production from formaldehyde in several articles or as a part of methanol steam reforming; however, they are not exactly intended for FSR. Since onboard fuel cell application research is focused mostly on methanol steam reforming reactions, relevant articles to formaldehyde steam reforming can be found of those which issue methanol steam reforming. The reason is that formaldehyde is an intermediate in methanol steam reforming reactions.

3.4.2.1. DFT Studies on FSR Reactions

There are a few density functional theory (DFT) studies about formaldehyde steam reforming reactions. Formaldehyde studies were essentially based on methanol steam reforming process as can be seen.

Kok Hwa Lim and his coworkers (2009) studied formaldehyde steam reforming on Cu (1 0 0) surface to employ this reaction for onboard fuel cell systems. They state that formaldehyde, formic acid and carbon dioxide bind weakly to the copper

surface weakly and has weak adsorption energies. However, O atoms on the surface makes it feasible and favorable for formaldehyde to react with it rather than empty surface and surface with OH (Bo *et al.*, 2009).

Xiang Li and Kok Hwa Lim (2012) investigated formaldehyde steam reforming reaction on Cu (2 2 1), PdZn (1 0 0), and Ir (1 0 0) surfaces, in order to find CO_2 selective catalyst for onboard fuel cell systems. Due to sintering of copper catalysts at relatively low temperatures, along with Cu, they have chosen PdZn alloy for high thermal stability and low selectivity for CO in methanol steam reforming, and Ir for its being good catalyst in methanol steam reforming. They proposed two reaction pathways for the system, namely, dehydrogenation and steam reforming which are given in Figure 3.13. Having estimated adsorption, reaction possibilities and energies, binding energies for formaldehyde and its intermediates in both reaction pathways, they found that CH_2O dehydrogenation is more favorable on Ir (1 0 0), whereas steam reforming of formaldehyde is favored to occur on defect sites that of Cu (2 2 1).

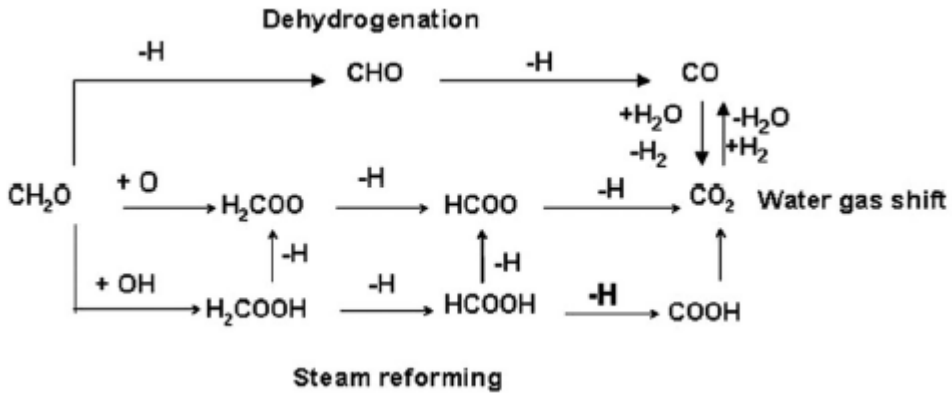

Figure 3.13: Reaction pathways for formaldehyde steam reforming reactions (Li & Lim, 2012)

In another study that is particularly focused on methanol steam reforming, possible reaction routes to $CO_2 + H_2$ products have been identified on Cu (1 1 1) surface (Lin *et al.*, 2011). It also includes the effects of adsorbate formaldehyde intermediate produced by methanol dehydrogenation step. They reported that they had found

plausible pathways to desired gas mixture for onboard fuel cell applications that are initiated by reaction between CH_2O* and OH* using a plane-wave DFT method.

Few other DFT studies for CO_2 selective methanol steam reforming include the effect of formaldehyde along the pathway of methanol dehydrogenation, but they do not contain essential information for FSR (Krajcí *et al.*, 2015; Zuo *et al.*, 2014). Furthermore, it is evident from these three articles that the literature is looking for a suitable feed stock to obtain H_2 + CO_2 product which is desired for onboard applications.

3.4.2.2. Experimental Studies

In the literature, there are few articles based on formaldehyde steam reforming. However, studies of hydrogen production from formaldehyde and methanol steam reforming can be linked to the topic.

As stated in the earlier sections of this chapter, hydrogen production from formaldehyde dates back to 19th century (Loew, 1887). After a long interval of time, no research on hydrogen from formaldehyde was seen until 1995, when Kapoor and his colleagues (1995) worked on the kinetics of hydrogen production from formaldehyde in basic aqueous solutions in order to estimate the amount of hydrogen gas released from nuclear waste products of ethylenediaminetetraacetic acid (EDTA) and (2-Hydroxyethyl) ethylenediaminetriacetic acid (HEDTA) containing formaldehyde and glyoxylate. The effects of NaOH and formaldehyde concentrations on hydrogen gas generation were investigated at 23, 45 and 60°C. Gas measurements were carried out using gas chromatography with thermal conductivity detector, molecular sieve 5A column at 23°C. Based on the experimental results they reported that reaction is first order in formaldehyde and approaches to second order at low formaldehyde concentrations and activation energy of 85 kJ/mol.

In a study of methanol steam reforming and dehydrogenation, Takezawa and Iwasa (1997) investigated the effect of formaldehyde in the reaction steps. In the study, supported copper and Group VIII metal catalysts (Rh, Ni, Pd, and Pt) were used. They found that in the presence of copper-based catalyst, methanol conversion to

CO and H_2 is normally infeasible. Instead, formaldehyde is involved in the steam reforming reaction, which is an intermediate produced by dehydrogenation of methanol. Furthermore, they reported that formaldehyde added to the inflow at 493 K was completely converted to CO_2 and H_2. At 403 K, they found that turnover frequency of formaldehyde and water to carbon dioxide and hydrogen reaction on unsupported catalyst was 1.7×10^{-3} s^{-1}. Similarly, turnover frequency of 10 % copper supported by silica catalyst was found as 1.3×10^{-3} s^{-1}. This study is useful considering the effect of copper on formaldehyde reactivity.

One of the first formaldehyde steam reforming (FSR) articles was published by Simon Penner and his coworkers in 2013. They reported the selectivity of methanol and formaldehyde steam reforming reactions separately in batch and flow reactor systems using unsupported bimetallic ZnPd, ZnO particles and ZnPd supported by ZnO as catalysts. 30 wt. % formaldehyde aqueous solution was used as the feed. Another methanol-water (1:9 volume ratio at STP) was also fed. Gas analysis was carried out using gas chromatograph allowing CO determination as low as 20 ppm using nitrogen as the carrier gas. Their results revealed high CO_2 selectivity on ZnO catalyst and this is illustrated in Figure 3.14. They reported that activation energies for methanol steam reforming (MSR) was found around 130-144 kJ/mol and for FSR 110 kJ/mol, very close to a reported MSR activation barrier value using Au/ZnO catalysts elsewhere. This could suggest that methanol dehydrogenation to formaldehyde is the rate-limiting step in methanol steam reforming.

Li and coworkers (2014) synthesized $Ag/\gamma\text{-}Al_2O_3$ catalyst to produce PEMFC grade hydrogen gas mixture. They worked with a liquid, vigorously stirred batch reactor with the feed of 0.87 M formaldehyde and 1 M NaOH (50 mL) and 50 mg catalyst powder at room temperature. Furthermore, concentration of NaOH, formaldehyde in the solution, N_2 and O_2 in the air and type catalyst were changed to observe their effects on hydrogen yield. Gas analyses were carried out using a GC equipped with TCD. Firstly, no carbon monoxide was found in the gas analyses. Apparently, rather than N_2, O_2 concentration in the air favorably affected the production of H_2. Increasing NaOH and formaldehyde concentrations gave a rise to the H_2 production

up to some levels for each of them. Supported Ag/γ-Al_2O_3 catalyst proved to be a better one compared to Ag nanoparticles.

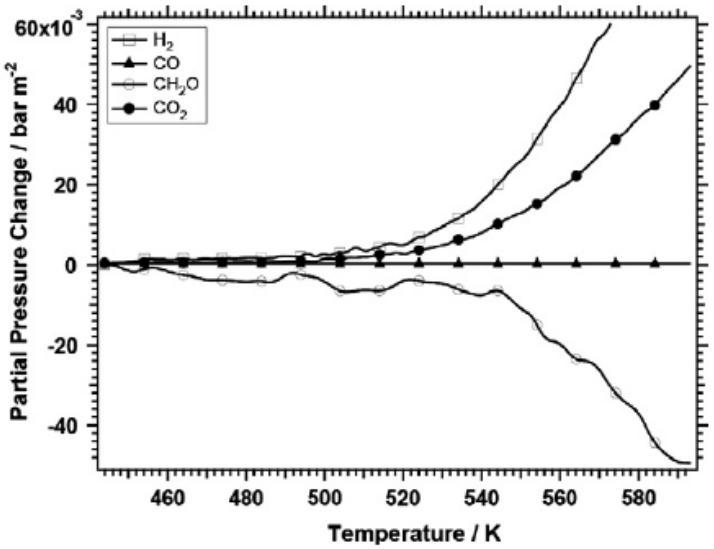

Figure 3.14: Production distribution in the product side of FSR experiments (from Lorenz *et al.*, 2013)

In another study of Bi and Lu (2008) Cu particles with nano size were used as the catalyst to produce PEMFC grade hydrogen again at room temperature. For comparison, Pt, Au and Ni catalysts were also used in the reaction. Activity tests were performed in a liquid, vigorously stirred batch reactor with the feed of 0.48 M formaldehyde and 1 M NaOH (50 mL) and desired amount of catalyst powders at room temperature. Gas analyses were performed using GC equipped with TCD using argon as the carrier gas. Among the catalysts, Cu nanoparticles proved the best hydrogen yield. Moreover, high concentrations of NaOH favorably affected the H_2 formation up to some point at which Cannizzaro reaction starts to compete with hydrogen production reaction.

Heim and coworkers (2014) published an article on formaldehyde assisted water-splitting using homogeneous catalysis. Formalin solution of 37 wt. % and para-formaldehyde and deionized water were used as the feedstock. Liquid batch reactor system (a small round-bottomed flask connected to the analyzer) with homogeneous catalyst of ruthenium ([$RuCl_2$(*p*-cumene)]$_2$) was used at a temperature range of 40-

140°C. K_3PO_4 was used as the pH buffer in the experiments in order to prevent acidity increase during the reaction causing a drop in the reaction rate. Stable formaldehyde conversions were observed between pH 2.4 (75 %) and 9 (73 %) and the highest formaldehyde (85%) conversion was achieved at pH 5.5.

Gas amount was measured using a mass flowmeter and gas composition was analyzed using mass spectrometer (MS) directly connected to the indicated reactor setup. Best catalyst performance was obtained at 95°C and high hydrogen yield (84 %) was achieved within an hour. Gaseous mixture of hydrogen and carbon dioxide was obtained during the reaction. Neither formaldehyde nor CO was found in the gas phase. In addition, to obtain more information on dehydrogenation and the composition of gaseous and liquid phases isotope labelled compounds such as deuterated FA and paraformaldehyde labelled with ^{2}H and ^{13}C were used in the feeds.

3.5. OBJECTIVES

PEMFC grade hydrogen demand, containing as low as carbon monoxide, has been increased in parallel with the climate concerns, onboard vehicle improvements and PEMFC availability for two decades. Methanol has been the liquid feedstock that is considered sustainable and economic, since it can be produced easily from natural gas and its production facilities are really wide around the planet. However, it has some restrictions that it could produce unwanted amounts of CO and cannot break thermodynamic equilibrium up to 450 K (177°C). On the other hand, formaldehyde has been proved to be thermodynamically eligible in terms of equilibrium conversion that it converts completely to product among which nearly no CO exists in equilibrium at low temperatures. Another advantage of formaldehyde is the fast-kinetics at lower temperatures compared to methanol. In Chapter 2, fast kinetics was a part of desired properties in an onboard fuel. Literature survey also supports the low (or no) CO content of hydrogen mixtures produced from formaldehyde. Furthermore, making low temperature operation available with suitable amount of catalyst, formaldehyde steam reforming can be much more economic than methanol steam reforming.

There has been very few amount of studies about FSR in the literature; therefore, in this thesis the works of:

- developing metal loaded mesoporous materials for the FSR reaction,
- performing different characterization techniques to gain information about the physical and chemical properties of the synthesized catalysts,
- and testing these catalysts for FSR in the low temperature ranges,
- producing hydrogen at low temperatures containing low amount of CO with a high yield.

CHAPTER 4

ORDERED MESOPOROUS MATERIALS

Ordered mesoporous materials are a branch of mesoporous materials in which pore sizes and structures can be controlled. Before knowing what they are, types of pores should be defined. International Union of Pure and Applied Chemistry (IUPAC) defined pore types into three categories: microporous (pore diameter less than 2 nm), mesoporous (pore diameter between 2-50 nm) and macroporous (pore diameter higher than 50 nm) (IUPAC, 1972). Each type has its particular use in materials science and engineering.

Mesoporous materials have been developed since the 1980s starting with pillared clays. However, ordered pores and regular pore size distributions could not be obtained until the 1990s, which led to the fact that the reagents and products could not easily transport through the pores resulting in coking in catalytic processes. In the last decade of 20^{th} century with the use of templates in the syntheses, vast amount of developments in ordered mesoporous material technology (Zhao & Wan, 2007). There are still ongoing studies in many areas of industry for the future nanotechnology applications and mesoporous materials are believed to have much of significance on nanotechnology.

4.1. THEIR PROPERTIES AND USES IN ENGINEERING

It is a known fact that Knudsen diffusion takes place for gases in porous media, if the mean free path of the molecule is higher than the pore diameter. This phenomenon is significantly observed in microporous materials, no matter how much surface area and pore volume exists inside the pore channels. However, the advantage of mesoporous materials over microporous ones comes from the

optimum pore size range in which the surface area is relatively high (up to 2500 m^2/g) and molecules still can be transported without extreme mass transfer limitations. Furthermore, uniform pore sizes are observed in ordered mesoporous materials which give the control on the processes. Eliminating mass transfer limitations up to some degree and having uniform pore sizes, these materials can be used as nanoreactors (Wan & Zhao, 2009).

Ordered mesoporous materials have uses such as adsorption, separation, catalysis, drug delivery, sensors, photonics, electrochemistry and nanodevices. In a few nanometers of scale, growing applications of emerging processes involving large molecules can be efficiently handled by using mesoporous structure (Zhao & Wan, 2007). The matter of this text is mainly focused on the applications of mesoporous materials in catalysis. In catalysis, ordered mesoporous materials are used either as a catalyst or a support for the suitable active site for a reaction.

There are certain types of geometries observed in ordered mesoporous materials given in Figure 4.1.

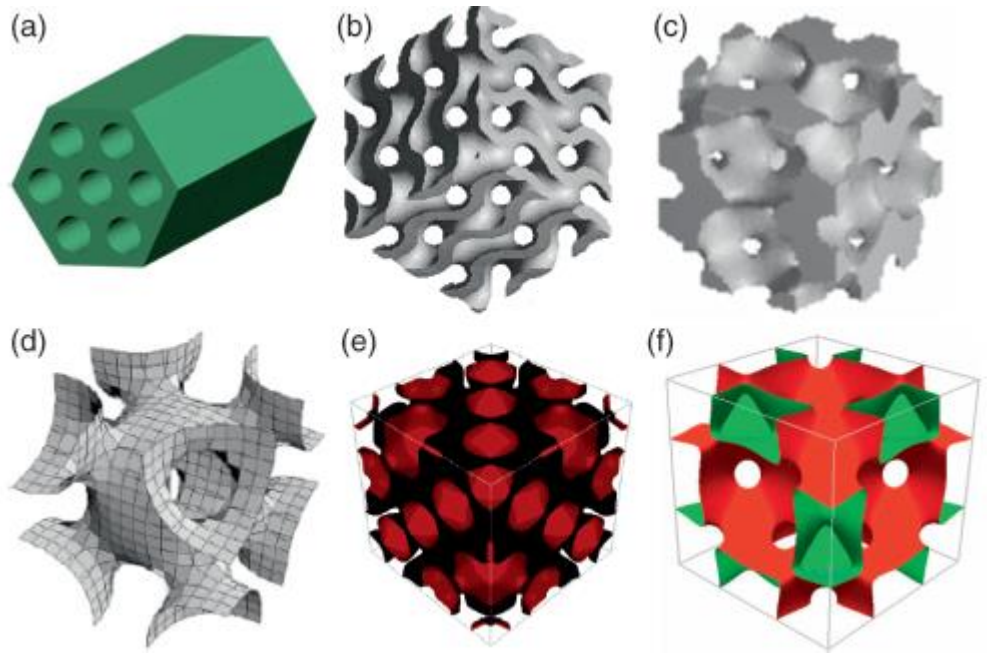

Figure 4.1: Different types of mesostructured symmetries a) *p6mm*, b) *la3d*, c) *Pm3n*, d) *lm3m*, e) *Fd3m*, f) *Fm3m* (from Wan & Zhao, 2009)

2-D hexagonally symmetric mesostructure material with cylindrical channels is *p6mm* and Mobile Company of Matter-41 (MCM-41), Santa Barbara Amorphous-3 (SBA-3) and SBA-15 are the examples. The rest five in Figure 4.1 are 3-D mesostructures, namely, cubic bicontinuous with *la3d* (MCM-48, FuDan University-5 (FDU-5) and Korean Advanced Institute of Technology-6 (KIT-6)) and *Pm3n* (Anionic-surfactant-templated Mesoporous Silica-10 (AMS-10)), simple cubic structures with *Pm3n* and *Pm3m* symmetry (SBA-1, SBA-6 and SBA-11), face-centered cubic structure with *Fm3m* (FDU-12, KIT-5) and *Fd3m* (FDU-2, AMS-8) symmetries and body centered cubic structures with *lm3m* symmetry (SBA-16 and Institute of Bioengineering and Nanotechnology-1 (IBN-1)). MCM-41, SBA-15 and MCM-48 are common interest in the literature (Wan & Zhao, 2009).

There are two types of synthesis in the ordered mesoporous materials. One is cooperative self-assembly of surfactant and the other one is liquid-crystal template pathway. The former is achieved using a surfactant such as triblock co-polymer to gather the inorganic species to form the structure and the latter involves semi-liquid crystal mesophases in the surfactant templating assembly. Both methods are used widely in different ordered mesoporous materials.

Depending on the molecules of structure, ordered mesoporous structures can be constructed by silica, carbon, metal oxides and non-oxides. In this context, only ordered mesoporous silica and carbon are issued.

4.2. ORDERED MESOPOROUS SILICA SBA-15

Silica (SiO_2) is one of the most preferred catalyst supports in the industry due to its economic aspect, durability to various conditions and abundance on the planet. Therefore, ordered mesoporous silica attracted attention of many scientists and professional engineers in the industry.

Ordered mesoporous silica was introduced to literature firstly by the Mobil Corp. laboratories as a part of silicate and aluminosilicate mesoporous molecular sieves (M41S) family in 1992 (Beck, et al., 1992). MCM-41 is one of the most extensively studied catalyst support material of M41S family (Kresge *et al.*, 1992). However,

due to thin pore walls, MCM-41 hydro-stability had been in question for some years, before the discovery of SBA-15.

In 1998, Dongyuan Zhao and his research team from University of California, Santa Barbara employed amphiphilic triblock copolymers as surfactant to synthesize silica network, called SBA-15, exhibiting high surface area (630-1040 m^2/g), uniform pore sizes between 5 to 30 nanometers and thicker pore wall than that of MCM-41. SBA-15 was found thermally stable in boiling water at least 24 hours, whereas thin-walled MCM-41 became amorphous and XRD patterns related to ordered structure disappeared in boiling water after 6 hours. The research team used reaction (hydrolysis) temperatures between 35-80°C for 20 hours in acidic medium (pH < 2) and hydrothermal condensation temperatures between 35-140°C for 11 to 72 hours. TEOS (tetraethyl orthosilicate) and pH 2 was determined due to isoelectric point of silica. Resulting materials were washed, filtered and triblock copolymer (mostly Pluronic P-123 ($EO_{20}PO_{70}EO_{20}$)) was removed by either calcination at 500°C for 6 hours or by solvent extraction with ethanol. Calcination was also used to increase hydrothermal stability of the material (Zhao *et al.*, 1998). SBA-15 shows 2D hexagonal *p6mm* symmetry with long cylindrical mesopores connected with micropores. These interconnector micropores are known to increase the stability of structure of SBA-15 in various conditions and provide possible route to nanocasting process (Lu & Schüth, 2006). Relevant information on nanocasting is to be given in the following pages. During the synthesis, addition of cosolvent like ethanol and a small amount of salts modifies the micellar shapes and results in the elimination of interconnecting micropores after the application of microwave hydrothermal treatment (Wan & Zhao, 2009). Hydrothermal treatment has quite significance on the pore size control. At higher temperatures, PEO blocks of the copolymer becomes hydrophobic retracting from the silicate walls. These resulting enlarged surfactant micelles lead to large pore sizes, thin pore walls and low micropore volumes. Furthermore, without the hydrolysis step at low temperature (i.e. 35-80°C for 20 hours) it was found that resulting solid was disordered silica (Galarneau, et al., 2003).

Synthesis solution pH is an important factor in the synthesis of SBA-15. Aktaş and coworkers (2011) studied the effect of synthesis solution pH during the synthesis of SBA-15 and mesocellular foam (MCF). Synthesized SBA-15 samples with pH values well below pH 1 and pH values higher than 1 showed really different structural and morphological properties. pH values 1 and below 1 showed mesoporous structure in BET and XRD analyses. pH 1.5 showed a complex, interconnected structure with increased amount of micropores in SBA-15 samples. pH 2 solutions led to amorphous disordered silica.

Silica network of SBA-15 was produced from TEOS in a series of reactions. As a part of sol-gel processes synthesis reactions of hydrolysis and hydrothermal condensation (for both ethanol and water) from silicon alkoxides can be shown as in Figure 4.2. (Brinker & Scherer, 1990).

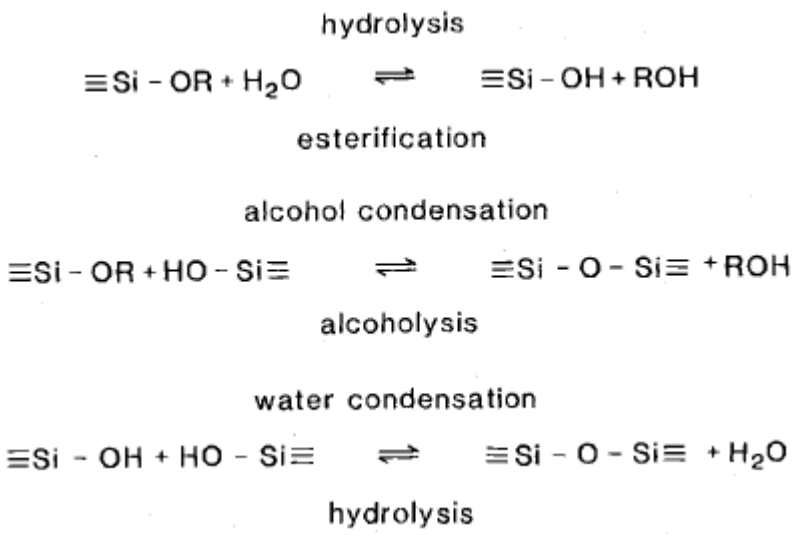

Figure 4.2: Hydrolysis and hydrothermal condensation reactions (Brinker & Scherer, 1990)

In the synthesis of SBA-15, generally TEOS was used as the silica precursor. Accordingly, maximum conversion from TEOS yields 28.8 % SiO_2, meaning that use of 100 g of TEOS results in the synthesis of 28.8 g SiO_2. Acid is used to provide necessary conditions for hydrothermal condensation and as catalyst for the hydrolysis reactions (Brinker & Scherer, 1990).

Nitrogen adsorption-desorption isotherm can be found in Figure 4.3. It shows the evident monolayer-multilayer adsorption, capillary condensation (around 0.75 P/P_0) and multilayer adsorption on the outer surfaces. Furthermore, it exhibits type IV isotherm with H1 hysteresis loop according to IUPAC description. This type is commonly attributed to the existence of a narrow distribution of relatively uniform cylindrical pores (Sing *et al.*, 1985).

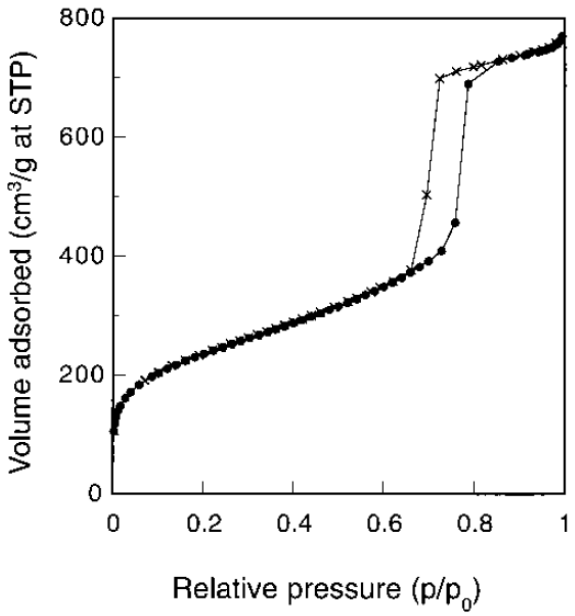

Figure 4.3: Nitrogen adsorption-desorption isotherm for calcined SBA-15 (adapted from Zhao *et al.*, 1998)

For illustration of the structures visually, SEM and TEM images are given in Figure 4.4 and 4.5, respectively. Different synthesis conditions lead to different pore sizes as seen from several TEM images in Figure 4.5.

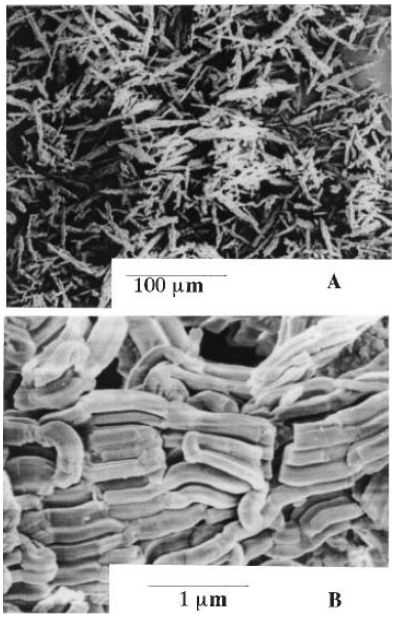

Figure 4.4: SEM images of SBA-15 without calcination step (adapted from Zhao *et al.*, 1998)

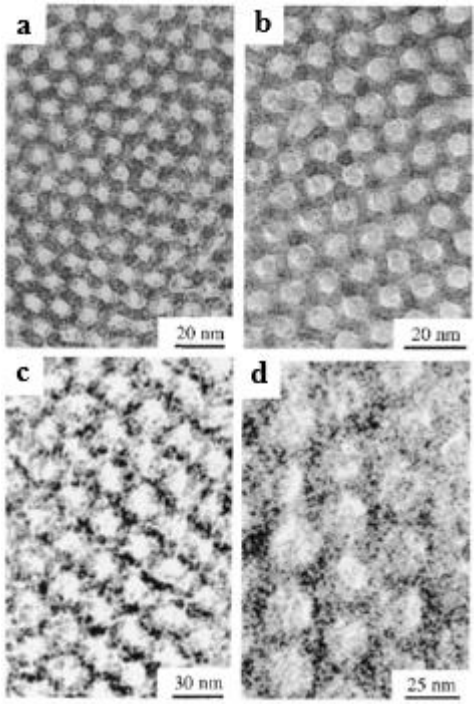

Figure 4.5: TEM images of SBA-15 with pore sizes a) 6.0 nm, b) 8.9 nm, c) 20.0 nm, and d) 26.0 nm (adapted from Zhao *et al.*, 1998)

4.3. NANOCASTING & ORDERED MESOPOROUS CARBON CMK-3

The term “nanocasting” has been used extensively in the field of material sciences and engineering in the recent years. As a commonly known process, casting is the procedure in which liquefied material is poured into a mold which is shaped for the individual purposes. After solidification, this mold is removed from the structure, either by breaking it or some other technique of ejection. As an example, teapot manufacture can be given (Figure 4.6).

Figure 4.6: Classic casting method for the manufacture of ceramic teapot (Lu *et al.*, 2010)

As its name implies nanocasting is the nano-scale version of the casting process. In ordered mesoporous material synthesis methods, nanocasting is very widely used where another mesoporous material play the role of mold, called template. Firstly, the desired raw material is placed in a template material. Then, reactions, thermal and hydrothermal treatments occur. When the final product is ready, template is removed by a suitable method preserving the desired material. By nanocasting process, different types of mesoporous carbon, metal oxides, metals, metal sulfides, polymers etc. could be produced. In the matter of this context, nanocast ordered mesoporous carbons are issued. There is also another way called supramolecular-templating approach in the synthesis of ordered mesoporous carbons rather than nanocasting, also known as hard-templating approach. A representative scheme showing nanocasting process is given in Figure 4.7.

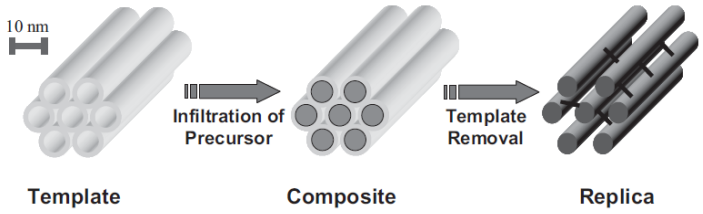

Figure 4.7: Nanocasting process (adapted from Lu & Schüth, 2006)

Mesoporous carbon synthesis by nanocasting process was firstly achieved in 1980s using spherical solid gel as the template (Liang *et al.*, 2008). The method they used in the synthesis was later preserved and is still used in ordered mesoporous carbon synthesis. After the discoveries of ordered mesoporous silica materials (MCM-41, MCM48, SBA-15), ordered mesoporous carbon research gave products consequently. First step to ordered mesoporous carbon was utilized using MCM-41 as the template; however, silica template was not removed (Wu & Bein, 1994). Acrylonitrile monomers were successfully introduced into mesopores of MCM-41, polymerized to polyacrylonitrile and pyrolized between 800-1000°C. However, it was later understood that MCM-41 cannot be utilized in mesoporous carbon synthesis. This was proved by Lee and his coworkers (2000) showing that disordered high surface area microporous carbon forms and XRD pattern related to ordered structure was disappeared, the patterns that Al-MCM-41 once had after the before silica removal from Al-MCM-41-carbon composite. Formaldehyde and phenol reaction producing resins, which are carbon precursors, were used in the synthesis. This effect is shown in Figure 4.8.

Figure 4.8: Absence of interconnecting micropores in MCM-41 leading to disordered mesoporous-microporous structure after nanocasting process (adapted from Ryoo *et al.*, 2001)

Ryoo and his research group (1999) utilized MCM-48 as the hard template to synthesize one of first ordered mesoporous carbons in the field, named CMK-1. Silica removal was performed by HF etching or dissolution in ethanolic NaOH solution. Ryoo's group continued experiments with existing ordered mesoporous silicates and one year later they successfully synthesized ordered mesoporous carbon CMK-3 using SBA-15 as the hard template (Jun *et al.*, 2000). CMK-1 and CMK-3 had similar synthesis procedure. After the synthesis of each hard template, they impregnated mesopores with sucrose dissolved in dilute sulfuric acid solution. After impregnation, they started heating of sucrose molecules at 100°C and 160°C. In order to guarantee the sugar loading in the template, they repeated impregnation and heating procedure once more. Pyrolysis and silica removal were the final steps of the synthesis. As stated previously in this chapter, stability of carbon network depended on the existence of micropores in SBA-15 (and MCM-48). After carbon loading those micropores held mesoporous pipes together without disruption of the structure.

CMK-3 has similar morphology and properties to that of SBA-15. It has 2D hexagonal structure with *p6mm* symmetry. Its BET surface area is about 1500 m^2/g with pore size of 4.5 nm central axes being 10 nm apart and pore volume of 1.3 cm^3/g. It gives three distinguishable peaks in XRD for (100), (110) and (200) diffractions (Jun *et al.*, 2000). Its nitrogen adsorption-desorption isotherm with pore size distribution compared to SBA-15 is given in Figure 4.9.

Figure 4.9 suggests that pore sizes narrow after nanocasting process from 8-9 nm to 4-5 nm. Furthermore, CMK-3 capillary condensation starts at lower pressure than that of SBA-15. TEM image of CMK-3 is given in Figure 4.10. TEM image shows the ordered mesoporous channels longitudinally and perpendicularly. Figure 4.10 also evidently shows that CMK-3 is the exact inverse replica of SBA-15.

CMK-3 has uses in several areas in the materials science and engineering. Firstly, it can be used in energy storage and conversion. It was proved to serve as an electrode after its oxidation with nitric acid in supercapacitor field. Secondly, it is used as the support material in the anode catalyst of fuel cells. Platinum is

impregnated on CMK-3 as an active species and this catalyst has high surface area (Lu *et al.*, 2010).

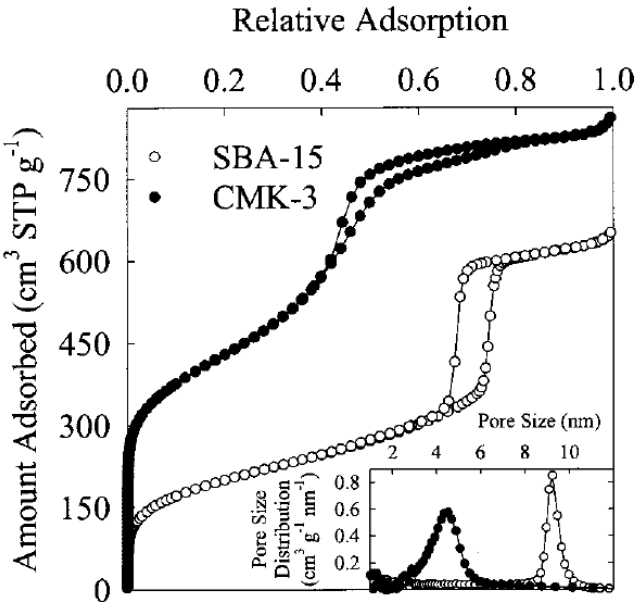

Figure 4.9: Nitrogen adsorption-desorption isotherm at 77 K and pore size distribution for CMK-3 and SBA-15 (adapted from Jun *et al.*, 2000)

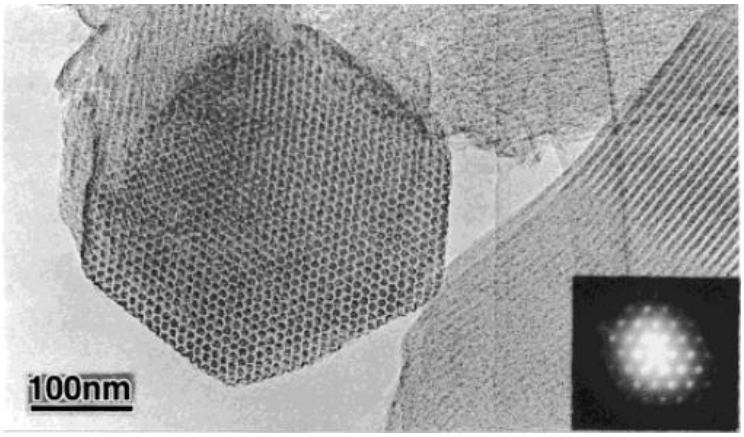

Figure 4.10: TEM images of ordered mesoporous carbon CMK-3 (adapted from Jun *et al.*, 2000)

Another use of CMK-3, perhaps the most important one for this context, is in the field of catalysis. There are reports for the use of Pd supported CMK-3 in Sonogashira reaction (Handa *et al.*, 2008). There are uses of CMK-3 in adsorption and separation field. Vinu and coworkers (2003) studied the adsorption property of

Cytochrome C on CMK-3 at different pH. They found that adsorption of Cytochrome C on CMK-3 is maximized at pH 9.6. Lastly, CMK-3 has found applications in storage of gases. In a study, it successfully stored hydrogen up to 2.27 wt. % at 77 K and 1 bar after several activation steps (Xia *et al.*, 2007).

CHAPTER 5

MODIFICATION AND CHARACTERIZATION OF MESOPOROUS MATERIALS FOR CATALYSIS

Better production can be provided by a better reactor in the plants which is loaded with a better catalyst. This requires a more kinetically active catalyst with an appropriate active metal. Therefore, preparation and gaining information on the physical properties of the catalyst is important in the field of catalysis. Support materials should be loaded with the most active metals for the reaction with a suitable procedure. In order to distinguish the catalyst properties, several characterization techniques are applied on the synthesized materials.

5.1. TECHNIQUES FOR CATALYST PREPARATION

Catalyst preparation techniques varies depending on properties of the support material, the active metal and the interaction between the two. For porous catalysts, active metals or mixtures of metals are desired to be distributed in the pore channels evenly without plugging and sintering. Furthermore, particle shape and reactor conditions are also taken into account in catalyst syntheses. Expected properties of catalysts are shown in Figure 5.1.

This study is mainly focused on the activity of formaldehyde steam reforming reaction without consideration of economic and engineering aspects. Therefore, activity, H_2 selectivity and chemical-mechanical stability of catalyst (also lifetime up to some degree) are to be considered during the study. For nanoporous catalysts, support material is loaded with active metal sites in the scales of nanometers. For visualization, a representative sketch showing a tiny section of a catalyst pellet is shown in Figure 5.2.

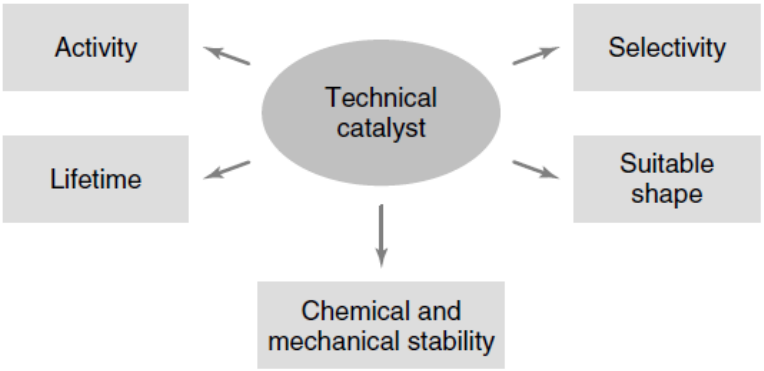

Figure 5.1: Important properties to be considered during catalyst design and synthesis (adapted from Gallei *et al.*, 2008)

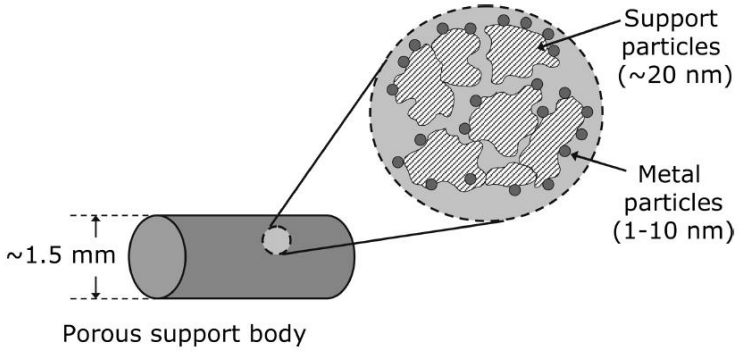

Figure 5.2: Representative sketch for magnified view of a section of a nanoporous catalyst pellet (adapted from de Jong, 2009)

Figure 5.2 also shows how the distribution of active sites occurs on the support particles. For ordered mesoporous catalysts with 2D hexagonal *p6mm* symmetry, these tiny particles are distributed along a nanopipe with particle diameters ranging from 2-30 nm. In order to prevent plugging of the pores with metal particles, pore sizes should be tuned to larger diameters than metal particle diameters.

There are different types of active metal loading in the preparation of porous solid catalysts. Major ones are electrostatic adsorption, impregnation, deposition precipitation, immobilization of organometallic precursors, coprecipitation and some sol-gel chemistry applications (de Jong, 2009). Among them precipitation and

impregnation techniques are very widely used in the industry. The procedure along these methods can be shown as in Figure 5.3.

As seen from Figure 5.3, precipitation includes steps of filtration-washing, drying, shaping, drying and calcination at high temperatures. Calcination steps may be applied after first drying or after shaping process. Excluding shaping step, lab scale catalyst research is nearly the same as in the procedure of Figure 5.3.

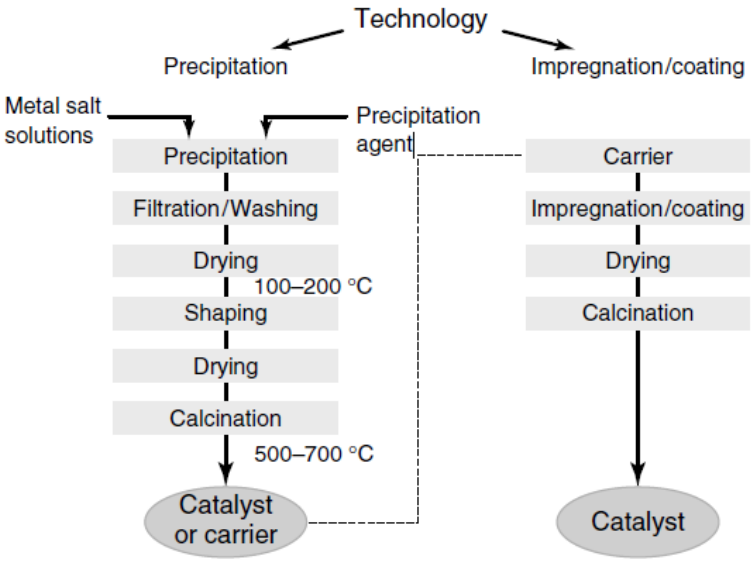

Figure 5.3: Precipitation and impregnation routes for solid catalyst synthesis in the industry (adapted from Gallei *et al.*, 2008)

Impregnation method followed by drying is very widely used technique in the laboratory scale research in heterogeneous catalysis. It is employed to achieve uniform distribution of precursor of the active phase through the support pore channels. Active metal precursor (metal salts, nitrates etc.) is firstly dissolved in the solvent that is the liquid phase. The solution is then contacted with the support material until they fill the pores. This is the exact procedure for the impregnation. There are two types of impregnation method, namely, incipient wetness impregnation (also called dry impregnation), and wet impregnation. Incipient wetness impregnation employs dissolved precursor solution with a volume the same as pore volume of the support, which means no excess amount of solution is applied. The solution is sucked into pore channels by capillary action driving the trapped air

outside. Wet impregnation, as the name implies, is performed in the diffusional conditions. In this case, support material is contacted with the active precursor solution having more volume than the pore volume of the support (Marceau *et al.*, 2009). In both impregnation methods, metal loading with respect to support has to be determined carefully. Loading precursor amounts higher than support could sustain leads to plugging and inefficient distribution of the active metal sites.

Following the impregnation, the solvent has to be removed from the heterogeneous mixture, the procedure called drying. Drying is important because of factors that can change the fate of the catalyst. Basically, after impregnation, the mixture is heated to a higher temperature close to boiling point of solvent or a lower temperature for gentle drying in static condition or under flow of gas. This drying temperature has to be chosen with consideration of the precursor salt that it might have relatively low melting point resulting in coalescence of their initially dispersed particles and exclusion from the pores. Moreover, heating rate is also crucial for dispersion of the precursor. High heating rates in drying operation are favored in some cases causing nearly no transport of the active metal precursor from the pores after impregnation (Marceau *et al.*, 2009).

Calcination step is important and applied for several possible reasons. Firstly, extra materials of volatile and unstable anions or cations that were previously introduced but not desired in the final product are to be removed. Secondly, high temperature ensures the strengthening of the catalyst structure causing incipient sintering. However, excessive sintering must be avoided due to reduction in activity of the catalyst by decreasing the surface area or the pore size. In metallic catalysts loaded by precursor materials, calcination is used for the first reason, to remove the volatile or ionic side of the molecule (Satterfield, 1996). Calcination is carried out in different gaseous atmospheres and different flow rates (or in stagnant gas). Studies towards the calcination conditions are ongoing for the synthesis of catalysts with high metal or metal oxide loadings. Krijn de Jong and his research team studied the effect of different gases during the thermal decomposition of nickel nitrate molecules (in calcination step) to see how the resulting NiO molecules at 24 wt. % distributed along the pore channels of SBA-15 (Sietsma *et al.*, 2007). They tried for

different gaseous conditions at 450°C: stagnant air, flowing air, helium and helium with 1 vol. % NO. Results were observed using High Angle Annular Dark Field - Scanning Transmission Electron Microscopy (HAADF-STEM) images of each material presented in Figure 5.4. The use of NO in helium appears to be effective method in the distribution of NiO crystals along SBA-15 channels as seen from Figure 5.4-d. Furthermore, calcination in Helium leads to better distribution and less active site diameter than the calcination in air Figure 5.4-b. Flow of air is also required to obtain better distribution of metal oxide because stagnant air calcination results in ineffective distribution of the active metals as shown in Figure 5.4-c.

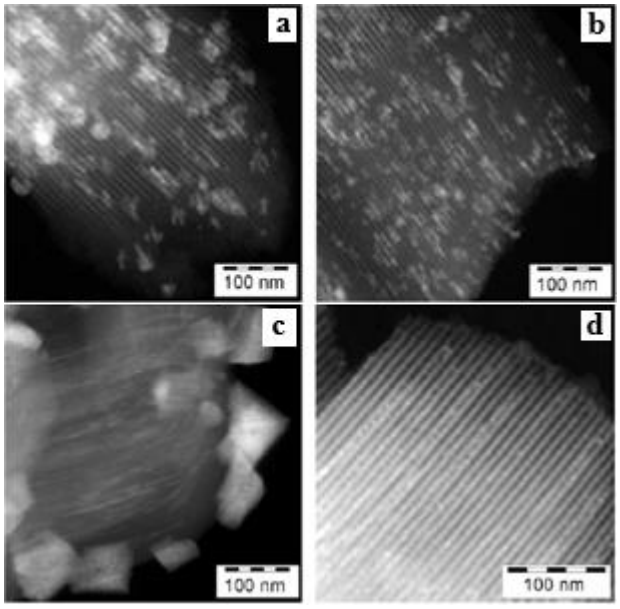

Figure 5.4: HAADF-STEM images of NiO particles distributed in SBA-15 as a result of calcination with **a)** air flow, **b)** helium flow, **c)** stagnant air, **d)** flow of 1 vol. % NO in helium at 450°C (adapted from de Sietsma *et al.*, 2007)

Consequently, XRD patterns supported HAADF-STEM results. NiO particle diameters were 4 nm, 7 nm, 10 nm, and 25 nm for NO-Helium mixture, Helium, air and stagnant air, respectively. Application of this method in high loadings of Co_3O_4 has also led to 4-5 nm particle sizes (Sietsma *et al.*, 2007).

Finally, if the elemental form of the metal is needed, reduction in H_2 is performed to obtain the catalyst. In this case, since most metals have lower sintering temperature than metal oxides have, a temperature lower than calcination

temperature must be selected to avoid sintering of the metal causing a reduction in the metal surface area, pore plugging and reduction in the reaction activity.

5.2. ACTIVE SITE SELECTION CRITERIA AND RELATED STUDIES

Active site material selection is very important step in the preparation of the catalyst. Chosen material can be metal, metal oxide or a mixture of the two.

For FSR reaction copper with zinc complexes are chosen as the active site materials. Firstly, it is very widely used active site in methanol steam reforming catalysts. As explained in Chapter 3, formaldehyde steam reforming occurs as a part of the methanol steam reforming due to dehydrogenation of methanol to formaldehyde (Takezawa & Iwasa, 1997). Secondly, copper was found very active in hydrogen production from formaldehyde in liquid phase experiments again explained in Chapter 3 (Bi & Lu, 2008; Heim *et al.*, 2014; Li *et al.*, 2014). Finally, there are DFT studies supporting the efficient activity of copper in formaldehyde steam reforming reaction (Bo *et al.*, 2009; Li & Lim, 2012).

Zinc is selected as an additional metal. It is not due to its activity in FSR, while it has, as found in Lorenz and coworkers' study (2013) visually shown in Figure 3.8. The main reason is that ZnO plays a role of structural promoter of spacing copper particles appropriately that copper crystallites are highly dispersed along the pore channels. Another reason is that it is electronic promoter providing Zn and O adspecies during reactions (Schimpf & Muhler, 2009).

There are studies preparing SBA-15 supported copper and copper/zinc based catalysts in the literature. Among them, de Jong's group has successfully loaded these metals with high loading (13-18 wt. %) (Munnik *et al.*, 2011; Prieto *et al.*, 2013).

Copper oxide loading to SBA-15 and silica gel was performed with different calcination procedures (Munnik *et al.*, 2011). Using incipient wetness impregnation method, copper nitrate trihydrate ($Cu(NO_3)_2 \cdot 3H_2O$) was loaded in the pores of SBA-15 and silica gel. Acidity of the medium was settled by nitric acid adjusting pH to 1. For 17 wt. % Cu loading 4 M and 13 wt. % 3 M solution of copper nitrate was

used in the procedure. Resulting silica gels were dried at room temperature for 15 minutes in a reactor with gas flow (air, N_2 and 2 % NO/N_2 gas mixtures were used) and calcined at 350°C afterwards. SBA-15 samples were dried at room temperature in a dessicator and calcined at the 350°C. In the calcination, air at different flowrate (including stagnant air), nitrogen and 2 vol. % NO/N_2 were used. According to characterization results calcination in air results in higher CuO crystallite sizes than those of N_2 and NO/N_2 mixtures in silica gels. The higher the air flowrate is, the lower the crystallite size and the higher specific copper surface area obtained there is. In terms of copper particle size, nitrogen and high flow rate air yielded the least values. In SBA-15, NO/N_2 mixture provided quite smaller CuO particle size than air. It was also proved that NO/N_2 provided small particle size and high dispersion of copper oxide particles. This was attributed to the phenomenon in the NiO example studied before by the same group (Sietsma *et al.*, 2008). Apparently, after transforming into nitrate salt from the hydrate form (nickel nitrate hexahydrate), nickel nitrate decomposition occurs in two different reactions.

$$Ni(NO_3)_2(s) \rightarrow NiO(s) + 2NO_2(g) + \frac{1}{2}O_2(g) \qquad \text{(Rxn 5.1)}$$

$$Ni(NO_3)_2(s) + NO \rightarrow NiO(s) + 3NO_2(g) \qquad \text{(Rxn 5.2)}$$

Reaction 5.1 has enthalpy of 241 kJ/mol and 5.2 has 184 kJ/mol. Therefore, the presence of NO, reaction 5.2 becomes thermodynamically favorable and 5.1 is suppressed. Furthermore, reaction 5.2 being less endothermic was attributed to the exothermic scavenging of oxygen radical by NO proved by MS that no O_2 was observed in the product gas. This results in the prevention of sintering and redistribution during nickel nitrate decomposition. This was also the starting point of the copper oxide study (Munnik *et al.*, 2011).

Another study of the same research group focuses on Cu/Zn loading of SBA-15 and silica gel materials and compares these with commercial $Cu/ZnO/Al_2O_3$ catalyst in methanol synthesis reaction (Prieto *et al.*, 2013). Incipient wetness impregnation using 4 M precursor metal aqueous solutions was performed using copper and zinc nitrate salts. As an important note, they arranged Cu/Zn atomic ratio as 65/35.

Impregnates were dried at room temperature for 12 hours under vacuum environment. Calcination was performed at 450°C for only 1 hour under pure N_2 and 2 vol. % NO/N_2 gas mixture at 10,000 h^{-1} GHSV. Before reaction experiments, materials were reduced at 250°C for 150 minutes under 20 vol. % H_2/Ar gas mixture. In order to see and compare the results of loaded SBA-15 catalysts, cross-sections through the 3D-reconstructed tomograms for both calcination gas mixtures are given in Figure 5.5.

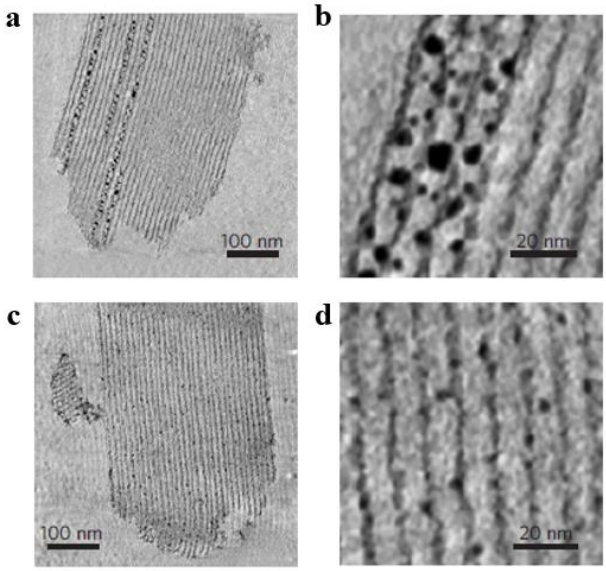

Figure 5.5: 3D reconstructed tomograms for calcined cross-sections of CuZn/SBA-15: (a-b) under 2 % NO/N_2; (c-d) under pure N_2 (adapted from Prieto *et al.*, 2013)

Cross-sections through the reconstructed 3D tomography results show that N_2 calcined samples were evenly distributed in the entire pore channels of SBA-15 as seen from Figure 5.5. However, these results were surprising in the case of 2 % NO/N_2 gas mixture. Unlike studies with nickel and cobalt nitrates (Sietsma *et al.*, 2007) mentioned in the previous section, NO gas mixture yielded larger copper particle size in this study and this was supported by XRD results. Furthermore, comparison of methanol synthesis reactions' activity tests at 260°C and 40 bar showed that N_2 calcined CuZn/SBA-15 was much more stable in terms of activity with 82 % of its initial activity at the end of 240 hour-tests. The value for NO/N_2 calcined catalyst was about 50 % of its initial activity. This was attributed to the high dispersion with small particle size in the case of N_2 calcined catalyst.

Therefore, N_2 calcined catalyst may be also efficiently active in FSR reaction and to be tried in the activity tests.

5.3. CHARACTERIZATION METHODS FOR MESOPOROUS CATALYSTS

When preparation process is complete, a catalyst should be characterized by a series of methods to gain knowledge about its physical and chemical properties.

Nitrogen adsorption-desorption analysis has been considered to be reliable in the determination of inner pore structure of materials such as surface area, pore volume and pore size distribution. Nitrogen adsorption at 77 K (cooled by liquid nitrogen at its boiling point) is recommended by IUPAC for the surface area and pore size distribution (Lu, *et al.*, 2010). Adsorption in mesopores is mainly dominated by capillary condensation, while in micropore structures it is determined by the strong interaction between adsorbate molecules and micropore walls which occurs at very low pressures. The experiments are carried out in a controlled gas environment, where volume of the adsorbed and desorbed gas changes are measured at different relative pressures. Afterwards an adsorption-desorption isotherm is plot in a volume adsorbed versus relative pressure (P/P_0). Physical properties are calculated using this data. For example, BET method, found and named after its inventors (Brunauer *et al.*, 1938), is used to calculate surface area of the porous channels. BJH model is commonly used for the determination of pore size distribution for mesoporous materials (not accurate for microporous materials) and is again named after its inventors (Barrett *et al.*, 1951).

Another major method in catalyst characterization is X-Ray Diffraction (XRD). Its working principle comes from the scattering of X-rays while travelling through a crystalline structure or partly solid medium. In a crystal structure, atoms have excellent periodicities and the aforementioned scattering occurs at each of the atom layers of the crystal showing the characteristics belonging to that materials. XRD gives the distance of regions with highest electron density, which is the distance from one crystal plane to the next, called d-spacing. This d-spacing can be calculated using Bragg's law, which is simply $n\lambda = 2d\sin(\theta)$. In the equation λ is the

wavelength of the X-Ray, *n* is an integer number, *d* is the distance between the adjusted crystal planes and θ is the Bragg angle. During the measurements, an intensity versus 2θ graph is plot. Normally, XRD is applied in two major types, namely, single-crystal and powder XRD. Since mesoporous silica materials do not have crystalline structure on the atomic scale, their structures are determined by powder XRD (Lu *et al.*, 2010).

Mesoporous channels have pore sizes less than those of the wavelength of visible light range. Therefore, they cannot be observed under optical microscope. However, these nano-scaled mesoporous (or any atomic-scale) structures can be observed by electron microscopy technique. Transmission electron microscope (TEM) uses accelerated electron beams to focalize onto samples by electromagnetic fields. Diffracted electrons are detected on a photographic film or a fluorescent screen. Yet, there are limitations in the resolution due to imperfection of the electromagnetic lenses which is applicable only down to 0.1 nm. Normally, this is sufficient for mesoporous materials. On the other hand, recent advances in digital imaging technology made it possible to capture images of atomic planes of separation less than 0.2 nm a technique called HRTEM (Lu *et al.*, 2010).

SEM (scanning electron microscope) is used to image the nanomaterials in which secondary or backscattered electrons emitted from the area irradiated by the scanning electron probe are recorded. Before imaging, surface of the specimen is prepared to be able to conduct electrons. This is done by metallic coating. Good resolution can be obtained by nano-objects such as Pt particles. Compared to TEM, SEM has lower resolution, which is down to 5-10 nm. However, it can give high depth of field and contrasted images of specimen surfaces with a 3D aspect (Gallezot & Bergeret, 2008).

Another method, thermogravimetric analysis (TGA) is a widely used technique in analytical chemistry. It is used to measure the change of a sample under certain atmosphere with a defined temperature increments per time. As a result, it gives the change of weight as a function of temperature. The gaseous atmosphere used can be chosen as an inert or reactive to the sample depending on the type of study.

TGA gives insights about physical-chemical phenomena, crystalline transition, fusion, vaporization, sublimation, adsorption-desorption, absorption, decomposition, oxidative degradation, solid-state and solid-gas reaction properties of the provided sample (Coats & Redfern, 1963). In addition, TGA can be used for post-activity spent catalyst analysis to check for coking or etc. and to obtain information about the thermal stability of the materials.

Temperature-programmed desorption (TPD) is a method to observe desorbed molecules from catalyst surfaces with an increasing temperature. By TPD, one can obtain: type and amount of the different forms of adsorbed species; the bond energies between adsorbate and surface; and possibly the type of bonding of the adsorbed species on the catalyst surface. Pretreated catalyst is placed in an environment to contact with the adsorptive gas. Excess gas is eliminated and the catalyst heated on linear ramp of temperature. Desorption gases are analyzed by a TCD or a mass spectrometer. Adsorptive gases should be adsorbed on the support minimally and react with active metal irreversibly (Gallezot & Bergeret, 2008). TPD is also used for the acidity analysis of the materials.

Infrared spectrophotometry is a reliable method to identify pure organic and inorganic compounds due to absorption of infrared radiation. Furthermore, each molecular species, except for the chiral molecules in crystalline state, has a unique infrared absorption spectrum. Infrared spectroscopy is not much satisfactory, when it comes to measure quantitatively high concentrations due to deviations from Beer's law. In addition, infrared absorbance measurements are considerably precise. On the other hand, Fourier transform infrared (FTIR) spectrometers offer high sensitivity, resolution and speed of data acquisition for the sample analysis. They do not contain any dispersing element, and they detect all wavelengths simultaneously, measured by a Michelson interferometer. FTIR types varies depending on the need. For research purposes, deeper resolution and high signal to noise ratio FTIR instruments are available (Skoog *et al.*, 2004). Furthermore, FTIR analyzes the chemical bonds present in the material and gives information about the composition of it.

X-Ray photoelectron spectroscopy (XPS) is widely employed to probe the electronic structure of atoms, molecules and condensed matter. When photons with energy are directed to a catalyst, it ejects photoelectrons with kinetic energy distribution made up of a series of discrete bands showing the sample's electronic structure. Most common X-Ray source are Al and Mg anodes, which give Kα photons with 1486.6 and 1253 eV energies, respectively (Moretti, 2008).

CHAPTER 6

EXPERIMENTAL

In this chapter, experimental procedures for catalyst preparation, characterization of synthesized catalysts and activity tests for formaldehyde steam reforming reactions are explained in detail.

6.1. CATALYST PREPARATION

Two types of catalyst support materials were synthesized, namely, SBA-15 and CMK-3. For active site loading, wet impregnation method was applied throughout this thesis work.

6.1.1. Preparation Method for SBA-15

SBA-15 is synthesized according to the synthesis procedure from the original work of Zhao and his coworkers (1998). The following materials and chemicals were used during the synthesis.

- Pluronic P-123 (Poly(ethylene glycol)-block-poly(propylene glycol)-block-poly(ethylene glycol)) (Aldrich)
- Tetraethyl orthosilicate (also called TEOS) (Merck)
- Hydrochloric acid fuming 37 % (EMSURE degree) (Merck)
- Deionized water

4 g Pluronic P-123 was added in 105 g deionized water and stirred by a magnetic stirrer overnight. Dissolving completely, 23.6 g of hydrochloric acid was added to the solution (2 M HCl is formed) and the solution was heated to 38°C in a water bath, with continuous stirring. After half an hour the solution reaches 38°C, 8.5 g

TEOS was added to the solution and vigorous stirring (about 800 rpm) started. Note that the solution was enclosed in a durable borosilicate glass vessel. 20 hours later the solution was directly placed in an oven at 90°C for hydrothermal synthesis. 24 hours later the solution was cooled, filtered and washed with 500 ml of deionized water. After filtration, the white paste was dried in a water bath at 45°C for slow drying under draft vacuum condition. Dried sample was calcined in dry air flow of 90 ml/min at 600°C for 6 hours with a temperature ramp of 1°C/min. After calcination resulting material was SBA-15.

6.1.2. Preparation for CMK-3

CMK-3 was synthesized according to its original article (Jun *et al.*, 2000). However, SBA-15, the template for CMK-3, was synthesized by aforementioned method. The materials and chemicals below were used during the synthesis.

- Pluronic P-123 (Poly(ethylene glycol)-block-poly(propylene glycol)-block-poly(ethylene glycol)) (Aldrich)
- Tetraethyl orthosilicate (also called TEOS) (Merck)
- Hydrochloric acid fuming 37 % (EMSURE degree) (Merck)
- Deionized water
- Sugar (Torku Şeker)
- Sulfuric acid 95-98 % (Merck)
- Sodium hydroxide (Merck)

Since the SBA-15 was the template for CMK-3, it was synthesized as the first step according to the procedure given in section 6.1.1. 1.25 g of sugar was dissolved in 5 ml aqueous mixture that contains 0.14 g sulfuric acid. When the sugar was dissolved completely, the solution was introduced to 1 g SBA-15 by impregnation method. The suspension was mixed by a magnetic stirrer overnight. The solution was put in the oven at 100°C for 6 hours and then 160°C for another 6 hours. The resulting solid was again impregnated with 0.8 g of sugar in a 5 ml aqueous solution containing 0.09 g sulfuric acid. The mixture was again mixed overnight. Obtained suspension was heated in the oven at 100°C for 6 hours and 160°C for another 6 hours. Resulting solid was carbonized in helium flow of 135 ml/min in a quartz

tubular reactor at 900°C for 6 hours with a temperature ramp of 5°C/min. A 100 ml 1 M NaOH solution with 50:50 vol % of water-ethanol solution was prepared at its boiling point (about 80°C in synthesis conditions) for silica removal. 1 M NaOH solution was prepared by dissolving 4 g of NaOH pellets in a 50 g deionized water and 39.5 g ethanol solution. Composite was introduced to the lean NaOH solution twice, stirred vigorously for 10 minutes each time and filtered at the end. After that the solid was washed with ethanol and dried in the oven at 120°C. Resulting solid was CMK-3.

6.1.3. Catalyst Active Site Loading via Wet Impregnation

Final catalyst preparations were carried out by wet impregnation technique. There are three catalysts synthesized in the thesis work. They were CuZn/SBA-15, Cu/SBA-15 and CuZn/CMK-3. The procedure from Prieto and coworkers' (2013) article was followed. The following metal nitrate hydrate salts were used as precursors.

- Copper (II) nitrate trihydrate (Merck)
- Zinc nitrate tetrahydrate (Merck)

The amount of salts with respect to specific amounts of each support material was calculated in Appendix B for each catalyst.

CuZn/SBA-15 was prepared by wet impregnation of copper and zinc nitrate hydrate salts together in SBA-15. Metal loading of 18 wt. % with 65:35 atomic ratio of copper to zinc was aimed. 0.445 g copper (II) nitrate trihydrate and 0.252 g zinc nitrate tetrahydrate was dissolved in 5 ml water and stirred by magnetic stirrer until the salts were completely dissolved. Salt solution was poured onto 1 g of SBA-15 dropwise with an additional 2 ml water, then the solution was stirred for 24 hours. After 24 hours of stirring the solution was dried at 45°C in a water bath under the hood in draft vacuum conditions. Dried sample was put in quartz tubular reactor and heated to 450°C at a temperature ramp of 5°C/min under nitrogen flow of 100 ml/min. Resulting solid was CuOZnO/SBA-15. In order to make it active and ready for reaction, the solid was reduced with hydrogen at 250°C just before each activity

test with a pure hydrogen flow of 40 ml/min for 150 minutes. 250°C was chosen as the reduction temperature in order to prevent copper sintering.

Cu/SBA-15 was prepared by wet impregnation of copper nitrate hydrate salt to SBA-15. 18 % copper loading correspond to 0.684 g of copper (II) nitrate trihydrate for 1 g of SBA-15. 7 ml of deionized water was used. The same wet impregnation procedure as CuZn/SBA-15 was applied in this case.

CuZn/CMK-3 was prepared again by wet impregnation of copper and zinc nitrate hydrate salts into CMK-3 pores. For 1 g of CMK-3, 0.445 g copper (II) nitrate trihydrate and 0.252 g zinc nitrate tetrahydrate was impregnated in 7 ml deionized water. The same drying, thermal decomposition and reduction procedures as in CuZn/SBA-15 were applied.

6.2. CHARACTERIZATION OF SYNTHESIZED CATALYSTS

In order to determine the physical and chemical properties of catalysts, different types of characterization methods were applied.

6.2.1. Nitrogen Physisorption

Nitrogen adsorption-desorption measurements were carried out in the Department of Chemical Engineering at METU. In the experiments multipoint BET surface area, pore volume and micropore-mesopore size distributions were investigated. All experiments were performed by Micromeritics Tristar II 3020. All synthesized materials were checked by nitrogen physisorption before proceeding to other characterization methods. Samples are outgassed at 240°C in vacuum before the measurement.

6.2.2. X-Ray Diffraction

X-Ray Diffraction experiments were carried out in METU Central Lab X-Ray Diffraction Laboratory (XRDL). Rigaku Ultima-IV X-Ray diffraction device with nickel filtered $CuK\alpha_1$ radiation was used in both wide-angle and low-angle experiments. For SBA-15, only the low-angle diffraction experiment was performed. On the other hand, both low-angle and wide-angle diffraction

experiments were performed for CMK-3 and synthesized catalysts. In low angle 1-10° interval was checked with 0.1°/min, whereas in wide angle 10-90 was checked with 2°/min. X-Ray was charged with 40 kV and 30 mA.

6.2.3. SEM

SEM images were also captured in METU Central Lab, Electron Microscopy Laboratory. All synthesized materials and spent catalysts were imaged by SEM. Before experiments, each sample was Au-Pd coated in order to increase the signal coming from electrons. Experiments were carried out by QUANTA 400F Field Emission high resolution scanning microscope having 1.2 nm resolution. Beam voltage was 240 kV.

6.2.4. TGA

TGA experiments were carried out in Department of Chemical Engineering at METU. Shimadzu Simultaneous TGA/DTA Analyzer DTG-60H was used in the experiments. CMK-3 and spent catalyst samples were investigated. In the experiments, dry air flow of 60 cc/min was applied. Temperature was increased to 900°C from room temperature with a heating rate of 5°C/min.

6.2.5. FT-IR

FT-IR experiments were carried at Prof. Dr. Suna Balcı's lab at Gazi University. DRIFTS spectra of all synthesized catalysts were analyzed as synthesized first. Then, pyridine was adsorbed on the catalysts and dried in the oven at 40°C. Upon drying, DRIFTS of pyridine adsorbed catalysts were also analyzed. Analysis wavenumber between 400-4000 cm^{-1}.

6.2.6. XPS

XPS experiments were performed at METU Central Lab, Surface Analysis Laboratory (YAL). SPECS EA 300 electron spectroscopy for chemical analysis device was used in the experiments. Fresh catalysts of CuZn/SBA-15, Cu/SBA-15 and CuZn/CMK-3 without reduction were given to analysis.

6.2.7. ICP

ICP analyses were performed at METU Central Lab, Chemical Analysis Laboratory (KAL). 0.02 g of sample was firstly digested in microwave digestion system. 3 ml HNO_3, 4 ml HCl and 3 ml HF were added to the vessels. Samples and blanks were digested once more. Complexation was performed by adding 15 ml 5 % boric acid. Samples and blanks were diluted to 50 ml by deionized water. Perkin Elmer Optima 4300DV ICP-OES device was used in determination of elements and molecules in the catalysts.

6.3. ACTIVITY TESTS FOR FSR REACTIONS

One of the significant part of the thesis work was the reaction activity test. In total, four different catalysts were tested to understand the behavior of the reaction with changing materials, morphologies and metal loadings.

6.3.1. Experimental Setup

Activity tests were conducted in a packed bed flow reactor system. Figure 6.1 shows the process diagram of the experimental setup. There are two main streams in the experimental setup. One is hydrogen production unit and other is catalyst reduction unit.

In the hydrogen production unit, formalin solution, ingredient of which is given in Appendix A, Table A.1, is pumped by a syringe pump (Cole Palmer TW-74905-02) having a stainless steel 50 ml syringe into an evaporator. In the evaporator, it is mixed and diluted at 150°C with the carrier gas that is Argon. Argon is used as carrier gas in GC too and it is used to pressurize the GC valve by a pneumatic line. Its pressure is reduced to 5 bar to work the pneumatic GC valve line. Argon flow to the system is arranged by an on-off valve, globe valve and rotameter, respectively. Upon leaving the evaporator, the gas mixture enters the reactor. Reactor is made of quartz with 13 mm inside diameter. It is packed with a catalyst fixed by a quartz wool in the middle.

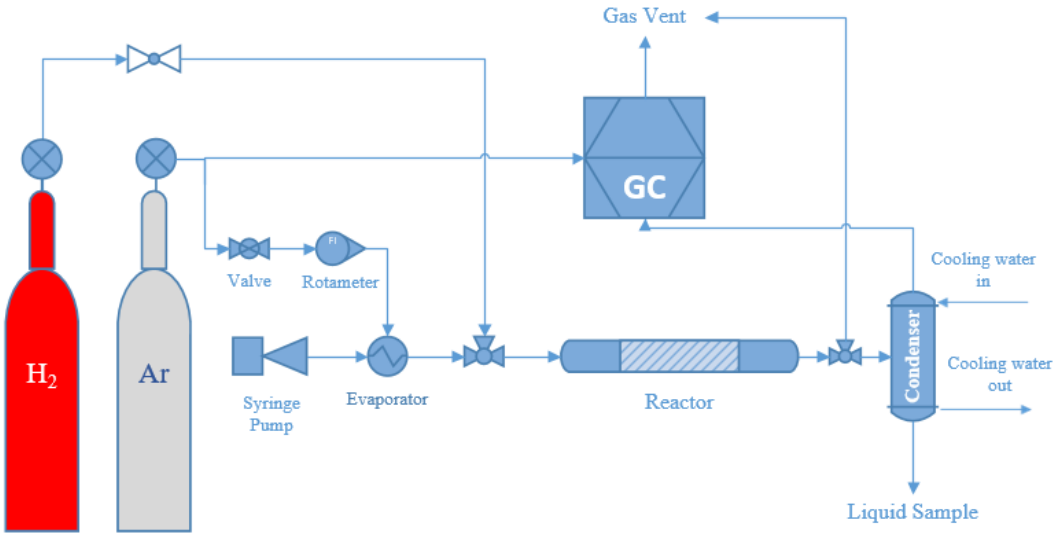

Figure 6.1: Experimental Setup

Reactor is heated by a tubular oven (Carbolite MTF 12/38/250) throughout the experiment. The tubes before and after the reactor and the parts of reactor staying outside the tubular oven are heated by heating tapes that are isolated by glass wool. Heating tapes are used in order to prevent condensation of reactants and products. There is a condenser made of glass after the reactor for condensable products. It is cooled to 3°C by a chiller water bath in order to obtain the condensable products to analyze them separately. This is also a precaution to condensation of any products in GC online gas valves. Liquid products are gathered at a compartment below the condenser and gaseous products leaves it by another stream. Gaseous products come to GC (Agilent Technologies 6850 Network GC System) and are analyzed by an on-line stream analyzer built into GC. Products are analyzed in the GC by 1/8" Alltech Porapak S packed column. Gaseous products leaving GC online analyzer go to soap bubble meter at the end where the gas flow is measured. Leaving the soap bubble meter, the gaseous products are vented.

In the catalyst reduction unit, synthesized catalysts are reduced to make them active for the reaction. Hydrogen is fed to system at 2 bar and further reduced by a globe valve. Then, it enters the reactor at 250°C with a flow of 40 mL/min and leaves it through soap bubble meter, where flow is measured. After that it is given to gas vent.

6.3.2. Experimental Procedure

Before starting experiments, calibration factors of gases for GC are calculated. Each molecular species' calibration factor for Porapak S column with a temperature program presented in Table 6.1 can be found in Appendix C, Table C.1.

For a typical experiment, 0.30 g of catalyst is placed in the middle of the quartz reactor and fixed by a quartz wool carefully in order to not to cause high pressure drop. Reactor is placed in the tubular oven and necessary connections for catalyst reduction unit is made. Hydrogen gas flow is opened at 40 ml/min that is measured by soap bubble meter. Then, oven is heated to 250°C with a temperature ramp of 5°C/min. The catalyst is kept at 250°C for 150 minutes and after that hydrogen is purged from the system by argon flow. H_2 reduction procedure was not followed for commercial copper based methanol reforming catalyst (HIFUEL R-120).

After catalyst reduction, hydrogen production unit is connected to the reactor. Evaporator is opened for heating. Heating tapes are connected, insulated and set for 150°C. Water bath is connected to the condenser, set to 3°C and its flow is started. The syringe is filled with formalin solution and mounted onto syringe pump. Argon rotameter is arranged to 30 ml/min. GC online gas analyzer is started and blank runs were performed before pumping of the feed. Syringe pump flow is started 15 minutes after when the set values of heating tapes, evaporator and water bath are reached. Formalin flow is started and set to 0.9 ml/h. During the experiment, GC analysis is carried out constantly. GC temperature program is presented in Table 6.1. It takes 9.5 minutes for a normal gas analysis. Temperature program starts at 38°C for permanent gases' (H_2, CO, CO_2) separation. When they are separated in 3 minutes, a temperature ramp starts and approaches to high temperature, where condensable species separate. Early experiments showed that all species separate and leave the column before the ramp is over. Therefore, the final holding time is kept less.

Table 6.1: Temperature program for gas analysis in GC

Initial Temperature (°C)	Final Temperature (°C)	Temperature Ramp (°C/min)	Holding Time (min)
38	38	-	3
38	175	24.1	-
175	175	-	0.8

Furthermore, important GC parameters used in this analysis are presented in Table 6.2.

Table 6.2: Gas chromatograph parameters used in gas analysis

Parameter	Set Value
Inlet Temperature	200°C
Detector Temperature	200°C
Total Gas Flowrate	40.3 ml/min
Detector Reference Flow	30 ml/min

Detector temperature is kept at higher temperature than the oven. Inlet temperature is chosen to be high in order to prevent condensation.

After the system reaches steady state, the system is shut off. The syringe pumping is closed, and the formaldehyde is evacuated from the system to prevent its polymerization to para-formaldehyde inside the tubes. Reactor is cooled with argon flow kept at 30 ml/min and after cooldown catalyst is taken out. Then, if there is any condensate, the liquid analysis of the condensate is started to measure the amount of unconverted formaldehyde and methanol. 0.5 μL of liquid sample is given to GC by a micro syringe. Temperature program of the liquid analysis is shown in Table 6.3. Liquid analysis takes about 3.6 minutes. Other parameters are the same as gas analysis shown in Table 6.2. In addition to Porapak S column, Carboxen 1000 custom packed column is used, since formaldehyde, methanol and water mixture do not separate at some concentrations.

Table 6.3: Temperature program for liquid analysis in GC

Initial Temperature (°C)	Final Temperature (°C)	Temperature Ramp (°C/min)	Holding Time (min)
90	90	-	0.1
90	175	24.1	-

Experimental conditions during activity tests are given in Table 6.4.

Table 6.4: Experimental Conditions for FSR Reaction

Condition	Value
Argon flow (ml/min)	30
Argon regulator pressure (bar)	5.1
Heating tape Temperature (°C)	150
Evaporator temperature (°C)	140
Formalin flow (ml/min)	0.9

CHAPTER 7

RESULTS AND DISCUSSION

In this chapter, characterizations and activity test results of four catalysts are presented. These catalysts are HIFUEL R120, CuZn/SBA-15, Cu/SBA-15, and CuZn/CMK-3. Synthesized catalysts were loaded with 18 wt. % copper or copper-zinc metals. Characterization results include nitrogen physisorption, XRD, XPS, SEM, ICP, TGA and DRIFTS. All catalysts were compared at 250°C. In addition, HIFUEL R120 was tested at 175, 200, and 225°C.

7.1. CHARACTERIZATION RESULTS

7.1.1. XRD Results

XRD results are presented for several reasons. Firstly, it is to determine if SBA-15 and CMK-3 have ordered structures. Second reason is to observe changes in catalysts before and after the use in the activity tests in terms of crystal sizes. Third reason is to determine crystal structures in the samples. Elemental and molecular species were identified by Bragg's law on XRD patterns and crystal sizes are calculated by Scherrer equation as shown in Appendix D.

Figures 7.1 and 7.2 show the XRD patterns of SBA-15 and CMK-3 at low angle. In Figure 7.1 SBA-15 has three reflection peaks at 1°, 1.8° and 2.2°. Consequently, it can be said that these three peaks are the signs that the synthesized SBA-15 support has highly ordered structure. In Figure 7.2, CMK-3 has also three reflection peaks and a conclusion of ordered structure can be made again. However, reflection peaks at 2θ values of 1.08°, 1.8° and 2.2° have lower intensity than that of SBA-15 has which could be an indication of low levels of disruption in the ordered structure.

Low angle peaks in Figures 7.1-2 show the same result as the literature (Jun *et al.*, 2000).

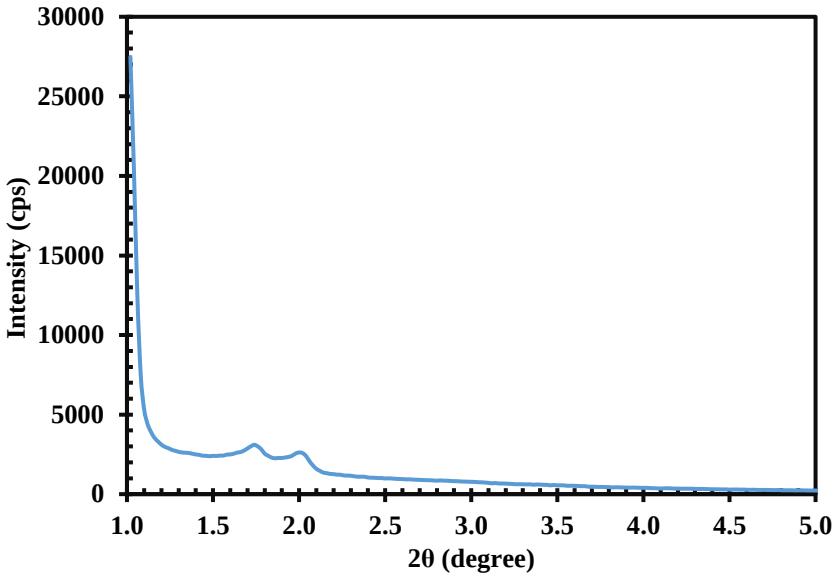

Figure 7.1: Low angle XRD pattern of SBA-15

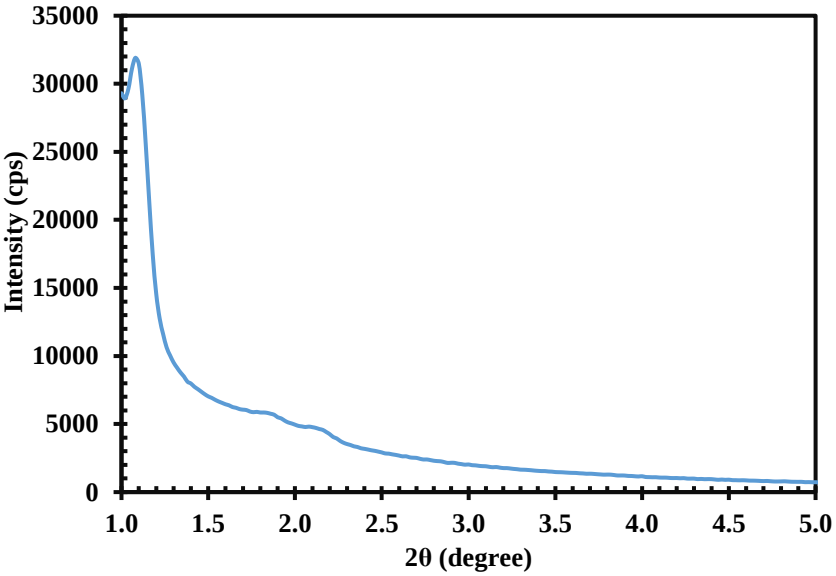

Figure 7.2: Low angle XRD pattern of CMK-3

Figure 7.3 shows the XRD pattern of HIFUEL R120 catalyst before and after the use. For the fresh catalyst peaks are observed at 26.52 (carbon with 31.4 nm cyrstal size), 32.0 (ZnO), 35.6 (CuO & ZnO together), 38.7 (CuO & Al_2O_3 together) degrees. XRD data for each metal and metal oxide can be found in Appendix D. For

the spent catalyst peaks are observed at 26.5 (carbon with 36.6 nm crystal size), 31.9 (Al_2O_3 and ZnO together), 36.3 (Al_2O_3, CuO and ZnO together), 43.0 (Cu with 7.2 nm crystal size) degrees. Firstly, fresh catalyst contains copper oxide, while spent catalyst has copper metal due to reduction by produced hydrogen during activity tests. Furthermore, ZnO did not appear in the fresh catalyst and appeared in the spent catalyst. This could be attributed to the small crystal size of ZnO that swells with time during activity tests. Furthermore, after the tests, alumina and copper crystal sizes may have increased.

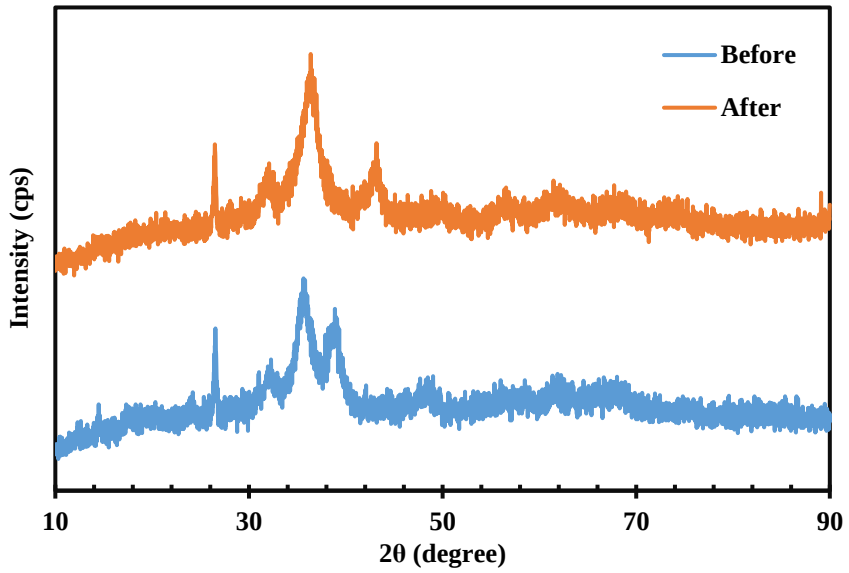

Figure 7.3: HIFUEL R120 XRD pattern before and after the activity test at 250°C

CuZn/SBA-15 and Cu/SBA-15 XRD patterns are given in Figure 7.4. There are peaks observed at 2θ values of 43.3°, 50.5° and 74.2°. These XRD peaks belong to metallic copper (Cu) and XRD data for Cu is given in Appendix D. XRD peak intensities in Cu/SBA-15 are higher than peak intensities of CuZn/SBA-15. The reason for higher peak intensity in Cu/SBA-15 is that it contains more copper than CuZn/SBA-15 catalyst.

CMK-3 and CuZn/CMK-3 XRD patterns are given in Figure 7.5. CMK-3 has an amorphous structure as confirmed by the broad peak between 22-26° 2θ values. XRD pattern for CMK-3 is compatible with the findings from the literature (Hao *et*

al., 2016). CuZn/CMK-3 gives peaks at 2θ values of 43.3°, 50.5°, and 74.2° as in the CuZn/SBA-15 catalyst. These peaks again belong to Cu.

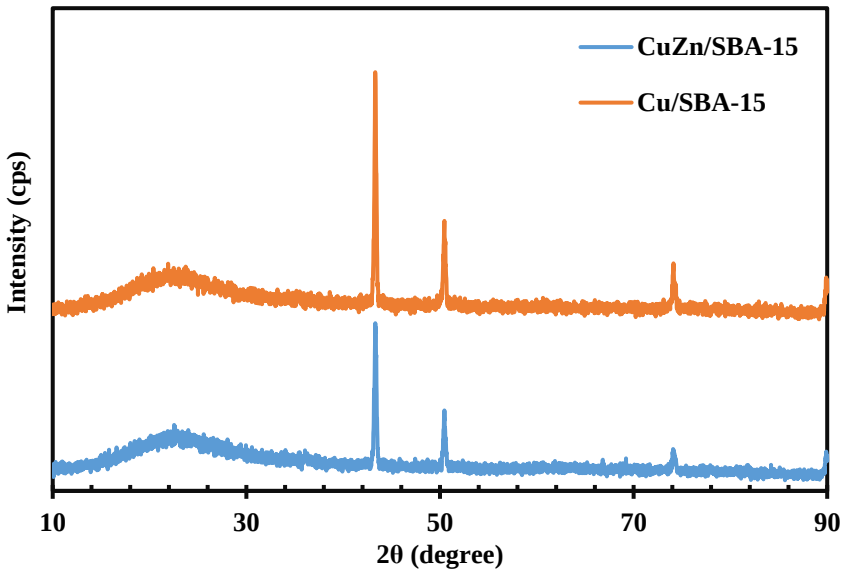

Figure 7.4: Comparison of wide angle XRD patterns of fresh CuZn/SBA-15 and Cu/SBA-15 catalysts

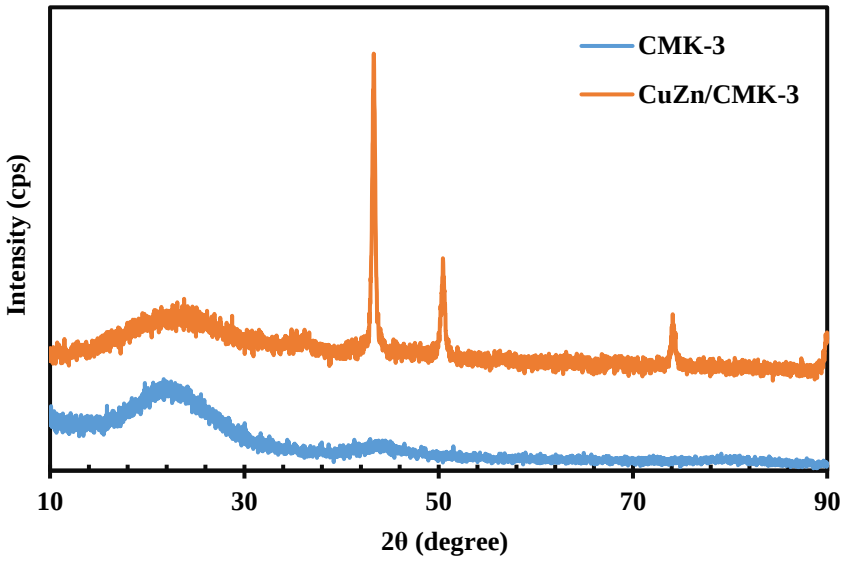

Figure 7.5: Comparison of wide angle XRD patterns of CMK-3 and fresh CuZn/CMK-3 catalyst

Spent catalyst XRD patterns are given in Appendix D, Figures D.1-3. They resembled the same patterns as fresh catalyts with more intensities. It is a sign of

crystal size increase. It is noteworthy that ZnO peaks were not observed in the fresh and the spent catalysts. Copper crystal sizes of fresh and spent catalysts were calculated using Scherrer equation in Appendix D. Crystal sizes are presented in Table 7.1. Among synthesized catalysts, CuZn/CMK-3 has the lowest crystal size with 27.8 nm. The highest copper crystal size was observed in Cu/SBA-15. This is possibly due to lack of copper dispersion provided by ZnO (Schimpf & Muhler, 2009). Furthermore, it is evident that the copper crystal sizes increased after the reaction activity tests. This is a proof of sintering of copper crystals in the catalysts.

Table 7.1: Copper crystal sizes in fresh and spent catalysts

Catalyst	Cu Crystal Size, nm	
	Fresh	Spent
HIFUEL R120	-	7.2
CuZn/SBA-15	40.3	46.4
Cu/SBA-15	47.6	56.6
CuZn/CMK-3	27.8	32.0

7.1.2. Nitrogen Physisorption

Nitrogen physisorption experiments for SBA-15, Cu/SBA-15, and CuZn/SBA-15 samples were carried out at 77 K. Figure 7.6 shows the absorption-desorption isotherms of these three samples. Furthermore, Table 7.2 shows the physical properties of SBA-15, Cu/SBA-15 and CuZn/SBA-15 obtained from N_2 physisorption at 77 K.

Table 7.2: Physical properties of SBA-15, CuZn/SBA-15 and Cu/SBA-15 samples

Material	Multipoint BET Surface Area (m^2/g)	BJH Desorption Pore Volume (cc/g)	BJH Desorption Average Pore Diameter (nm)	Microporosity (%)
SBA-15	516	0.668	4.8	19.3
CuZn/SBA-15	382	0.541	4.8	18.4
Cu/SBA-15	394	0.546	4.8	19.2

According to Table 7.2, pore volume changes slightly after metal impregnation. In the same way, BET surface area decreases due to impregnation.

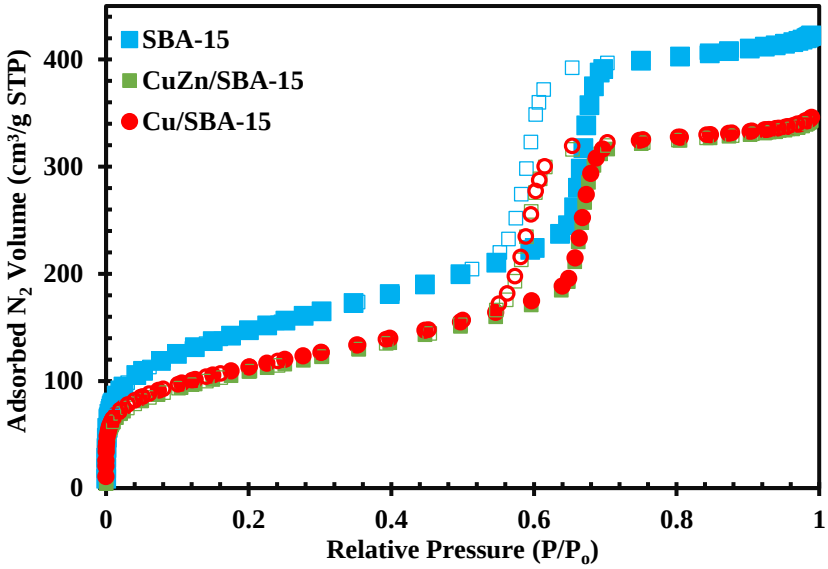

Figure 7.6: Nitrogen adsorption-desorption isotherms of SBA-15, CuZn/SBA-15, and Cu/SBA-15 samples with respect to relative pressure (solid boxes: adsorption branch; blank boxes desorption branch)

Synthesized SBA-15 has multipoint BET surface area of 516 m^2/g, and BJH desorption pore volume of 0.668 cm^3/g. It has type IV isotherm which is the characteristic of mesoporous materials. A well-defined capillary condensation step was observed at a relative pressure range of 0.55 and 0.70, which indicates the formation of uniform pore size distribution. Observed hysteresis is type H1 in which corresponding structure is cylinder. Furthermore, adsorption-desorption branches are perpendicular to each other and parallel. This is an indication of pore sizes being uniform and in a narrow interval.

Similarly, CuZn/SBA-15 and Cu/SBA-15 showed the same type of isotherm having multipoint BET surface area of 382 and 394 m^2/g, respectively. Impregnated samples' isotherms show that there are pore volume decreases in the micropore and mesopore regions. This may be the result of metal active sites being placed on these micro and mesopores and there is possibility of plugging of these regions.

Figure 7.7 shows the pore size distributions of SBA-15, CuZn/SBA-15 and Cu/SBA-15. All samples had BJH desorption pore diameter of 4.8 nm which is the indication of mesoporous materials. It is evident that SBA-15 had narrow uniform

pore size distribution according to Figure 7.7 and this was also supported by Figure 7.6 by capillary condensation. Upon impregnation there was no appreciable change in pore sizes. However, pore volumes decrease at 4.8 nm pore size.

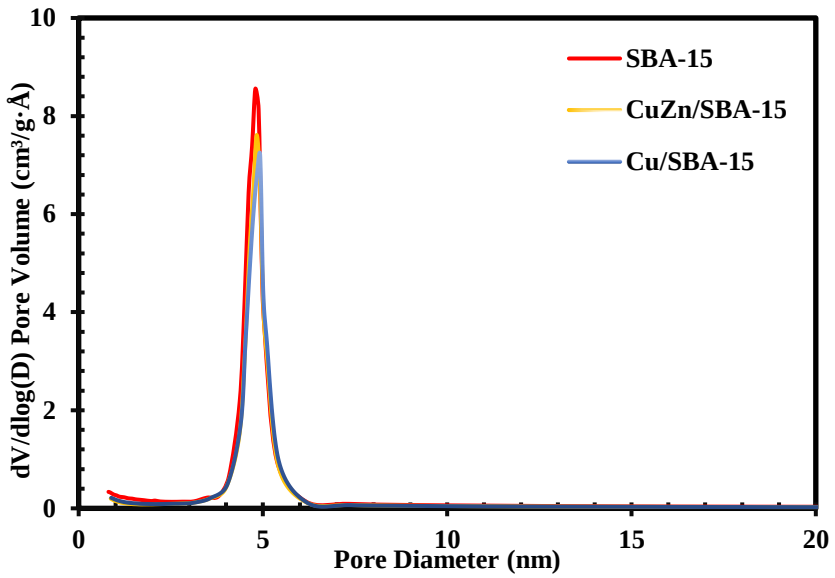

Figure 7.7: Pore size distributions of metal loaded SBA-15 with respect to pore diameter

Figure 7.8 shows the nitrogen adsorption-desorption isotherms of both CMK-3 and fresh CuZn/CMK-3 catalyst. Both isotherms resemble type IV isotherm, which is for mesoporous materials. There are apparent changes in CMK-3 after metal impregnation. Capillary condensation is wider than that of SBA-15 in terms of relative pressure that it is in between relative pressures of 0.41 and 0.94. Capillary condensation for CuZn/CMK-3 catalyst is between relative pressures of 0.46 and 0.90, which is narrower than that of lean CMK-3. Adsorbed nitrogen volume has a difference increasing with relative pressure. The difference is more apparent in mesopore regions. This may be the result of more metal placement of mesopores. H2 type hysteresis was observed in both isotherms. In hysteresis region, the desorption branch is much steeper than the adsorption branch.

Table 7.3 shows the physical properties of CMK-3 and CuZn/CMK-3. CMK-3 has BET surface area of 825 m^2/g, whereas CuZn CMK-3 has 548 m^2/g. According to the table, pore volume of the CMK-3 was nearly halved after impregnation of

metals. BJH desorption pore diameters slightly increased after impregnation. Microporosity has increased from 24.1 % to 35.3 % that is another indication of metals being placed mostly on mesopores.

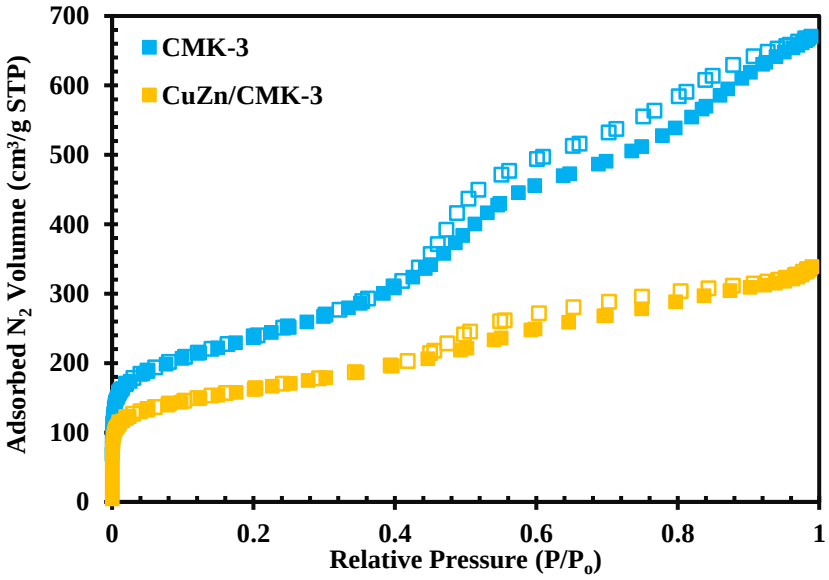

Figure 7.8: Nitrogen adsorption-desorption isotherms of CMK-3 and CuZn/CMK-3 with respect to relative pressure

Table 7.3: Physical properties CMK-3 and CuZn/CMK-3 samples

Material	Multipoint BET Surface Area (m^2/g)	BJH Desorption Pore Volume (cc/g)	BJH Desorption Average Pore Diameter (nm)	Microporosity (%)
CMK-3	825	1.069	3.62	24.1
CuZn/CMK-3	548	0.568	3.86	35.3

Figure 7.9 shows the pore size distribution of CMK-3 and fresh CuZn/CMK-3 catalyst with respect to pore diameter. There is appreciable pore volume decrease on pore having diameter more than 5 nm. On the other hand, pore volume of pore having diameter between 1-2 nm increased upon impregnation. Accordingly, it is obvious that metals were impregnated on big and small pores other than uniform mesopores as seen from Figure 7.9. Furthermore, pore size distribution results match suitably to the adsorption-desorption isotherms in Figure 7.9. In addition,

HIFUEL R-120 has surface area of 67.6 m^2/g, BJH desorption pore volume of 0.20 cm^3/g and BJH desorption pore diameter of 3.81 nm (Çelik, 2012).

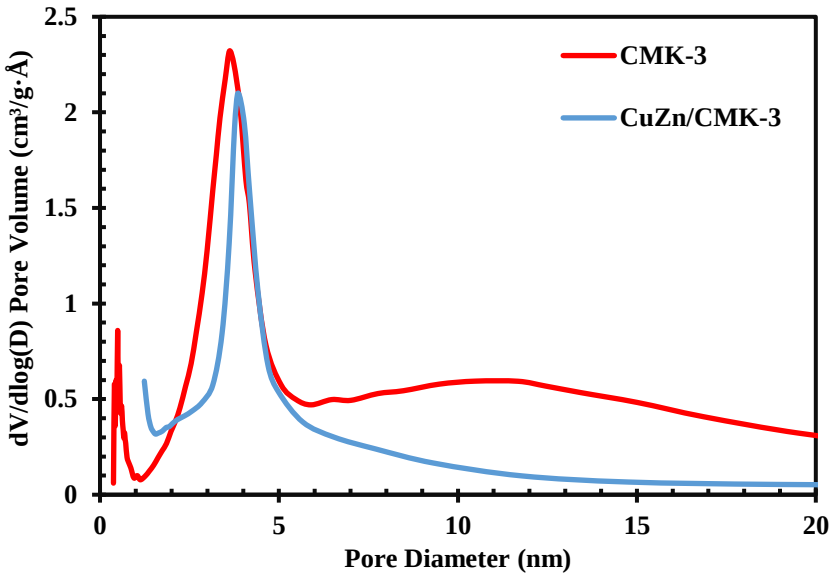

Figure 7.9: Pore size distribution of CMK-3 and CuZn/CMK-3 samples

7.1.3. XPS Results

In order to see the contents of the fresh synthesized catalysts, XPS was used. XPS spectra of CuZn/SBA-15, Cu/SBA-15, and CuZn/CMK-3 are given in Figures 7.10-12. It is important to note that the catalysts were not reduced and were metal oxides.

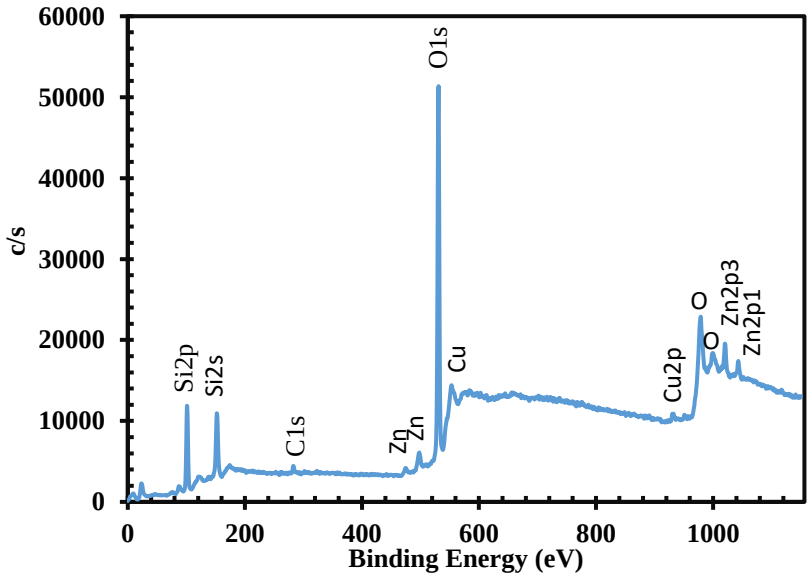

Figure 7.10: XPS spectrum of freshly synthesized CuZn/SBA-15

According to the XPS results in Figure 7.10 copper and zinc elements were observed as expected. Carbon peak at 285 eV comes from the carbon tape used in the experiment. The peaks at 1022 eV belongs to ZnO, and 934 eV to CuO. This is an evidence for the presence of ZnO in synthesized catalyst. The peak at 103 eV belongs to SiO_2. CuZn:SiO_2 ratio is 1.9 % which is lower than the synthesis ratio. This could be due to Zn being insufficiently joining the structure or the inefficient distribution of Zn in the catalyst. Everywhere in the catalyst is not uniform when it comes to distribution of active metal sites and XPS can measure only one plane of the powder and its depth is low. Furthermore, Zn or ZnO was not found in XRD pattern of the catalyst which is another proof that no place in the catalyst is the same. Metals and metal oxides were not distributed the same on the catalyst. In addition, a sample which is only a tiny portion of a catalyst do not resemble all the properties of it.

Figure 7.11 shows the XPS result of Cu/SBA-15 fresh catalyst. Similar to Figure 10, carbon peak comes from the carbon tape used in the analysis at 285 eV. The peak at 934 eV belongs to CuO. The peak at 103 eV belongs to SiO_2. Cu:SiO_2 ratio is 1.0 % which is lower than the desired ratio. As explained, this is due to XPS not analyzing the whole of the sample but a particular plane.

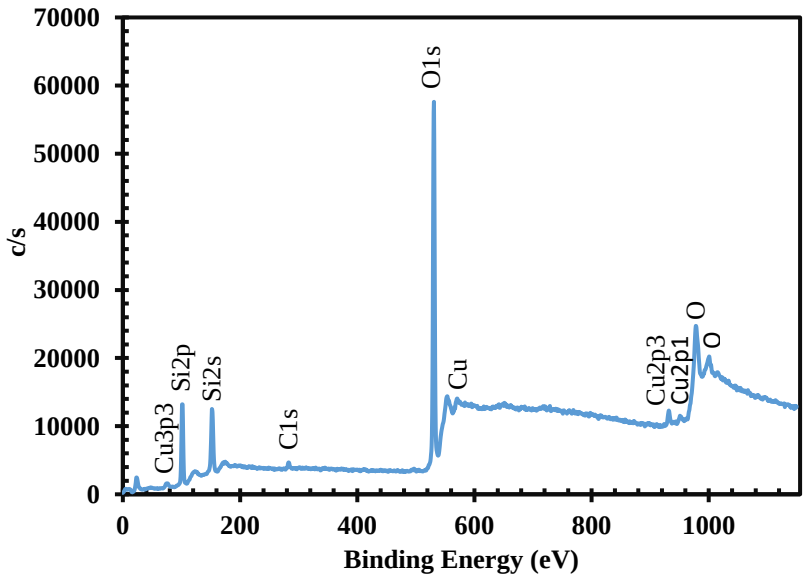

Figure 7.11: XPS spectrum of freshly synthesized Cu/SBA-15 catalyst

Figure 7.12 shows the XPS spectrum of fresh CuZn/CMK-3 catalyst. Carbon atoms were observed as majority of the sample as expected with the peak at 285 eV. CuO peak can be observed at 933 eV. However, no Zn or ZnO peak was observed in the XPS spectrum. This can be attributed to the depth of the measurement and one plane. There are oxygen atoms, since the catalyst was not reduced. More importantly, there are presence of sodium and silica. This is the indication of insufficient silica removal. Therefore, more silica removal with NaOH solution should be employed during the synthesis with washing the residual sodium hydroxide off the sample. CuZn:C ratio of the sample results in 0.7 % which is lower than the expected amount.

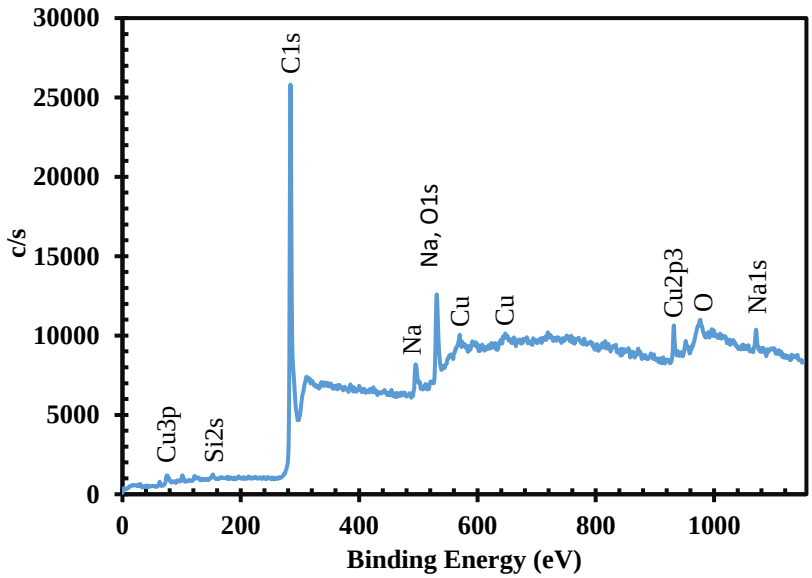

Figure 7.12: XPS spectrum of fresh CuZn/CMK-3 catalyst

7.1.4. ICP Results

ICP results are shown in Table 7.4. Since carbon analysis is not possible with ICP, it is not included in the results. In the table, CuZn/SBA-15 has 9.84 wt. % copper and 4.95 wt. % zinc in which case they were impregnated as 11.7 wt. % copper and 6.3 wt. % zinc. It is an indication that these metals enter the structure sufficiently. There is 0.25 wt. % sodium observed as an error. It may result from the blank solution used in ICP or from the water that is used in the impregnation steps.

Table 7.4: ICP results of all fresh catalysts

Element, wt. %	CuZn/SBA-15	Cu/SBA-15	CuZn/CMK-3	HIFUEL R120
Si	32.8±0.4	32.5±1.0	9.60±0.16	0.27±0.02
Cu	9.84±0.12	15.8±0.4	12.8±0.2	35.0±0.5
Zn	4.95±0.02	-	-	20.7±0.2
Al	-	-	-	7.73±0.22
Na	0.25±0.01	0.27±0.01	1.51±0.06	0.064±0.004

Secondly, copper enters the structure 15.8 wt. % in Cu/SBA-15 in which 18 wt.% metal was impregnated. Similar to CuZn/SBA-15, it includes sodium as an error. This may result from ICP blank sample or impregnation water.

On the other hand, CuZn/CMK-3 did not resemble the desired amounts that only 12.8 wt. % of Cu was analyzed with 9.60 wt. % of silicon and 1.51 wt. % sodium. Zinc did not appear in the result that may be a result of inhomogeneity of the catalyst or insufficient analysis technique for this material. Silicon and sodium are the indications of insufficient silica removal with NaOH solution and washing steps during CMK-3 synthesis.

Finally, HIFUEL R-120 catalyst contained higher loading of desired metals than synthesized catalysts with 35.0 wt. % copper and 20.7 wt. % zinc supported by 7.73 wt. % alumina. It was reported that a black precipitate was observed during dissolution of the sample which corresponds to carbon observed in XRD patterns in Figure 7.3. Furthermore, small amounts of silicon and sodium were observed.

7.1.5. SEM

SEM images of different samples were captured at several magnifications. In order to navigate metal sites, backscattering detector was used in some of the samples.

Figure 7.13 shows the SEM images of SBA-15 at 5000X and 100000X magnifications. Figure 7.13-a shows the agglomeration of SBA-15 particles and it is similar to that of literature (Zhao *et al.*, 1998). Figure 7.13-b image shows the formation of hexagonal particles clinging on each other which also suits the earlier findings of Zhao and coworkers.

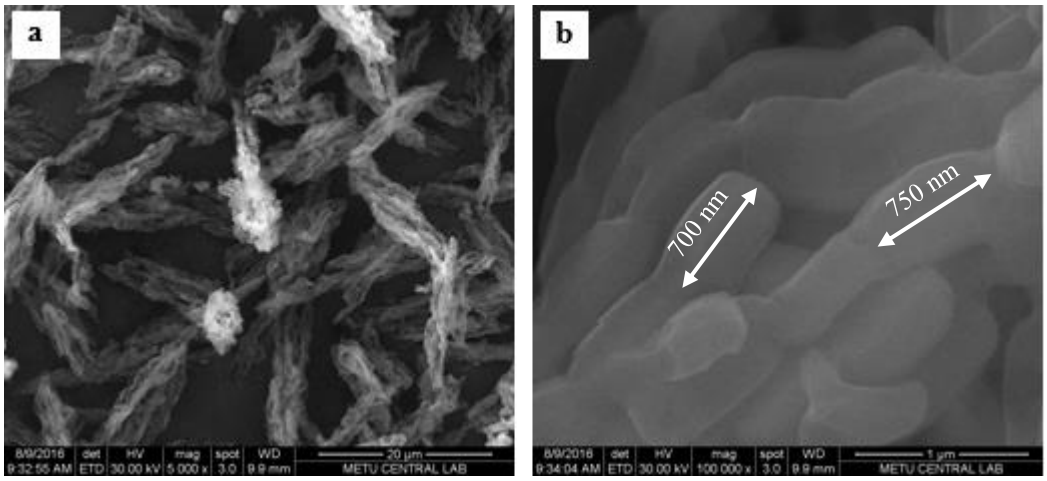

Figure 7.13: SEM images of SBA-15 at **a)** 5000X, and **b)** 100000X magnifications

Figure 7.14 shows the SEM images of CMK-3 at 5000X and 400000X magnifications. CMK-3 had a different morphology than SBA-15. Figure 7.14-b shows a CMK-3 particle broken and suitable for planar observation. The different interconnected pores are obvious and marked by red circles in the figure. In addition, these pores have variable sizes.

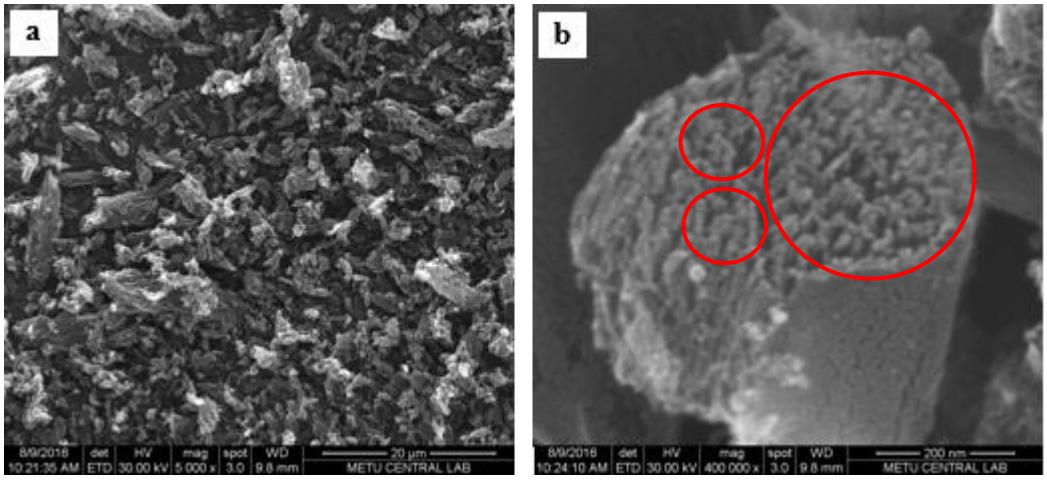

Figure 7.14: SEM images of CMK-3 at **a)** 5000X, and **b)** 400000X magnifications

Figure 7.15 shows the SEM backscattering image of fresh CuZn/SBA-15 catalyst at 500X magnification. Shiny dots in the figure represent Cu and Zn elements. 2000X magnification of this image is shown in Figure 7.16.

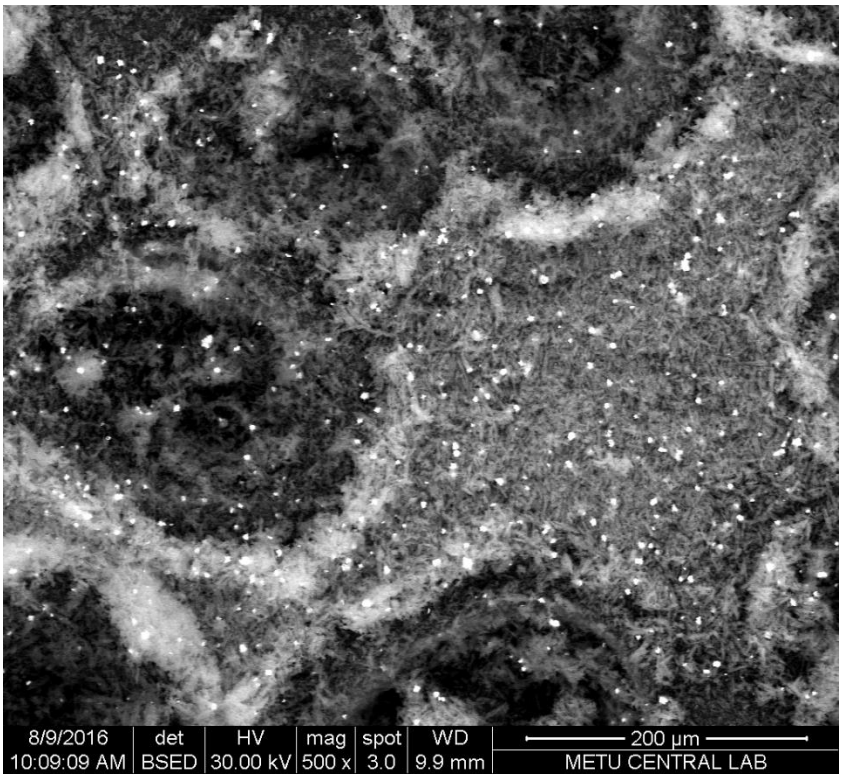

Figure 7.15: Copper particle distribution in fresh CuZn/SBA-15 catalyst captured by SEM backscattering detector at 500X magnification

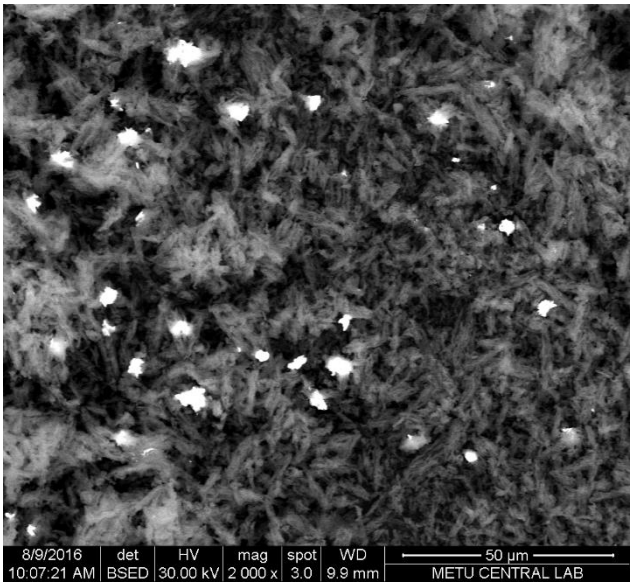

Figure 7.16: SEM image of fresh CuZn/SBA-15 catalyst at 2000X magnification captured by backscattering detector

Figure 7.17 shows the EDX spectrum of fresh CuZn/SBA-15 SEM image (Figure 7.16). As observed from the spectrum, the plane contains Cu and Zn elements. Carbon observed in the spectrum comes from the carbon tape that the sample was put and attached on. Si and O elements result from the silica that is the structure of SBA-15.

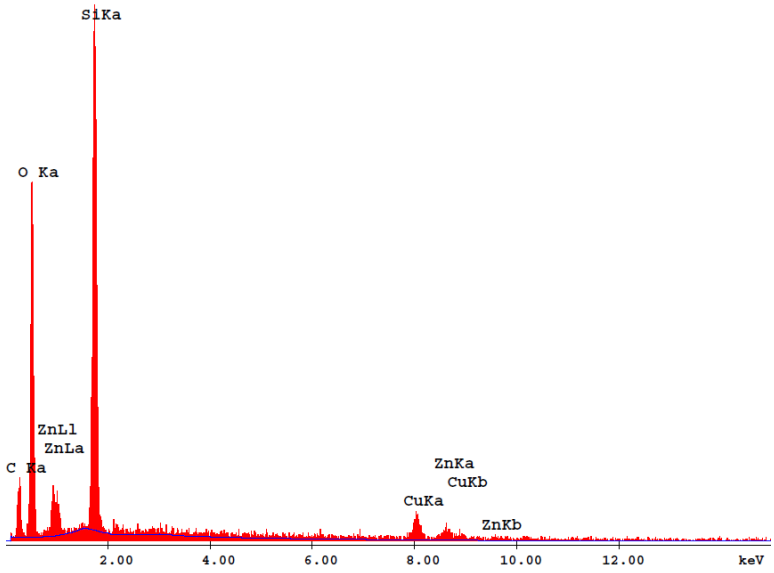

Figure 7.17: EDX analysis result of fresh CuZn/SBA-15 catalyst plane

Figure 7.18 shows the secondary electron SEM image of fresh CuZn/SBA-15 at 100000X magnification. As seen from the figure, there is a copper crystal having size more than 1 μm and Cu-Zn presence in this image was proved by EDX result shown in Figure 7.19. In addition, a close look at Figure 7.18 can visualize that the SBA-15 structure was preserved and it was again agglomerated.

Figure 7.20 shows SEM images of the spent CuZn/SBA-15 catalyst at 5000X and 100000X magnifications. Metal sites were observed to be sintered having particle size of 3 μm in Figure 7.20-b. In Figure 7.21 backscattered SEM image shows the sintered active metal sites at 2000X magnification. Figure 7.22 magnifies Figure 7.21 to 100000X and shows the 4-5 μm sintered crystals more evidently. EDX result in Figure 7.23 proves that the sintered metal sites in spent CuZn/SBA-15 catalyst (Figure 7.22) are composed of copper. Carbon in the figure comes the carbon tape again.

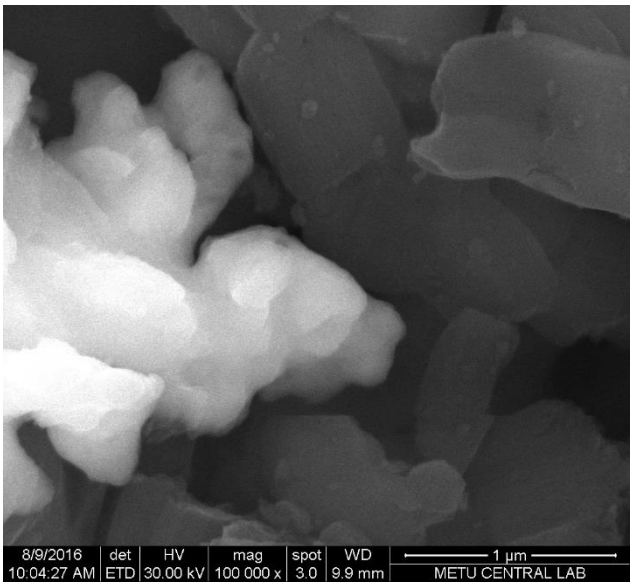

Figure 7.18: SEM image of fresh CuZn/SBA-15 catalyst focused on copper particle on the surface at 100000X magnification

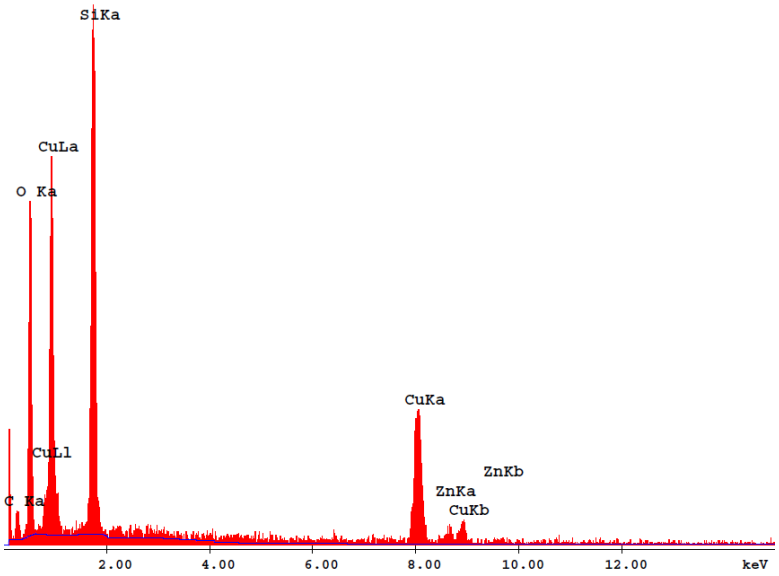

Figure 7.19: EDX analysis result of fresh CuZn/SBA-15 catalyst plane

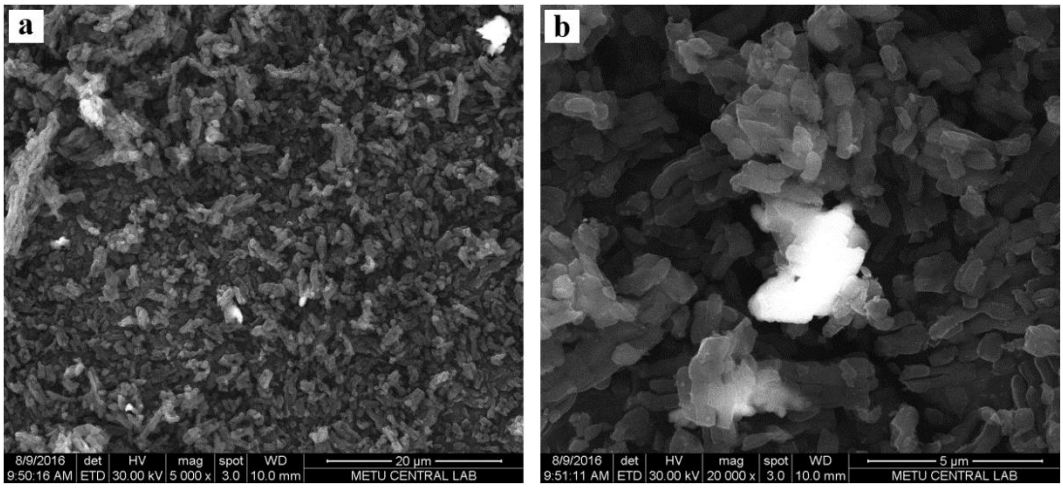

Figure 7.20: SEM images of spent CuZn/SBA-15 catalyst at **a)** 5000X, **b)** 100000X magnifications

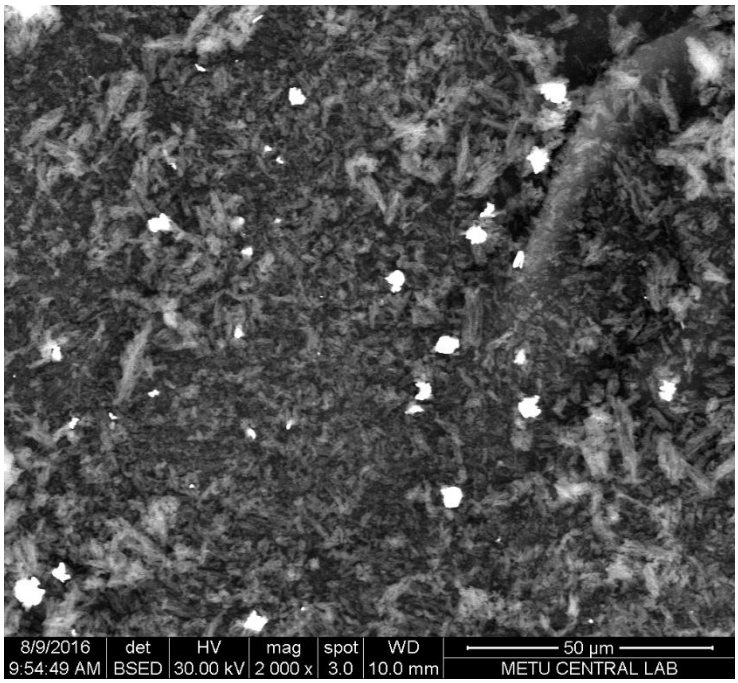

Figure 7.21: SEM image of spent CuZn/SBA-15 showing sintered metal sites at 2000X magnification captured by backscattering detector

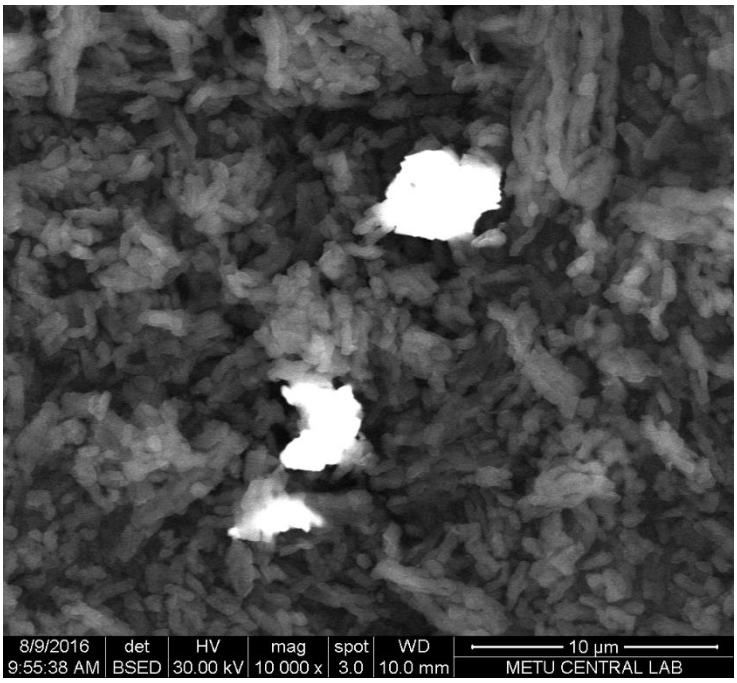

Figure 7.22: SEM image of spent CuZn/SBA-15 focused on sintered metal sites at 10000X magnification captured by backscattering detector

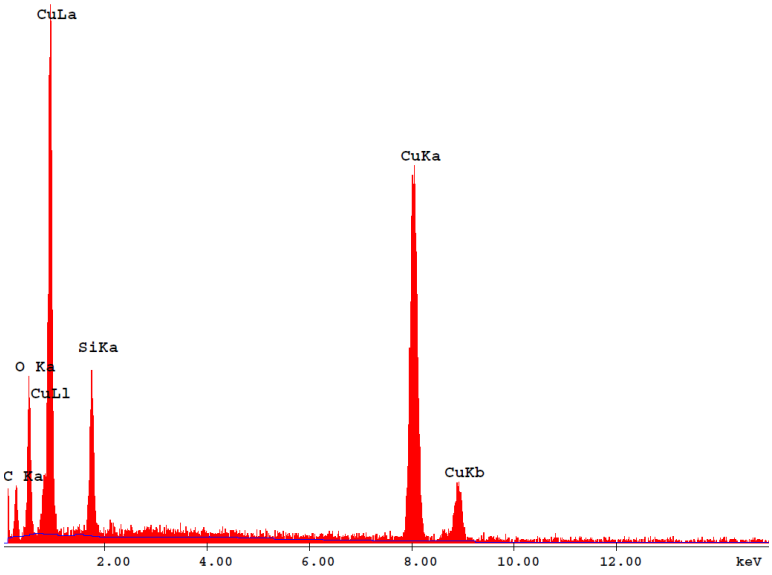

Figure 7.23: EDX analysis result of spent CuZn/SBA-15 catalyst plane

Figure 7.24 shows the SEM image of fresh Cu/SBA-15 catalyst at 5000X magnification. Large copper crystals can be seen in the figure up to 10 µm particle size. However, there are nanometer size copper crystals also and these are seen in SEM image illustrated in Figure 7.25. Copper particles were well-distributed on

SBA-15 particle with sizes between 1 nm to 40 nm in the figure. EDX spectrum of Figure 7.25 proves the presence of well-distributed copper crystals on the support.

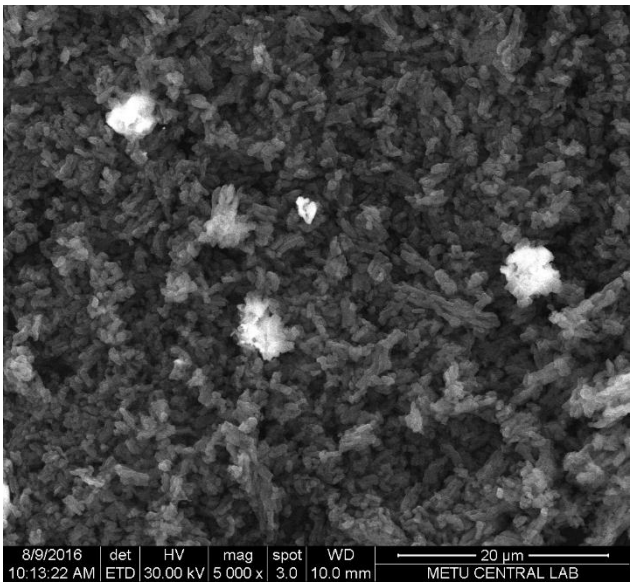

Figure 7.24: SEM image of fresh Cu/SBA-15 catalyst at 5000X magnification

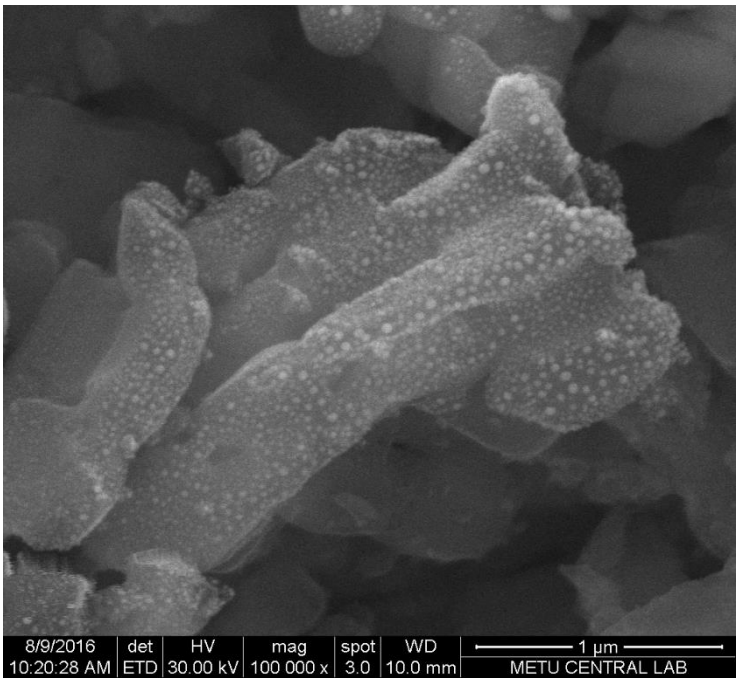

Figure 7.25: SEM image of fresh Cu/SBA-15 catalyst showing well dispersion of copper particles on SBA-15 surfaces at 100000X magnification

White dots on the support (Figure 7.25) are copper metals which is proved by EDX analysis (Figure 7.26).

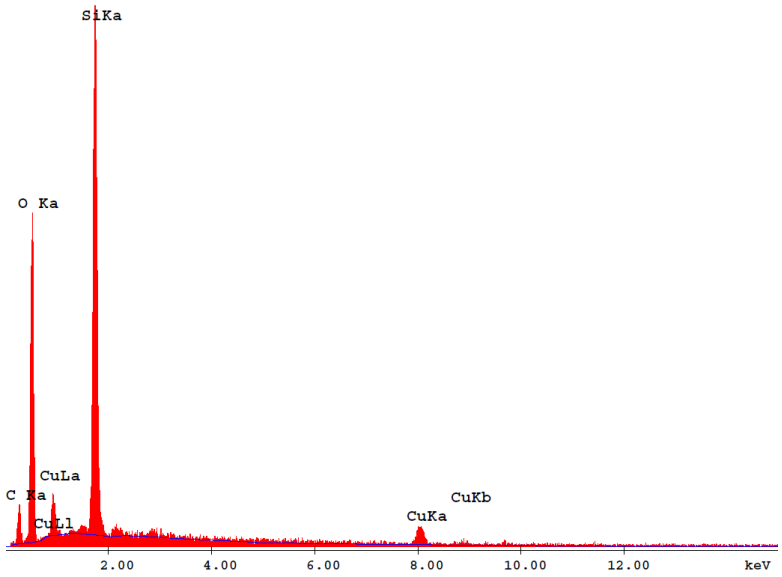

Figure 7.26: EDX analysis result of fresh Cu/SBA-15 catalyst plane

For a better picture, Figure 7.27 show the catalyst's distributed plane by secondary electron detector at 200000X magnification. How tiny the copper crystals are can be clearly observed in this figure.

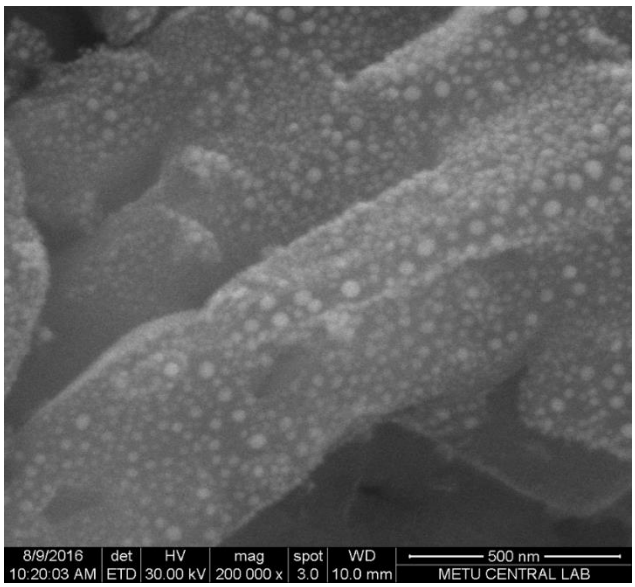

Figure 7.27: SEM image of fresh Cu/SBA-15 catalyst showing dispersion of copper particles on SBA-15 surfaces at 200000X magnification

Figures 7.28 shows the backscattered image of spent Cu/SBA-15 catalyst at 5000X magnifications. As can be seen, shiny dots represent the sintered copper crystals with particle sizes between 5-10 μm. Unlike fresh catalyst, there was no well-distributed plane encountered during the imaging of spent catalyst.

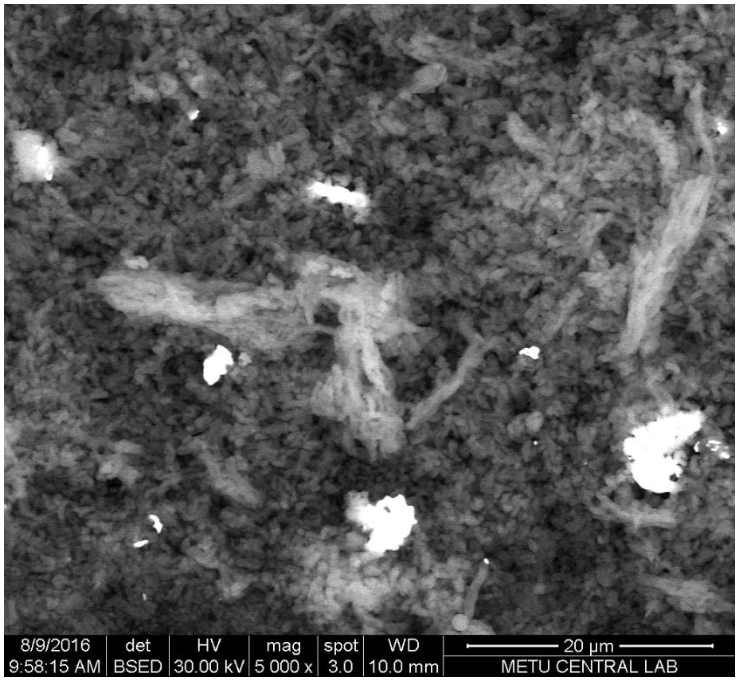

Figure 7.28: SEM image of spent Cu/SBA-15 catalyst showing sintered metal sites at 5000X magnification captured by backscattering detector

Figure 7.29 shows the magnified 20000X image of sintered copper crystal in the spent Cu/SBA-15 catalyst (Figure 7.28). EDX spectrum in Figure 7.30 shows how intense copper gathered in the plane.

Figure 7.31 shows the SEM images of fresh CuZn/CMK-3 catalyst at 5000X and 100000X magnifications. Fresh CuZn/CMK-3 in Figure 7.31-a resembles a similar morphology to lean CMK-3 in Figure 7.14-a. In Figure 7.31-b, a 1.5 μm copper crystal can be seen. Figure 7.32 shows the micron size metallic particle distribution on CMK-3 surface at 1000X by backscattering detector.

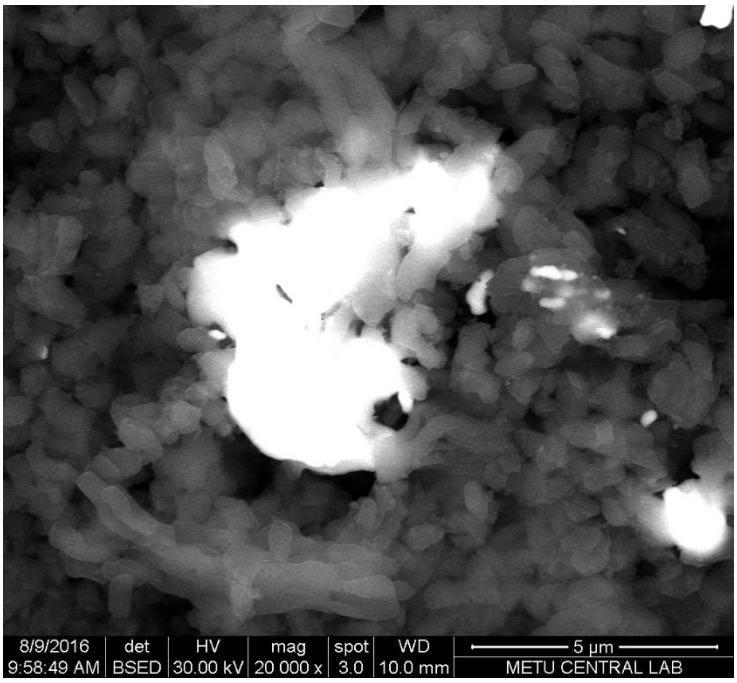

Figure 7.29: SEM image of spent Cu/SBA-15 catalyst focused on a sintered metal site at 20000X magnification captured by backscattering detector

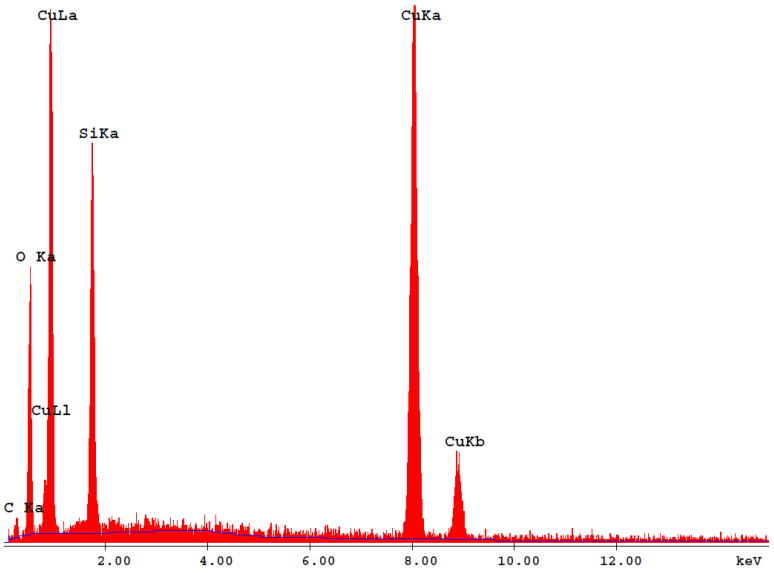

Figure 7.30: EDX analysis result of spent Cu/SBA-15 catalyst plane

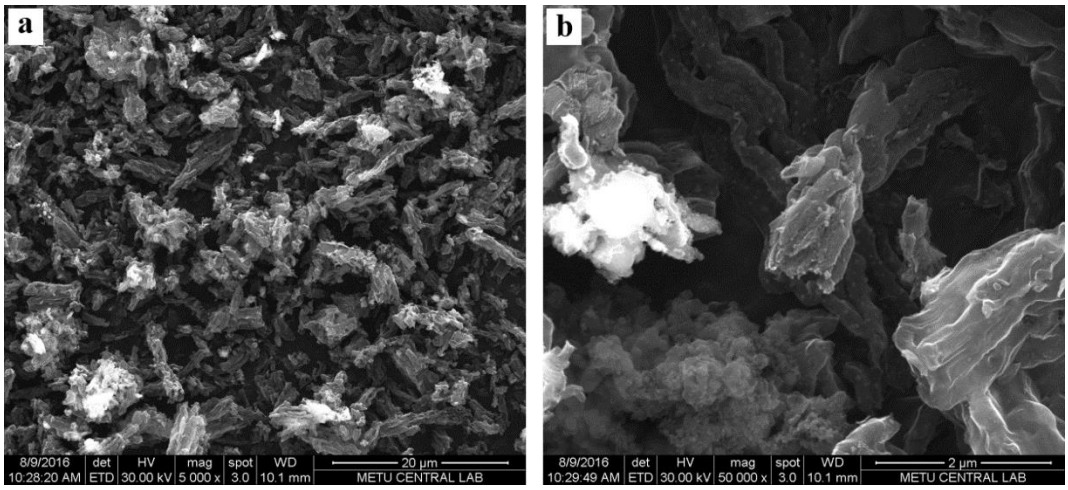

Figure 7.31: SEM images of fresh CuZn/CMK-3 catalyst at **a)** 5000X, **b)** 100000X magnifications

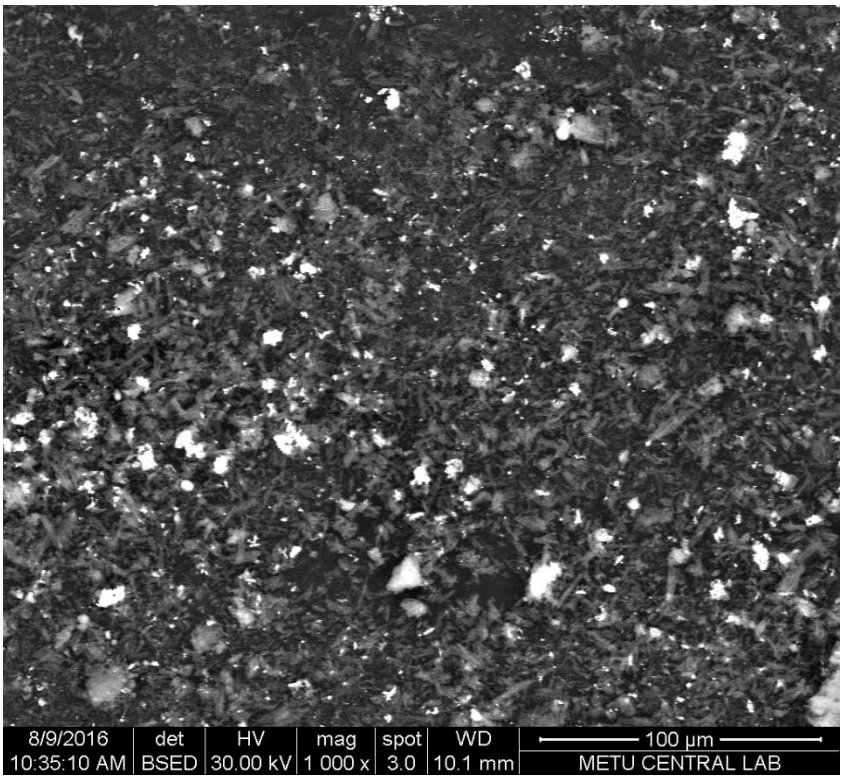

Figure 7.32: SEM image of fresh CuZn/CMK-3 showing copper particles at 1000X magnification captured by backscattering detector

In Figure 7.33, widely dispersed white dots resemble the Cu metal. These dots have variable particle sizes and show how well the copper was distributed. EDX result

of fresh CuZn/CMK-3 SEM image (Figure 33-b) shows the presence of copper in Figure 7.34.

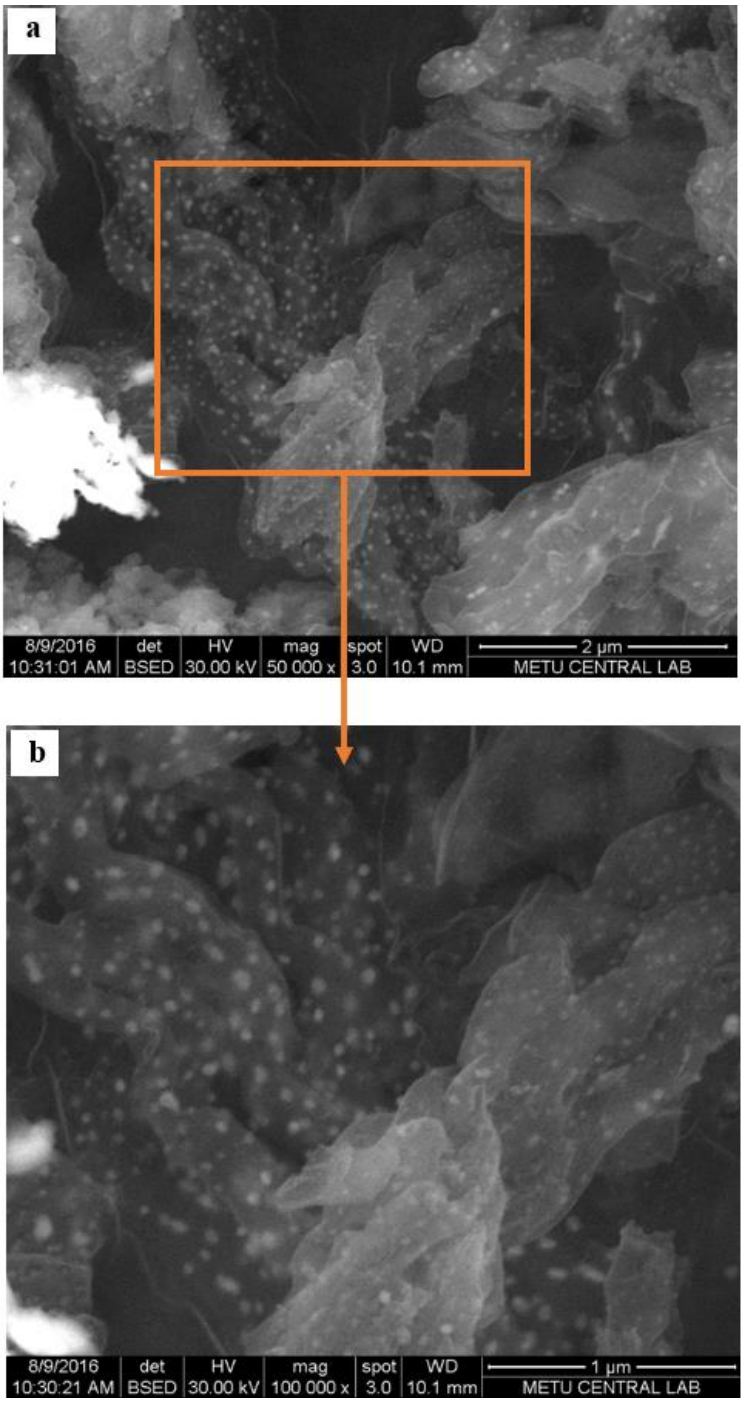

Figure 7.33: Fresh CuZn/CMK-3 catalyst with dispersed copper particles on the surface captured by backscattering detector at **a)** 50000X, **b)** 100000X magnifications

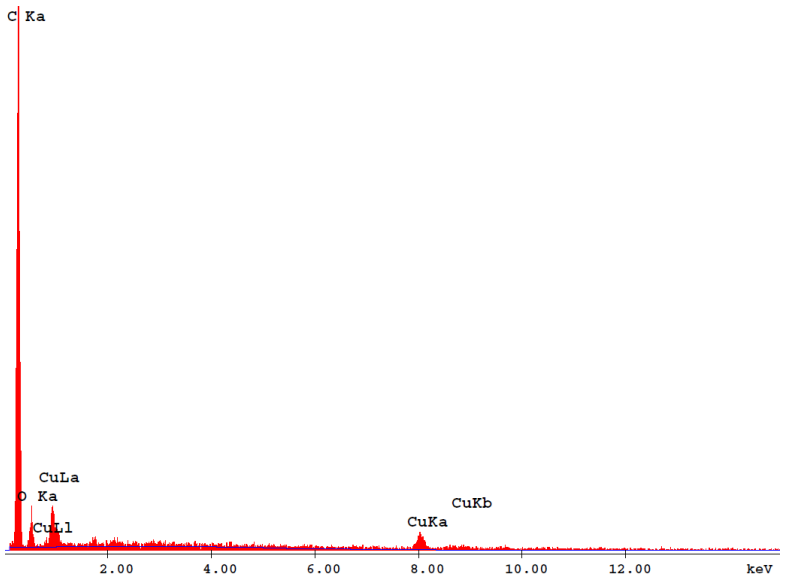

Figure 7.34: EDX analysis result of fresh CuZn/CMK-3 catalyst plane

Figure 7.35 shows the EDX Zn mapping of fresh CuZn/CMK-3 catalyst at 5000X magnification. Zn mapping shows that the metal was well distributed on the catalyst surface.

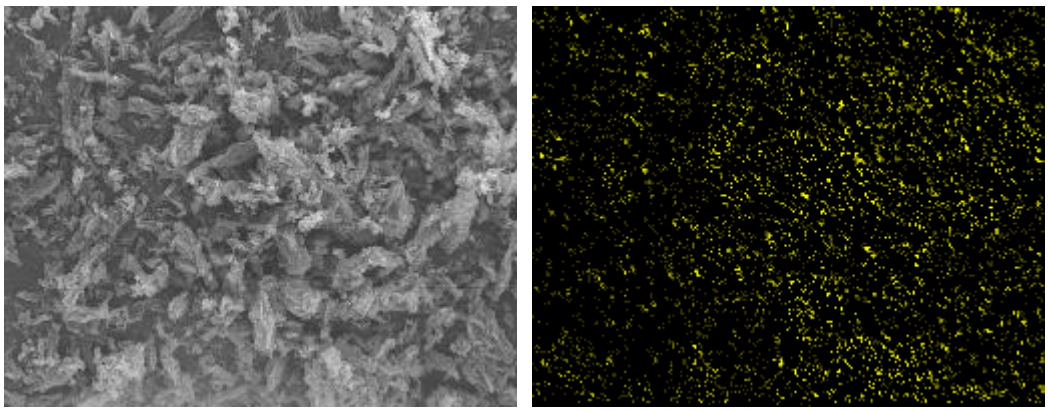

Figure 7.35: EDX Zn mapping of fresh CuZn/CMK-3 catalyst at 5000X magnification

Figure 7.36 shows the backscattered SEM image of spent CuZn/CMK-3 catalyst at 5000X magnification. Shiny dots indicate the presence of sintered Cu and silica particles. Small particles being well distributed on CMK-3 surface as in Figure 7.33 were not encountered in during SEM imaging of the spent catalyst.

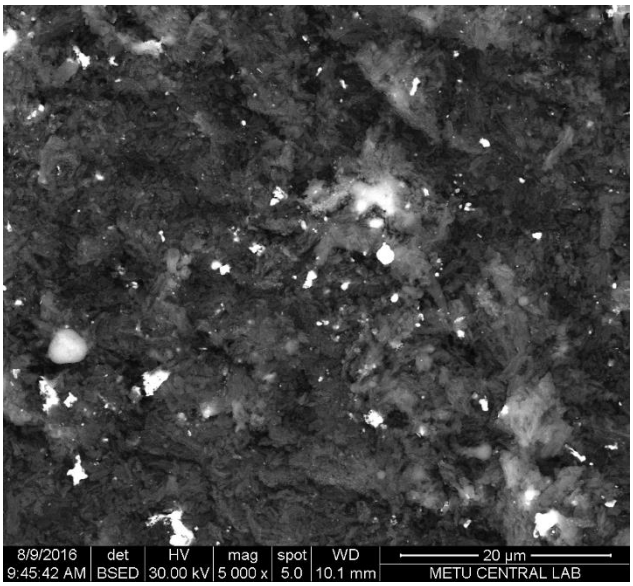

Figure 7.36: SEM image of spent CuZn/CMK-3 catalyst at 5000X magnification captured by backscattering detector

Figure 7.37 shows the magnified SEM image of CuZn/CMK-3 catalyst in Figure 7.36 at 20000X magnification. The white hazy particle in middle of the of figure is silica as proved by the EDX spectrum (Figure 7.38). Other shiny dots are copper crystals distributed on the support plane.

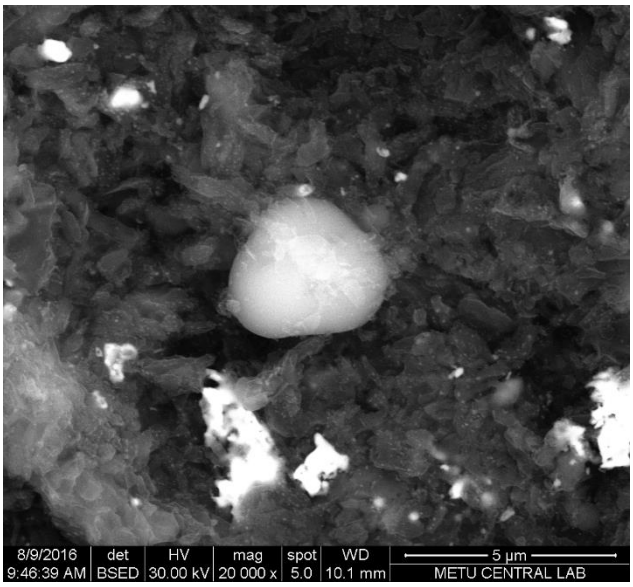

Figure 7.37: SEM image of spent CuZn/CMK-3 catalyst focused on a silica particle at 20000X magnification captured by backscattering detector

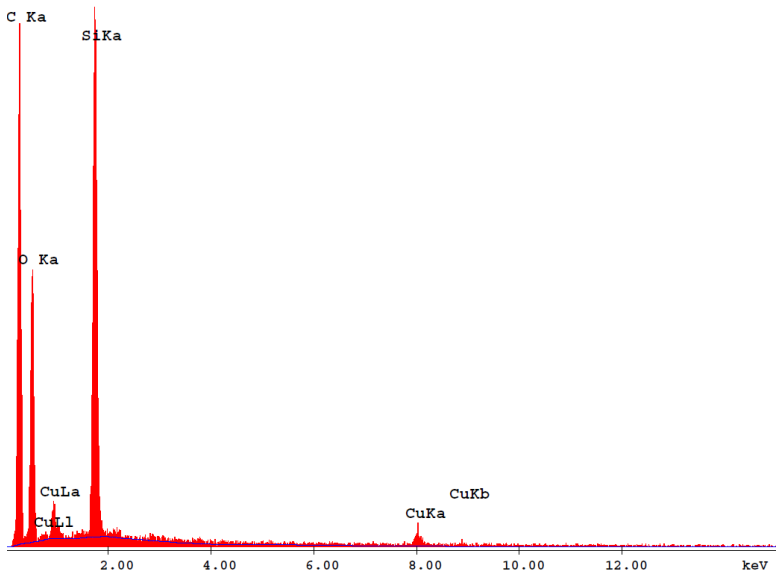

Figure 7.38: EDX analysis result of the area shown in SEM image of spent CuZn/CMK-3

7.1.6. TGA Results

In order to gain some information on carbon deposition, spent catalysts CuZn/CMK-3, Cu/SBA-15, and CuZn/SBA-15 were investigated by TGA. Furthermore, CMK-3 was also analyzed to observe the amount of impurities other than carbon.

Figure 7.39 shows the TGA result of CMK-3 support. First major weight loss was between 45-178°C due to water in the samples. Second major weight loss starts at 371°C where amorphous carbon starts to burn. In the literature, CMK-3 was explained to be composed of only carbon and trace amount of silica (Jun *et al.*, 2000). Accordingly, nearly its whole mass should be burnt in TGA. However, figure indicates that there was a residue of 38.1 wt. % of the original sample. This result supports the presence of NaOH and silica found in XPS spectrum (Figure 7.12) and ICP result in (Table 7.4). There are three unusual diagonal peaks observed between 396-464°C. They are due to poor temperature control against the carbon combustion.

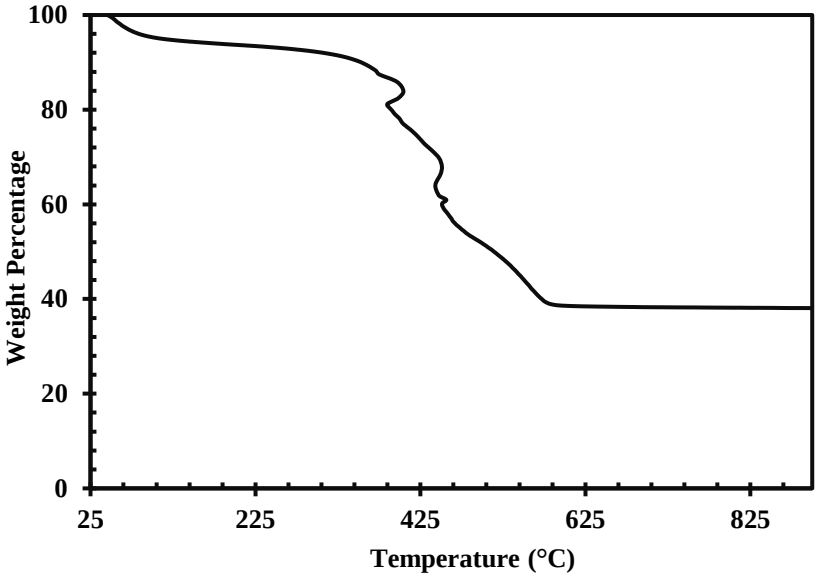

Figure 7.39: TGA result of CMK-3

Figure 7.40 shows the TGA result of CuZn/SBA-15 spent catalyst. Between 45-113°C water vaporizes. However, there is additional weight loss between 680-900°C which is the indication of coke formation. 2.8 wt. % of coke formation was observed in the spent catalyst.

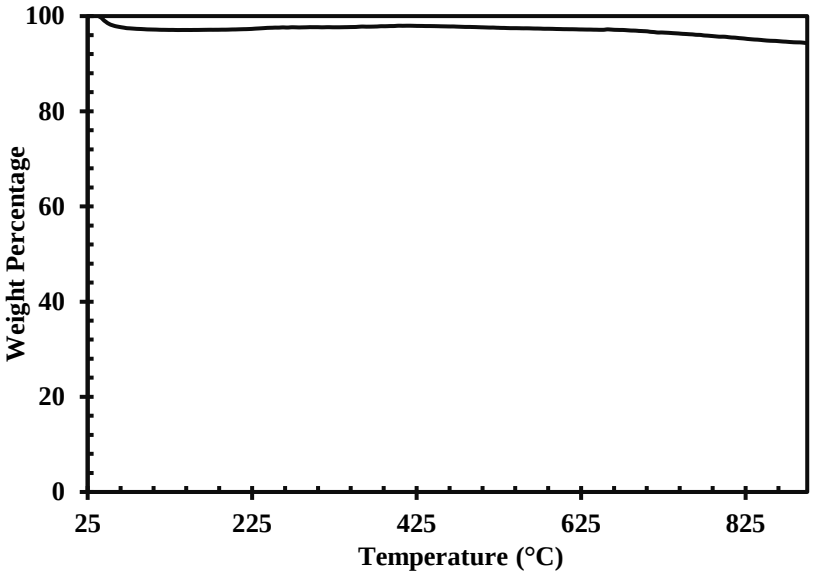

Figure 7.40: TGA result of spent CuZn/SBA-15 catalyst

Figure 7.41 shows the TGA result of Cu/SBA-15 spent catalyst. Similar to Figure 7.40, water vaporization can be observed between 26-113°C. 1 wt. % coke formation was observed indicated by the weight loss between 484-900°C.

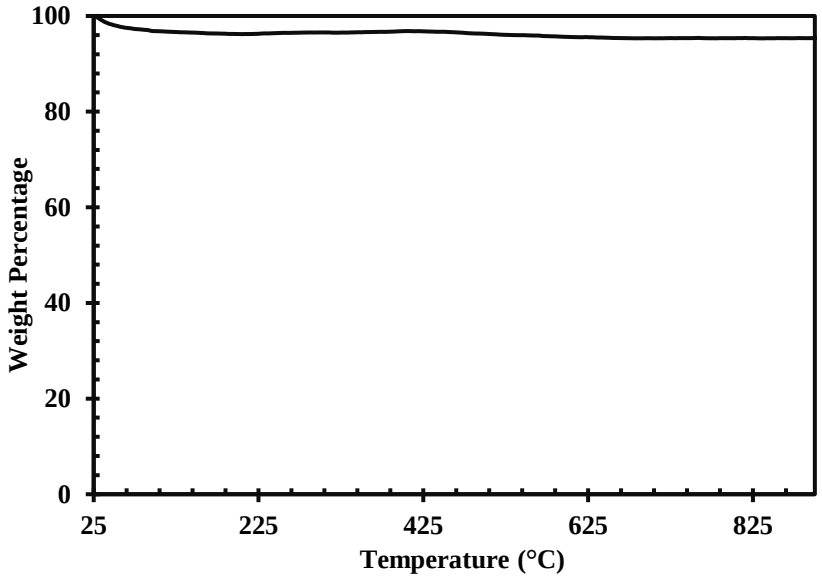

Figure 7.41: TGA result of spent Cu/SBA-15 catalyst

Figure 7.42 shows the TGA result of CuZn/CMK-3 spent catalyst.

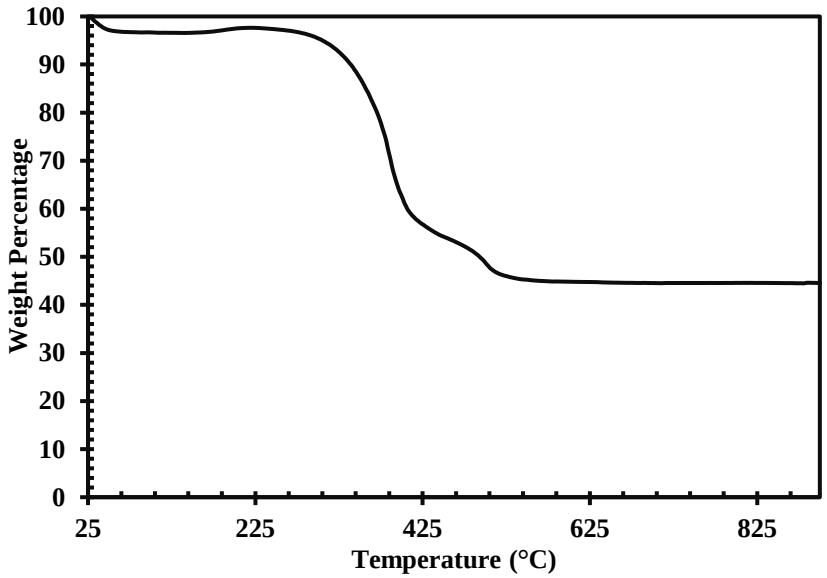

Figure 7.42: TGA result of spent CuZn/CMK-3 catalyst

Water vaporization was observed between 25-81°C. Second major weight loss starts at 303°C where amorphous carbon starts to combust. There is a diagonal peak

starting from 444°C and continues until the curve becomes linear. It is due to poor control against carbon combustion during analysis. Finally, 44.5 wt. % residue was observed after the analysis. The residue may contain oxidized active metals, residual silica and NaOH.

7.1.7. FTIR

DRIFTS measurements were performed in order to learn the characteristic information from the catalysts whether there are Lewis or Brønsted acid sites. Lewis acid site can be observed by bands at 1447 $cm^{-1}$and 1598 cm^{-1}, whereas Brønsted acid sites can observed at 1540 and 1640 cm^{-1} bands in DRIFTS. There is also observed band at 1489 cm^{-1} indicating the contribution of both Lewis and Brønsted acid sites (Corma, 1995).

DRIFTS of pyridine adsorbed fresh catalysts CuZn/SBA-15, Cu/SBA-15, and CuZn/CMK-3 and DRIFTS of these three fresh catalysts without pyridine adsorption were measured. The difference of spectra of samples with and without adsorption of pyridine are plotted and shown in Figure 7.43.

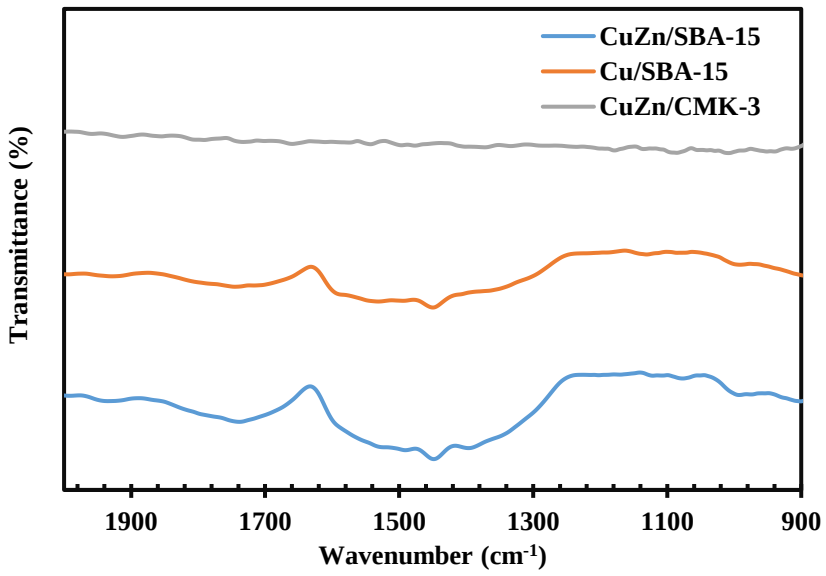

Figure 7.43: DRIFTS spectra of fresh catalysts CuZn/SBA-15, Cu/SBA-15, and CuZn/CMK-3

There are peaks at band 1448 cm^{-1} at CuZn/SBA-15 and Cu/SBA-15 fresh catalysts. This peak indicates presence of the aforementioned Lewis acid sites in the catalysts. Furthermore, transmittance signal coming from CuZn/SBA-15 was 1.55 times that of Cu/SBA-15 catalyst's transmittance. Therefore, Zn impregnation increased the acidity of the catalyst. In addition, in both catalysts, Brønsted acidity was observed, since the peak seen in Figure 7.18 is broad. The peak includes 1540 cm^{-1} band that is for Brønsted acid sites. There is a little peak at 1490 cm^{-1} band that accounting for contribution of both Lewis and Brønsted acid sites. On the other hand, CuZn/CMK-3 did not give any peaks at both Lewis and Brønsted acid sites. Consequently, CuZn/CMK-3 catalyst is not acidic as other two catalysts.

7.2. REACTION ACTIVITY RESULTS

FSR is tested with different catalysts at different temperatures. HIFUEL R120 catalyst was tested at 175, 200, 225, and 250°C. These temperatures were selected after evaluation of the Gaseq results. CuZn/SBA-15, Cu/SBA-15, and CuZn/CMK-3 catalysts were tested at 250°C. Reaction products were analyzed in both gas (on-line) and liquid samples in GC. GC calibration factors are given in Appendix C, Table C.1. Methanol and formaldehyde conversion values, selectivity of products and hydrogen yield were calculated. Their calculation methods are presented in Appendix A. Composition of reactor effluent stream at desired temperature for different catalysts are given in Appendix E.

7.2.1. Commercial Methanol Reforming Catalyst (HIFUEL R-120) Activity Results

Firstly, copper based methanol reforming catalyst (HIFUEL R-120) was tested. Four temperatures are selected for the activity tests for this catalyst that are 175, 200, 225, and 250°C.

Figures 7.44-48 show activity results at 175°C. The experiment lasted for 165 minutes. Figure 7.44 shows the component distribution during the operation. In the reactor effluent stream, H_2, CO_2, CH_3OH and H_2O were observed. CH_3OH amount stood stable in 165 minutes, whereas H_2 and CO_2 decreased after 105 minutes. This decrease may be attributed to deactivation of the catalyst over time. Furthermore,

CO was not encountered during the experiment. These operating conditions and the catalyst are concluded to be suitable for a sustainable onboard PEMFC operation.

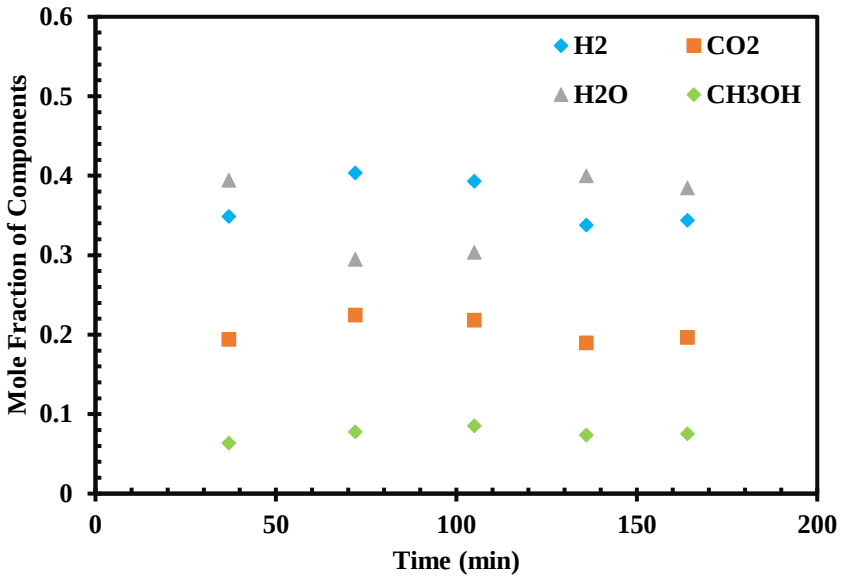

Figure 7.44: Mole fraction of each component in the presence HIFUEL R-120 catalyst at 175°C

Figure 7.45 shows the selectivity of products. Only H_2 and CO_2 were given in the figure, since there was not any CO formation. Figure 7.46 shows the hydrogen yield. It slowly decreased over time, but on the whole the activity decrease was not so effective. Actual hydrogen yield resulted in 54.2 % of the maximum theoretical hydrogen yield.

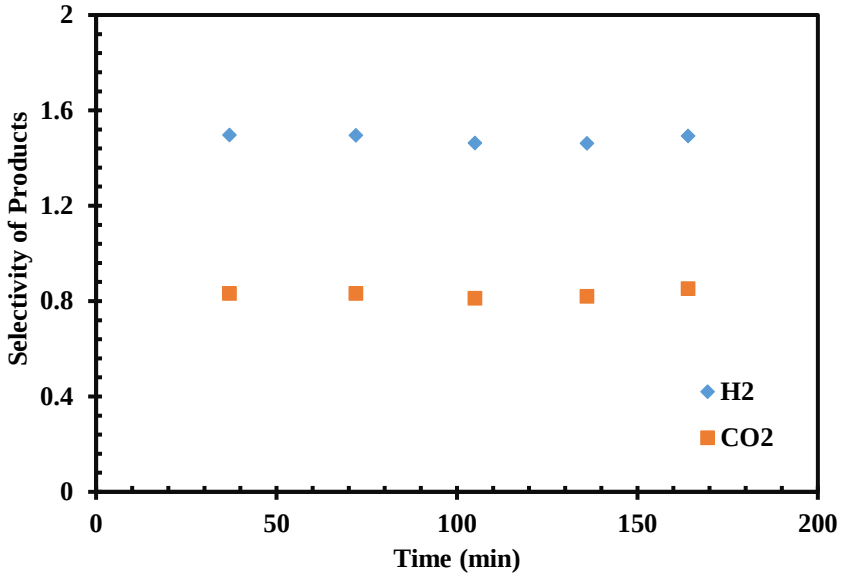

Figure 7.45: Selectivity of products in the presence of HIFUEL R-120 catalyst at 175°C

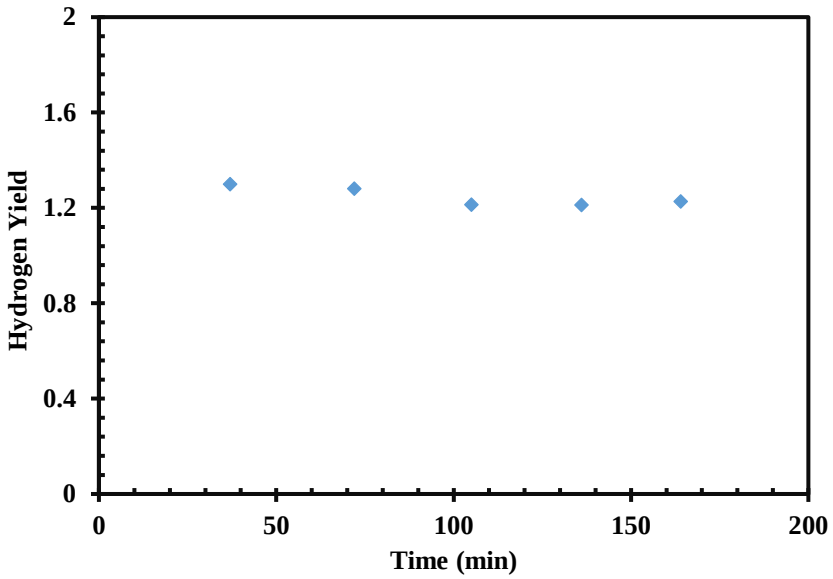

Figure 7.46: Hydrogen yield in the presence of HIFUEL R-120 catalyst at 175°C

No formaldehyde was found in the liquid sample and the gas analyses, so formaldehyde conversion was 100 %. Figure 7.47 shows the overall conversion. Unlike methanol conversion profile shown in Figure 7.48, overall conversion was not affected much. This is due to methanol consisting only 12 wt. % of the feed and formaldehyde, major carbon source of the feed, being converted 100 %.

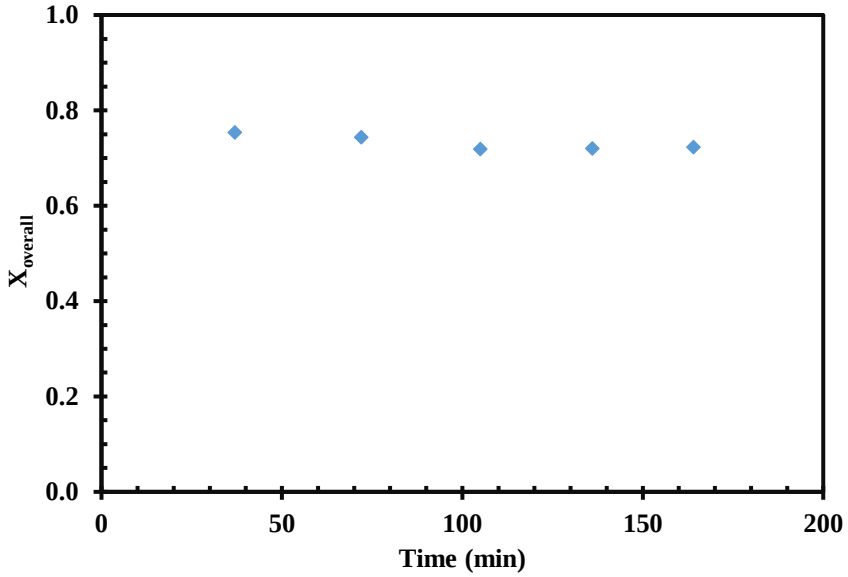

Figure 7.47: Overall conversion in the presence of HIFUEL R-120 catalyst at 175°C

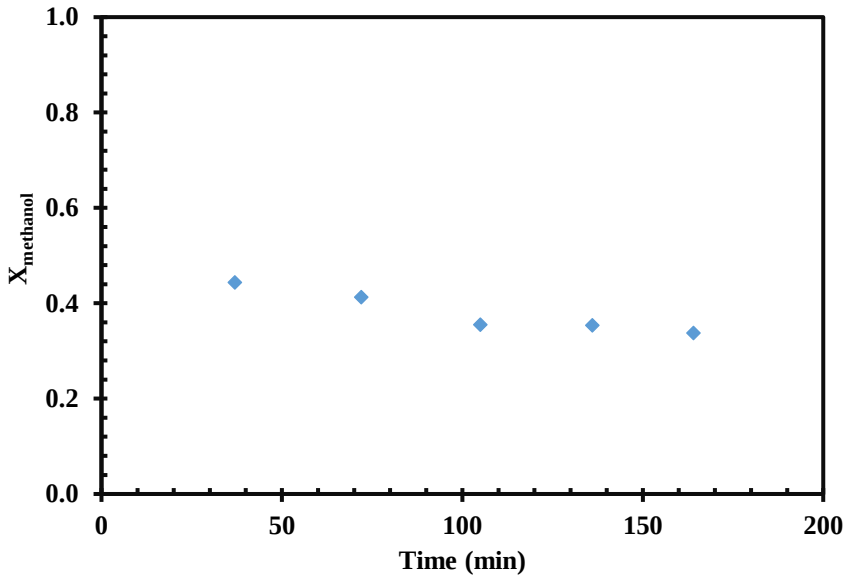

Figure 7.48: Methanol conversion in the presence of HIFUEL R-120 catalyst at 175°C

Figures 7.49-53 show the results of experiment at 200°C. The experiment lasted for 149 minutes and no formaldehyde was found in both liquid and gas sample analyses. Figure 7.49 shows the mole fraction of the components. Methanol increases with time and H_2 and CO_2 amounts firstly increase and decrease

proportionally. This H_2 and CO_2 decrease can be observed after 60 minutes possibly due to catalyst deactivation. No CO was observed during the experiment meaning that the syngas supplied at this temperature using HIFUEL R-120 is suitable for a sustainable onboard PEMFC application.

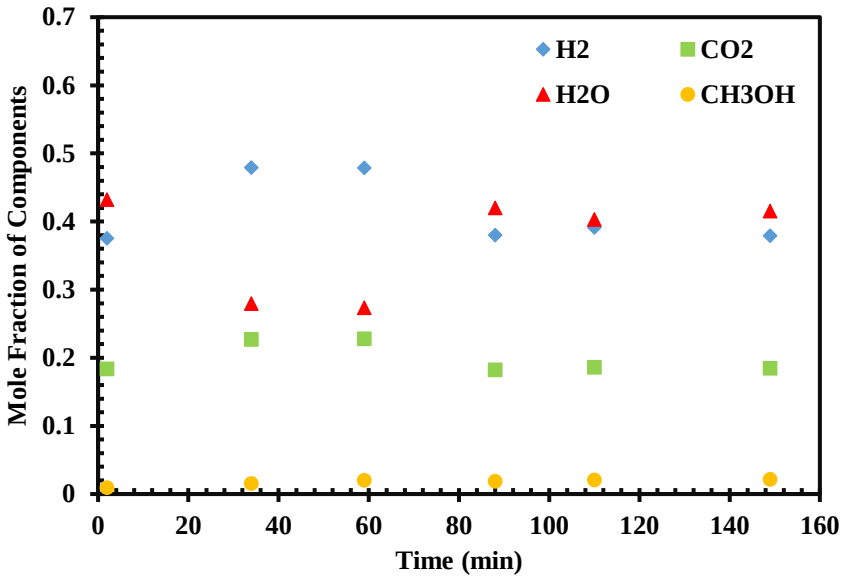

Figure 7.49: Mole fraction of each component in the presence HIFUEL R-120 catalyst at 200°C

Figure 7.50 shows the selectivity profiles of the product stream with respect to reaction time.

Figure 7.51 shows the hydrogen yield over time. After 60 minutes, there is negative deviation in the hydrogen yield which again could be due to catalyst deactivation. Actual hydrogen yield was around 95.0 % of the maximum theoretical hydrogen yield.

Figures 7.52-53 show overall and methanol conversions over time, respectively. There was constant decrease in methanol conversion, while this decrease did not affect the overall conversion that much, since the methanol in the feed was low.

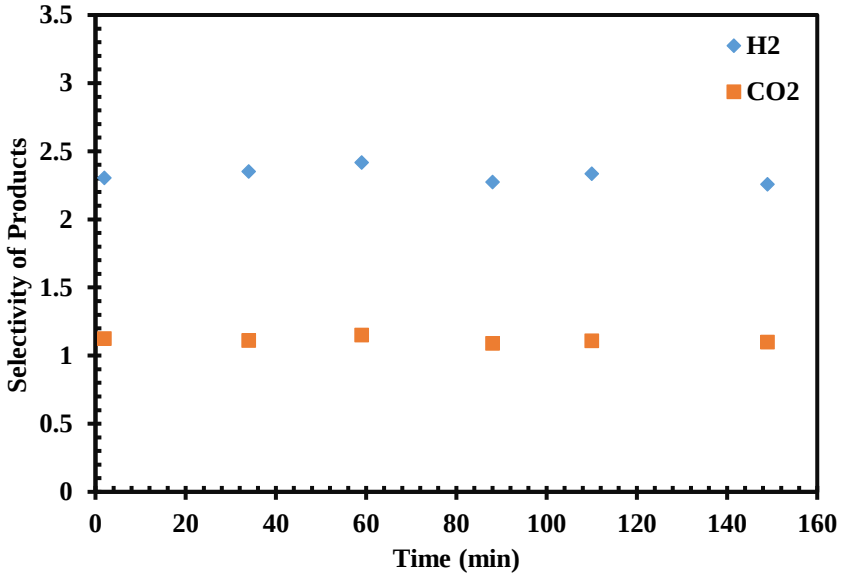

Figure 7.50: Selectivity of products in the presence of HIFUEL R-120 catalyst at 200°C

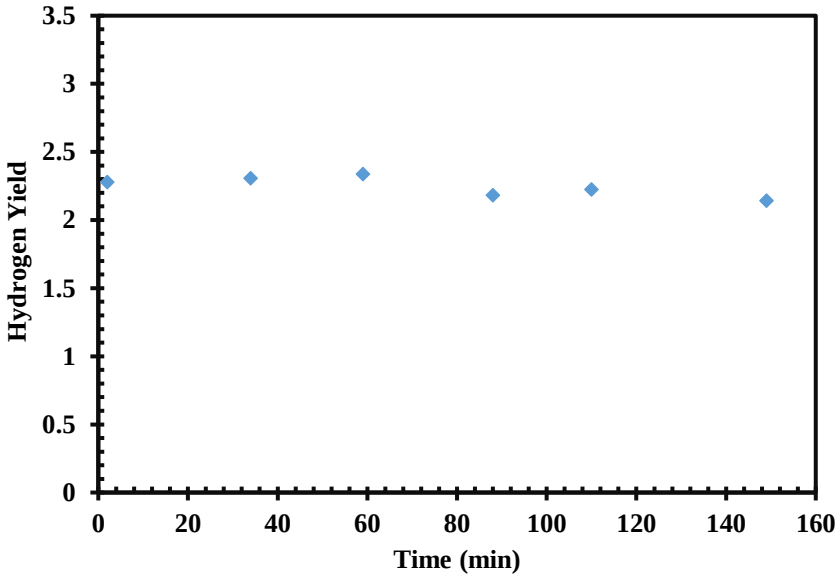

Figure 7.51: Hydrogen yield in the presence of HIFUEL R-120 catalyst at 200°C

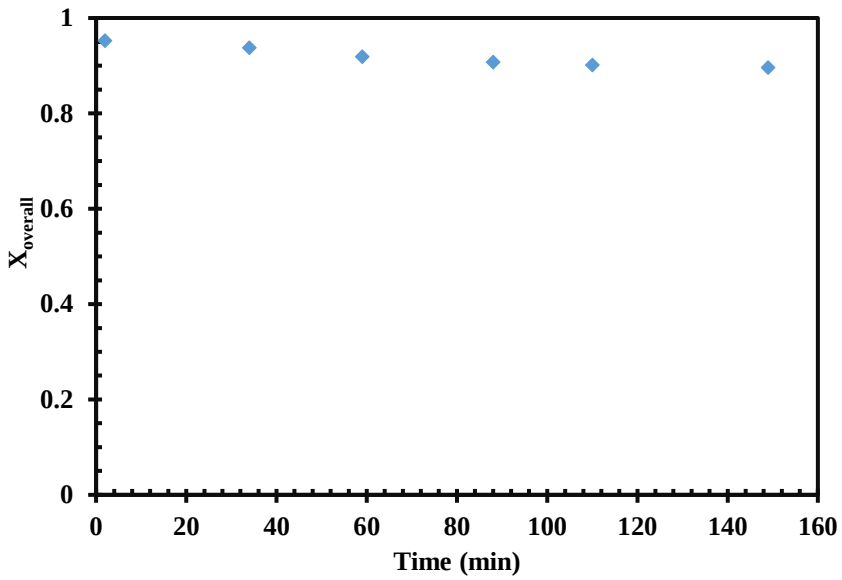

Figure 7.52: Overall conversion in the presence of HIFUEL R-120 catalyst at 200°C

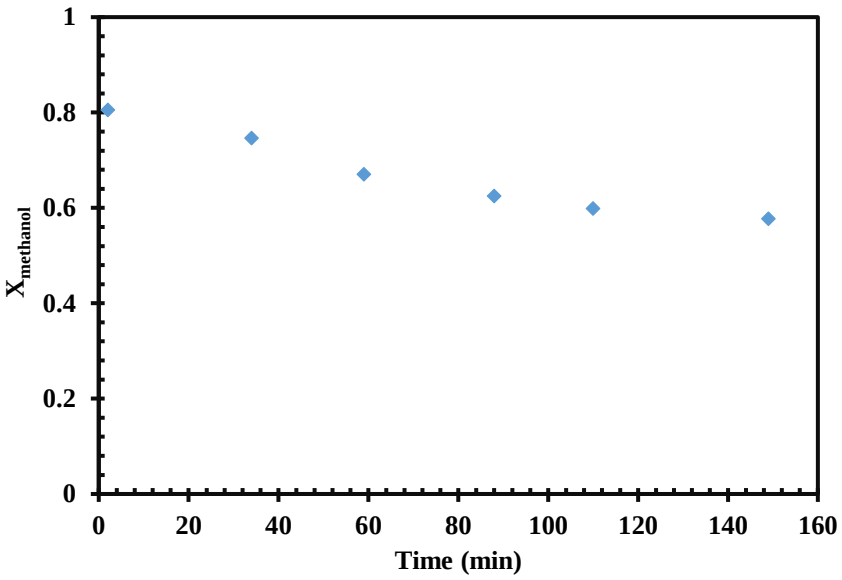

Figure 7.53: Methanol conversion in the presence of HIFUEL R-120 catalyst at 200°C

Figures 7.54-58 show the activity results at 225°C. The experiment lasted for 104 minutes. No formaldehyde was found in the liquid sample and the gas analyses, so formaldehyde conversion was 100 %. Figure 7.54 shows the mole fraction of components over time.

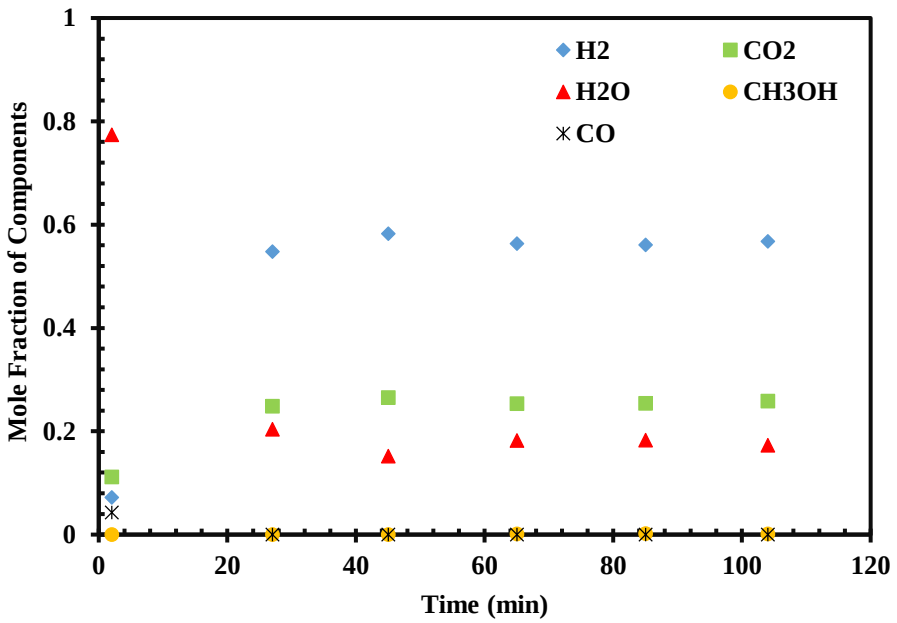

Figure 7.54: Mole fraction of each component in the presence HIFUEL R-120 catalyst at 225°C

Methanol starts to appear after 65 minutes possibly due to catalyst deactivation. However, its amount do not reach to 0.2 mole %. CO appeared with a mole fraction of 0.04 at 2nd minute of the experiment and disappeared afterwards. This is important because this catalyst can be used at 225°C onboard PEMFC vehicles. However, a startup treatment that prevents CO from the system and PEMFC catalyst from poisoning is required. As explained in Chapter 2, PEMFC platinum catalyst is negatively affected by CO in the feed at concentrations higher than 10 ppm. CO concentration was tolerable up to 1 % in the feed gas for these systems. The discussion for possible reasons of CO formation at the startup is given in the HIFUEL R-120 at 250°C experiment results.

Figure 7.55 shows the the selectivity of products at 225°C over time. Apparently, after 25 minutes system nearly reaches steady-state and changes are so small. Figure 7.56 shows hydrogen yield over time. Actual hydrogen yield was around 97 % of the maximum theoretical hydrogen yield.

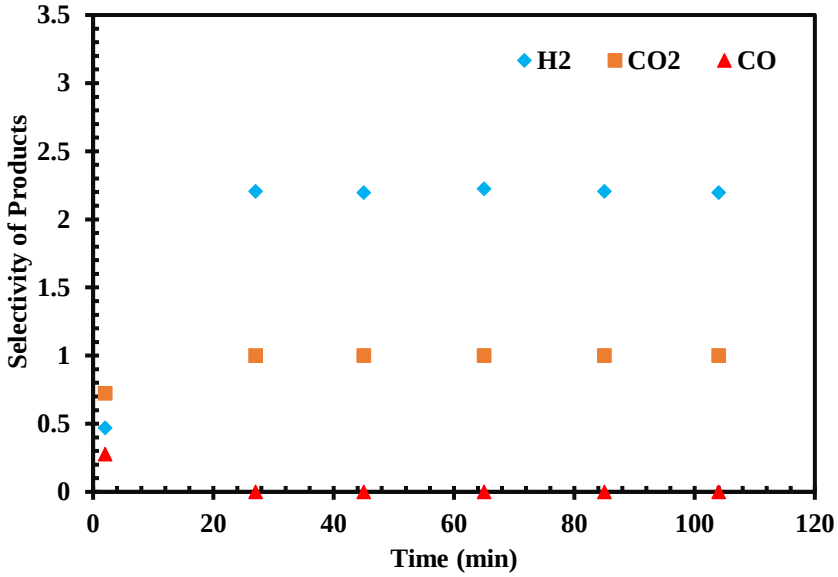

Figure 7.55: Selectivity of products in the presence of HIFUEL R-120 catalyst at 225°C

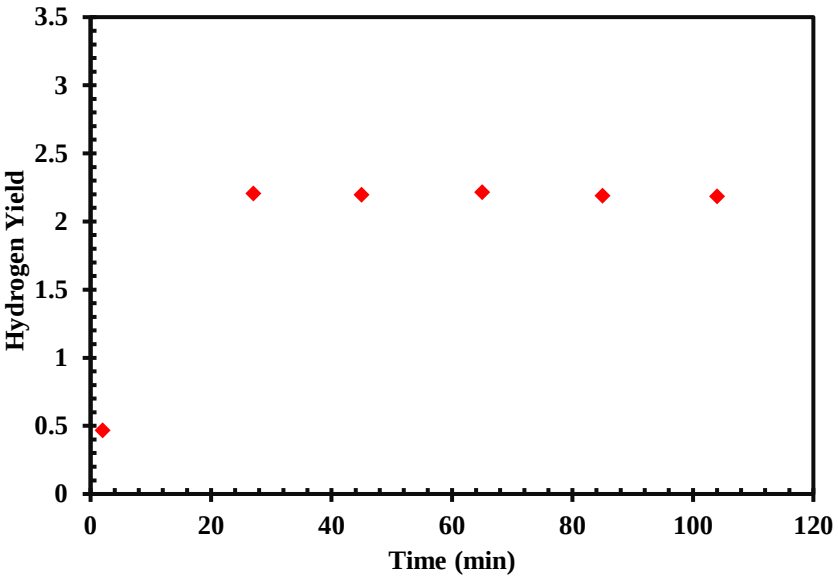

Figure 7.56: Hydrogen yield in the presence of HIFUEL R-120 catalyst at 225°C

Figures 7.57-58 show overall and methanol conversion with respect to reaction time. Methanol conversion starts with 100 % and start to shift down little after 65 minutes.

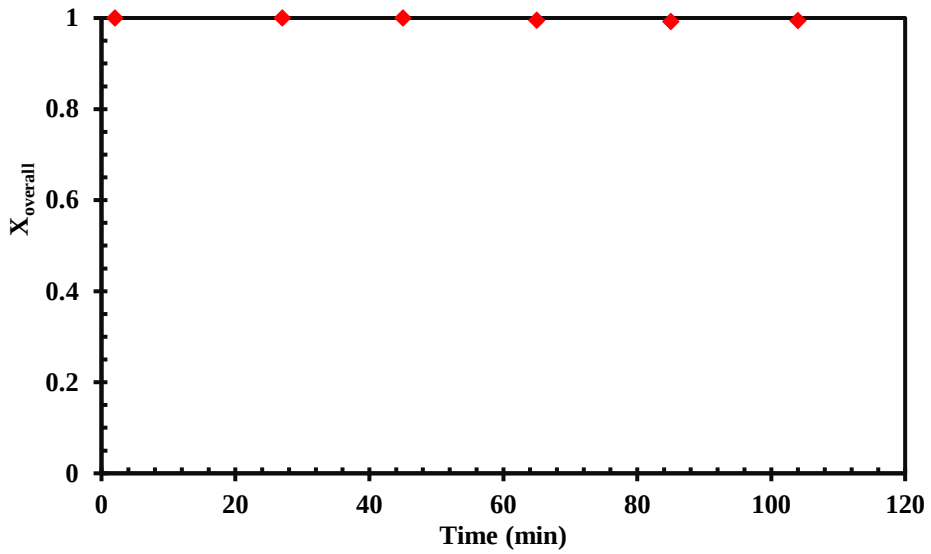

Figure 7.57: Overall conversion in the presence of HIFUEL R-120 catalyst at 225°C

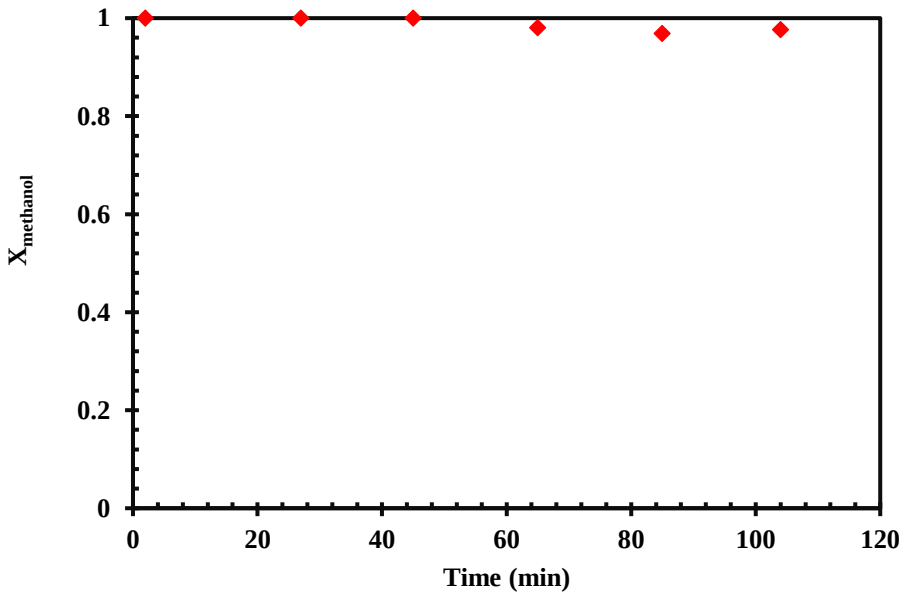

Figure 7.58: Methanol conversion in the presence of HIFUEL R-120 catalyst at 225°C

Figures 7.59-63 show activity results at 250°C. The experiment lasted for 182 minutes. Mole fraction of components with respect to time is given in Figure 7.59. At the 25th minutes 0.045 mole fraction of CO was observed and disappeared afterwards. However, at this concentration PEMFC catalyst is prone to poisoning. Furthermore, CO concentration at 250°C is higher than that of 225°C. One reason

for this phenomenon can be explained by HIFUEL R-120 XRD results in Figure 7.3. Before the experiment, the catalyst contained copper oxide crystals. However, after the experiment these were converted to metallic copper. This is a sign of activation of the catalyst in the beginning of experiment. Note that synthesized catalysts were reduced by pure hydrogen for 2.5 hours before the experiment and HIFUEL R-120 was not reduced at all. Therefore, this CO formation can be the result of copper oxide reduction with the feed formalin solution.

There were no major changes in methanol and formaldehyde amounts due to their very high conversion. Fluctuations in H_2, H_2O and CO_2 mole fractions can be seen after 125 minutes. It is due to water content increase into analysis may be due to insufficient condensation of products during that period of the experiment.

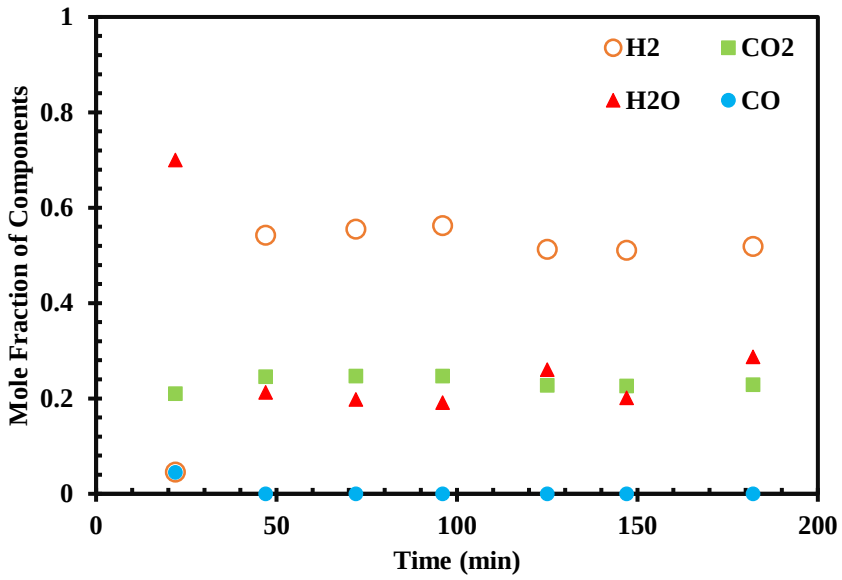

Figure 7.59: Mole fraction of each component in the presence HIFUEL R-120 catalyst at 250°C

Figure 7.60 shows the selectivity of products at 250°C with respect to time. Other than aforementioned CO appearance in the first 25 minutes, there is no major change in selectivity values of H_2 and CO_2. Figure 7.61 shows the hydrogen yield of the catalyst over time at 250°C. Hydrogen yield started with a low amount (8 % of the maximum possible yield) and reached steady state at 47th minute of operation and to its 100 % of theoretical maximum value that is 2.25.

Figures 7.62-63 show overall conversion and methanol conversion over reaction time, respectively. No formaldehyde was found in the liquid sample and the gas analyses, so formaldehyde conversion was 100 % in all 182 minutes. Furthermore, methanol conversion was also 100 % until 182nd minute, an indication of catalyst deactivation.

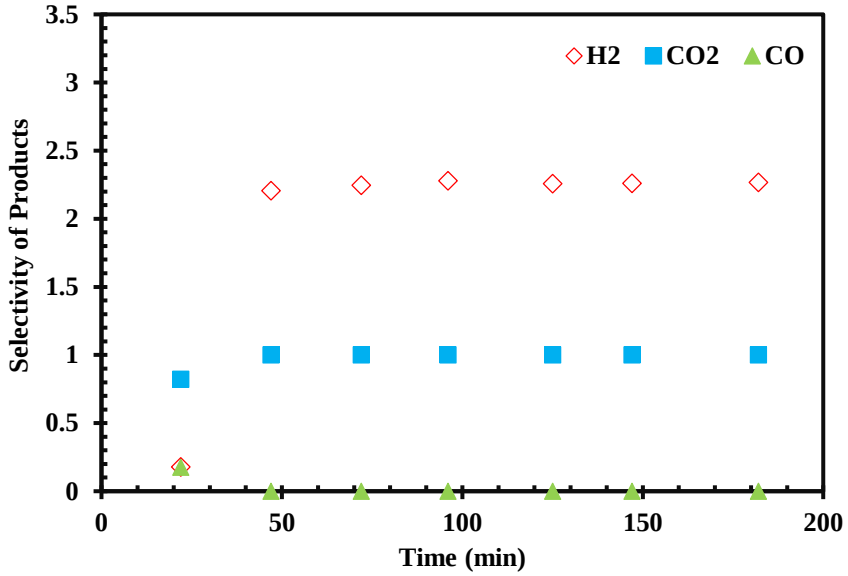

Figure 7.60: Selectivity of products in the presence of HIFUEL R-120 catalyst at 250°C

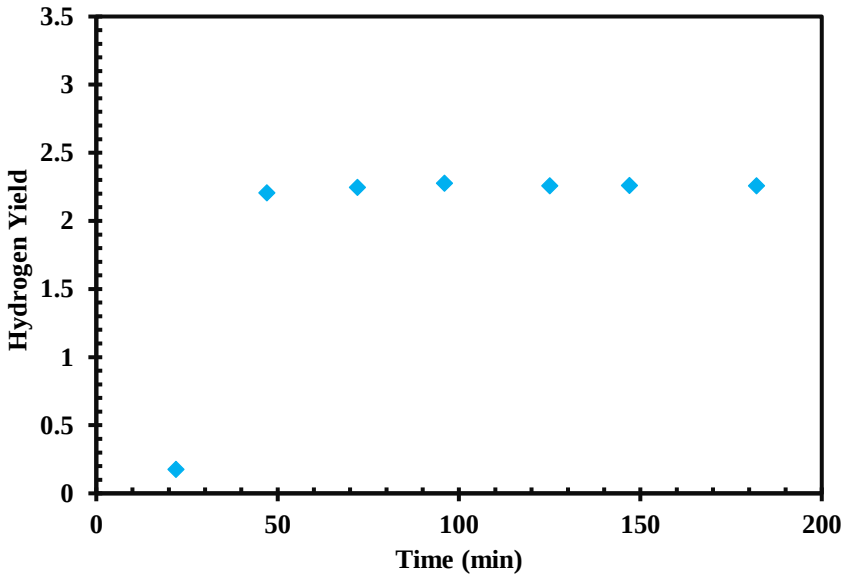

Figure 7.61: Hydrogen yield in the presence of HIFUEL R-120 catalyst at 250°C

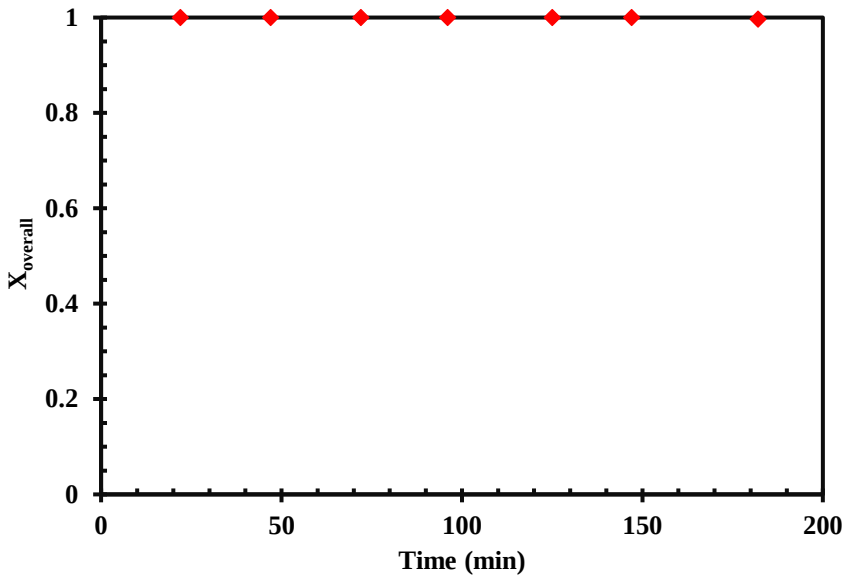

Figure 7.62: Overall conversion in the presence of HIFUEL R-120 catalyst at 250°C

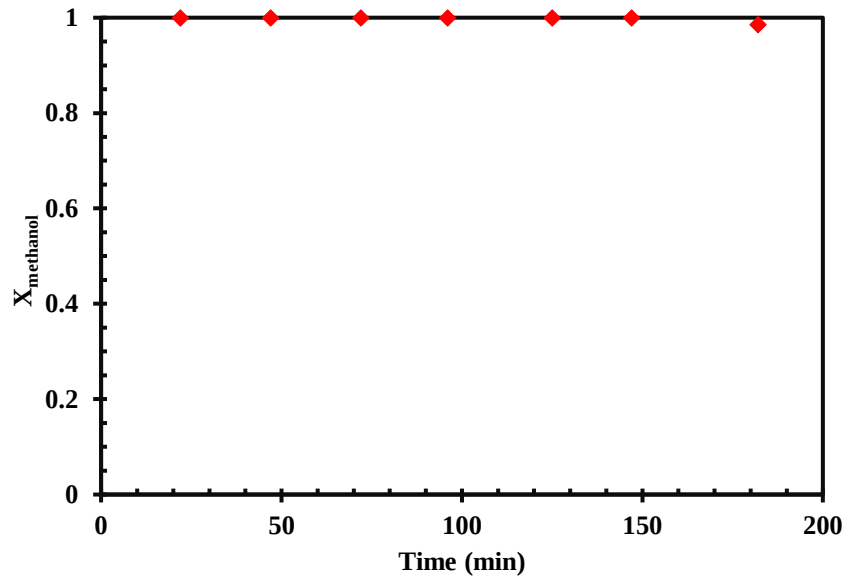

Figure 7.63: Methanol conversion in the presence of HIFUEL R-120 catalyst at 250°C

Finally, in Figures 7.64-67 HIFUEL R-120 catalyst's results are compared with respect to temperature. All gathered data corresponds to analyzed value at the end

of each experiment. They are 165 minutes for 175°C, 149 minutes for 200°C, 104 minutes for 225°C and 182 minutes for 250°C.

Figure 7.64 shows the selectivity of products with respect to temperature. It is clear that with increasing temperature upto 194°C (hypothetically) selectivity of values H_2 and CO_2 increased and reached their maximum. In terms of selectivity, this temperature is sufficient for PEMFC operation with advantage of no CO formation.

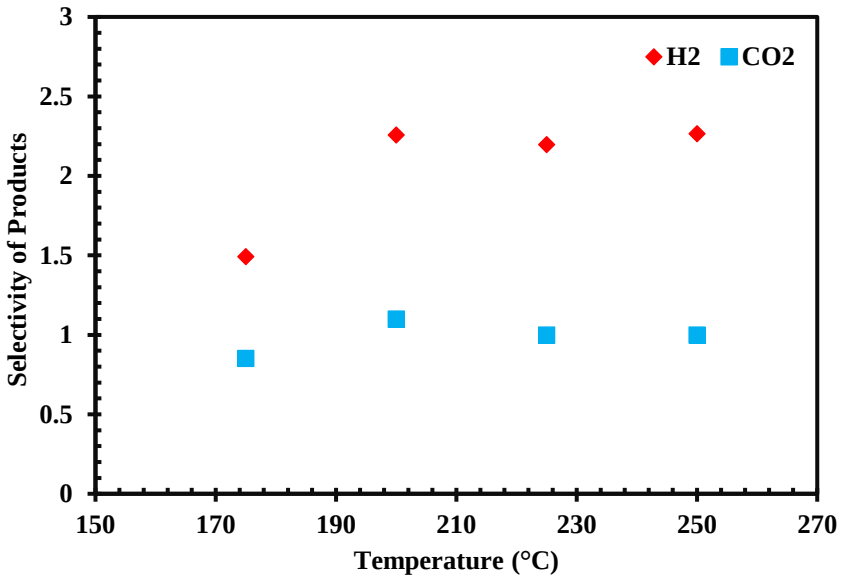

Figure 7.64: Selectivity of H_2 and CO_2 with respect to temperature in the presence of HIFUEL R-120 catalyst

Figure 7.65 shows the hydrogen yield of HIFUEL R-120 catalyst with respect to temperature. Hydrogen yield follows a similar trend to selectivities of hydrogen and carbon dioxide, but it reaches its maximum theoretical value, 2.25, not before 250°C. On the other hand, hydrogen yield of 2.18 was reached at 225°C.

Figures 7.66-67 show overall conversion and methanol conversion with respect to temperature. Observing the trend for overall conversion, it can be concluded that the overall conversion increases with temperature and reaches maximum, that is 100 %, about 225°C. Similarly, methanol conversion increases sharper than overall conversion with increasing temperature and reaches the maximum 100 % about the same temperature. As mentioned earlier, CO produced at 225°C was observed shorter reaction time than that of 250°C, and CO mole fraction was also lower at

225°C. Therefore, 225°C could be selected to be appropriate for sustainable onboard fuel cell applications.

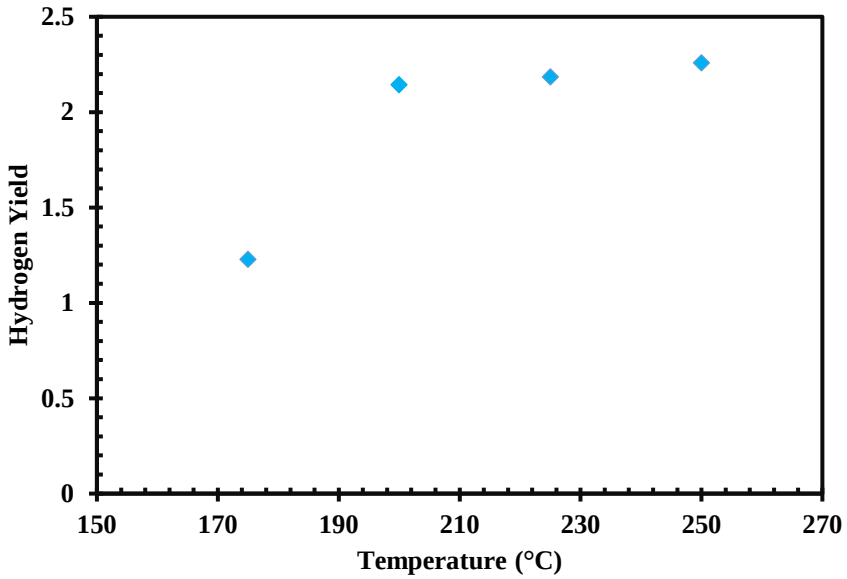

Figure 7.65: Hydrogen yield of HIFUEL R-120 catalyst with respect to temperature

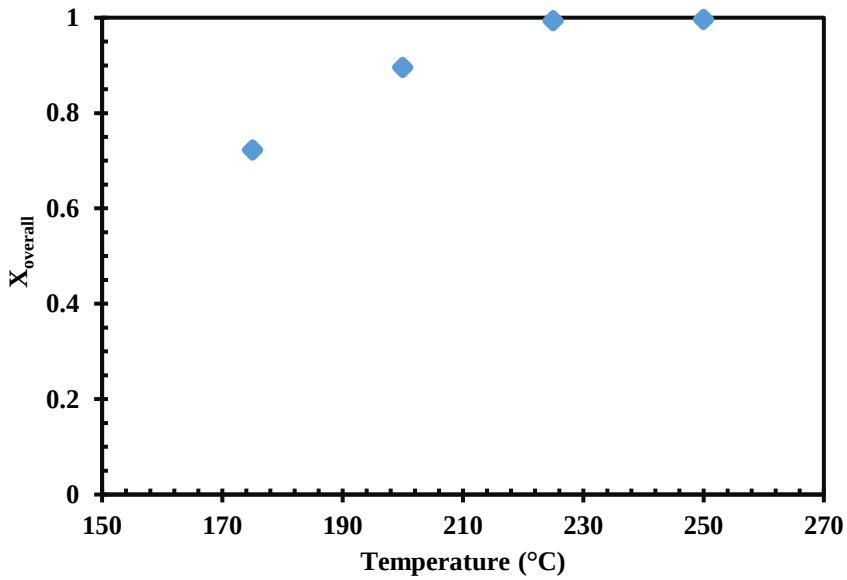

Figure 7.66: Overall conversion with respect to temperature in the presence of HIFUEL R-120 catalyst

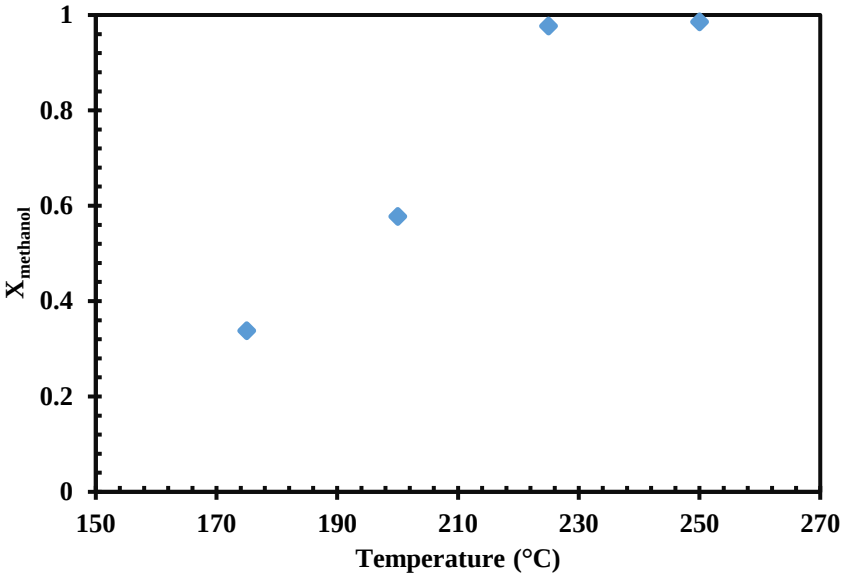

Figure 7.67: Methanol conversion with respect to temperature in the presence of HIFUEL R-120 catalyst

7.2.2. CuZn/SBA-15 Catalyst Activity Results

In this section, CuZn/SBA-15 catalyst activity results are presented. The experiment is carried out at 250°C. The run was continued 166 minutes. Figure 7.68 shows the mole fraction of components with respect to time.

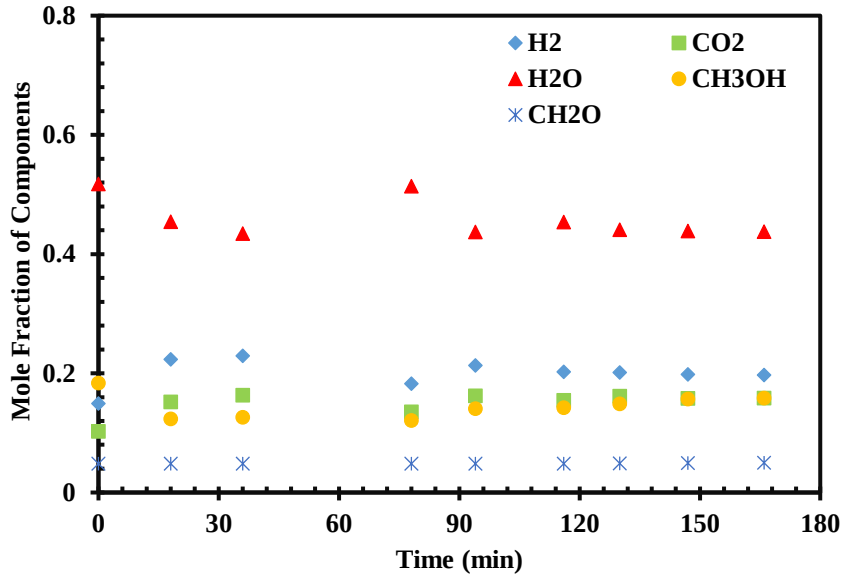

Figure 7.68: Mole fraction of each component in the presence CuZn/SBA-15 catalyst at 250°C

Accordingly, there was stable distribution over time except for 78th minute. In the 78th minute there was a problem with the argon flow that was later solved and stability settled. This stability in the results can be attributed to the Zn addition to the catalyst in the synthesis. Accordingly, Zn could be stabilizing copper during the experiment so that it does not sinter fast. This stability was observed also in HIFUEL R-120, which contains high amount of copper and zinc.

No CO was observed during the experiment. This is an indication that this catalyst at this temperature produces syngas that does not poison the PEMFC platinum catalyst.

Figure 7.69 shows the selectivity of hydrogen and carbon dioxide over time at 250°C. Other than aforementioned sharp change at 78th minutes, there was gradual decrease in H_2 selectivity value over time. This is probably due to copper sintering observed in SEM images in Figures 7.20-22. Furthermore, XRD results in Table 7.1 show that copper particle size increased from 40.3 nm to 46.4 nm.

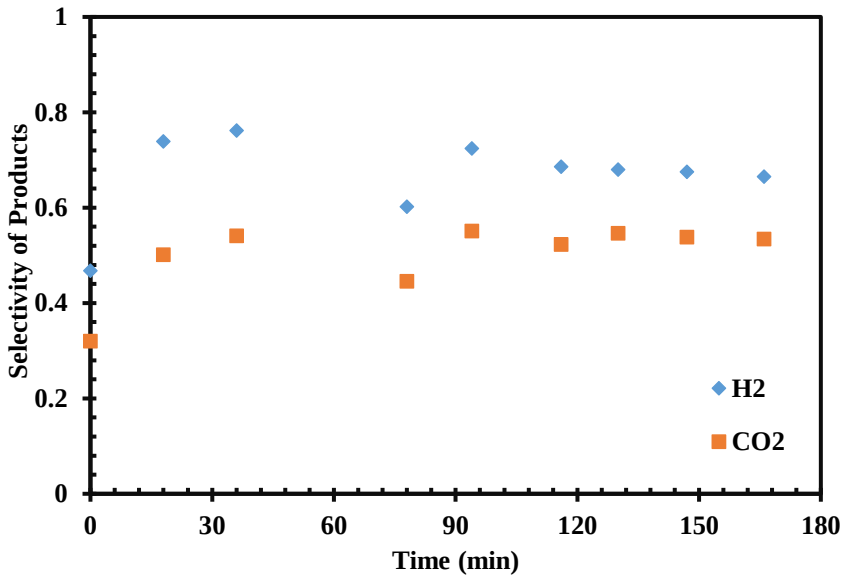

Figure 7.69: Selectivity of each product in the presence CuZn/SBA-15 catalyst at 250°C

Figure 7.70 shows the hydrogen yield of CuZn/SBA-15 catalyst at 250°C over time. Maximum hydrogen yield was attained at 36th minute, where it was 26.2 % of the maximum theoretical hydrogen yield. Similar to selectivity of both products,

hydrogen yield gradually decreases with time. The disruption at 78th minute can also be seen in hydrogen yield.

Figures 7.71-72 show overall conversion and methanol conversion over time at 250°C. Formaldehyde conversion was calculated cumulatively, since it was found only in the liquid product stream. It was 81.8 %. Overall conversion decreased slower than methanol conversion over time indicating that catalyst degrades over time. This can be attributed to sintering shown by SEM image in Figures 7.20-22.

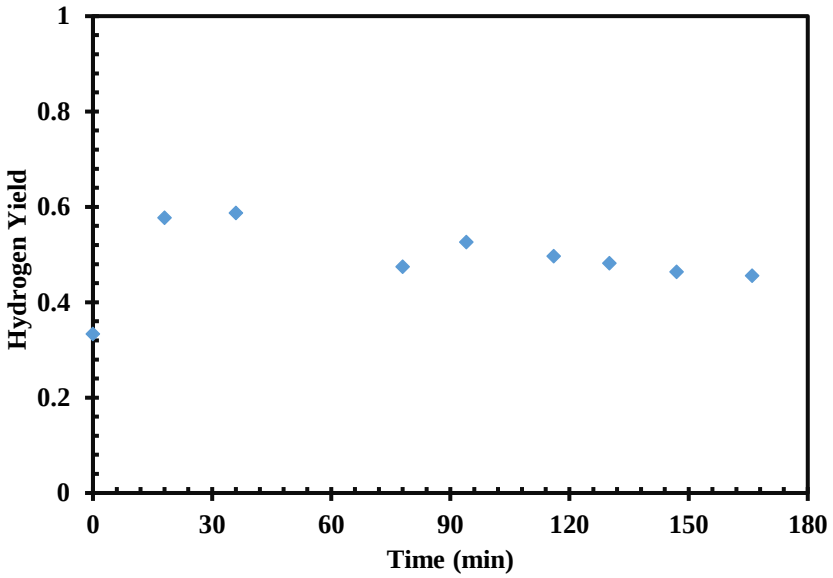

Figure 7.70: Hydrogen yield of CuZn/SBA-15 catalyst at 250°C

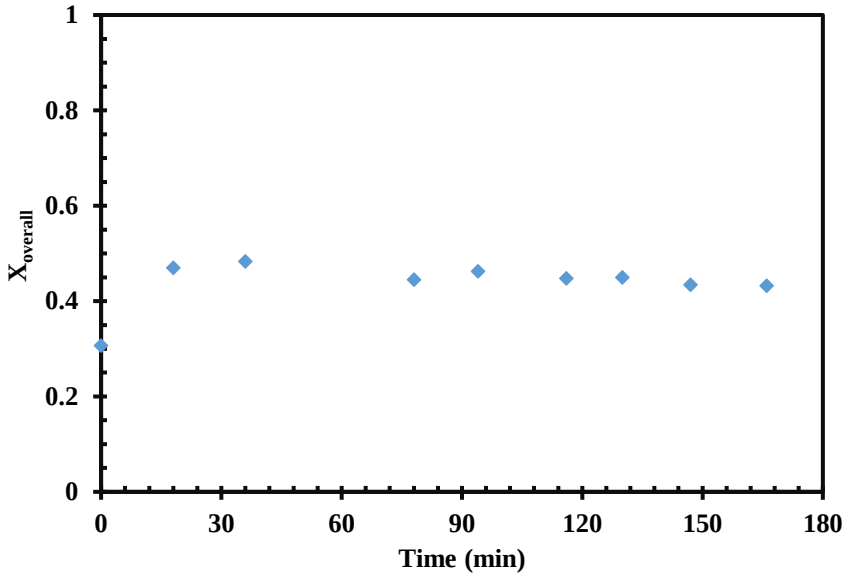

Figure 7.71: Overall conversion in the presence of CuZn/SBA-15 at 250°C

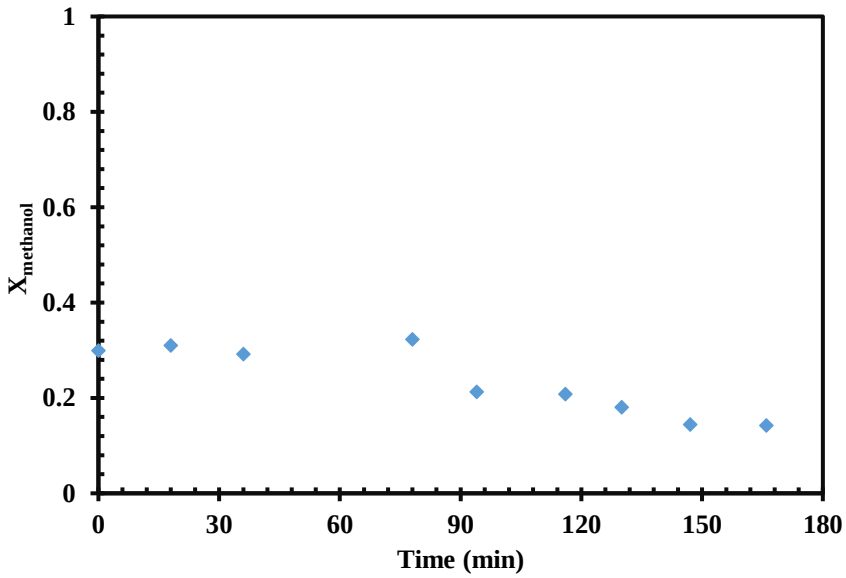

Figure 7.72: Methanol conversion in the presence of CuZn/SBA-15 at 250°C

7.2.3. Cu/SBA-15 Catalyst Activity Results

In this section, activity results of Cu/SBA-15 catalyst at 250°C is presented. The run continued for 152 minutes. Figure 7.73 shows the mole fraction of each component in the reactor effluent stream.

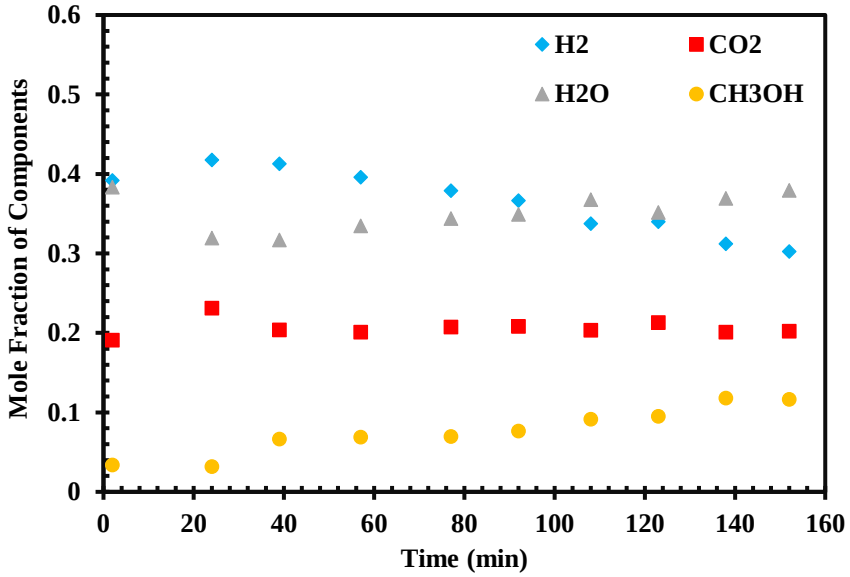

Figure 7.73: Mole fraction of each component in the presence Cu/SBA-15 catalyst at 250°C

Mole fraction of hydrogen decreases fast, whereas carbon dioxide stays nearly the same. Methanol amount keeps rising nearly at the same speed of hydrogen drop. This fast drop of hydrogen and rise of methanol are the indications of catalyst deactivation. Indeed, the catalyst was deactivated as the results from XRD in Table 7.1 state that copper crystal size increased from 47.6 nm to 56.6 nm. Furthemore, SEM image in Figures 7.28-29 compared to fresh catalyst images in 7.24-27 prove the sintering.

Water content increases reversely proportional to hydrogen amount. This catalyst and operating conditions were suitable for onboard PEMFC applications, since there was no CO formed during the experiment. Figure 7.74 shows the selectivity of products over time. Similar to Figure 7.73, hydrogen selectivity keeps decreasing, whereas carbon dioxide selectivity stays nearly stable at around 0.77-0.87.

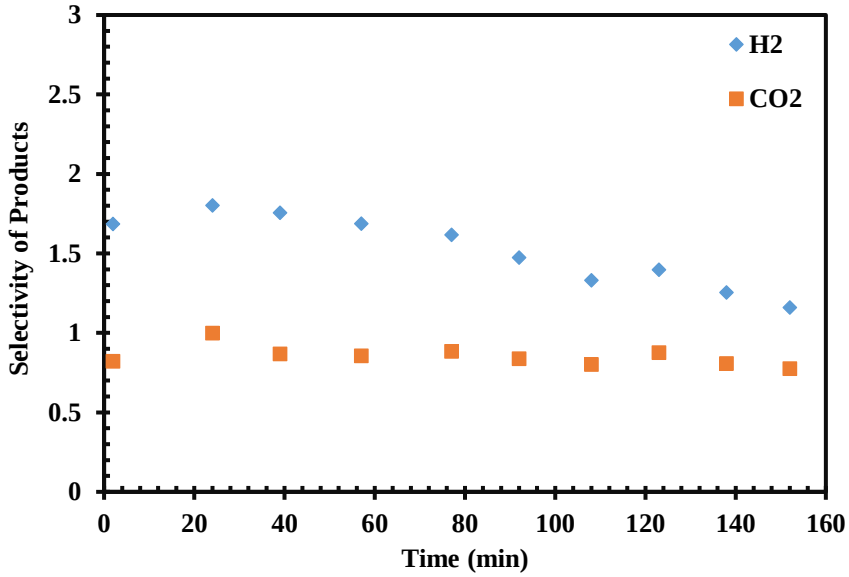

Figure 7.74: Selectivity of each product in the presence Cu/SBA-15 catalyst at 250°C

Figure 7.75 present the hydrogen yield with respect to time. Hydrogen yield reaches its maximum value at 24th minute with 1.73, which is 76.9 % of the maximum theoretical hydrogen yield. Fast decreasing trend observed in mole fraction and selectivity of hydrogen can also be seen from this graph.

Figures 7.76-77 show the overall conversion and methanol conversion over time. No formaldehyde was observed from the gas and the liquid analyses, so formaldehyde conversion was 100 % throughout. Overall conversion started high at about 84 % and peak about 88 % 24th minute after which activity decreased. Methanol conversion changed so dramatically that at the end of reaction (152nd minute) it was only 10.7 %. This could be attributed to aforementioned catalyst sintering. Finally, this catalyst contains solely copper as the metal loading. It has higher copper loading than that of CuZn/SBA-15, but its stable operation is not long-lived. This may be the result of Zn, increasing catalyst stability in the reaction, in addition to its copper dispersive duty during the catalyst synthesis.

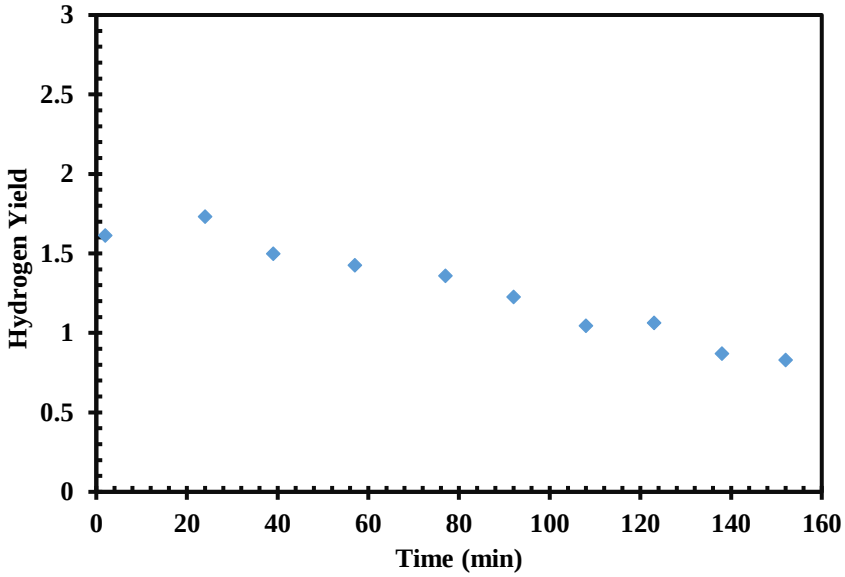

Figure 7.75: Hydrogen yield of Cu/SBA-15 catalyst at 250°C

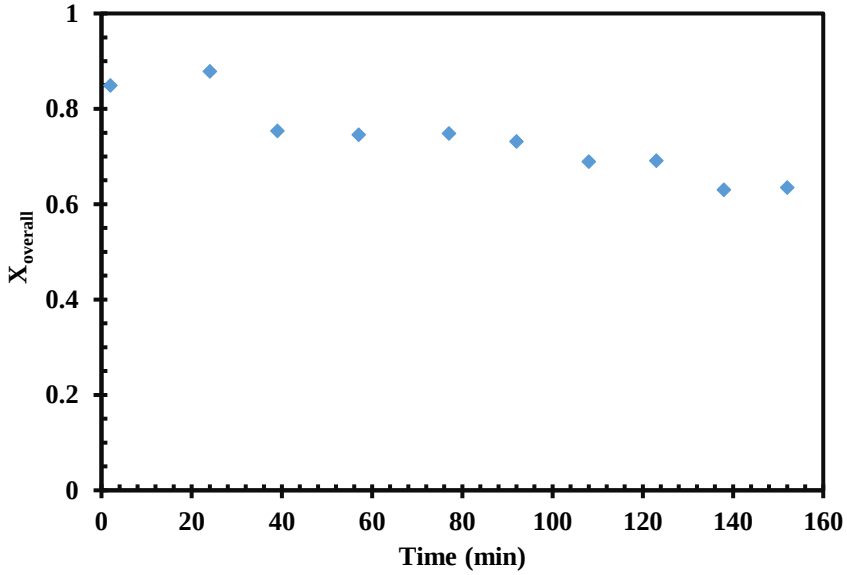

Figure 7.76: Overall conversion in the presence of Cu/SBA-15 at 250°C

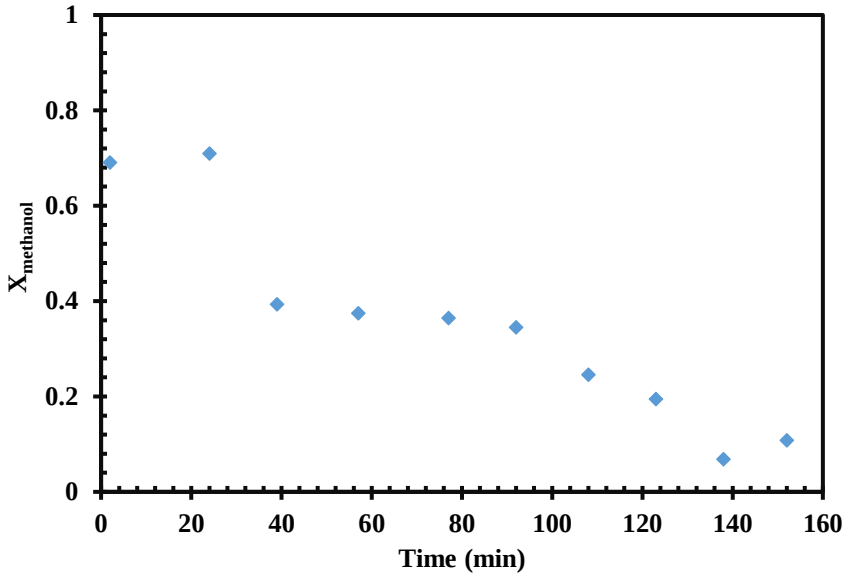

Figure 7.77: Methanol conversion in the presence of Cu/SBA-15 at 250°C

7.2.4. CuZn/CMK-3 Catalyst Activity Results

In this section, activity of CuZn/CMK-3 catalyst at 250°C is presented. The run continued for 169 minutes. Figure 7.78 shows the mole fraction of the components in the effluent stream over time.

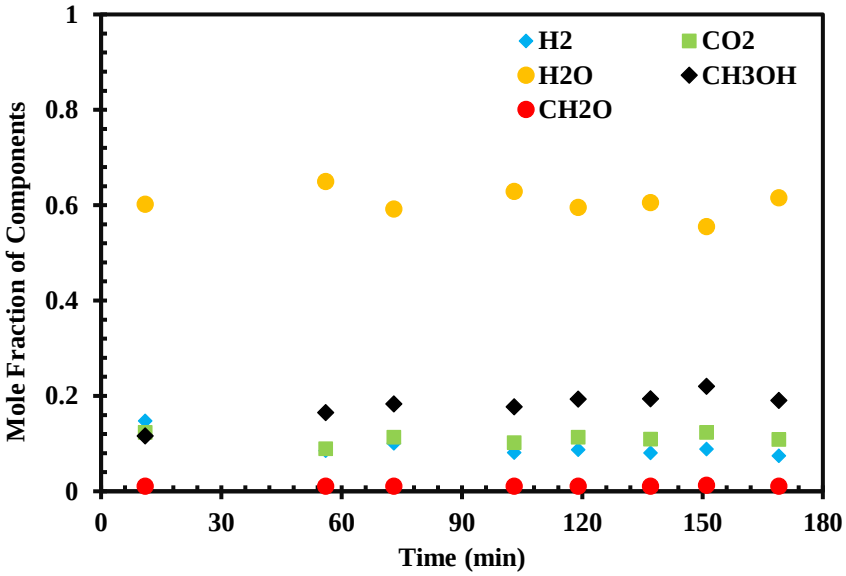

Figure 7.78: Mole fraction of each component in the presence CuZn/CMK-3 catalyst at 250°C

In Figure 7.78, H_2 and CO_2 mole fractions stood stable around 0.1, whereas CH_3OH increased slowly to 0.2 that higher from its original feed value. There was formaldehyde observed around 0.01. Consequently, water content was high. Most importantly, CO was not observed throughout the operation. Therefore, it can be used suitably in onboard PEMFC vehicles. The presence of Zn in the catalyst affected the activity in a way that mole fraction changes were small over time.

Figure 7.79 shows the selectivity of products over time for CuZn/CMK-3 catalyst. Hydrogen selectivity decreased slowly over time, as CO_2 selectivity stood nearly stable. However, they were both far from the desired maximum selectivity values.

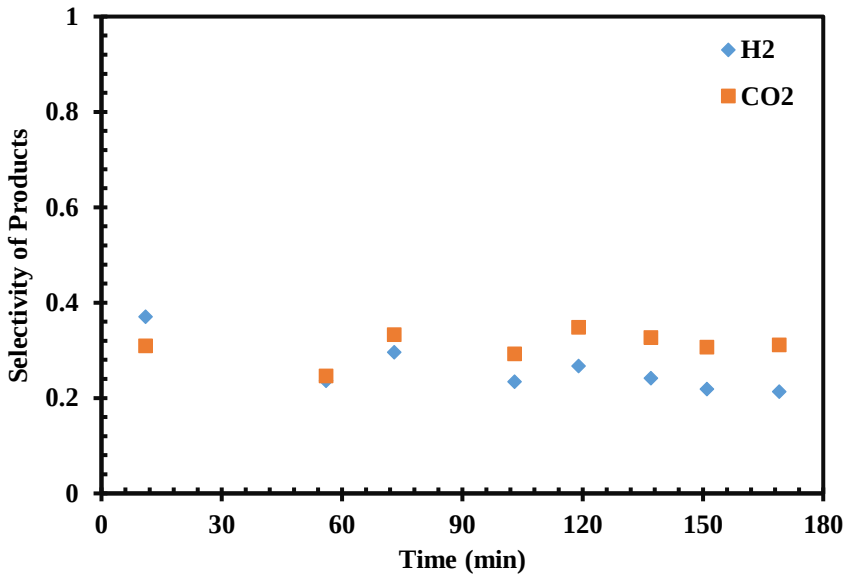

Figure 7.79: Selectivity of each product in the presence CuZn/CMK-3 catalyst at 250°C

Figure 7.80 presents the hydrogen yield of CuZn/CMK-3 catalyst over time at 250°C. Maximum hydrogen yield was attained at 11th minute, and it was 13.8 % of the maximum theoretical hydrogen yield. It shows the gradual decrease of hydrogen yield over time.

Figures 7.81-82 present the overall conversion and methanol conversion over time. Formaldehyde conversion from this run was calculated cumulatively from the liquid sample and was 97.1 %. While overall conversion dropped sharply and stood stable after 56th minute, methanol conversion suddenly went to negative values after this

minute. This phenomenon raises question whether there was hydrogenation of formaldehyde in the following reaction.

$$CH_2O + H_2 \longleftrightarrow CH_3OH$$

It was investigated if it is thermodynamically favored at this temperature. K_{eq} value resulted in 528.7 from Van't Hoff equation. This number proves that hydrogenation to methanol is thermodynamically favored. Calculation procedure for this reaction is given in Appendix F.

One reason for this can be the result of sintering of copper crystals shown in SEM images in Figures 7.35-36 and XRD crystal size increase in Table 7.1. Another reason could be the fact that the catalyst has no activity for MSR due to lack of acid sites as shown in DRIFTS spectra in Figure 7.43. The catalyst apparently has activity for FSR, since hydrogen was continued to be produced.

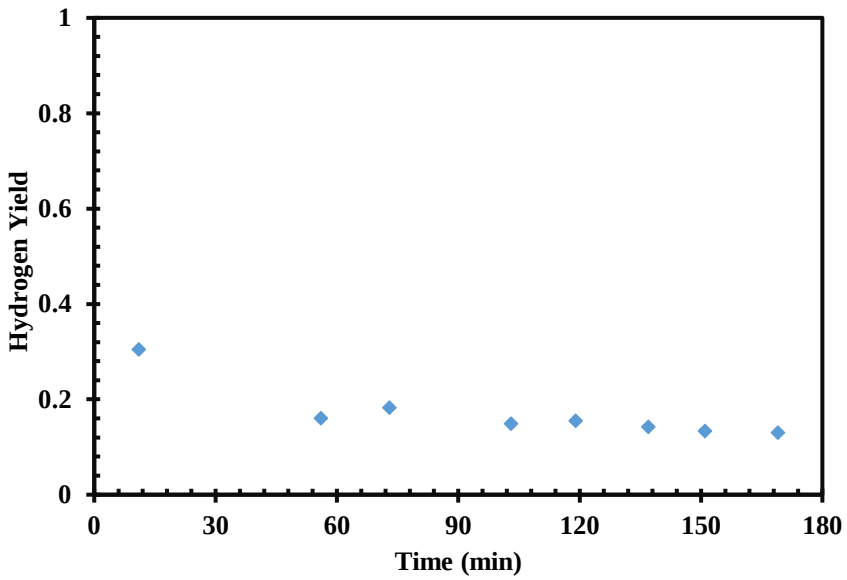

Figure 7.80: Hydrogen yield of CuZn/CMK-3 catalyst at 250°C

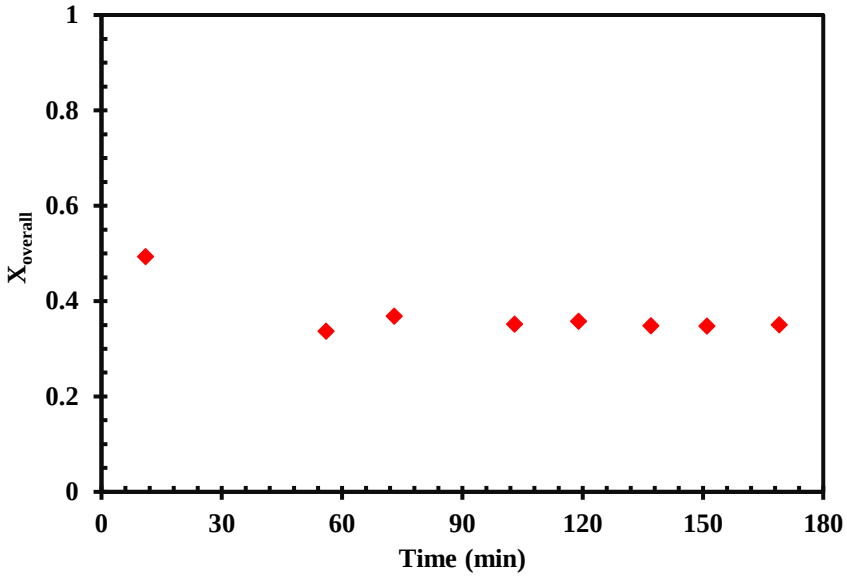

Figure 7.81: Overall conversion in the presence of CuZn/CMK-3 at 250°C

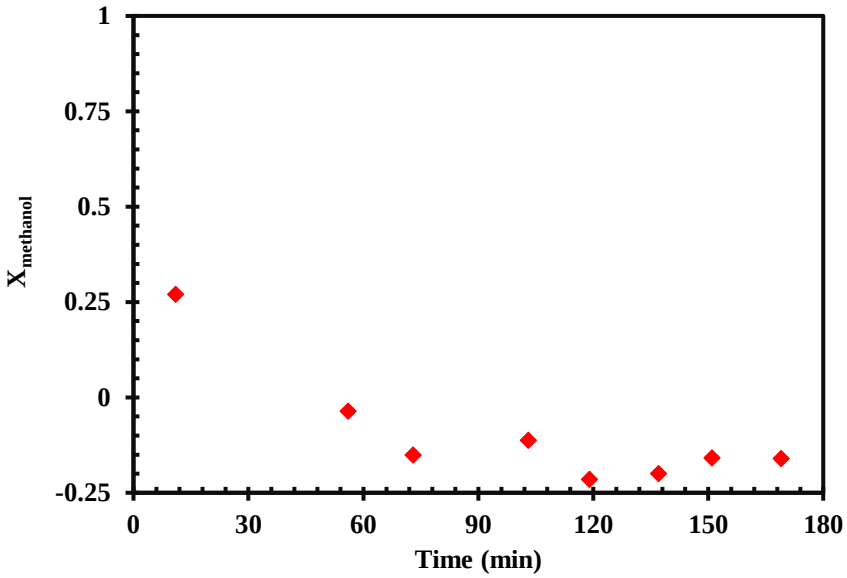

Figure 7.82: Methanol conversion in the presence of CuZn/CMK-3 at 250°C

7.2.5. Comparison of the Catalysts

All the catalyst used in the experiments are compared in this section. Table 7.5 shows the overall conversion, formaldehyde conversion and methanol conversion, of the analysis results of each catalyst run at 250°C at the end of reaction.

It is clear that HIFUEL R-120 has the most successful performance in terms of conversion. CuZn/SBA-15 has lower conversion of both formaldehyde and

methanol but has longer times of stability than Cu/SBA-15. As explained Cu/SBA-15 has higher activity than that of CuZn/SBA-15, but no stability during the operation. This gives importance to zinc that it acts not only in the copper dispersion during catalyst synthesis, but also in the stability of steam reforming reactions. Furthermore, HIFUEL R-120 contains higher loading of Cu and Zn than any other catalyst as shown by ICP results in Table 7.4. Similar to CuZn/SBA-15, its longer stability also comes from the high amounts of zinc.

CuZn/CMK-3 consumes most of the formaldehyde with 97.1 % conversion; however, negative methanol conversion shows that not all of formaldehyde was converted to the syngas, but some was hydrogenated to methanol. This was previously supported by the thermodynamic calculations of K_{eq}. In DRIFTS spectra in Figure 7.43, CuZn/CMK-3 catalyst did not show any acidity, whereas other two synthesized catalysts did show both Lewis and Brønsted acid sites. Apparently, acidity in catalysts was an important factor to convert formaldehyde and methanol to hydrogen.

Table 7.5: Comparison of all four catalysts in terms of conversion at 250°C

Catalyst	Overall Conversion (%)	Formaldehyde Conversion (%)	Methanol Conversion (%)
HIFUEL R120	99.6	100.0	98.6
CuZn/SBA-15	43.2	81.8	14.2
Cu/SBA-15	63.4	100	10.8
CuZn/CMK-3	35.0	97.1	-16.0

Table 7.6 shows the comparison between all four catalysts in terms of hydrogen yield, hydrogen and carbon dioxide selectivity of the last analysis of each experiment at 250°C. As shown in Table 7.6, HIFUEL R-120 was the most successful catalyst for hydrogen yield, selectivity and carbon dioxide selectivity with the maximum possible values. Furthermore, HIFUEL R-120 reached to maximum theoretical hydrogen yield, which is 2.25.

All catalysts were successful for producing no CO in the product stream. The values of CuZn/CMK-3 supports the formaldehyde hydrogenation because of being the least at all categories in table with so much formaldehyde conversion.

Table 7.6: Comparison of all four catalysts in terms of hydrogen yield and selectivity at 250°C

Catalyst	Hydrogen Yield	Hydrogen Selectivity	Carbon Dioxide Selectivity
HIFUEL R120	2.25	2.27	1
CuZn/SBA-15	0.46	0.65	0.53
Cu/SBA-15	0.83	1.16	0.78
CuZn/CMK-3	0.13	0.21	0.31

Figure 7.83 shows the mole fraction of hydrogen in the reactor effluent stream. HIFUEL R-120 produced the highest concentration, whereas CuZn/CMK-3 produced the least hydrogen concentration.

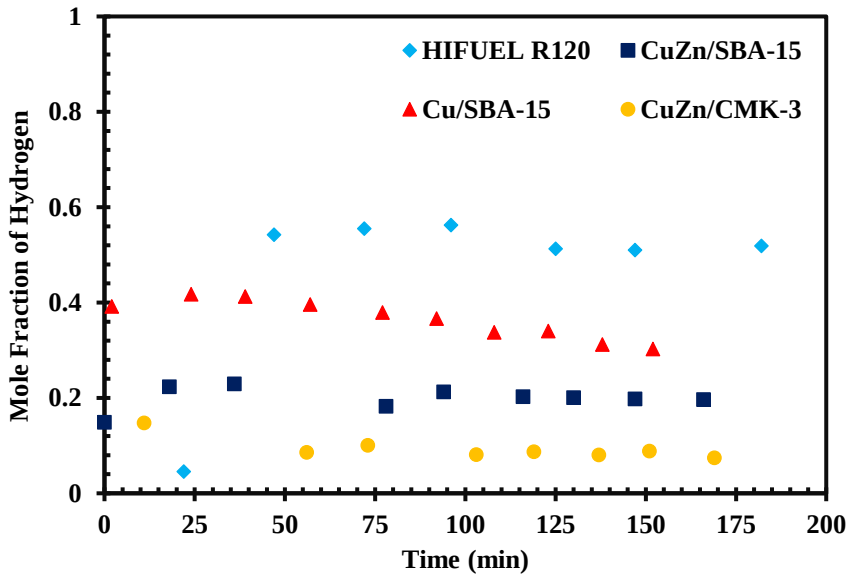

Figure 7.83: Hydrogen mole fraction over time for all catalysts at 250°C

Among all the experiments, only the ones in the presence of HIFUEL R-120 catalyst at 225 and 250°C produced CO in the beginning of the experiment. For 225°C, CO

was produced by mole fraction of 0.04 during first 2 minutes of operation. However, this time interval was higher in 250°C experiment that it took 22 minutes for CO to disappear with a mole fraction of 0.045. This phenomenon was explained in the previous section as the catalyst activation. Considering these, HIFUEL R-120 at 225°C can be the best candidate for onboard PEMFC applications, if CO formation problem during the catalyst activation could be solved. Figure 7.84 shows the CO_2 mole fraction at the reactor effluent. HIFUEL R-120 produces the maximum CO_2.

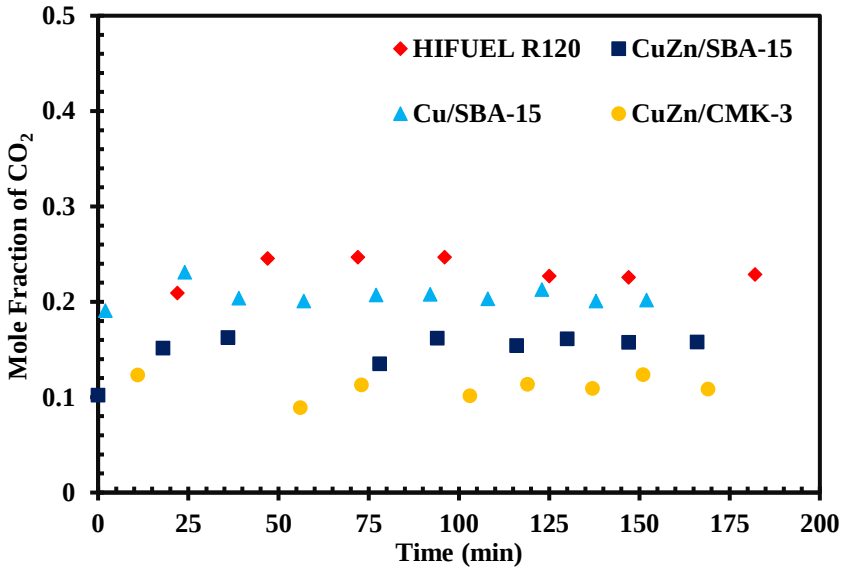

Figure 7.84: CO_2 mole fraction over time for all catalysts at 250°C

Figure 7.85 shows the hydrogen selectivity of all catalysts over time. It is evident that HIFUEL R-120 is the most successful catalyst catalyst in terms of hydrogen selectivity. Figure 7.86 shows the CO_2 selectivity of all catalysts over time, where HIFUEL R-120 was the most successful again. Besides, Cu/SBA-15 catalyst was the closest to HIFUEL R-120 in terms of CO_2 selectivity. Figure 7.87 shows the hydrogen yield of all catalysts with respect to reaction time.

CuZn/SBA-15 was found more acidic than other two synthesized catalysts in DRIFTS spectra. However, its hydrogen yield and selectivities were lower than Cu/SBA-15 (Figures 7.85-87). This was mainly due to copper loading being less than that of Cu/SBA-15 catalyst.

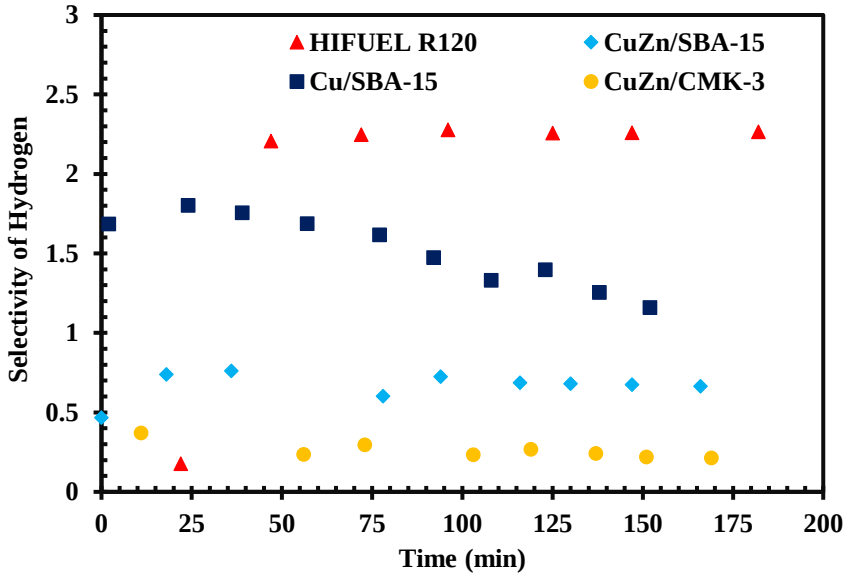

Figure 7.85: Hydrogen selectivity over time for all catalysts at 250°C

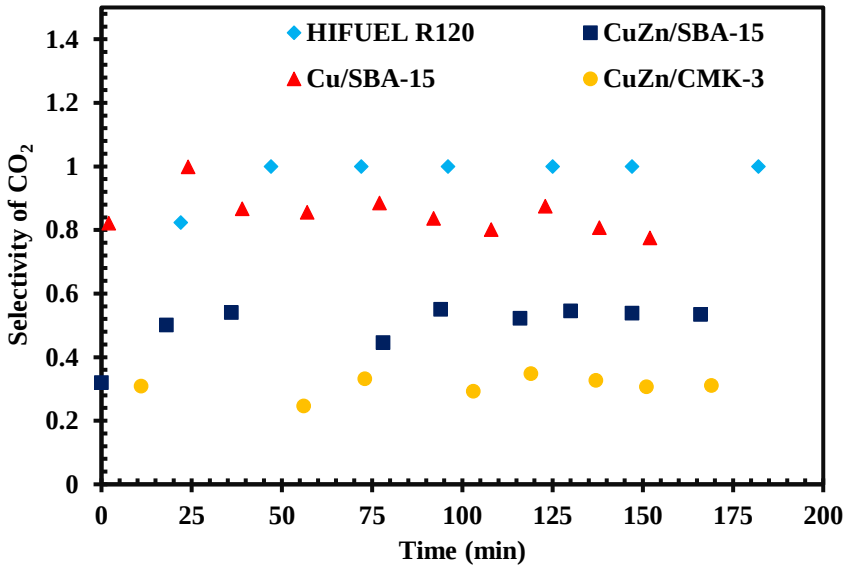

Figure 7.86: CO_2 selectivity over time for all catalysts at 250°C

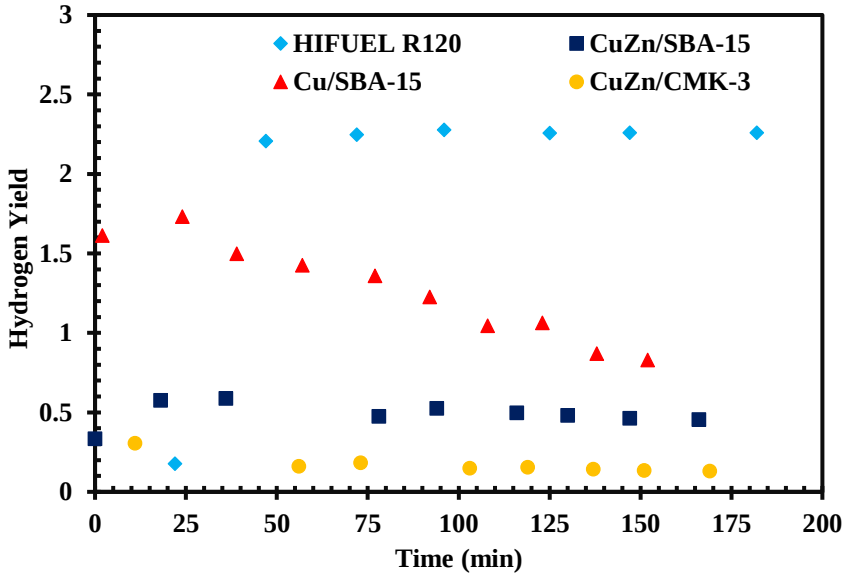

Figure 7.87: Hydrogen yield of all catalysts over time at 250°C

Figures 7.88-89 show the overall conversion and methanol conversion over time at 250°C. HIFUEL R-120 was by far the most successful catalyst in terms of both conversions. CuZn/CMK-3 was the least successful and reached negative methanol conversion due to hydrogenation of formaldehyde.

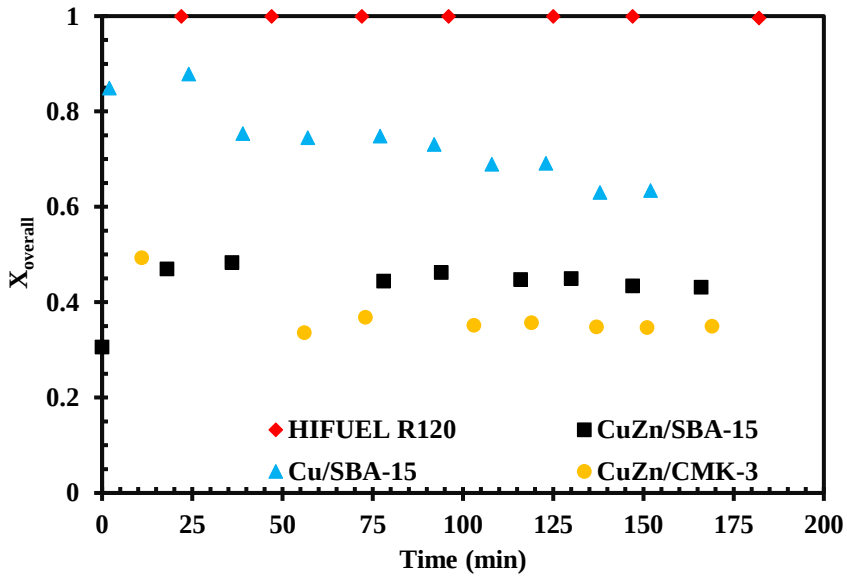

Figure 7.88: Overall conversion over time with all catalysts at 250°C

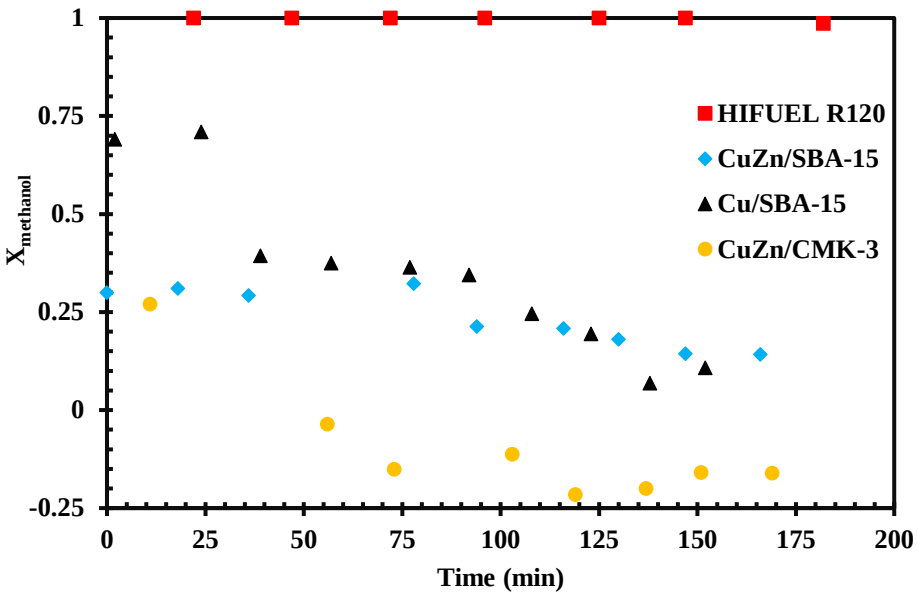

Figure 7.89: Methanol conversion over time with all catalysts at 250°C

CHAPTER 8

CONCLUSIONS AND RECOMMENDATION

In this study, FSR is investigated with synthesized and a commercial copper based catalysts. Activity of HIFUEL R-120 catalyst was tested at 175, 200, 225, and 250°C. Synthesized catalysts were CuZn/SBA-15, Cu/SBA-15, and CuZn/CMK-3 and were tested at 250°C. A flow reactor system was used in these experiments.

- Cu and Zn successfully impregnated into the structures of SBA-15 and CMK-3. Presence of copper and zinc was seen in the characterization of catalysts. Furthermore, ordered mesoporous structures were observed in the XRD patterns.
- CuZn/SBA-15, Cu/SBA-15 and CuZn/CMK-3 had BET surface areas of 381 m^2/g, 394 m^2/g and 548 m^2/g, respectively. Pore diameters of SBA-15 supported catalysts did not change and was 4.8 nm. CuZn/CMK-3 had pore diameter of 3.86 nm. All three catalysts resembled Type IV isotherm in which SBA-15 supported ones had H1 hysteresis loop and CuZn/CMK-3 had H2 hysteresis loop. Crystal size of copper increased after activity tests in all synthesized catalysts.
- According to ICP results, 9.84 wt. % Cu and 4.95 wt. % Zn were impregnated to CuZn/SBA-15; 15.8 wt. % Cu was impregnated to Cu/SBA-15; and 12.8 wt. % Cu was impregnated to CuZn/CMK-3 successfully.
- SEM results have shown that copper and zinc were well-distributed on the catalyst surface. In addition, SEM images of spent catalysts have shown the signs of sintering.

- TGA results showed that a little amount of coke was observed in silica supported catalysts.
- DRIFTS results show that CuZn/SBA-15 and Cu/SBA-15 have observable acid sites. Zn metal addition increased the acidity of the CuZn/SBA-15. However, CuZn/CMK-3 has not any observable acid sites.
- **In none of the FSR experiments, CO was observed** except for startup times of the experiments at 225 and 250°C in the presence of HIFUEL R-120.
- CuZn/SBA-15 with 18 wt. % metal loading was stable during operation. Conversion values, mole fraction and selectivity of products and hydrogen yield did not change appreciably in the activity test. However, its formaldehyde conversion was about 81.8 %.
- Cu/SBA-15 was most active catalyst that it was better in conversion of formaldehyde to hydrogen and carbon dioxide with 100 %. It was not so stable as CuZn/SBA-15 and its activity swiftly decreased over time.
- CuZn/CMK-3 was somewhat different than other three catalysts. It had formaldehyde conversion of 97 %. However, hydrogen production was the lowest among other catalyst and it had negative conversion of methanol after 56 minutes. This is attributed to the formaldehyde hydrogenation reaction that is also thermodynamically favorable at 250°C, and CuZn/CMK-3 being active for FSR, but not so active for MSR.
- Zn was not responsible for FSR reaction activity. However, it significantly improved the stability of the catalysts.
- Hydrogen yield reached to maximum theoretical value, when HIFUEL R-120 was used as the catalyst.
- According to SEM images, activity drop of all three synthesized catalysts was attributed to the sintering of copper crystals.
- HIFUEL R120, was the most successful catalyst among four of them. It has converted formaldehyde 100 % at 175, 200, 225, 250°C proving that formaldehyde steam reforming can be used at lower temperatures than that of methanol steam reforming.

Finally, these results are promising for the onboard PEMFC vehicles' future, since there was no CO formed in the syngas and high formaldehyde conversion at low temperatures.

There are some recommendations for the future work on this subject. Firstly, during ordered mesoporous carbon CMK-3 synthesis, there were many steps along with silica removal step. Silica requires a special effort to be removed. Therefore, for ordered mesoporous carbon, other means of synthesis should be found. Secondly, 18 wt. % metal loading was successfully performed to mesoporous supports by thermal decomposition in an inert environment. There are suggestions that inert gases containing little amount of NO improves the distribution of metal crystals in the pores. With this method, higher than 18 wt. % metal loading can be achieved and HIFUEL R-120's activity can be reached.

REFERENCES

Aktas, O., Yasyerli, S., Dogu, G., & Dogu, T. (2011). Structural variations of MCF and SBA-15 like mesoporous materials as a result of differences in the synthesis solution pH. Materials Chemistry and Physics, 131(1-2), 151-159.

Arrhenius, S. (1896). On the Influence of Carbonic Acid in the Air upon the Temperature of the Ground. Philosophical Magazine and Journal of Science, 41(5), 237-276.

Barrett, E. P., Joyner, L. G., & Halenda, P. P. (1951). The Determination of Pore Volume and Area Distributions in Porous Substances. I. Computations from Nitrogen Isotherms. Journal of American Chemical Society, 73(1), 373-380.

Beck, J., Vartuli, J., Roth, W. J., Leonowicz, M. E., Kresge, C. T., Schmitt, K. D., Schlenker, J. L. (1992). A New Family of Mesoporous Molecular Sieves Prepared with Liquid Crystal Templates. Journal of American Chemical Society, 114(27), 10834-10843.

Bi, Y., & Lu, G. (2008). Nano-Cu catalyze hydrogen production from formaldehyde solution at room temperature. International Journal of Hydrogen Energy, 33(9), 2225-2232.

Bo, J. Y., Zhang, S., & Lim, K. H. (2009). Steam Reforming of Formaldehyde on Cu(100) Surface: A Density Functional Study. Catalysis Letters, 129(3), 444-448.

Brinker, C. J., & Scherer, G. W. (1990). Hydrolysis and Condensation II: Silicates. In Sol-Gel Science (pp. 97-234). Academic Press, Inc.

Broecker, W. S. (1975). Climatic Change: Are We on the Brink of a Pronounced Global Warming? Science, 189(4201), 460-463.

Brunauer, S., Emmett, P. H., & Teller, E. (1938). Adsorption of Gases in Multimolecular Layers. Journal of American Chemical Society, 60(2), 309-319.

Callendar, G. S. (1938). The Artificial Production of Carbon Dioxide and Its Influence on Temperature. Quarterly Journal of the Royal Meteorological Society, 64(275), 223-240.

Callendar, G. S. (1958). On the Amount of Carbon Dioxide in the Atmosphere. Tellus, 10(2), 243-248.

Çelik, G. (2012). Bi-Functional Nanostructured Novel Catalysts For Dimethyl Ether Synthesis. M.S. Thesis, Middle East Technical University, Department of Chemical Engineering, Ankara.

Coats, A. W., & Redfern, J. P. (1963). Thermogravimetic Analysis. A Review. Analyst, 88(1053), 906-924.

Corma, A. (1995). Inorganic Solid Acids and Their Use in Acid-Catalyzed Hydrocarbon Reactions. Chemical Reviews, 95(3), 559-614.

de Jong, K. P. (2009). General Aspects. In K. P. de Jong, Synthesis of Solid Catalysts (pp. 3-11). WILEY-VCH Verlag GmbH & Co. KGaA.

Dean, C. (2009). Rising Acidity Is Threatening Food Web of Oceans, Science Panel Says. The New York Times, A12.

Dhere, N. G., & Bennur, R. S. (2009). Use of Solar Energy to Produce Hydrogen. In Hydrogen Fuel Production, Transport and Storage (pp. 228-282). CRC Press, Taylor & Francis Group, LLC.

Diem, H., Matthias, G., Aicher, A., Schreiber, H., Haas, H., & Sperber, H. (1975). United States Patent No. 3928461.

EIA. (n.d.). What is U.S. electricity generation by energy source? Retrieved May 16, 2016, from U.S. Energy Information Administration: https://www.eia.gov/tools/faqs/faq.cfm?id=427&t=3

Galarneau, A., Cambon, H., Di Renzo, F., Ryoo, R., Choi, M., & Fajula, F. (2003). Microporosity and connections between pores in SBA-15 mesostructured silicas as a function of the temperature of synthesis. New Journal of Chemistry, 27(1), 73-79.

Gallei, E. F., Hesse, M., & Schwab, E. (2008). Preparation of Solid Catalysts. In G. Ertl, H. Knözinger, F. Schüth, & J. Weitkamp, Handbook of Heterogeneous Catalysis (pp. 57-721). Wiley-VCH Verlag GmbH & Co. KGaA.

Gallezot, P., & Bergeret, G. (2008). Particle Size and Dispersion Measurements. In G. Ertl, H. Knözinger, F. Schüth, & J. Weitkamp, Handbook of Heterogeneous Catalysis (pp. 739-764). Wiley-VCH Verlag GmbH & Co. KGaA.

Gerberich, H. R., & Seaman, G. C. (2013). Formaldehyde. In Kirk-Othmer Encyclopedia of Chemical Technology (pp. 1-22). John Wiley & Sons, Inc.

Gupta, R. B., & Pant, K. K. (2009). Fundamentals and Use of Hydrogen as a Fuel. In Hydrogen Fuel Production, Transport and Storage (pp. 1-29). Florida: CRC Press Taylor & Francis Groups, LLC.

Hakim, D. (2002, November 17). An Electrovan, Not an Edsel. Retrieved March 28, 2016, from The New York Times: http://www.nytimes.com/2002/11/17/business/yourmoney/17PROF.html?pagewanted=all

Handa, P., Witula, T., Reis, P., & Holmberg, K. (2008). ARKIVOC(vi), 107.

Hansen, J., Johnson, D., Lacis, A., Lebedeff, S., Lee, P., Rind, D., & Russell, G. (1981). Climate Impact of Increasing Atmospheric Carbon Dioxide. Science, 213(4511), 957-966.

Hao, L., Wang, J., Shen, L., Zhu, J., Ding, B., & Zhang, X. (2016). Synthesis and electrochemical performances of mixed-valence vanadium oxide/ordered mesoporous carbon composites for supercapacitors. RSC Advances, 6(30), 25056-25061.

Hardinger, S. (n.d.). Illustrated Glossary of Organic Chemistry. Retrieved May 10, 2016, from Organic Chemistry at UCLA: http://www.chem.ucla.edu/~harding/IGOC/F/formaldehyde.html

Häussinger, P., Lohmüller, R., & Watson, A. M. (2000). Hydrogen, 6. Uses. In Ullmann's Encyclopedia of Industrial Chemistry (pp. 1-40). Wiley-VCH Verlag GmbH & Co. KGaA.

Heim, L. E., Schlörer, N. E., Choi, J.-H., & Prechtl, M. H. (2014). Selective and mild hydrogen production using water and formaldehyde. Nature Communications, 5, 1-7.

Heinzel, A., Cappadonia, M., Stimming, U., Kordesch, K. V., & de Oliveira, J. C. (2010). Fuel Cells. In Ullmann's Encyclopedia of Industrial Chemistry. Wiley-VCH Verlag GmbH & Co. KGaA.

IARC. (1987). IARC Monographs on the Evaluation of Carcinogenic Risks to Humans. Lyon: World Health Organization.

IUPAC. (1972). Manual of Symbols and Terminology, appendix 2, Pt.1, Colloid and Surface Chemistry. Pure Appl. Chem., 31(4), 578-638.

Jun, S., Joo, S., Ryoo, R., Kruk, M., Jaroniec, M., Liu, Z., Terasaki, O. (2000). Synthesis of New, Nanoporous Carbon with Hexagonally Ordered Mesostructure. Journal of American Chemical Society, 122(43), 10712-10713.

Kapoor, S., Barnabas, F. A., Sauer, Jr., M. C., Meisel, D., & Jonah, C. D. (1995). Kinetics of Hydrogen Formation from Formaldehyde in Basic Aqueous Solutions. J. Phys. Chem., 99(18), 6857-6863.

Kent, J. A. (1968). Synthetic Organic Chemicals. In Riegel's Industrial Chemistry (pp. 894-895). Reinhold Book Corporation.

Krajcí, M., Tsai, A. -P., & Hafner, J. (2015). Understanding the selectivity of methanol steam reforming on the (111) surfaces of NiZn, PdZn and PtZn: Insights from DFT. Journal of Catalysis, 330, 6-18.

Kresge, C. T., Leonowicz, M. E., Roth, W. J., Vartuli, J. C., & Beck, J. S. (1992). Ordered mesoporous molecular sieves synthesized by a liquid-crystal template mechanism. Nature, 359, 710-712.

Larminie, J. (2002). Fuel Cells. In Kirk-Othmer Encyclopedia of Chemical Technology (pp. 199-228). John Wiley & Sons, Inc.

Lauermann, G., Lohmüller, R., Watson, A. M., & Häussinger, P. (2013). Hydrogen, 1. Properties and Occurence. In Ullman's Encyclopedia of Industrial Chemistry (pp. 1-3). Wiley-VCH Verlag GmbH & Co. KGaA.

Lee, J., Yoon, S., Oh, M., Shin, C.-H., & Hyeon, T. (2000). Development of a New Mesoporous Carbon Using an HMS Aluminosilicate Template. Advanced Materials, 12(5), 359-362.

Li, X., & Lim, K. H. (2012). DFT Study of Steam Reforming of Formaldehyde on Cu, PdZn, and Ir. ChemCatChem, 4(9), 1311-1320.

Li, Y., Chen, T., Wang, T., Zhang, Y., Lu, G., & Bi, Y. (2014). Highly efficient hydrogen production from formaldehyde over Ag/γ-Al2O3 catalyst at room temperature. International Journal of Hydrogen Energy, 39(17), 9114-9120.

Liang, C., Li, Z., & Dai, S. (2008). Mesoporous Carbon Materials: Synthesis and Modification. Angewandte Chemie International Edition, 47(20), 3696-3717.

Lin, S., Johnson, R. S., Smith, G. K., Xie, D., & Guo, H. (2011). Pathways for methanol steam reforming involving adsorbed formaldehyde and hydroxyl intermediates on Cu(111): density functional theory studies. Physical Chemistry Chemical Physics, 13(20), 9622-9631.

Loew, O. (1887). Einige Bemerkungen über Formose. Berichte der deutschen chemischen Gesellschaft, 20(1), 141-144.

Lohmüller, R., Häussinger, P., & Watson, A. M. (2000). Hydrogen, 2. Production. In Ullmann's Encyclopedia of Industrial Chemistry (pp. 251-307). Wiley-VCH Verlag GmbH & Co. KGaA.

Lorenz, H., Friedrich, M., Armbrüster, M., Klötzer, B., & Penner, S. (2013). ZnO is a CO2-selective steam reforming catalyst. Journal of Catalysis, 297, 151-154.

Lu, A.-H., & Schüth, F. (2006). Nanocasting: A Versatile Strategy for Creating Nanostructured Porous Materials. Advanced Materials, 18(14), 1793-1805.

Lu, A.-H., Zhao, D., & Wan, Y. (2010). Nanocasting A Versatile Strategy for Creating Nanostructured Porous Materials. RSC Publishing.

Lu, A.-H., Zhao, D., & Wan, Y. (2010). Principles of Nanocasting. In Nanocasting A Versatile Strategy for Creating Nanostructured Porous Materials (pp. 1-44). Royal Society of Chemistry.

Marceau, E., Carrier, X., & Che, M. (2009). Impregnation and Drying. In K. P. de Jong, Synthesis of Solid Catalysts (pp. 59-82). WILEY-VCH Verlag GmbH & Co. KGaA.

McBride, B. J., & Gordon, S. (1992). Computer Program for Calculating and Fitting Thermodynamic Functions. NASA Reference Publication.

Moretti, G. (2008). X-Ray Photoelectron and Auger Electron Spectroscopy. In G. Ertl, H. Knözinger, F. Schüth, & J. Weitkamp, Handbook of Heterogeneous Catalysis (pp. 1029-1039). Wiley-VCH Verlag GmbH & Co. KGaA.

Moulijn, J. A., Makkee, M., & van Diepen, A. E. (2013). Methanol. In Chemical Process Technology 2nd Edition (pp. 199-201). John Wiley & Sons Ltd.

Munnik, P., Wolters, M., Gabrielsson, A., Pollington, S. D., Headdock, G., Bitter, J. H., de Jong, K. P. (2011). Copper Nitrate Redispersion To Arrive at

Highly Active Silica-Supported Copper Catalysts. The Journal of Physical Chemistry C, 115(30), 14698-14706.

National Academy of Sciences. (2004). The Hydrogen Economy: Opportunities, Costs, Barriers and R&D Needs. Washington, D.C.: The National Academies Press.

NOAA National Centers for Environmental Information. (2016, January). State of the Climate: Global Analysis for Annual 2015. Retrieved April 6, 2016, from National Oceanic and Atmospheric Administration: https://www.ncdc.noaa.gov/sotc/global/201513

Olah, G. A., Goeppert, A., & Prakash, G. K. (2011). Beyond Oil and Gas: The Methanol Economy. Wiley-VCH.

Peters, R. (2008). Fuel Cell Related Catalysis. In G. Ertl, H. Knoezinger, F. Schueth, & Weitkamp J., Handbook of Heterogeneous Catalysis (pp. 3045-3060). Weinheim: Wiley-VCH.

Prieto, G., Zecevic, J., Friedrich, H., de Jong, K. P., & de Jongh, P. E. (2013). Towards stable catalysts by controlling collective properties of supported metal nanoparticles. Nature Materials, 12, 34-39.

Reuss, G., Disteldorf, W., Gamer, A. O., & Hilt, A. (2000). Formaldehyde. In Ullmann's Encyclopedia of Industrial Chemistry (pp. 735-763). Wiley-VCH Verlag GmbH & Co. KGaA.

Ryoo, R., Joo, S. H., & Jun, S. (1999). Synthesis of Highly Ordered Carbon Molecular Sieves via Template-Mediated Structural Transformation. The Journal of Physical Chemistry B, 103(37), 7743-7746.

Ryoo, R., Joo, S. H., Kruk, M., & Jaroniec, M. (2001). Ordered Mesoporous Carbons. Advanced Materials, 13(9), 677-681.

Ryoo, R., Jun, S., Joo, S., Kruk, M., Jaroniec, M., Liu, Z., . . . Terasaki, O. (2000). Synthesis of New, Nanoporous Carbon with Hexagonally Ordered Mesostructure. J. Am. Chem. Soc., 122, 10712-10713.

Satterfield, C. N. (1996). Catalyst Preparation and Manufacture. In Heterogeneous Catalysis in Industrial Practice (pp. 87-130). Krieger Publishing Company.

Satyapal, S., & Thomas, G. J. (2009). Targets for Onboard Hydrogen Storage Systems: An Aid for the Development of Viable Onboard Hydrogen Storage Technologies. In Hydrogen Fuel Production, Transport, and Storage (pp. 327-339). CRC Press, Taylor & Francis Group, LLC.

Schimpf, S., & Muhler, M. (2009). Methanol Catalysts. In K. P. de Jong, Synthesis of Solid Catalysts (pp. 329-351). WILEY-VCH Verlag GmbH & Co. KGaA.

Sietsma, J. R., Friedrich, H., Broersma, A., Versluijs-Helder, M., van Dillen, A. J., de Jongh, P. E., & de Jong, K. P. (2008). How nitric oxide affects the decomposition of supported nickel nitrate to arrive at highly dispersed catalysts. Journal of Catalysis, 260(2), 227-235.

Sietsma, J. R., Meeldijk, J. D., Breejen, J. P., Versluijs-Helder, M., van Dillen, A. J., de Jongh, P. E., & de Jong, K. P. (2007). The Preparation of Supported NiO and Co3O4 Nanoparticles by the Nitric Oxide Controlled Thermal Decomposition of Nitrates. Angewandte Chemie International Edition, 46(24), 4547-4549.

Sing, K. S., Everett, D. H., Haul, R., Moscou, L., Pierotti, R. A., Rouquerol, J., & Siemieniewska, T. (1985). Reporting physisorption data for gas/solid systems with special reference to the determination of surface area and porosity. Pure and Applied Chemistry, 57(4), 603-619.

Skoog, D. A., West, D. M., Holler, F. J., & Crouch, S. R. (2004). Molecular Absorption Spectrometry. In Fundamentals of Analytical Chemistry (pp. 785-824). Brooks/Cole, Cengage Learning.

Strahan, S. E., Douglass, A. R., Newman, P. A., & Steenrod, S. D. (2014). Inorganic chlorine variability in the Antarctic vortex and implications for ozone recovery. Journal of Geophysical Research: Atmospheres, 119(24), 14098-14109.

Takezawa, N., & Iwasa, N. (1997). Steam reforming and dehydrogenation of methanol: Difference in the catalytic functions of copper and group VIII metals. Catalysis Today, 36(1), 45-56.

Tosun, I. (2013). Minimization of Gibbs Energy. In The Thermodynamics of Phase and Reaction Equilibria (pp. 642-644). Elsevier B.V.

Vinu, A., Streb, C., Murugesan, V., & Hartmann, M. (2003). Adsorption of Cytochrome C on New Mesoporous Carbon Molecular Sieves. Journal of Physical Chemistry B, 107(33), 8297-8299.

Walker, J. F. (1944). Formaldehyde. Reinhold Publishing Corporation.

Wan, Y., & Zhao, D. (2007). On the Controllable Soft-Templating Approach to Mesoporous Silicates. Chemical Reviews, 107(7), 2821-2856.

Wan, Y., & Zhao, D. (2009). Ordered Mesoporous Materials. In K. P. de Jong, Synthesis of Solid Catalysts (pp. 277-299). Wiley-VCH Verlag GmbH & Co. KGaA.

Wu, C. G., & Bein, T. (1994). Conducting Carbon Wires in Ordered, Nanometer-Sized Channels. Science, 266(5187), 1013-1015.

Xia, K., Gao, Q., Wu, C., Song, S., & Ruan, M. (2007). Activation, characterization and hydrogen storage properties of the mesoporous carbon CMK-3. Carbon, 45(10), 1989-1996.

Zhao, D., Feng, J., Huo, Q., Melosh, N., Fredrickson, G. H., Chmelka, B. F., & Stucky, G. D. (1998). Triblock Copolymer Syntheses of Mesoporous Silica with Periodic 50 to 300 Angstrom Pores. Science, 279(5350), 548-552.

Zuckerman, B., Buhl, D., Palmer, P., & Snyder, L. E. (1970). Observation of Interstellar Formaldehyde. The Astrophysical Journal, 160, 485-506.

Zuo, Z. J., Wang, L., Han, P. D., & Huang, W. (2014). Insights into the reaction mechanisms of methanol decomposition, methanol oxidation and steam reforming of methanol on Cu(111): A density functional theory study. Internation Journal of Hydrogen Energy, 39(4), 1664-1679.

APPENDICES

APPENDIX A

CONVERSION, SELECTIVITY AND YIELD CALCULATIONS

Evaluation of analysis results from the Gas Chromatograph can be divided into two depending on the product composition in the liquid phase. Calculations are straightforward and independent of flowrates, if there is no carbonaceous compound in liquid phase. However, one has to take into account both liquid and gaseous molar flowrates, if the presence of carbon compound detected in the liquid.

Before starting calculations from GC analysis, formaldehyde solution molar composition should be determined.

A.1. DETERMINATION OF FORMALDEHYDE MOLAR COMPOSITION

In all activity tests, formaldehyde solution 34.5 wt. % was used. According to content of formalin from Sigma-Aldrich mass percentages of each compound in the solution are 53.5, 34.5 and 12 for water, formaldehyde and methanol, respectively. Density of solution is given to be 1.09 g/ml at 25°C. Molecular weights of water, formaldehyde and methanol are 18.02, 30.03 and 32.04 g/mol, respectively. For a 1 ml formalin solution as basis, moles of each compound can be found as follows

$$N_{H_2O,\,0} = (1\,ml)\left(1.09\,\frac{g}{ml}\right)\left(\frac{53.5\,g\,water}{100\,g}\right)\left(\frac{1\,mol}{18.02\,g\,water}\right) = 0.0324\ mol\ H_2O$$

$$N_{FA,\,0} = (1\,ml)\left(1.09\,\frac{g}{ml}\right)\left(\frac{34.5\,g\,FA}{100\,g}\right)\left(\frac{1\,mol}{30.03\,g\,FA}\right) = 0.0125\ mol\ FA$$

$$N_{CH_3OH,0} = (1\ ml)\left(1.09\ \frac{g}{ml}\right)\left(\frac{34.5\ g\ CH_3OH}{100\ g}\right)\left(\frac{1\ mol}{32.04\ g\ CH_3OH}\right) = 0.0041\ mol\ CH_3OH$$

Total number of moles for this basis is

$$N_{tot,0} = 0.03236 + 0.01252 + 0.00408 = 0.0490\ mol\ .$$

Finally, dividing number of moles of each component by total number of moles in the system is to yield the molar fractions.

$$x_{H_2O,0} = \frac{0.03236}{0.04896} = 0.661$$

$$x_{FA,0} = \frac{0.01252}{0.04896} = 0.256$$

$$x_{CH_3OH} = \frac{0.00408}{0.04896} = 0.083$$

For illustration mass and molar percent of each component in formalin feed solution is given in Table A.1.

Table A.1: Mass and molar percent of each component in formalin feed solution

Molecule	Mass %	Mole %
H_2O	53.5	66.1
CH_2O	34.5	25.6
CH_3OH	12.0	8.3

A.2. CALCULATIONS BASED ONLY ON THE GAS PRODUCT STREAM

If there is no formaldehyde or methanol found in liquid analysis, the calculation procedure is based on gas phase carbon atomic balance. Starting with simplistic carbon balance initially methanol and formaldehyde present and at the reactor effluent stream carbon monoxide, carbon dioxide, unconverted methanol and formaldehyde exist. Atomic species balance on carbon yields

$$N_{CH_3OH,0} + N_{FA,0} = N_{CH_3OH} + N_{FA} + N_{CO_2} + N_{CO} \qquad \text{(Equation A.1)}$$

Using Equation A.1, overall conversion of carbonaceous feed can be found as

$$X_{overall} = \frac{N_{CO} + N_{CO_2}}{N_{CH_3OH} + N_{FA} + N_{CO_2} + N_{CO}} \qquad \text{(Equation A.2)}$$

Moles of each component in the analysis can be found by using their signal's area under the curve, A_i, and their correction factor, β_i, designated for each carbonaceous component i. Using equations C.1 for number of moles, A.1 and A.2 altogether overall conversion now becomes

$$X_{overall} = \frac{A_{CO_2}\beta_{CO_2} + A_{CO}\beta_{CO}}{A_{CH_3OH}\beta_{CH_3OH} + A_{FA}\beta_{FA} + A_{CO}\beta_{CO} + A_{CO_2}\beta_{CO_2}} \qquad \text{(Equation A.3)}$$

Furthermore, formaldehyde and methanol conversions can be calculated separately. By definition of conversion for a component,

$$X_{CH_3OH} = \frac{N_{CH_3OH,0} - N_{CH_3OH}}{N_{CH_3OH,0}} \qquad \text{(Equation A.4)}$$

and

$$X_{FA} = \frac{N_{FA,0} - N_{FA}}{N_{FA,0}} \qquad \text{(Equation A.5)}$$

These two equations can be simplified by defining

$$\alpha = \frac{N_{CH_3OH,0}}{N_{FA,0}} \qquad \text{(Equation A.6)}$$

and

$$N_{C,total} = N_{CH_3OH} + N_{FA} + N_{CO} + N_{CO_2} \qquad \text{(Equation A.7)}$$

Note that $N_{C,total}$ is the total moles of carbonaceous compounds in the system. Derivation continues as

$$N_{C,total} = N_{CH_3OH,0} + N_{FA,0} \qquad \text{(Equation A.8)}$$

$$N_{FA,\,0} = N_{C,\,total} - \alpha N_{FA,\,0} \qquad \text{(Equation A.9)}$$

$$N_{FA,\,0} = \frac{N_{C,\,total}}{\alpha + 1} \qquad \text{(Equation A.10)}$$

$$N_{CH_3OH,\,0} = \alpha N_{FA,\,0} = \left(\frac{\alpha}{\alpha + 1}\right)\left(N_{C,\,total}\right) \qquad \text{(Equation A.11)}$$

Finally, conversion expressions for formaldehyde and methanol distinctly can be written using Equations A.10-11

$$X_{CH_3OH} = \frac{\left(\frac{\alpha}{\alpha+1}\right)\left(N_{C,\,total}\right) - N_{CH_3OH}}{\left(\frac{\alpha}{\alpha+1}\right)\left(N_{C,\,total}\right)} \qquad \text{(Equation A.12)}$$

$$X_{FA} = \frac{\left(\frac{N_{C,\,total}}{\alpha+1}\right) - N_{FA}}{\left(\frac{N_{C,\,total}}{\alpha+1}\right)} \qquad \text{(Equation A.13)}$$

Hydrogen yield by definition is

$$Y_{H_2} = \frac{N_{H_2}}{N_{CH_3OH,\,0} + N_{FA,\,0}} \qquad \text{(Equation A.14)}$$

For two main reactions occurring in the reactor that are

$$CH_3OH + H_2O \longrightarrow CO_2 + 3\,H_2$$

$$CH_2O + H_2O \longrightarrow CO_2 + 2\,H_2$$

maximum hydrogen yield with 34.5 wt. % formalin solution can become

$$Y_{H_2,\,\max} = \frac{3\,N_{CH_3OH,\,0} + 2\,N_{FA,\,0}}{N_{CH_3OH,\,0} + N_{FA,\,0}} = \frac{(3)(0.083) + (2)(0.256)}{0.08337 + 0.256} = 2.25$$

Selectivity towards each product species (H_2, CO and CO_2) can be calculated by the expressions of

$$S_{H_2} = \frac{N_{H_2}}{N_{CH_3OH,\,reacted} + N_{FA,\,reacted}} \qquad \text{(Equation A.15)}$$

$$S_{CO} = \frac{N_{CO}}{N_{CH_3OH,\,reacted} + N_{FA,\,reacted}} \qquad \text{(Equation A.16)}$$

$$S_{CO_2} = \frac{N_{CO_2}}{N_{CH_3OH,\,reacted} + N_{FA,\,reacted}} \qquad \text{(Equation A.17)}$$

For instance, conversion values of a FSR experiment performed at 250°C using 0.3 g HIFUEL R120 catalyst (Experiment No: 9101) can be calculated as follows. The raw data for 200th minute's analysis, where steady state was established, are given in Table A.2.

Table A.2: Raw Data for Experiment 9101 at 200th minute

Species	Retention Time (min)	Area Under the Curve
H_2	0.762	5613.7
CO_2	1.515	291.8
H_2O	6.820	351.3
CH_3OH	7.886	114.4

Beta calibration factor for CO_2 and CH_3OH is required only that are 3.3 and 1, respectively. It is noticeable that there is no formaldehyde and carbon monoxide present in the gas phase. Furthermore, liquid analysis resulted in the presence of solely water. Therefore, formaldehyde conversion was mathematically **100 %** at all times. Overall conversion is

$$X_{overall} = \frac{(291.8)(3.3)}{(114.4)(1) + (291.8)(3.3)} = 0.894$$

In the feed, methanol is 12 wt. % and formaldehyde is 34.5 wt. %. The α and $N_{C,total}$ values accordingly can be calculated as (by equations A.6 and A.7, respectively)

$$\alpha = \frac{N_{CH_3OH,\,0}}{N_{FA,\,0}} = \frac{\dfrac{12\,g}{32.04\,\dfrac{g}{mol}}}{\dfrac{34.5\,g}{30.03\,\dfrac{g}{mol}}} = 0.3260$$

$$N_{C,\,total} = (291.8)(3.3) + (114.4)(1) = 1077.34 \text{ moles}$$

Finally, methanol conversion per pass is calculated using equation A.12.

$$X_{CH_3OH} = \frac{\left(\dfrac{\alpha}{\alpha+1}\right)\left(N_{C,\,total}\right) - N_{CH_3OH}}{\left(\dfrac{\alpha}{\alpha+1}\right)\left(N_{C,\,total}\right)} = \frac{\left(\dfrac{0.3260}{0.3260+1}\right)(1077.34) - 114.4}{\left(\dfrac{0.3260}{0.3260+1}\right)(1077.34)} = 0.568$$

Overall conversion as a function of time and methanol conversion as a function of time can be found in Figure A.1 & A.2, respectively.

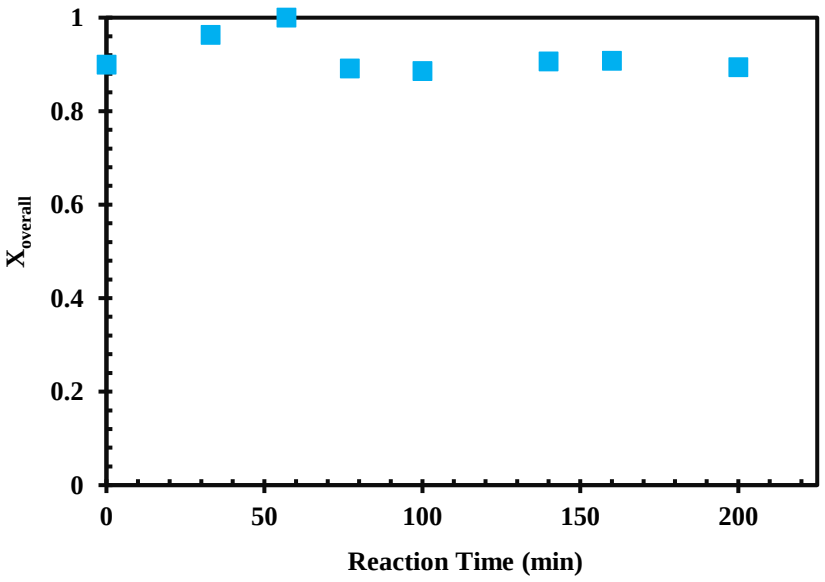

Figure A.1: Overall conversion with respect to time elapsed at 250°C operation

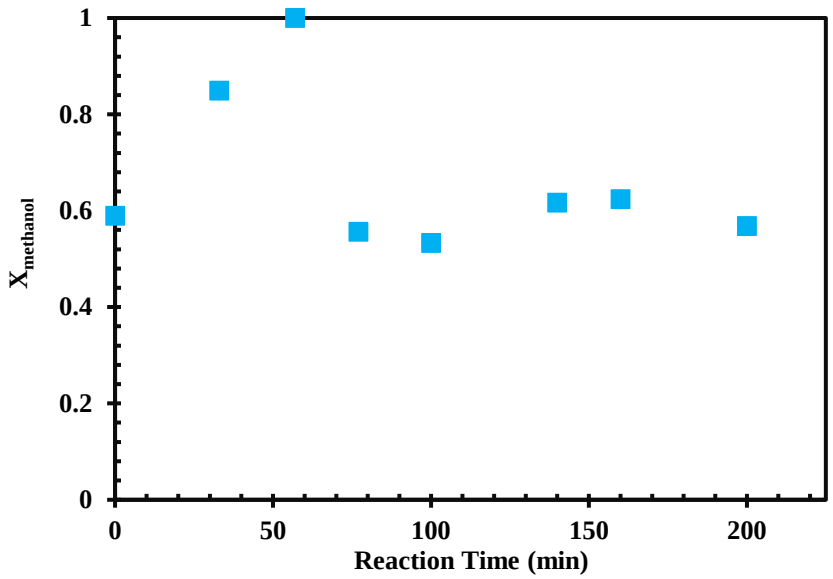

Figure A.2: Methanol conversion with respect to time elapsed at 250°C operation

A.3. CALCULATIONS BASED ON BOTH THE GAS AND THE LIQUID PRODUCT STREAMS

If there are carbonaceous compounds such as formaldehyde and methanol found in the liquid product stream, calculation procedure for conversion basically changes. Presence of the carbon containing compounds in liquid phase has to be also included in the mole balance. Some variables can be defined for formaldehyde and methanol.

Reaction time: τ (min)

Gathered liquid: M (g)

Liquid mass flow rate: m_L (g/min)

Methanol molar flowrate in liquid phase: $F_{CH_3OH,\,L}$

Formaldehyde molar flowrate in liquid phase: $F_{FA,\,L}$

$$m_L = \frac{M}{\tau} \qquad \text{(Equation A.18)}$$

For liquid phase, formaldehyde and methanol molar flowrates will be

$$F_{FA,\,L} = m_L \frac{x_{FA}}{\left(x_{CH_3OH}\right)\left(MW_{CH_3OH}\right) + \left(x_{H_2O}\right)\left(MW_{H_2O}\right) + \left(x_{FA}\right)\left(MW_{FA}\right)} \qquad \text{(Equation A.19)}$$

$$F_{CH_3OH,\,L} = m_L \frac{x_{CH_3OH}}{\left(x_{CH_3OH}\right)\left(MW_{CH_3OH}\right) + \left(x_{H_2O}\right)\left(MW_{H_2O}\right) + \left(x_{FA}\right)\left(MW_{FA}\right)} \quad \text{(Equation A.20)}$$

where MW_i is the molecular weight for each component i (g/mol), formaldehyde mole fraction in liquid phase is x_{FA} and methanol mole fraction in liquid phase is x_{CH_3OH}. They are calculated by the liquid analysis data

$$x_{FA} = \frac{A_{FA,\,L}\,\beta_{FA}}{A_{CH_3OH,\,L}\,\beta_{CH_3OH} + A_{H_2O,\,L}\,\beta_{H_2O} + A_{FA,\,L}\,\beta_{FA}} \quad \text{(Equation A.21)}$$

$$x_{CH_3OH} = \frac{A_{CH_3OH,\,L}\,\beta_{CH_3OH}}{A_{CH_3OH,\,L}\,\beta_{CH_3OH} + A_{H_2O,\,L}\,\beta_{H_2O} + A_{FA,\,L}\,\beta_{FA}} \quad \text{(Equation A.22)}$$

For the gas phase, with the assumption of gas mixture behaving ideally at the analysis conditions (1 atm, 25°C)

$$F_{FA,\,G} = Q_{others}\,C_{G,\,total}\,y_{FA} \quad \text{(Equation A.23)}$$

$$F_{CH_3OH,\,G} = Q_{others}\,C_{G,\,total}\,y_{CH_3OH} \quad \text{(Equation A.24)}$$

and

$$C_{G,\,total} = \frac{P}{R\,T} \quad \text{(Equation A.25)}$$

where $F_{CH_3OH,\,G}$ is the gaseous molar flowrate of methanol (mol/min), $F_{FA,\,G}$ is gaseous flow rate of formaldehyde (mol/min) and Q_{others} is

$$Q_{others} = Q_{total} - Q_{Ar} \quad \text{(Equation A.26)}$$

the gaseous volumetric flowrate of the analysis gas mixture without carrier gas Argon Q_{Ar} (mL/min), R is gas constant (atm.L/(mol.K)), P is pressure (atm), T is temperature at the analysis conditions (K), $C_{G,total}$ is the total gas concentration

(mol/mL). Total number of moles gaseous mixture of analysis mixture found by GC analysis is defined by $N_{G,total}$

$$N_{G,\,total} = N_{CH_3OH} + N_{FA} + N_{CO_2} + N_{CO} + N_{H_2} + N_{H_2O} \quad \text{(Equation A.27)}$$

Equation A.24 can be represented in order to conform to analysis data

$$N_{G,\,total} = A_{CH_3OH,\,G}\,\beta_{CH_3OH} + A_{FA,\,G}\,\beta_{FA,\,G} + A_{CO_2}\beta_{CO_2} + A_{CO}\beta_{CO} + A_{H_2}\beta_{H_2} + A_{H_2O,\,G}\beta_{H_2O} \quad \text{(Equation A.28)}$$

Vapor mole fraction of formaldehyde and methanol can be calculated by equation A.29 and A.30.

$$y_{FA} = \frac{A_{FA,\,G}\,\beta_{FA}}{N_{G,\,total}} \quad \text{(Equation A.29)}$$

$$y_{CH_3OH} = \frac{A_{CH_3OH,\,G}\,\beta_{CH_3OH}}{N_{G,\,total}} \quad \text{(Equation A.30)}$$

Conversion values for formaldehyde and methanol flow systems can be written as

$$X_{FA} = \frac{F_{FA,\,0} - F_{FA}}{F_{FA,\,0}} \quad \text{(Equation A.31)}$$

$$X_{CH_3OH} = \frac{F_{CH_3OH,\,0} - F_{CH_3OH}}{F_{CH_3OH,\,0}} \quad \text{(Equation A.32)}$$

In addition, overall conversion is estimated by equation A.33.

$$X_{overall} = \frac{F_{CO} + F_{CO_2}}{F_{CH_3OH} + F_{FA} + F_{CO} + F_{CO_2}} \quad \text{(Equation A.33)}$$

A new variable is defined for the denominator of equation A.33.

$$F_{C,\,total} = F_{CH_3OH,\,L} + F_{CH_3OH,\,G} + F_{FA,\,L} + F_{FA,\,G} + F_{CO} + F_{CO_2} \quad \text{(Equation A.34)}$$

$$F_{C,\,total} = Q_{others}\, C_{G,\,total}\left(y_{CH_3OH} + y_{FA} + y_{CO} + y_{CO_2}\right) + F_{CH_3OH,\,L} + F_{FA,\,L} \qquad \text{(Equation A.35)}$$

Overall conversion can be simplified to

$$X_{overall} = \frac{Q_{others}\, C_{G,\,total}\left(A_{CO}\beta_{CO} + A_{CO_2}\beta_{CO_2}\right)}{F_{C,\,total}\, N_{G,\,total}} \qquad \text{(Equation A.36)}$$

With new variables, also the selectivity and yield calculations change.

$$S_{H_2} = \frac{F_{H_2}}{F_{CH_3OH,\,0}\, X_{CH_3OH} + F_{FA,\,0}\, X_{FA}} \qquad \text{(Equation A.37)}$$

$$S_{CO} = \frac{F_{CO}}{F_{CH_3OH,\,0}\, X_{CH_3OH} + F_{FA,\,0}\, X_{FA}} \qquad \text{(Equation A.38)}$$

$$S_{CO_2} = \frac{F_{CO_2}}{F_{CH_3OH,\,0}\, X_{CH_3OH} + F_{FA,\,0}\, X_{FA}} \qquad \text{(Equation A.39)}$$

$$Y_{H_2} = \frac{F_{H_2}}{F_{CH_3OH,\,0} + F_{FA,\,0}} \qquad \text{(Equation A.40)}$$

As an example, sample calculation procedure of a FSR experiment performed at 175°C using 0.3 g HIFUEL R120 catalyst (Experiment No: 9106) can be performed as follows. The raw gas analysis data for 136th minute's analysis is given in Table A.3.

Table A.3: Raw data for gas analysis results in Experiment 9106 at 136th minute

Species	Retention Time (min)	Area Under the Curve
H_2	0.763	4367.3
CO_2	1.888	259.8
H_2O	7.384	822.3
CH_3OH	8.438	161.2

Total gas flowrate was measured as 39.70 mL/min including 30 mL/min flow of Argon as carrier gas. Furthermore, there was also methanol found in liquid phase. Liquid analysis results are given in Table A.4.

Table A.4: Raw data for liquid analysis results in Experiment 9106

Species	Retention Time (min)	Area Under the Curve
H_2O	6.495	7092.8
CH_3OH	7.779	1144.8

Beta factors for all four components present can be found in Table C.1. Liquid collected by the condenser (M) was 0.4687 and elapsed time for total experiment was (τ) 165 minutes. Therefore,

$$m_L = \frac{0.4687\,g}{165\,min} = 0.002841\,\frac{g}{min}$$

No formaldehyde was found in both gas and liquid analysis. Consequently, its flowrate in both gas and liquid phases are zero. Moreover, it can be concluded that formaldehyde has 100 % conversion. Rest of the calculations are to be made for methanol merely. Methanol molar fraction in liquid phase is

$$x_{CH_3OH} = \frac{(1144.8)(1)}{(1144.8)(1) + (7092.8)(0.96)} = 0.1439$$

and methanol molar flowrate in liquid phase becomes

$$F_{CH_3OH,\,L} = (0.002841)\frac{(0.1439)}{(0.1439)(32.04) + (1-0.1439)(18.02)} = 2.040\,\text{x}\,10^{-5}\,\frac{mol}{min}\ .$$

Gas flowrate without carrier gas is calculated by equation A.26.

$$Q_{others} = 39.70 - 30 = 9.70\,\frac{ml}{min}$$

At 1 atm and 25°C, total gas concentration is

$$C_{G,\,total} = \frac{1\,atm}{\left(0.08206\,\frac{atm.L}{mol.K}\right)\left(\frac{1000\,mL}{1\,L}\right)(298\,K)} = 4.089\,\text{x}\,10^{-5}\,\frac{mol}{mL}$$

by equation A.25. Before calculation of molar flowrate of methanol in liquid phase, gaseous mole fraction must be calculated using equations A.28 and A.30.

$$N_{G,\,total} = (161.2)(1) + (259.8)(3.3) + (4367.3)(0.35) + (822.3)(0.96) = 3336.5$$

$$y_{CH_3OH} = \frac{(161.2)(1)}{3336.5} = 0.0483$$

Molar flowrate of methanol by equation A.23 is

$$F_{CH_3OH,\,G} = (9.70)\left(4.089 \text{ x } 10^{-5}\right)(0.04831) = 1.917 \text{ x } 10^{-5} \frac{mol}{min} \ .$$

Molar feed of methanol can be calculated as in Equation A.41.

$$F_{i,\,0} = \frac{Q_L \, \rho_L \, x_i}{MW_i} \qquad \text{(A.41)}$$

and

$$F_{CH_3OH,\,0} = \left(0.9 \frac{mL}{hr}\right)\left(\frac{1\,hr}{60\,min}\right)\left(1.09 \frac{g}{mL}\right)\left(\frac{12}{100}\right)\left(\frac{1\,mol}{32.04\,g}\right) = 6.12 \text{ x } 10^{-5} \frac{mol}{min}$$

Methanol conversion is calculated according to equation A.32.

$$X_{CH_3OH} = \frac{6.12 \text{ x } 10^{-5} - \left(2.040 \text{ x } 10^{-5} + 1.917 \text{ x } 10^{-5}\right)}{6.12 \text{ x } 10^{-5}} = 0.3534$$

Before calculating overall conversion, CO_2 mole fraction should be determined. It can be seen from Table A.3 that no CO exists at the exit.

$$y_{CO_2} = \frac{(259.8)(3.3)}{3336.5} = 0.2570$$

Total carbonaceous species molar flow in the system can be calculated by equation A.35.

$$F_{C,\,total} = (9.70)\left(4.089 \text{ x } 10^{-5}\right)(0.04831 + 0.2570) + 2.040 \text{ x } 10^{-5} = 1.415 \text{ x } 10^{-4} \frac{mol}{min}$$

Having calculated all necessary constants, overall conversion can be calculated as in equation A.36.

$$X_{overall} = \frac{(9.70)\left(4.089 \text{ x } 10^{-5}\right)(259.8)(3.3)}{\left(1.415 \text{ x } 10^{-4}\right)(3336.5)} = 0.7202$$

Lastly, selectivity of each product and hydrogen yield calculations are to be made. Since, there was no CO found in the analysis, CO selectivity is zero. Hydrogen mole fraction is

$$y_{H_2} = \frac{(4367.3)(0.35)}{3336.5} = 0.4581$$

and formaldehyde molar feed can be calculated as

$$F_{FA,\,0} = \left(0.9\,\frac{mL}{hr}\right)\left(\frac{1\,hr}{60\,min}\right)\left(1.09\,\frac{g}{mL}\right)\left(\frac{34.5}{100}\right)\left(\frac{1\,mol}{30.03\,g}\right) = 1.878 \text{ x } 10^{-4}\frac{mol}{min}$$

Hydrogen and carbon dioxide selectivity values are

$$S_{H_2} = \frac{(9.70)\left(4.089 \text{ x } 10^{-5}\right)(0.4581)}{\left(6.12 \text{ x } 10^{-5}\right)(0.3534) + \left(1.878 \text{ x } 10^{-4}\right)(1)} = 0.868\ ,$$

$$S_{CO_2} = \frac{(9.70)\left(4.089 \text{ x } 10^{-5}\right)(0.2570)}{\left(6.12 \text{ x } 10^{-5}\right)(0.3534) + \left(1.878 \text{ x } 10^{-4}\right)(1)} = 0.487\ .$$

Hydrogen yield is

$$Y_{H_2} = \frac{(9.70)\left(4.089 \text{ x } 10^{-5}\right)(0.4581)}{\left(6.12 \text{ x } 10^{-5}\right) + \left(1.878 \text{ x } 10^{-4}\right)} = 0.730\ .$$

APPENDIX B

CATALYST LOADING CALCULATIONS

In catalyst syntheses, copper and zinc metals are loading by a known amount to the designated support materials. Copper nitrate trihydrate ($Cu(NO_3)_2 \cdot 3H_2O$) and zinc nitrate tetrahydrate ($Zn(NO_3)_2 \cdot 4H_2O$) salts were employed as the metal precursors. Aforementioned wet impregnation technique was used. Molecular weights are 241.6 g/mol for $Cu(NO_3)_2 \cdot 3H_2O$, 63.55 g/mol for Cu, 261.4 g/mol for $Zn(NO_3)_2 \cdot 4H_2O$ and 65.38 g/mol for Zn.

B.1. CALCULATIONS FOR CuZn/SBA-15 and CuZn/CMK-3

For 1 g of SBA-15 18 wt. % metal loading was aimed in which 65/35 copper to zinc atomic ratio was held. Metallic copper (m_{Cu}) and zinc (m_{Zn}) are

$$m_{Cu} = (0.65)(0.18)(1) = 0.117\ g\,Cu\ ,$$

$$m_{Zn} = (0.35)(0.18)(1) = 0.0.63\ g\,Zn\ .$$

These metal loadings correspond to following salt amounts to be impregnated.

$$m_{Cu(NO3)2\,\cdot\,3\,H2O} = \frac{(0.117)(241.6)}{63.55} = 0.445\ g\ Cu\left(NO_3\right)_2 \cdot 3\,H_2O$$

$$m_{Zn(NO3)2\,\cdot\,4\,H2O} = \frac{(0.063)(261.4)}{65.38} = 0.252\ g\ Zn\left(NO_3\right)_2 \cdot 4\,H_2O$$

Similarly, for 1 g of CMK-3 18 wt. % metal loading with 65/35 copper to zinc atomic ratio was aimed. Calculation procedure is the same as CuZn/SBA-15. Therefore, 0.445 g $Cu(NO_3)_2 \cdot 3H_2O$ and 0.252 g $Zn(NO_3)_2 \cdot 4H_2O$ are to be impregranated.

B.2. CALCULATIONS FOR Cu/SBA-15

For 1 g of SBA-15 18 wt. % metallic copper loading was aimed. For 1 g SBA-15, copper amount to be loaded (m_{Cu}) is

$$m_{Cu} = (1)(0.18) = 0.18\ g\,Cu\ .$$

This corresponds to copper nitrate trihydrate amount (to be impregnated) of

$$m_{Cu(NO3)2 \cdot 3\,H2O} = \frac{(0.18)(241.6)}{63.55} = 0.684\ g\ Cu\left(NO_3\right)_2 \cdot 3\,H_2O\ .$$

APPENDIX C

GAS CHROMATOGRAPHY CONSTANTS

In this chapter, gas chromatography constants used in conversion, yield and selectivity calculations are presented. For a mixture of A and B, GC calibration factor for B (β_B) is calculated using Equation C.1.

$$\beta_B = \frac{n_B \beta_A A_A}{n_A A_B} \qquad \text{(Equation C.1)}$$

where A_i is the area under the peak and n_i is the number of moles of species i. Taking A as reference, β_A becomes one and Equation C.1 finally converts to Equation C.2 for any other molecule i.

$$\beta_i = \frac{n_i A_A}{n_A A_i} \qquad \text{(Equation C.2)}$$

Gas calibration factors for Porapak S column were performed with temperature program shown in Table 6.1 are presented in Table C.1. Methanol is taken as reference materials and correction factors are calculated according to Equation C.2.

Table C.1: Calibration factors for gaseous species for Porapak S column

Species	Retention Time (min)	Correction Factor (β)
H_2	0.80	0.35
CO	0.95	4.4
CO_2	1.50	3.3
CH_2O	6.80	1.23
H_2O	7.04	0.96
CH_3OH	8.30	1

APPENDIX D

XRD RELATED DATA AND CRYSTAL SIZE CALCULATIONS

In this chapter, PDF cards for the elements and molecules used are supplied and XRD patterns of spent synthesized catalysts are presented. Furthermore, the use of Scherrer equation to calculate crystal size is illustrated with an example.

D.1. PDF CARDS FOR ELEMENTS AND MOLECULES USED

In this section, PDF cards of different species are given in Table D.1-5.

Table D.1: PDF card for CuO

Formula: CuO
PDF Card No: 10800076
Radiation: $CuK\alpha_1$
Wavelength: 1.54060 Å

2θ, °	d-spacing (Å)	Intensity, %	h k l
32.48	2.754	5.5	1 1 0
35.39	2.535	25.8	0 0 2
35.54	2.524	100.0	-1 1 1
38.64	2.328	44.2	1 1 1
38.97	2.309	16.4	2 0 0
46.25	1.961	1.4	-1 1 2
48.85	1.863	19.4	-2 0 2
51.23	1.782	0.9	1 1 2
53.36	1.716	6.9	0 2 0
56.59	1.625	0.6	0 2 1
58.16	1.585	9.6	2 0 2
61.52	1.506	8.1	-1 1 3
65.66	1.421	9.6	0 2 2
66.34	1.408	6	-3 1 1
66.51	1.405	3.4	3 1 0
67.73	1.382	8.5	1 1 3

Table D.1 (cont'd): PDF card for CuO

2θ, °	d-spacing (Å)	Intensity, %	h k l
68.02	1.377	8.9	2 2 0
68.85	1.363	0.3	-2 2 1
71.84	1.313	0.2	-3 1 2
72.34	1.305	6.3	3 1 1
72.81	1.298	0.3	2 2 1
74.86	1.267	3.3	0 0 4
75.23	1.262	3.6	-2 2 2
79.56	1.204	0.1	0 2 3
80.26	1.195	1.1	-2 0 4
82.54	1.168	3.7	-3 1 3
82.86	1.164	3.2	2 2 2
83.34	1.159	0.2	3 1 2
83.69	1.155	2.1	4 0 0
86.81	1.121	0.8	-4 0 2
87.74	1.112	0.1	1 1 4
89.57	1.093	1.4	-1 3 1
91.44	1.076	3	1 3 1
95.27	1.043	0.6	2 0 4
96.59	1.032	0.1	-1 3 2
98.17	1.019	1.3	0 2 4
99.44	1.010	1.3	3 1 3
100.37	1.003	0.1	1 3 2
101.85	0.992	0.5	4 0 2
103.26	0.983	1.7	-1 1 5
103.53	0.981	2	-2 2 4
105.91	0.965	0.1	-4 2 1
107.05	0.958	1	4 2 0
109.23	0.945	1.8	-1 3 3
110.33	0.938	1.5	-4 2 2
111.59	0.931	0.8	-4 0 4
113.11	0.923	0.9	1 1 5
113.89	0.919	1.7	-3 3 1
115.30	0.912	0.7	1 3 3
117.14	0.903	1.3	-5 1 1
119.68	0.891	1.3	2 2 4
120.19	0.889	1.3	3 3 1
120.75	0.886	1	-5 1 2
122.42	0.879	0.1	3 1 4
123.89	0.873	0.1	0 2 5
127.48	0.859	1.1	4 2 2
127.78	0.858	0.5	0 4 0
128.10	0.857	0.7	-2 2 5
128.26	0.856	0.9	5 1 1
131.49	0.845	1	-5 1 3
132.57	0.841	0.6	-3 3 3
133.57	0.838	0.6	3 3 2
136.14	0.83	0.1	-1 1 6
140.45	0.819	0.7	-4 2 4

Table D.1 (cont'd): PDF card for CuO

2θ, °	d-spacing (Å)	Intensity, %	h k l
142.87	0.813	1	0 4 2
146.63	0.804	1	2 4 0
148.07	0.801	0.1	-2 4 1

Table D.2: PDF card for ZnO

Formula: ZnO

PDF Card No: 10751526

Radiation: $CuK\alpha_1$

Wavelength: 1.54060 Å

2θ, °	d-spacing (Å)	Intensity, %	h k l
32.07	2.789	56.2	1 0 0
34.47	2.600	40.4	0 0 2
36.53	2.458	100.0	1 0 1
47.79	1.902	20.0	1 0 2
57.17	1.610	28.3	1 1 0
63.10	1.472	25.7	1 0 3
67.07	1.394	3.6	2 0 0
68.49	1.369	19.0	1 1 2
69.77	1.347	9.6	2 0 1
72.67	1.300	1.5	0 0 4
77.64	1.229	2.8	2 0 2
81.65	1.178	1.5	1 0 4
90.31	1.086	5.8	2 0 3
93.91	1.054	1.8	2 1 0
96.44	1.033	5.5	2 1 1
99.21	1.011	2.9	1 1 4
104.11	0.977	2	2 1 2
104.46	0.974	4.6	1 0 5
108.21	0.951	0.6	2 0 4
111.93	0.93	2.2	3 0 0
117.59	0.901	5.6	2 1 3
123.29	0.875	2.7	3 0 2
125.44	0.867	0.4	0 0 6
135.04	0.834	2.2	2 0 5
137.09	0.828	0.6	1 0 6
140.39	0.819	0.7	2 1 4
146.22	0.805	1.5	2 2 0

Table D.3: PDF card for Al_2O_3

Formula: Al_2O_3 **PDF Card No:** 10709085 **Radiation:** $CuK\alpha_1$ **Wavelength:** 1.54060 Å			
2θ, °	**d-spacing (Å)**	**Intensity, %**	**h k l**
19.48	4.554	6.8	1 1 1
32.07	2.788	37.7	2 2 0
37.80	2.378	100.0	3 1 1
39.55	2.277	5.9	2 2 2
45.99	1.972	47.4	4 0 0
50.39	1.809	0.1	3 3 1
57.17	1.610	10.4	4 2 2
60.99	1.518	29.7	5 1 1
67.07	1.394	57.5	4 4 0
70.59	1.333	0.4	5 3 1
71.75	1.314	0.1	4 4 2
76.29	1.247	3.3	6 2 0
79.65	1.203	6.8	5 3 3
80.76	1.189	0.1	6 2 2
85.16	1.138	4.1	4 4 4
88.45	1.104	0.3	5 5 1
93.92	1.054	3.4	6 4 2
97.21	1.027	9.4	7 3 1
102.76	0.986	5.6	8 0 0
106.15	0.964	0.1	7 3 3
107.29	0.956	0.1	6 4 4
111.93	0.929	1.6	8 2 2
115.52	0.911	5.6	7 5 1
116.73	0.905	0.1	6 6 2
121.75	0.882	4.3	8 4 0
125.69	0.866	0.1	9 1 1
127.05	0.861	0.1	8 4 2
132.75	0.841	0.7	6 6 4
137.39	0.827	4.4	9 3 1
146.24	0.805	12.8	8 4 4

Table D.4: PDF card for Cu

Formula: Cu **PDF Card No:** 10714610 **Radiation:** CuKα_1 **Wavelength:** 1.54060 Å			
2θ, °	**d-spacing (Å)**	**Intensity, %**	**h k l**
43.29	2.088	100.0	1 1 1
50.42	1.809	42.7	2 0 0
74.08	1.279	17.2	2 2 0
89.87	1.091	15.6	3 1 1
95.08	1.044	4.2	2 2 2
116.83	0.904	1.8	4 0 0
136.34	0.83	5.7	3 3 1
144.51	0.809	5.4	4 2 0

Table D.5: PDF card for C

Formula: C **PDF Card No:** 411487 **Radiation:** CuKα_1 **Wavelength:** 1.54060 Å			
2θ, °	**d-spacing (Å)**	**Intensity, %**	**h k l**
26.68	3.376	100.0	0 0 2
42.22	2.139	2.0	1 0 0
44.39	2.039	6.0	1 0 1
50.45	1.807	1.0	1 0 2
54.54	1.681	4.0	0 0 4
59.69	1.548	1.0	1 0 3
77.24	1.234	3.0	1 1 0
83.18	1.160	3.0	1 1 2
86.82	1.121	1.0	0 0 6
93.59	1.057	1.0	2 0 1

D.2. XRD PATTERNS OF SPENT SYNTHESIZED CATALYSTS

XRD patterns of fresh and spent synthesized catalysts are given in Figures D.1-3.

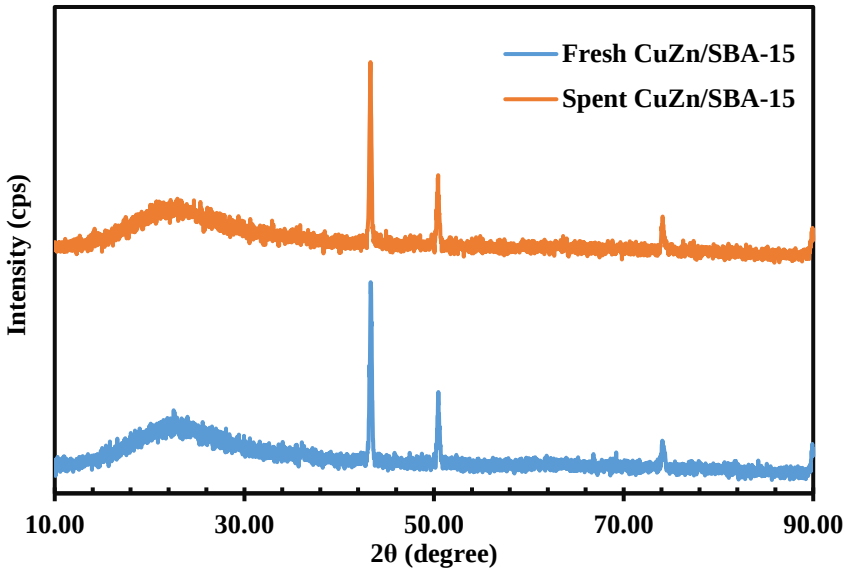

Figure D.1: XRD patterns of fresh and spent CuZn/SBA-15 catalysts

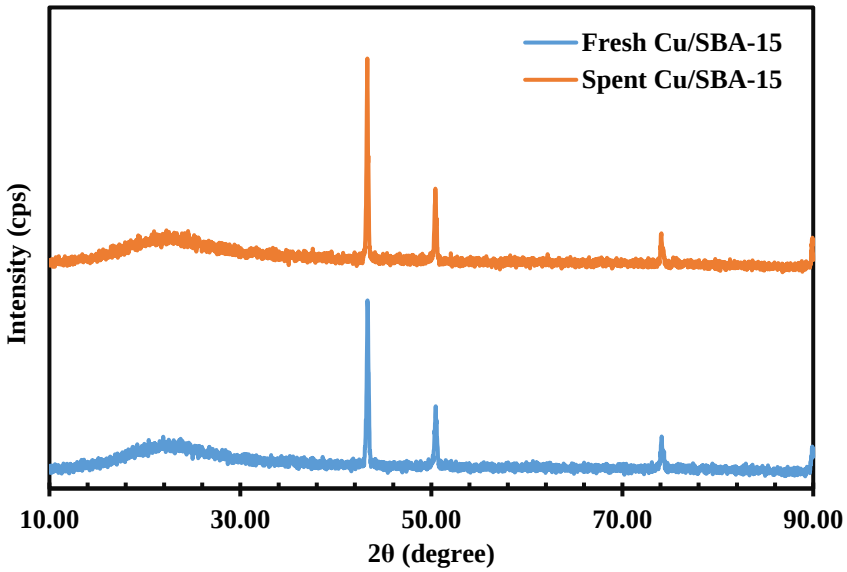

Figure D.2: XRD patterns of fresh and spent Cu/SBA-15 catalysts

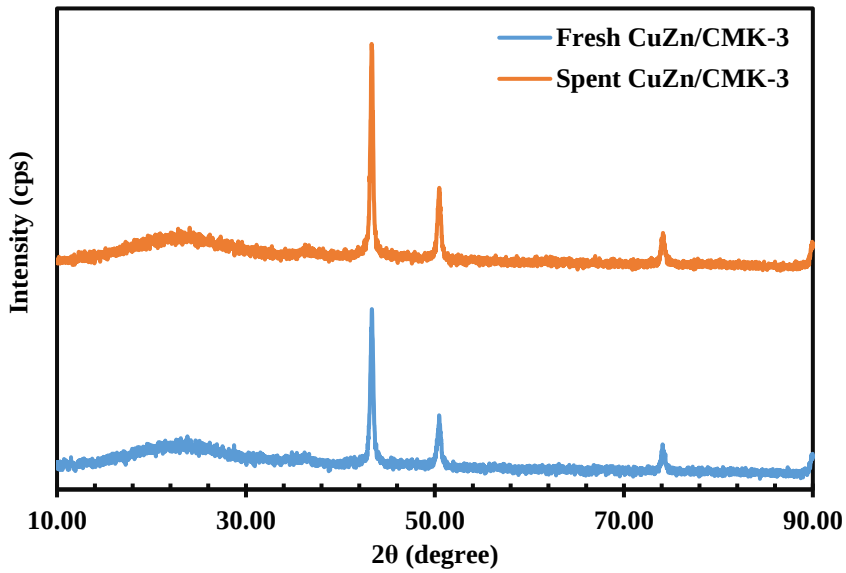

Figure D.3: XRD patterns of fresh and spent CuZn/CMK-3 catalysts

D.3. SAMPLE USE OF SCHERRER EQUATION TO CALCULATE CRYSTAL SIZES

In Chapter 7, copper crystal sizes for different catalysts were calculated by Scherrer equation. As an example Figure D.4 belonging to XRD spectrum of fresh CuZn/SBA-15 is used.

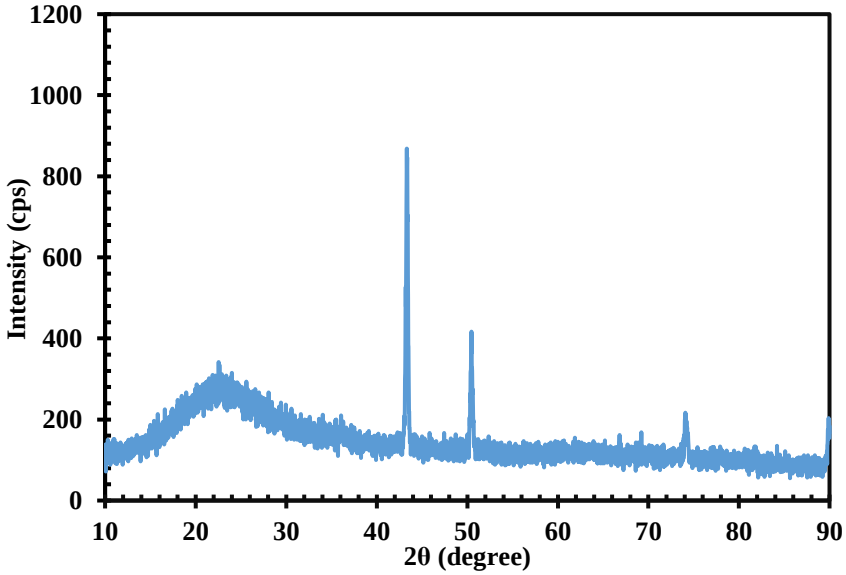

Figure D.4: Wide angle XRD pattern of fresh CuZn/SBA-15 catalyst

XRD peaks can be observed at 43.32°, 50.46°, 74.14° and 89.90° 2θ. These peaks belong to copper according to PDF card in Table D.4. Major peak, where the intensity of 100 %, is 43.32° according to PDF card. Therefore, crystal size is to be calculated from that 2θ angle. Scherrer equation can be written as the following.

$$t_{particle} = \frac{c\ \lambda}{\mathrm{B}\cos(\theta)}$$

where $t_{particle}$ is the crystal size (nm), c is the crystal shape factor that is 0.89, λ is the wavelength of the radiation, B is the full width at half max in radian, and θ is the Bragg angle in radian. B is observed to as 0.21°, λ is 0.10546 nm and 2θ is 43.32°. Finally, crystal size, $t_{particle}$, can be calculated as follows.

$$t_{particle} = \frac{(0.89)(0.15406)}{\left(\frac{0.21\,\pi}{180}\right)\left(\cos\left(\frac{43.32\,\pi}{(2)(180)}\right)\right)} = 40.3\ \text{nm}$$

APPENDIX E

RAW DATA

In this chapter, raw data of reaction activity tests are given in Table E.1-7.

Table E.1: Reaction activity test in the presence of HIFUEL R-120 at 175°C (liquid product sample: 0.469 g)

Time (min)	Mole Fraction			
	H_2	CO_2	H_2O	CH_3OH
37	0.349	0.194	0.394	0.063
72	0.403	0.224	0.295	0.077
105	0.393	0.218	0.303	0.085
136	0.338	0.189	0.400	0.073
164	0.344	0.196	0.384	0.075

Table E.2: Reaction activity test in the presence of HIFUEL R-120 at 200°C (liquid product sample: 0.389 g)

Time (min)	Mole Fraction			
	H_2	CO_2	H_2O	CH_3OH
2	0.375	0.183	0.432	0.009
34	0.479	0.227	0.279	0.015
59	0.479	0.228	0.273	0.020
88	0.380	0.182	0.420	0.018
110	0.391	0.186	0.403	0.020
149	0.379	0.185	0.415	0.021

Table E.3: Reaction activity test in the presence of HIFUEL R-120 at 225°C (liquid product sample: no liquid was obtained)

Time (min)	Mole Fraction				
	H_2	CO_2	H_2O	CH_3OH	CO
2	0.072	0.111	0.774	0.000	0.043
27	0.548	0.248	0.204	0.000	0.000
45	0.583	0.265	0.152	0.000	0.000
65	0.564	0.253	0.182	0.001	0.000
85	0.561	0.254	0.183	0.002	0.000
104	0.567	0.258	0.173	0.001	0.000

Table E.4: Reaction activity test in the presence of HIFUEL R-120 at 250°C (liquid product sample: no liquid was observed)

Time (min)	Mole Fraction			
	H_2	CO_2	H_2O	CO
22	0.045	0.210	0.700	0.045
47	0.542	0.246	0.212	0.000
72	0.555	0.247	0.198	0.000
96	0.562	0.247	0.191	0.000
125	0.513	0.227	0.260	0.000
147	0.510	0.226	0.201	0.000
182	0.519	0.229	0.287	0.000

Table E.5: Reaction activity test in the presence of CuZn/SBA-15 at 250°C (liquid product sample: 0.479 g)

Time (min)	Mole Fraction				
	H_2	CO_2	H_2O	CH_3OH	CH_2O
0	0.149	0.102	0.517	0.183	0.048
18	0.223	0.152	0.454	0.123	0.048
36	0.229	0.163	0.434	0.126	0.048
78	0.182	0.135	0.514	0.121	0.048
94	0.213	0.162	0.437	0.140	0.048
116	0.202	0.154	0.453	0.142	0.048
130	0.201	0.161	0.441	0.149	0.049
147	0.198	0.158	0.439	0.156	0.049
166	0.197	0.158	0.437	0.158	0.050

Table E.6: Reaction activity test in the presence of Cu/SBA-15 at 250°C (liquid product sample: 0.384 g)

Time (min)	Mole Fraction			
	H_2	CO_2	H_2O	CH_3OH
2	0.392	0.191	0.383	0.034
24	0.417	0.231	0.319	0.032
39	0.413	0.204	0.317	0.067
57	0.396	0.201	0.334	0.069
77	0.379	0.207	0.344	0.070
92	0.366	0.208	0.349	0.076
108	0.337	0.203	0.368	0.092
123	0.340	0.213	0.352	0.095
138	0.312	0.201	0.369	0.118

Table E.7: Reaction activity test in the presence of CuZn/CMK-3 at 250°C (liquid product sample: 0.783 g)

Time (min)	Mole Fraction				
	H_2	CO_2	H_2O	CH_3OH	CH_2O
11	0.148	0.123	0.602	0.116	0.011
56	0.086	0.089	0.650	0.165	0.011
73	0.101	0.113	0.592	0.183	0.011
103	0.081	0.102	0.629	0.177	0.011
119	0.087	0.114	0.595	0.193	0.011
137	0.081	0.109	0.605	0.194	0.011
151	0.088	0.124	0.555	0.220	0.013
169	0.074	0.109	0.616	0.190	0.011

APPENDIX F

THERMODYNAMIC CALCULATION OF HYDROGENATION OF FORMALDEHYDE

In Chapter 7, CuZn/CMK-3 catalyst was thought to convert formaldehyde to methanol according to the following reaction.

$$CH_2O + H_2 \longleftrightarrow CH_3OH$$

In order to determine which way the reaction is to proceed, K_{eq}, equilibrium constant at the reaction temperature, 250°C, has to be found. Gibbs free energy change of reaction equation is given below.

$$RT\ln\left(K_{eq}\right) = -\Delta G^{o}_{rxn} \qquad \text{(Equation F.1)}$$

Using F.1, one can find K_{eq} value of the reaction at the reference state, which 298 K and 1 atm. Van't Hoff equation is normally presented as in Equation F.2.

$$\frac{\mathrm{d}\ln\left(K_{eq}\right)}{\mathrm{d}T} = \frac{\Delta H^{o}_{rxn}}{RT^2} \qquad \text{(Equation F.2)}$$

However, Equation F.2 can be integrated to Equation F.3, if the heat of reaction is independent of temperature.

$$\ln\left(\frac{K_2}{K_1}\right) = -\frac{\Delta H^{o}_{rxn}}{R}\left(\frac{1}{T_2} - \frac{1}{T_1}\right) \qquad \text{(Equation F.3)}$$

For the aforementioned reaction, Gibbs free energy and heat of formation data is given in Table F.1.

Table F.1: Heat and Gibbs free energy of formation data for CH_2O and CH_3OH

Molecule	ΔH_f^o (kJ/mol)	ΔG_f^o (kJ/mol)
CH_2O	-115.97	-109.99
CH_3OH	-200.66	-161.96

Next step is to find the Gibbs free energy and heat of reaction, respectively.

$$\Delta G_{rxn}^{o} = -161.96 - (-109.99) = 51.97\ kJ/mol$$

$$\Delta H_{rxn}^{o} = -200.66 - (-115.97) = -84.69\ kJ/mol$$

Equation F.1 can be used now to find K_{eq} at 298 K.

$$K_{eq} = e^{\left(-\frac{-51970}{(8.314)(298)}\right)} = 1.288 \times 10^{9}$$

Assuming that the heat of reaction of formaldehyde hydrogenation does not change with respect to temperature appreciably, Equation F.3 can be used to find equilibrium constant at 250°C, which is 523 K.

$$K_{523} = \left(1.288 \times 10^{9}\right)\left(e^{\left(-\frac{-84690}{8.314}\left(\frac{1}{523}-\frac{1}{298}\right)\right)}\right) = 528.7$$

Finally, equilibrium constant (K_{eq}) for this reaction is 528.7 meaning that the reaction favors the methanol's side at this temperature.